

Investigation of Nanoparticle-Based Self-Assembly and Excitation Energy Transfer Processes

Ph.D. Thesis

by

JAMUNA KANARAM VAISHNAV



DISCIPLINE OF CHEMISTRY
INDIAN INSTITUTE OF TECHNOLOGY INDORE
FEBRUARY 2020

Investigation of Nanoparticle-Based Self-Assembly and Excitation Energy Transfer Processes

A THESIS

Submitted in partial fulfillment of the requirements for the award of the degree of
DOCTOR OF PHILOSOPHY

by

JAMUNA KANARAM VAISHNAV



DISCIPLINE OF CHEMISTRY
INDIAN INSTITUTE OF TECHNOLOGY INDORE
FEBRUARY 2020



INDIAN INSTITUTE OF TECHNOLOGY INDORE

CANDIDATE'S DECLARATION

I hereby certify that the work which is being presented in the thesis entitled **Investigation of Nanoparticle-Based Self-Assembly and Excitation Energy Transfer Processes** in the partial fulfilment of the requirements for the award of the degree of **DOCTOR OF PHILOSOPHY** and submitted in the **Discipline of Chemistry, Indian Institute of Technology Indore**, is an authentic record of my own work carried out during the time period from **June 2015** to **February 2020** under the supervision of **Dr. Tushar Kanti Mukherjee**, Associate Professor, Discipline of Chemistry, Indian Institute of Technology Indore. The matter presented in this thesis has not been submitted by me for the award of any other degree of this or any other institute.

Jamuna
26/02/2020

Signature of the student with date
(**JAMUNA KANARAM VAISHNAV**)

This is to certify that the above statement made by the candidate is correct to the best of my/our knowledge.

Tushar kanti Mukherjee
26-02-2020

Signature of Thesis Supervisor with date
(**DR. TUSHAR KANTI MUKHERJEE**)

MS. JAMUNA KANARAM VAISHNAV has successfully given her Ph.D. Oral Examination held on 05-11-2020

[Signature]
Dr. P. R. Sanyal

[Signature]

Tushar kanti Mukherjee

Signature of Chairperson (OEB)
Date: 05-11-2020

Signature of External Examiner
Date: 05-11-2020

Signature(s) of Thesis supervisor(s)
Date: 05-11-2020

[Signature]

[Signature]

Tushar kanti Mukherjee

Signature of PSPC Member #1
Date: 05-11-2020

Signature of PSPC Member #2
Date: 05-11-2020

Signature of Convener, DPGC
Date: 05-11-2020

[Signature]
Signature of Head of Discipline
Date: 05-11-2020

Acknowledgements

Firstly, I would like to express my sincere gratitude to my research supervisor Dr. Tushar Kanti Mukherjee for his careful guidance, constant encouragement and suggestions during the course of my Ph.D. research. His expertise and continuous effort in work have helped me to achieve the research goals successfully. The journey of my Ph.D. would not be easy without his help and diligent participation. I would like to thank him for his immense efforts to train me to become a good researcher and develop my skills in the experiments. All my learning from him will assist me in the future to become an independent researcher.

It's my great pleasure to thank my PSPC members Dr. Apurba K. Das and Dr. Satyajit Chatterjee, for their fruitful discussions and suggestions to improve our results.

I wish to express my gratitude to the Director of IIT Indore for his continuous support in every aspect.

I would like to thank IIT Indore for providing infrastructure and financial support.

I express my sincere thanks to former group members Dr. Surajit Chatterjee, Dr. Arpan Bhattacharya, and Dr. Roopali Prajapati for their great help to perform the experiments and it was a great pleasure to work with them. I am grateful to my juniors Bhaswati Sarkar, Somnath Das, Shallu Tanwar, Pushpender Yadav, Punam Pawe, Chinmaya K. Patel, Arun Dhanagar, Shivendra Singhs and Yashveer Yadav for their generous help and co-operation.

I would also like to thank Mr. Ravinder Kumar, Mr. Kinny Pandey, Mr. Ghanshyam Bhavsar, Mr. Manish Kushwaha, Ms. Vinita Kothari, and Mr. Rameshwar Dauhare for their technical support. I would also like to thank Ms. Anjali Bandiwadekar, Mr. Rajesh Kumar, and all library staff for their constant help, whenever required.

Further, I would like to acknowledge SIC, IIT Indore for instrumentation facilities. I would like to thank IISER Pune for TEM, AFM, and DLS facilities. I would also like to thank IISER Bhopal and SAIF, IIT Bombay, for zeta potential and XPS measurements, respectively. I sincerely thank Professor Anindya Datta from IIT Bombay for his help during DLS measurements.

I would personally like to extend my heartiest thanks to Dr. Santosh Kumar Singh for all his supports throughout my Ph.D. course. Without his help, it would not have been possible for me to achieve my goal. I am thankful to my friends Dibya Yadav and Shagufi Ansari for their continuous support and lively company.

Most importantly, it would have been impossible for me to reach here without the support, care, and love of my family.

JAMUNA K. VAISHNAV

Dedicated to
My Grandparents
&
My Parents

Abstract

Nanotechnology is an emerging scientific field having great potential for fundamental research and future technology. As the name implicit, nanomaterials are condensed matters having sizes in the nanometer range i.e., larger than atoms, but smaller than bulk solids. They are too big to behave like atoms but too small to act like the bulk solid. In the last two decades, various functional nanomaterials have been fabricated. These materials can be zero (0D), one (1D), two (2D), and three (3D) dimensional. Quantum dots (QDs) are theoretically described as a point like, or a 0D entity. QDs are typically composed of either single-element (Silicon (Si) or Germanium (Ge)) or binary compounds formed from combinations of II-VI (CdSe, CdTe, CdS, ZnO, ZnS, etc.), III-V (InP, GaAs), or IV-VI (PbS, PbSe) group elements. They are very important nanomaterials as they exhibit broad excitation spectra, size- and composition-tunable narrow emission from ultraviolet to near-infrared wavelength range, high luminescence quantum yield, and better stability against photobleaching compared to organic dyes. Similarly, metal nanoparticles (NPs) are nanoscopic materials with an overall dimension below 100 nm. Several transition metal NPs including gold (Au), silver (Ag), iron oxides (Fe_2O_3), copper (Cu) have been designed for various applications. Metal NCs are another class of nanomaterials that consist of few to several metal atoms with a core size in the range of 1-2 nm.

In recent times, there has been growing interest in designing new multifunctional self-assembled nanocomposites such as hybrid vesicles, polymersomes, hydrogels, nanocapsules, and colloidal coacervate droplets because of their vast potential in basic research as well as in technology-related fields. Self-assembly among the charged molecules such as synthetic and natural polymers, fatty acids, biological macromolecules, poly or oligopeptides are reported in literature and provide great details of the mechanism, structure, stability, and

sequestration properties of a wide range of coacervate droplets prepared mainly from organic molecules but there are no reports on the fabrication of organic-inorganic hybrid droplets. Vesicles from other amphiphilic molecules such as block copolymers, dendrimers, polypeptides, surfactants, and fatty acid have been fabricated successfully with enhanced colloidal and mechanical stability compared to conventional phospholipid vesicles. Although these recent studies highlight the multifunctional properties of organic-inorganic hybrid plasmonic vesicles, there is a growing interest in the fabrication of stable stimuli-responsive inherently luminescent hybrid vesicles for in vivo bioimaging applications. There are various applications of QD based self-assembled nanoassemblies including chemical and biological sensing, energy harvesting, and excitation energy transfer (EET) processes.

EET from various photoexcited donors to ground-state acceptors have been studied thoroughly in the recent past due to its importance in photovoltaics, light-emitting diodes, sensors, and bioimaging. The EET from a photoexcited donor to a nearby acceptor is mainly described by Förster resonance energy transfer (FRET) and nanometal surface energy transfer (NSET) mechanisms. The tuning of intermolecular FRET has been demonstrated in various systems such as micelles, reverse micelles, polymer matrices, spherical vesicles, and proteins. Among these, FRET processes across the liposome bilayer are of particular interest due to its potential in exploring various membrane related biophysical processes such as membrane fusion, trafficking, and receptor-ligand interactions. On the other hand, metal and semiconductor NPs based donor-acceptor nanocomposite systems have attracted considerable attention due to their size-dependent optoelectronic properties, which allow easy tuning of various energy transfer related parameters. Several studies have shown that the intrinsic emission properties of QDs/dyes can be efficiently tuned near a plasmonic NP as a consequence of long-range electromagnetic coupling between exciton and localized surface

plasmon resonance (LSPR) of NPs. Extensive experimental and theoretical studies have been performed to understand the fundamental mechanism behind this long-range electromagnetic coupling and subsequent fluorescence quenching at the metal NP surface. The quenching of excited donors in the presence of metal surface is demonstrated earlier by Chance *et al.* and later extended by Persson and Lang by using a Fermi golden rule. Modification of the CPS-Kuhn expression by including the size-dependent electronic terms proved to be an efficient method to explain the size-dependent NSET. These EET theories have been extensively utilized to understand the various complex chemical and biological processes across lipid bilayers of liposomes and cell membranes. Various cell membrane mimicking systems such as micelles, liposomes, and polymersomes with biocompatible interfaces have been utilized to understand the fundamental interactions with various NPs.

In this thesis, the photophysical properties of MSA-capped CdTe QDs have been investigated using various spectroscopic, microscopic techniques and utilized them as a luminescent marker to understand the self-assembly process in the presence of poly (diallyldimethylammonium chloride) (PDADMAC) polymer and hexadecyltrimethylammonium bromide (CTAB) surfactant. Furthermore, the detailed mechanism and tuning of EET in the presence of liposome from various photoexcited donors such as MSA-capped CdTe QDs and 4',6-diamidino-2-phenylindole (DAPI) to gold (Au) NPs, silver (Ag) NPs and Ag NC as acceptors have been demonstrated.

The overall aim of the work described in the thesis is to explore the interaction of luminescent QDs with oppositely charged polymers and surfactants as well as to understand EET across the lipid bilayers of liposomes.

The contents of each chapter included in the thesis are discussed briefly as follows:

1. Introduction

In this chapter, a brief overview of optoelectronic and physicochemical properties of different NPs, such as QDs, metal NPs, and NCs have been provided. In addition, various NP-based self-assembly processes have been briefly explained. Finally, different theories of EET have been discussed in detail.

2. Materials and Experimental Techniques

This chapter contains the details of all the materials utilized for the work described in this thesis. The complete synthesis methods of CdTe QDs, Au NPs, Ag NPs, and Ag NCs, as well as their detailed characterization, have been discussed here. This chapter also covers the details of various experimental techniques/instruments used for the work described in this thesis.

3. Highly Photostable and Two-Photon Active Quantum Dot–Polymer Multicolor Hybrid Coacervate Droplets

The formation of a new class of luminescent hybrid coacervate droplets from a binary mixture of CdTe QDs and PDADMAC in aqueous medium has been demonstrated in this chapter. These hybrid droplets are found to be stable over a broad range of composition, pH, and ionic strength of the medium. The confocal laser scanning microscopy (CLSM) and epifluorescence imaging reveal its intrinsic luminescent, photostable, and nonbleaching PL properties. Our study indicates that electrostatic interactions between negatively charged QDs and positively charged PDADMAC lead to coacervation. These hybrid droplets exhibit preferential sequestration of organic dyes and serum albumins. In addition, using two-photon (2P) confocal microscopy, it has been shown that these hybrid droplets are ideal candidates for 2P bio-imaging applications.

4. Surfactant-Induced Self-assembly of CdTe Quantum Dots into Multicolor Luminescent Hybrid Vesicle

In this chapter, the interactions of CdTe QDs with CTAB surfactant and subsequent formation of self-assembled multicolor luminescent vesicles in the aqueous medium have been demonstrated. A continuous phase sequence from clear (C1) to turbid (T1), precipitate (P), turbid (T2), and clear (C2) has been observed for QD solution upon increasing the concentration of positively charged CTAB, indicating dynamic equilibrium between various self-assembled supramolecular structures. Spherical vesicles are observed in the T1 and T2 regions, and they are inherently luminescent due to the presence of self-assembled QDs. Fabrication of multicolor luminescent vesicles has been demonstrated by tuning the size of CdTe QD. These self-assembled vesicles are shown to encapsulate Rhodamine 6G dye without any structural disruption. Furthermore, it has been shown that these luminescent vesicles are quite stable in neutral and basic pH (pH = 6.5–11), however, unstable in acidic pH (pH = 4.5–5.5). It has been observed that this pH-responsive structural change is totally reversible.

5. Tuning of Resonance Energy Transfer from 4',6-Diamidino-2-Phenylindole to an Ultrasmall Silver Nanocluster Across the Lipid Bilayer

Fabrication of a simple liposome-based donor-acceptor FRET system using DAPI as the donor and an ultrasmall ligand-capped Ag NC as the acceptor has been discussed in this chapter. The synthesized dipalmitoylphosphatidylcholine (DPPC) liposomes are small unilamellar vesicles (SUV) with a mean hydrodynamic diameter of 86.91 ± 6.41 nm. The synthesized Ag NCs have the majority of Ag₄ and Ag₅ cores. For the present study, two distinct DAPI-liposome nanocomposites have been fabricated where DAPI binds either at the outer surface or hydrophilic core of the liposome. The steady-state and time-resolved fluorescence spectroscopic studies revealed that the

FRET efficiency is strongly dependent on the location of donor DAPI within the DPPC liposome matrix. Energy transfer efficiency decreases when DAPI is associated at the outer surface of liposome compared to that in the bulk aqueous medium. On the other hand, encapsulation of DAPI into the hydrophilic aqueous core of liposome results in complete inhibition of the FRET process as a consequence of increased separation distance beyond the FRET range. Our study illustrates that the present DAPI–Ag NC pair can be used as a FRET marker to explore various fundamental processes across the cell membrane.

6. Long-Range Resonance Coupling-Induced Surface Energy Transfer from CdTe Quantum Dot to Plasmonic Nanoparticle

In this chapter, the size and wavelength-dependent NSET between CdTe QDs and plasmonic NPs (Au and Ag) have been demonstrated by using steady-state and time-resolved PL spectroscopy. Three differently sized CdTe QDs are synthesized namely, 2.1 ± 0.7 , 3.1 ± 0.4 , and 3.9 ± 0.3 nm with emission in green, yellow, and red region of the electromagnetic spectrum, respectively. Our results show that both the luminescence intensity and lifetime of green QDs quench significantly in the near field of 20 nm-sized Au NPs. In contrast, the luminescent intensity and lifetime of yellow and red QDs remain unaltered in the presence of Au NPs. Furthermore, it has been observed that quenching efficiency of the green QD-Au NP pair decreases due to ligand exchange at the surface of Au NPs with poly (ethylene glycol) methyl ether thiol (PEG-SH). These results have been explained by considering a size-dependent NSET model proposed by Strouse *et al.* On the contrary, irrespective of the sizes of QDs, significant PL quenching has been observed in the presence of 10 nm-sized citrate-capped Ag NPs as a consequence of photoinduced electron transfer (PET). The current findings of size and wavelength-dependent long-range energy transfer in a hybrid QD-metal NP system can be useful to

understand and optimize the performance of various nanophotonic devices.

7. Selective Uptake and Modulation of Nanometal Surface Energy Transfer from Quantum dot to Au Nanoparticle Across Lipid Bilayer of Liposomes

The time-dependent selective uptake of 2.3 ± 0.5 nm-sized CdTe QDs into SUV of DPPC in its gel phase and subsequent alteration of NSET with 18.0 ± 0.2 nm-sized citrate-capped Au NPs have been demonstrated in this chapter. The interactions between CdTe QD and Au NP across the lipid bilayer of DPPC liposomes have been explored by monitoring the NSET process using PL spectroscopy. The time-dependent selective partitioning of QDs into the liposomal phase has been demonstrated using CLSM and atomic force microscopy (AFM). It has been observed that instant mixing of QDs and Au NPs with liposomes does not alter the extent of NSET between QD-Au NP pairs relative to that in the absence of liposome. However, equilibrating the binary mixture of liposome and QDs for 24 h at room temperature leads to the formation of liposome-encapsulated QD (LipQD) which does not take part in NSET with Au NPs. In contrast, equilibrating the ternary mixture of QDs, liposomes, and Au NPs for 24 h results in the formation of Au NP adsorbed QD-encapsulated liposomes (AuLipQD) which exhibit a moderate amount of NSET from encapsulated QDs to the adsorbed Au NPs at the surface of liposomes. It has been observed that the efficiency of NSET decreases from 62% in the bulk aqueous medium to 24% in the AuLipQD complex. Our present findings may be useful to understand the fundamental interaction of other metal and semiconductor NPs with liposomes and cell membranes for various drug-delivery and bio-imaging applications.

8. Conclusions and Future Scope

The conclusions of the thesis can be described as follows:

- 1) It has been shown that electrostatic interactions between oppositely charged CdTe QDs and PDADMAC lead to the formation of self-assembled inherently luminescent coacervate droplets in an aqueous medium.
- 2) The interactions of negatively charged CdTe QDs with positively charged CTAB surfactants lead to the formation of the pH-responsive multicolor hybrid vesicle in an aqueous medium.
- 3) The selective association of donor DAPI with the lipid bilayer of DPPC liposomes significantly alters the FRET process between DAPI and Ag NC. The energy transfer efficiency decreases from a value of 0.76 in bulk aqueous medium to a value of 0.39 for surface-associated DAPI in the presence of liposome.
- 4) The long-range EET from negatively charged CdTe QDs to negatively charge citrate-capped Au NPs shows the size as well as wavelength-dependent electromagnetic coupling. In contrast, the observed PL quenching of CdTe QDs in the presence of Ag NPs having LSPR significantly off resonance with the excitonic emission of all the three differently-sized QDs arises due to nonradiative PET process.
- 5) The study reveals the effect of the partitioning of QDs and Au NPs across the lipid bilayer of DPPC liposomes on the extent of EET. It has been observed that the efficiency of NSET decreases from 62% in bulk aqueous medium to 24% in AuLipQD nanocomposites due to the increase in the effective mean separation distance from 18.7 to 21.0 nm.

Further, the relevant future scope of the work described in this thesis has been discussed briefly.

List of Publications

- 1) **Vaishnav J. K.**, Mukherjee T. K. (2019), Highly photostable and two-photon active quantum dot–polymer multicolor hybrid coacervate droplets. *Langmuir*, 35, 11764-11773. (DOI: 10.1021/acs.langmuir.9b01783) (Impact Factor: **3.68**)
- 2) **Vaishnav J. K.**, Mukherjee T. K. (2019), Surfactant-induced self-assembly of CdTe quantum dots into multicolor luminescent hybrid vesicles. *Langmuir*, 35, 6409-6420. (DOI: 10.1021/acs.langmuir.9b00357) (Impact Factor: **3.68**)
- 3) **Vaishnav J. K.**, Mukherjee T. K. (2017), Tuning of resonance energy transfer from 4',6-diamidino-2-phenylindole to an ultrasmall silver nanocluster across the lipid bilayer. *Phys. Chem. Chem. Phys.*, 19, 27305-27312. (DOI:10.1039/C7CP05225A) (Impact Factor: **3.67**)
- 4) **Vaishnav J. K.**, Mukherjee T. K. (2018), Long-range resonance coupling-induced surface energy transfer from CdTe quantum dot to plasmonic nanoparticle. *J. Phys. Chem. C*, 122, 28324-28336. (DOI: 10.1021/acs.jpcc.8b08757) (Impact Factor: **4.31**)
- 5) **Vaishnav J. K.**, Mukherjee T. K. (2020), Selective uptake and modulation of nanometal surface energy transfer from quantum dot to Au nanoparticle across lipid bilayer of liposomes, *J. Photochem. Photobiol. A*, 401, 112773. (DOI: 10.1016/j.jphotochem.2020.112773) (Impact Factor: **3.3**)

Table of Contents

1.	List of Schemes	xxiii
2.	List of Figures	xxv
3.	List of Tables	xxxiii
4.	Acronyms	xxxv
5.	Nomenclature	xxxvii
 Chapter 1: Introduction		 1-52
1.1.	Evolution of Nanoparticles	2
	1.1.1. Metal NPs	3
	1.1.2. Metal Nanocluster (NCs)	7
	1.1.3. Semiconductor NPs or Quantum Dots	9
1.2.	QD-Based Self-Assembled Nanostructure	11
	1.2.1. QD-Polymer Self-Assembled Coacervates	12
	1.2.2. QD-Surfactant Self-Assembled Vesicles	14
1.3.	Excitation Energy Transfer (EET)	16
	1.3.1. Förster Resonance Energy Transfer (FRET)	18
	1.3.1.1. FRET in Liposome	19
	1.3.2. Metal NP-Based Excitation Energy Transfer	21
	1.3.2.1. The Gersten-Nitzan (G-N) Model	21
	1.3.2.2. CPS-Kuhn Model	22
	1.3.2.3. Size-Dependent NSET Theory	22
	1.3.2.4. NSET Processes in Liposome	26

1.4.	Overview of the Thesis	27
1.5	References	29
Chapter 2: Materials and Experimental Techniques		53-67
2.1.	Introduction	54
2.2.	Chemicals	54
2.3.	Synthesis	54
	2.3.1. MSA-Capped CdTe QDs	54
	2.3.2. Citrate- Capped Au NPs	55
	2.3.3. Citrate- Capped Ag NPs	56
	2.3.4. PEG-Capped Au NPs	56
	2.3.5. Dihydrolipoic Acid-Capped Silver Nanoclusters (Ag NCs)	56
2.4.	Sample Preparations	57
2.5.	Instrumentation	59
	2.5.1. UV-visible Spectroscopy	59
	2.5.2. PL Spectroscopy	59
	2.5.3. Time-Correlated Single Photon Counting Technique (TCSPC)	60
	2.5.4. Fourier Transform Infrared (FTIR) Spectrometer	60
	2.5.5. Transmission Electron Microscope (TEM)	60
	2.5.6. Field-Emission Scanning Electron Microscope (FE-SEM)	61
	2.5.7. Dynamic Light Dcattering (DLS) and Zeta Potential	61
	2.5.8. Confocal Laser Scanning Microscopy (CLSM)	61

2.5.9. Epifluorescence Imaging	61
2.5.10. Atomic Force Microscopy	62
2.5.11. Liquid Chromatography-Mass Spectrometer (LC-MS)	62
2.5.12. Powder X-ray Diffractometer (PXRD)	63
2.5.13. X-ray Photoelectron Spectroscopy (XPS)	63
2.6. References	64
Chapter 3: Highly Photostable and Two-Photon Active Quantum Dot–Polymer Multicolor Hybrid Coacervate Droplets	68-91
3.1. Introduction	69
3.2. Results and Discussion	70
3.2.1. Characterization of CdTe QDs	70
3.2.2. Initial Nanocomposite Formation between QD and PDADMAC	72
3.2.3. Coacervation and Hybrid Droplet Formation	75
3.2.4. Colloidal Stability as a Function of pH and Ionic Strength	80
3.2.5. PL Behavior of Hybrid Droplets	81
3.2.6. Fabrication of Mixed Two-Color and Two-Photon Active Hybrid Droplets	84
3.3. Conclusions	86
3.4. References	87

Chapter 4: Surfactant-Induced Self-Assembly of CdTe Quantum Dots into Multicolor Luminescent Hybrid Vesicles	92-121
4.1. Introduction	93
4.2. Results and Discussion	94
4.2.1. Phase Behavior of Binary Mixtures of QD and Different Surfactants	94
4.2.2. PL Behavior of QD-CTAB Binary Mixture in the C1 and C2 Region	96
4.2.3. FESEM, AFM and DLS Measurements of Self-Assembled Structures in the T1 and T2 Region	102
4.2.4. Confocal Imaging of the Luminescent Vesicles and Encapsulation of Rh6G	108
4.2.5. pH-Responsive Reversible Assembly and Disassembly of Luminescent Vesicles	112
4.3. Conclusions	116
4.4. References	117
Chapter 5: Tuning of Resonance Energy Transfer from 4',6-Diamidino-2-Phenylindole to an Ultrasmall Silver Nanocluster Across the Lipid Bilayer	122-141
5.1. Introduction	123
5.2. Results and Discussion	124
5.2.1. Characterization of Liposomes and Ag NC	124
5.2.2. Interaction of DAPI with Ag NC and Liposomes	126
5.2.3. Interaction of Complex I (Surface) with Ag NC	129
5.2.4. Interaction of Complex II (Core) and Ag NC	133

5.3.	Conclusions	136
5.4.	References	137
Chapter 6: Long-Range Resonance Coupling-Induced Surface Energy Transfer from CdTe Quantum Dot to Plasmonic Nanoparticle		142-180
6.1.	Introduction	143
6.2.	Results and Discussion	144
	6.2.1. Characterization of Au NPs	144
	6.2.2. PL Measurements of CdTe QDs in the Presence of Au NPs	146
	6.2.3. Effect of Ligand Exchange on the EET	161
	6.2.4. Mechanism of EET from QDs to Au NPs	165
6.3.	Conclusions	169
6.4.	References	171
Chapter 7: Selective Uptake and Modulation of Nanometal Surface Energy Transfer from Quantum Dot to Au Nanoparticle Across Lipid Bilayer of Liposomes		181-208
7.1.	Introduction	182
7.2.	Results and Discussion	184
	7.2.1. Interactions of QDs and Au NPs with Liposome	184
	7.2.2. Influence of Au NPs on the PL Properties of LipQD and AuLipQD Nanocomposites.	192
7.3.	Conclusions	199
7.4.	References	201

Chapter 8: Conclusions and Future Scope	209-214
8.1. Conclusions	210
8.2. Scope for Future Works	213

List of Schemes

Chapter 1

Scheme 1.1.	Organic and inorganic nanoparticles.	3
Scheme 1.2.	Schematic diagram illustrating the localized surface plasmon resonance in metal NPs.	4
Scheme 1.3.	Schematic representation of various applications of NCs.	8
Scheme 1.4.	Illustration of quantum confinement effect in bulk and semiconductor.	9
Scheme 1.5.	Schematic representation of different types of self-assembled nanomaterials.	11
Scheme 1.6.	Schematic representation of coacervation process.	12
Scheme 1.7.	Schematic representation of different type of surfactant aggregates (a) spherical, (b) globular, (c) rod, and (d) spherical bilayers like structures.	15
Scheme 1.8.	Spectral overlap between emission spectrum of the donor and excitation spectrum of the acceptor.	17
Scheme 1.9.	Schematic representation of different regions of liposome.	20

Chapter 2

Scheme 2.1.	Synthesis of MSA- capped CdTe QDs.	55
Scheme 2.2.	Schematic representation of our home- built epi-fluorescence microscopy.	62

Chapter 3

Scheme 3.1.	Schematic representation of the droplet formation in the T1 and T2 regions via QD-PDADMAC nanocomposites.	78
--------------------	---	----

Chapter 4

Scheme 4.1.	Schematic representation of the self-assembly processes in the QD-CTAB binary mixture.	106
--------------------	--	-----

Chapter 5

- Scheme 5.1.** Schematic representation of liposome mediated tuning of FRET between DAPI and Ag NC. 135

Chapter 6

- Scheme 6.1.** Schematic representation of valence band (VB) and conduction Band (CB) position of green, yellow and Red QDs with respect to fermi level of Au and Ag NPs. 155

List of Figures

Chapter 3

- Figure 3.1.** AFM images of (a) green, (b) yellow and (c) red CdTe QDs. The insets show the height profile histograms with mean height. (d) TEM image of green CdTe QDs. The insets show the size distribution histograms with mean sizes. (e) Normalized absorption and PL spectra of green, yellow, and red QDs. (f) The estimated zeta potential of green, yellow and red QDs. (g) XRD pattern of CdTe QDs. (g) X-ray diffraction (XRD) pattern of CdTe QDs. (h) FTIR spectra of MSA (upper panel) and synthesized MSA-capped CdTe QD (lower panel). XPS spectra of (i) Cd 3d and (j) Te 3d. 71
- Figure 3.2.** Changes in the (a) absorpition spectra, (b) PL spectra ($\lambda_{ex} = 445$ nm), and (c) PL decay traces ($\lambda_{ex} = 445$ nm; $\lambda_{em} = 523$ nm) of green QDs in the presence of 5.2 μ M PDADMAC. (d) SEM image of QD-PDADMAC binary mixture in the C1 region. Confocal images (e) DIC, (f) fluorescence, and (g) merge of QD-PDADMAC binary mixture. 72
- Figure 3.3.** Change in the PL intensity ratio of green QD in the presence of different concentrations of PVP. 75
- Figure 3.4.** (a) Photographs of QD-PDADMAC binary solution in the presence of 25.5 (T1), 52.0 (P), and 130 μ M (T2) of PDADMAC (Red circle indicates the precipitate phase of QD-PDADMAC binary mixture). (b) Plot of turbidity against PDADMAC monomer molar concentrations. FESEM images of the binary mixtures in the (c) T1, and (d) T2 regions of the phase profile. (e) Hydrodynamic size distribution of droplets in the T1 and T2 regions. (f) ξ potentials of droplets in the T1 and T2 regions. 76
- Figure 3.5.** Size distribution histograms estimated from FESEM images of droplets in the (a) T1, and (b) T2 region. 77
- Figure 3.6.** FESEM images of droplets in the (a) T1, and (b) T2 regions showing coalescence 77

- phenomenon. (Red arrows indicate representative coalescence intermediates).
- Figure 3.7.** (a) Changes in the turbidity of the binary mixture as a function of solution pH in the T1 and T2 regions. The inset shows the FESEM image of the T1 region at pH 3. (b) Changes in the turbidity of the binary mixture as a function of NaCl concentrations in the T1 and T2 regions. 80
- Figure 3.8.** Confocal images (DIC, fluorescence, and merge) of coacervate droplets prepared with green QDs in the (a) T1, and (b) T2 region along with droplets prepared from red QDs in the (c) T1 region. (d) Confocal image showing coalescence of green and red color coacervate droplets prepared separately from green and red color QDs with PDADMAC aqueous solution. Yellow color appears due to the coalescence of green and red color droplets. 81
- Figure 3.9.** Epifluorescence images of droplets in the (a) T1, and (b) T2 regions. (c) Representative intensity trajectories of individual coacervate droplets in the T1 and T2 regions of the binary mixture along with green QD. 83
- Figure 3.10.** (a) Illustration of the mixed two-color droplet formation from green and red QDs mixture. (b) Confocal images in the green and red channels along with their DIC and merge images showing the formation of mixed two-color droplets from green and red QDs. (c) Schematic representation of the 2P excitation and emission of mixed two-color droplets upon 800 nm laser irradiation. (d) 2P confocal images of mixed two-color droplets in the green (490-550 nm) and red (570-670 nm) channels along with their merge image. 84

Chapter 4

- Figure 4.1.** (a) Photographs of QD-CTAB binary mixtures at different concentrations of CTAB (Red circles indicate the precipitate phase of the QD- 94

	CTAB binary mixture). (b) Phase sequences of the binary mixture as a function of CTAB concentrations. (c) Plot of absorbance at 650 nm with molar concentrations of CTAB in the binary mixture. The concentration of QD is fixed at 0.33 μ M.	
Figure 4.2.	Changes in the absorbance ($\lambda=650$ nm) of QD in the presence of different concentrations of (a) SDS and (b) TX-100 surfactants.	95
Figure 4.3.	Changes in the (a) Absorption spectra, (b) PL spectra ($\lambda_{ex}=445$ nm), and (c) PL decay traces ($\lambda_{ex}=445$ nm; $\lambda_{em}=520$ nm) of green QDs in the presence of 0.01 and 10 mM CTAB.	96
Figure 4.4.	Changes in the PL intensity ratio of QD in the presence of (a) SDS, and (b) TX-100 surfactants.	97
Figure 4.5.	The Hill plot using fluorescence intensity of QD in the absence and presence of different concentrations of CTAB in the C1 region of the phase profile.	98
Figure 4.6.	PL images of green QDs in the presence of (a) 0 mM, (b) 0.01 mM, and (c) 10 mM CTAB. Representative intensity profiles of luminescent spots in the presence of (d) 0 mM, (e) 0.01 mM, and (f) 10 mM CTAB.	101
Figure 4.7.	FESEM images of QD-CTAB binary mixture in the presence of (a), (b) 0.08 mM, (c), (d) 0.2 mM, and (e), (f) 1.5 mM CTAB. Size distribution histograms estimated from FSEM measurements for (g) 0.08 mM, (h) 0.2 mM, and (i) 1.5 Mm concentration of CTAB. (j) AFM Image of QD-CTAB binary mixture at 0.2 mM CTAB with cross section analysis.	103
Figure 4.8.	Size distribution histograms obtained from DLS measurements of QD-CTAB binary mixture in the presence of (a) 0.08 mM, (b) 0.2 mM, and (c) 1.5 mM CTAB. (d) Changes in the ζ values of self-assembled vesicles as a function of CTAB concentrations.	105
Figure 4.9.	Confocal microscopy images of green QDs in the presence of (a) 0.08 mM, (b) 0.2 mM, and (c) 1.5 mM CTAB. Pink arrows indicate fusion	109

of vesicles. (d) Confocal microscopy images of red QDs in the presence of 0.5 mM CTAB.

- Figure 4.10.** Confocal images of the binary mixture in the presence of (a) 0.08, (b) 0.2, and (c) 1.5 mM CTAB showing fusion events with various fusion intermediates (Red arrows showing few representative fusion events). 110
- Figure 4.11.** Confocal microscopy images showing encapsulation of Rh6G dye inside the self-assembled vesicles formed in the presence of 1.5 mM CTAB. 111
- Figure 4.12.** Photographs of QD-CTAB binary mixture in the presence of 0.2 mM CTAB (T1 region) at pH 4.7 and 7.5. 112
- Figure 4.13.** (a) PL spectra and (b) PL lifetime decay curves of QD and binary mixture in the T2 region at pH 4.7. 112
- Figure 4.14.** (a) Photographs of QD-CTAB binary mixture at pH 4.7 and 7.5 in the presence of 1.5 mM CTAB. FESEM images QD-CTAB binary mixture at pH (b) 7.5, (c) 4.7 and (d) 7.5 in the presence of 1.5 mM CTAB. 113
- Figure 4.15.** FESEM images of QD-CTAB binary mixture in the presence of 0.2 mM CTAB upon continuous change in pH from (a) 7.5, (b) 4.7, and (c) 7.5. 114
- Figure 4.16.** Confocal microscopy images of QD-CTAB binary mixture in the presence of 1.5 mM CTAB upon continuous change in pH from (a) 7.5, (b) 4.7, and (c) 7.5. 115

Chapter 5

- Figure 5.1.** (a) SEM image of liposome. Size distribution histogram of liposomes estimated from (b) SEM and (c) DLS measurements. 125

Figure 5.2.	FTIR spectra of dihydrolipoic acid (DHLA) and synthesized DHLA-capped Ag NC.	124
Figure 5.3.	(a) HRTEM image of Ag NC. (b) Electrospray ionization (ESI) mass spectrum of DHLA-capped Ag NC in 1:1 water-methanol mixture (L represents DHLA ligand). (c) The normalized absorption (blue line) and PL (red line) spectra of Ag NC.	126
Figure 5.4.	(a) Normalized absorption spectrum of Ag NC (blue line) and fluorescence spectrum (black line) of 2.5 μ M DAPI ($\lambda_{\text{ex}} = 375$ nm). The black dotted region shows the spectral overlap between the absorption spectrum of Ag NC and fluorescence of DAPI. (b) Changes in the emission spectra of DAPI (black line) and Ag NC (red line) upon mixing (green line). The excitation wavelength is 375 nm.	127
Figure 5.5.	Confocal microscopy images of (a) complex I (surface) and (b) complex II (core).	128
Figure 5.6.	(a) Changes in the fluorescence spectra ($\lambda_{\text{ex}} = 375$ nm) of DAPI in complex I (surface) upon addition of Ag NC. (b) Fluorescence decay traces of complex I (surface) in the absence and presence of Ag NC.	129
Figure 5.7.	Spectral overlap of (a) Complex I (surface)-Ag NC and (b) complex II (core)-Ag NC.	131
Figure 5.8.	(a) Changes in the fluorescence spectra ($\lambda_{\text{ex}} = 375$ nm) of DAPI in complex II (core) upon addition of Ag NC. (b) Fluorescence decay traces of DAPI and complex II (core).	134

Chapter 6

Figure 6.1.	(a) AFM image of citrate-capped Au NPs. The inset shows the height profile histogram with mean size. (b) Histogram of hydrodynamic diameter of Au NPs with mean hydrodynamic diameter estimated from DLS measurement. The inset shows the zeta potential of citrate-capped Au NPs. (c) Spectral overlap between	145
--------------------	---	-----

absorption spectrum of Au NPs (black line) with emission spectra ($\lambda_{\text{ex}} = 376 \text{ nm}$) of green, yellow, and red QDs.

- Figure 6.2.** Changes in the (a) Absorption and (b) PL spectra ($\lambda_{\text{ex}} = 482 \text{ nm}$) of green QDs upon gradual addition of Au NPs (0, 20, 40, 60 and 80 pM). (c) Stern-Volmer plots for the PL quenching of green QDs in the presence of Au NPs at three different excitation wavelengths. 146
- Figure 6.3.** Changes in the PL spectra (a and b) and PL decay traces (c and d) of green QDs upon addition of citrate-capped Au NPs at 376 and 445 nm excitation wavelength. 148
- Figure 6.4.** (a) Changes in the PL decay traces ($\lambda_{\text{ex}} = 482 \text{ nm}$) of green QDs upon addition of citrate – capped Au NPs. Black solid lines represent fitted decay functions. (b) Stern–Volmer plots for the PL quenching of green QDs at three different excitation wavelengths (375, 445 and 482 nm) as a function of Au NP concentrations. 149
- Figure 6.5.** Changes in the PL spectra ($\lambda_{\text{ex}} = 482 \text{ nm}$) of (a) yellow and (b) red QDs upon gradual addition of Au NPs. PL decay traces ($\lambda_{\text{ex}} = 482 \text{ nm}$) of (c) yellow and (d) red QDs upon gradual addition of Au NPs. 152
- Figure 6.6.** Normalized absorption (black) and PL spectra (green, yellow, and red) of Ag NPs and three differently sized QDs, respectively. 156
- Figure 6.7.** Changes in the absorption spectra of (a) green, (b) yellow and (c) red QDs upon addition of citrate-capped Ag NPs. Changes in the PL spectra of (d) green, (e) yellow and (f) red QDs upon addition of citrate-capped Ag NPs at λ_{ex} of 376 nm. 157
- Figure 6.8.** Changes in the PL decay traces of (a) green, (b) yellow and (c) red QDs upon addition of citrate capped Ag NPs $\lambda_{\text{ex}} = 376 \text{ nm}$. 157
- Figure 6.9.** Steady-state and time-resolved Stern-Volmer plots for (a) green, (b) yellow and (c) red QDs 159

in the presence of Ag NPs at an excitation wavelength of 376 nm.

Figure 6.10. (a) Schematic representation of ligand exchange reaction of citrate-capped Au NPs with PEG-SH ligand. (b) Normalized absorption spectrum of citrate and PEG-capped Au NPs. (c) Size distribution histogram of PEG-capped Au NPs from DLS measurement. The mean hydrodynamic diameter is mentioned with the standard deviation. The Inset compares the estimated zeta potentials of citrate and PEG-capped Au NPs. (d) Changes in the PL spectra ($\lambda_{\text{ex}} = 482$ nm) of green QDs in the absence (black line) and presence of 80 pM PEG (solid red line) and citrate (dash dot magenta line)-capped Au NPs. (e) Changes in the PL decay traces ($\lambda_{\text{ex}} = 482$ nm) of green QDs in the absence (black) and presence of 80 pM PEG (red) and citrate (magenta)-capped Au NPs. The black solid lines are the fitted curves.

Figure 6.11. FTIR spectra of (a) Poly (ethylene glycol) methyl ether thiol (PEG-SH) and (b) synthesized PEG-capped Au NPs.

Figure 6.12. (a) Changes in the absorption spectra and PL spectra of green QD upon addition of PEG-capped Au NPs at λ_{ex} of (b) 376 nm and (c) 445 nm.

Figure 6.13. Changes in the PL decay traces of green QD upon addition of PEG-capped Au NPs at λ_{ex} of (a) 376 nm and (b) 445 nm.

Chapter 7

Figure 7.1. Change in the (a) absorption and (b) PL ($\lambda_{\text{ex}} = 450$ nm) spectra of CdTe QDs in the presence of liposome at 0 and 24 h of equilibration. (c) Change in the peak position and PL intensity ratio of CdTe QDs in the presence of liposome as a function of equilibration time. (d) PL lifetime decay traces ($\lambda_{\text{ex}} = 445$ nm; $\lambda_{\text{em}} = 520$ nm) of QDs in the absence and presence of liposomes at 0 and 24 h of equilibration. (e)

	Confocal images of QD-liposome binary mixtures at 0 and 24 h of equilibration.	
Figure 7.2.	(a) Changes in the absorption spectra of Au NPs in the presence of liposome at 0 and 24 h of equilibration. (b) Plot of LSPR peak positions of Au NPs in the presence of liposome against equilibration time. (c) AFM image of liposome-Au NP system after 24 h of equilibration. (d) Magnified AFM image showing the adsorption of Au NPs on the surface of liposome (red arrows indicate adsorbed Au NPs). Cross-section analysis of liposome-Au NPs system for (e) liposome, and (f) adsorbed Au NP.	189
Figure 7.3.	Confocal microscopy images of AuLipQD complex upon 24 h of equilibration. The inset shows the enlarged DIC image of surface adsorbed Au NPs on a liposome. The red arrows in the DIC image indicate surface adsorbed Au NPs.	191
Figure 7.4.	Spectral Overlap between PL spectra of QDs and LSPR band of Au NPs in the absence and presence of liposomes for the present system.	192
Figure 7.5.	Changes in the (a) PL spectra and (b) PL decay traces of QDs in the presence of 80 pM Au NPs.	193
Figure 7.6.	Changes in the PL spectra ($\lambda_{ex} = 450$ nm) of QDs in the presence of Au NPs for (a) QD-Liposome, (c) LipQD, and (e) AuLipQD systems. Changes in the PL lifetime decay traces ($\lambda_{ex} = 445$ nm; $\lambda_{em} = 520$ nm) of QDs in the presence of Au NPs for (b) QD-liposome, (d) LipQD, and (f) AuLipQD systems.	194

List of Tables

Chapter 3

Table 3.1. PL decay parameters of green QD in the absence and presence of PDADMAC. 74

Table 3.2. Estimated partition coefficients (K) of dyes and proteins inside coacervate droplets (T2 region). 79

Chapter 4

Table 4.1. PL decay parameters of green QD in the absence and presence of 0.01 and 10 mM CTAB. 99

Chapter 5

Table 5.1. Estimated quantum yields (ϕ_D), spectral overlap integral ($J(\lambda)$), energy transfer efficiency (ϕ_{eff}), Förster distance (R_0) and calculated distance (r) between DAPI and the Ag NC. 132

Table 5.2. Fluorescence decay parameters of complex I (surface) in the absence and presence of Ag NCs. 133

Chapter 6

Table 6.1. Steady-state and time-resolved SV constants (K_{sv}) for green QDs in the presence of citrate-capped Au NPs. 149

Table 6.2. PL Decay Parameters ($\lambda_{\text{em}} = 522$ nm) of Green QDs in the Absence and Presence of Citrate and PEG-Capped Au NPs at λ_{ex} of 482 nm. 150

Table 6.3. PL decay parameters of green QD in the absence and presence of citrate-capped Au NPs at 376 nm and 445 nm. 151

Table 6.4. PL decay parameters of yellow and red QDs in the absence and presence of citrate-capped Au NPs at λ_{ex} of 482 nm. 153

Table 6.5. Estimated quantum yields, average PL lifetimes, radiative rates, nonradiative rates, energy transfer rates and efficiencies of energy transfer for green CdTe QDs ($\lambda_{\text{ex}} = 482$ nm) in the absence 154

	and presence of citrate and PEG-capped Au NPs.	
Table 6.6.	PL decay parameters of green, yellow, and red QD in the absence and presence of citrate-capped Ag NPs at $\lambda_{\text{ex}} = 376$ nm.	158
Table 6.7.	Steady-state and time-resolved SV constants (K_{sv}) for green, yellow, and red QD in presence of citrate-capped Ag NPs.	159
Table 6.8.	Experimental and theoretical SET parameters for green, yellow and red QDs in the presence of citrate-capped Au NPs.	168
 Chapter 7		
Table 7.1.	PL lifetime decay parameters of CdTe QD in the absence and presence of Au NPs and Liposome at different incubation times.	186
Table 7.2.	Estimated EET parameters of QD and Au NPs pair in the absence and presence of liposomes.	197
Table 7.3.	Experimental and theoretical size-dependent NSET parameters for QD and LipQD complex in the presence of 80 pM Au NP.	198

Acronyms

AFM	Atomic force microscopy
Ag NP	Silver nanoparticle
Ag NC	Silver nanocluster
Au NP	Gold nanoparticle
Au Lip	Gold nanoparticle liposome nanocomposite
CLSM	Confocal laser scanning microscopy
CTAB	Cetyl trimethyl ammonium bromide
CPS-Kuhn	Chance, Prock, Silbey-Kuhn
DLS	Dynamic light scattering
DAPI	4',6-diamidino-2-phenyl indole
DPPC	Dipalmitoylphosphatidylcholine
DSC	Differential scanning calorimetry
ESI	Electrospray ionization
EET	Excitation energy transfer
FESEM	Field-emission scanning electron microscopy
FTIR	Fourier transform spectroscopy
FWHM	Full width at half maxima
Fl	Fluorescence
G-N	Gersten-Nitzan
IRF	Instrument response function
LCMS	Liquid chromatography mass-spectrometer
LipQD	Liposome quantum dot nanocomposites
LSPR	Localized surface plasmon resonance
LEDs	Light emitting diodes

MSA	Mercaptosuccinic acid
NSET	Nanometal surface energy transfer
O. D.	Optical density
PL	Photoluminescence
PVP	Poly(vinylpyrrolidone)
PVA	Poly(vinyl alcohol)
PVs	Plasmonic vesicles
PEG-SH	Poly(ethylene glycol)methyl ether thiol
PET	Photoinduced electron transfer
QD	Quantum dot
QY	Fluorescence quantum yield
SDS	Sodium dodecyl sulfate
SUV	Small unilamellar vesicles
SET	Surface energy transfer
SAXS	Small angle X-ray scattering
ST	Standard sample
TEM	Transmission electron microscope
TX-100	Triton X-100
TCSPC	Time-correlated single photon counting
UV-vis	Ultraviolet-visible
XPS	X-ray photoelectron spectrometer
XRD	X-ray diffraction

Nomenclature

λ	Wavelength
ε	Extinction coefficient
α	Alfa
β	Beta
Φ	Fluorescence quantum yield
\AA	Angstrom
nm	Nanometer
cm	Centimeter
$^{\circ}$	Degree
K	Kelvin
mM	Millimolar
μM	Micromolar
mL	Milliliter
μL	Microliter
a.u.	Arbitrary unit
τ	Lifetime
λ_{ex}	Excitation wavelength
λ_{em}	Emission wavelength
χ^2	Reduced chi-square
k_{r}	Radiative decay rate
k_{nr}	Non-radiative decay rate

ψ_0	Surface potential
r_H	Hydrodynamic radius
pH	The negative logarithm of hydronium-ion concentration
pK_a	Dissociation constant of an acid in ground state
mg	Milligram
M	Molar
I	Integrated fluorescence intensity
η	Refractive index of the medium
A	Optical density
ST	Standard sample
μm	Micrometer
kV	Kilovolt
m/z	Mass to charge ratio
ps	Picosecond
ϕ_{eff}	Energy transfer efficiency
κ^2	Orientation factor of the transition dipoles
$J(\lambda)$	Spectral overlap integral
mm	Millimeter
R_0	Förster distance
r	Radius
kDa	Kilodalton
T	Turbidity
rpm	Revolutions per minute
K	Partition coefficient
ζ	Zeta potential

Pa	Pascal
mA	Milli-ampere
fs	Femtosecond
MHz	Megahertz
W	Watt
mV	Millivolt
eV	Electronvolt
θ	Theta
I_{\min}	Minimum saturation intensity
K_D	Dissociation constant
n	Hill coefficient
R^2	Correlation coefficient
EET	Excitation energy transfer
α	Orientation of the donor transition dipole to metal plasmon vector
d	Average separation distance
MW	Molecular weight
ns	Nanosecond
pM	Picomolar
k_{ET}	Energy transfer rate
ε	Dielectric constant
Γ_r	Size-dependent damping constant
ω	Dipole frequency
l	Mean free path
N_A	Avogadro number
V	Volume

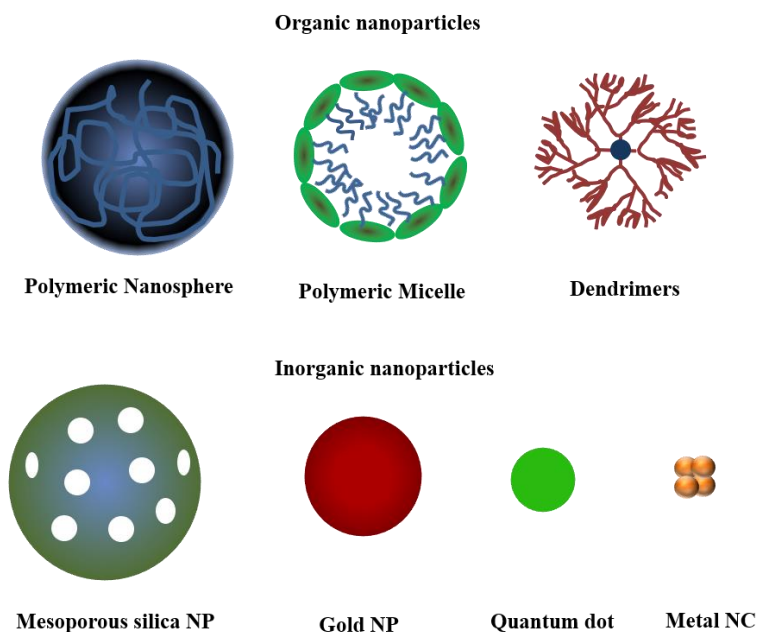
Chapter 1

Introduction

1.1. Evolution of Nanoparticle

Nanotechnology is one of the utmost exciting areas of research in modern material science. This field started to progress in the mainstream of society during mesopotemic era, and this is evident by the several arts made from gold or silver sols in that generation [1,2]. For instance, the ancient Romans used to color the glasses with intense red, yellow, or mauve shades by using different concentrations of gold and silver. They prepared transparent ruby-red glasses by reducing gold salt to colloidal gold by mixing and annealing with glasses [3]. Although nanotechnology's genesis occurred during mesopotamic era, the term was coined in 1974 by Norio Taniguchi. "Nano" is a Greek word meaning "dwarf," implies nanometer (nm), which is one-billionth of a meter [4].

Interestingly, far before the majestic evolution of nanoscience, an extensive amount of literature was available to understand the philosophy of the small particles' formation and nature [5]. Therefore, designing nanoparticles with different structures and functions became a primary interest in biomedical, electronic, optical, and technical fields. One of the essential parameters in designing the nanoparticles is to control their morphology and size. Therefore, interests in the fabrication of organic and inorganic nanoparticles with different compositions, shapes, and particle sizes arise rapidly, leading to the emergence of the nanotechnology research field [6]. Nanoparticles can be broadly classified into two sub-sections: organic and inorganic nanoparticles, depending on the compositions (Scheme 1.1).



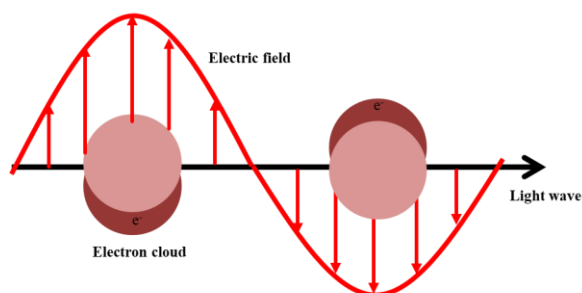
Scheme 1.1. Organic and inorganic nanoparticles.

In recent times, scientists have focused their attention on developing organic nanoparticles as these materials self-assemble into highly aligned superlattice at room temperature that has potential applications in organic light-emitting diodes (OLED), sensors, and medical diagnosis [7-9]. Various nanoparticles have been fabricated during the last two decades [10]. The structures of these materials can be zero (0D), one (1D), two (2D), and three (3D) dimensional [11,12]. The synthesis, photophysical properties as well as applications of metal nanoparticles (NPs), semiconductor NPs or quantum dots (QDs), and Metal nanoclusters (NCs) are described below in brief.

1.1.1. Metal NPs

Metal NPs are nanoscopic materials with an overall dimension below 100 nm. They exhibit unique physical, optical, and chemical properties that differ from bulk metal [13]. For example, bulk gold is a conductor, displays a golden yellow color, and has a high melting point. In contrast, Au NPs display wine-red to brown color depending upon its size and melt at a much lower temperature [14]. The remarkable physical and optical properties of metal NPs is attributed to their small size and the

large surface-to-volume ratio [15]. In fact, the properties of metal NPs can be controlled by changing their size and shape.



Scheme 1.2. Schematic diagram illustrating the localized surface plasmon resonance in metal NPs.

One of the unique size-dependent optical properties displayed by metal NPs is localized surface plasmon resonance (LSPR) (Scheme 1.2). LSPR is a characteristic phenomenon of metal NPs, which is observed if the size of the NPs is smaller than the wavelength of the incident light. As in LSPR, the electromagnetic field of the incident light excites the surface electrons of a metal NP; this results in coherent localized oscillation of the electron density with a resonant frequency that depends upon the size and shape of NPs as well as dielectric of metal and surrounding medium [16]. The LSPR band of metal NPs can be tuned from visible to near-infrared regions by varying the size of the NPs; this property makes them highly suitable for imaging and sensing applications in the field of biomedical science [17]. Several transition metal NPs including gold (Au), silver (Ag), iron oxides (FeO), copper (Cu) have been designed for medical applications [18]. However, Au and Ag NPs have gained special attention because they can absorb in the visible region of the solar spectrum and show low cytotoxicity [16].

Au NPs can be synthesized into various shapes, including nanospheres, nanorods, nanocages, and nano prisms [19]. The size and shape of Au NPs can be controlled during their synthesis. Various aqueous medium based methods have been developed to control the dimensions and functionality of Au NPs. One of the most commonly

used methods for synthesizing spherical Au NPs was pioneered by Turkevich *et al.* and later remodified by Frens *et al.*; this method involves reduction of the gold salt (hydrogen tetrachloroaurate; HAuCl₄) using citric acid in the aqueous medium. Apart from reducing the Au ions, the citric acid also stabilizes the Au NPs by acting as a capping agent. The size of the spherical Au NPs can be controlled by altering the gold-to-citrate ratio [20]. The Au nanospheres display dark red to purple color in solution as the size increases and show LSPR band in the region of 500-550 nm [21]. Au NPs are also known to quench the fluorescence emission of proximal fluorophores as a consequence of spectral overlap between LSPR of the Au NPs and the emission spectrum of a fluorophore [22]. Furthermore, the surfaces of Au NPs can be easily functionalized with biopolymers such as oligonucleotides, proteins, and antibodies [23-25]. These unique properties make them promising candidates for several applications such as sensing, therapeutics, bioimaging, and excellent quenchers in energy transfer systems [26-28]. For example, Au NPs conjugated with poly(para-phenylenethylene) have been exploited for the detection of cancerous cells and different bacteria species. Aptamer-conjugated Au NPs have also been used to detect lymphoma cells with very high sensitivity [29]. Au NPs have also been utilized for drug delivery and gene regulation [30]. Mirkin *et al.* have demonstrated the use of Au NP-oligonucleotide conjugate for controlling protein expression in cells [31]. The LSPR of metal NPs quenches or enhances the fluorescence of the nearby fluorophore in many nanocomposite systems. Among these nanocomposite systems, QD-metal NP hybrid nanostructures find special attention due to their significant potential in technology related nanophotonic devices [32-33]. For example, Li *et al.* have demonstrated the effect of metal NPs size on the mechanism of the EET process between CdSe/ZnS QDs and Au NPs [34]. Several studies have reported efficient transfer and release of the drug inside the cell through the Au NPs-drug complex [35]. The optical properties of Au NPs have been beneficial for cell imaging in various techniques, including computed tomography (CT), raman spectroscopy and photoacoustic imaging [36].

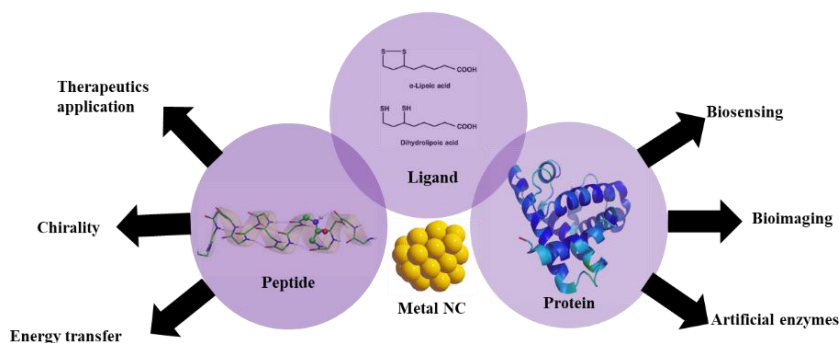
Like Au NPs, Ag NPs also exhibit LSPR that depends upon the size and shape of the particle. Ag NPs can be synthesized into various shapes such as spherical, nanoprisms, and nanocubes [19,37]. In general, Ag NPs can be synthesized by three different methods; physical and chemical [38,39]. The chemical method is the most common approach as it gives a high yield, low cost, and can be performed easily in aqueous solution. The chemical approach requires silver salts such as silver nitrate (AgNO_3) or silver perchlorate (AgClO_4), a reducing agent, and a capping agent. The silver salt is treated with a reducing agent to form colloidal silver. The most commonly used reducing agents are sodium borohydride (NaBH_4) and trisodium citrate [38]. Monosaccharides such as glucose, fructose, and maltose can also be used as a reducing agent in the synthesis of Ag NPs [40]. These reducing agents convert silver ions into silver atoms. When the concentration of silver atoms increases enough in the solution, they bind together to form a nucleus. This nucleus grows into a particle as more silver atoms diffuse through the solution and attach at the surface [41]. To control the size of these particles, capping/stabilizing agents are used in the reaction medium. These capping agents bind at the surface of the particles and control the colloidal stability of NPs from reaching the surface [42]. The attachment of capping agents eventually stops the growth of the particle. The most commonly used capping agents are trisodium citrate ($\text{Na}_3\text{C}_6\text{H}_5\text{O}_7$) and polyvinylpyrrolidone (PVP) [43, 44]. The trisodium citrate can act as both reducing as well as capping agent. Therefore, the synthesis of Ag NPs using citrate is the most commonly used approach.

The optoelectronic properties of Ag NPs have great importance in the field of biological and material sciences. For example, Ag NPs are exploited in industries, textiles, water treatment, cosmetics, and health care products [18]. Their optical properties are utilized for developing optical sensors, optical probes, and imaging techniques [45]. Ag NPs have also been used in therapeutics as anticancer, antibacterial, antioxidative agents as well as for drug delivery [46]. In this thesis, we

have synthesized citrate/PEG-capped Au NP and citrate-capped Ag NP. The LSPR of Au NPs and Ag NPs have been exploited to investigate the size and wavelength-dependent excitation energy transfer from quantum dots (QDs) to plasmonic NPs. These hybrid QD-metal NP system can be useful to understand and optimize the performance of various nanophotonic devices such as photovoltaics, LEDs, and photodetectors [47-49].

1.1.2 Metal Nanocluster (NCs)

Ultrasmall metal NPs with a diameter of less than 2.0 nm are known as metal NCs. In recent years, metal NCs have gained immense importance due to their ultra-small size and unique optoelectronic properties [50]. In bulk metal, the energy gap between the conduction band and valence band is absent therefore, electrons can move freely. On the contrary, in metal NCs, the cluster's size is below 2 nm, and the continuous band structure is broken into discrete energy levels, similar to the energy levels of the molecule [51]. This results in the origin of several unique properties in metals NCs such as tunable photoluminescence (PL), quantized charging, molecular chirality, and magnetism [50]. Although there are several studies on the synthesis of metal NCs since 2002s, a method developed by Dickson's group formed a base for the routine preparation of metal NCs in the aqueous phase [52]. In general, the preparation of metal NCs in an aqueous solution requires a reducing agent which reduces the metal ions to a zero valence state [53]. It also requires an appropriate scaffold to avoid the reaction of metal NCs with each other and their irreversible self-aggregation. It is intriguing to note here that the scaffolds not only stabilize but can also functionalize the surface of the metal NCs and also governs their sizes and PL properties. The most commonly used scaffolds for the metal NCs are thiols, polymers, dendrimers, proteins, peptides, oligonucleotides, and DNA (Scheme 1.3) [54-56].



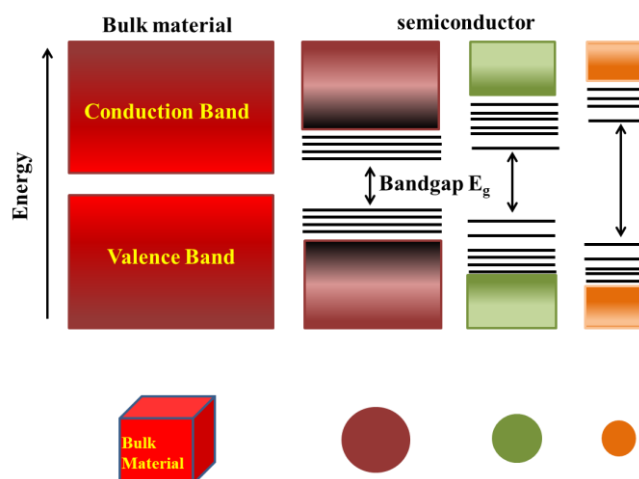
Scheme 1.3. Schematic representation of various applications of NCs.

Several metal NCs including Au, Ag, and Cu with different scaffolds have been widely used for biological applications [57]. For example, Au and Ag NCs functionalized with thiolated ligands provide long-term colloidal stability, which makes them highly suitable for imaging and sensing applications [58]. Metal NCs conjugated with biomolecules have important significance in the field of biomedical science. Metal NCs can bind to biopolymers more easily and exhibit minimal cytotoxicity compared to metal NPs. There are several reports of DNA-protected metal NCs that are developed for cell targeting, specific binding, and imaging applications [59]. Similarly, protein-functionalized metal NCs have been used for targeting and specific binding to cancer cells [50]. One of the primary advantages of protein protected NCs is that protein molecules provide several binding sites (carboxylic acid, amine, thiol groups) for further functionalization of metal NCs. Functionalization through dendrimers and polymers provides higher stability to metal NCs in aqueous solution and facilitates the synthesis [60]. These metal NCs exhibit high quantum yield (QY) with improved stability. The chelating dendrimers can also promote synthesis of bimetallic NCs. In this thesis, the influence of dihydrolipoic acid (DHHLA)-capped Ag NCs on the fluorescence properties of diamidino-2-phenylindole (DAPI) across the lipid bilayer has been demonstrated.

1.1.3. Semiconductor NPs or Quantum Dots

Over the last few decades, nanometer-sized quantum dots (QDs) or colloidal semiconductor nanocrystals have attracted significant attention due to their unique optical and electronic properties [61]. The term “quantum dot” was first used by Mark A. Reed in 1988 to describe a spatially quantized system where the electron-hole pairs (i.e., excitons) are confined in all three spatial dimensions [62]. The average distance between the electron and hole is called the exciton Bohr radius. When the size of the QDs is less than its exciton Bohr radius, they show size-dependent PL properties due to the quantum confinement effect [63].

It is important to note that in bulk, the dimension of semiconducting materials is much larger than the exciton Bohr radius and the energy bands are continuous. However, as the size of the particle approaches near or below the exciton Bohr radius, the motion of excitons are spatially confined in the dimensions of QDs. As a consequence, the energy bands become discrete, and the properties of the particles become size-dependent [64] (Scheme 1.4).



Scheme 1.4. Illustration of the influence of particle size on the band gap and quantum confinement effect in semiconductor.

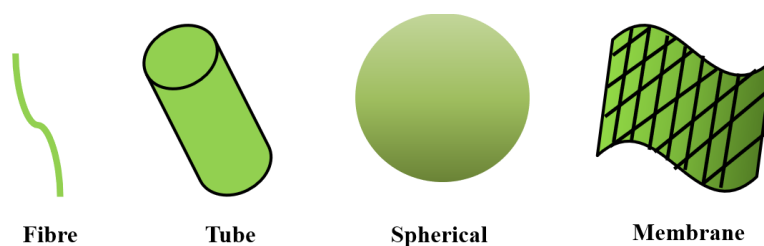
QDs exhibit broad excitation spectra, size- and composition-tunable narrow emission from ultraviolet to near-infrared wavelength range, high luminescence QY, and better stability against photobleaching compared to organic dyes [65]. They also exhibit excitation wavelength-dependent emission mainly because of heterogeneous size distribution. Another characteristic PL property of QD, which is useful in single-molecule experiments, is their emission intermittency or “blinking” [66]. One of the reasons behind this blinking is the trapping of charge carriers at the surface defect states before radiative recombination [67-69]. Among all others, CdX QDs (X= Te and Se) have attracted significant attention due to their tunable and stable PL properties in the visible to NIR region. Here, in this thesis, we have mainly explored the PL properties of MSA-capped CdTe QDs and their self-assembly processes.

Among II-VI semiconductor compounds, CdTe QDs are the most imperative semiconductor material because it shows narrow bandgap of 1.47 eV as well as a large exciton Bohr radius of 7.3 nm, which makes them widely applicable in various field [70]. CdTe QDs show excellent crystallinity and emit in the green-to-red region of the electromagnetic spectrum (450–700 nm) with high luminescence quantum yield (QY) of 20–85% [70, 71]. CdTe QDs can be synthesized in aqueous as well as in organic medium. Resch *et al.* first synthesized CdTe QDs in an aqueous medium in the presence of hexametaphosphate [72]. The commonly used ligands for the aqueous synthesis of CdTe QDs are thiol-containing compounds, namely, thioglycolic acid (TGA), 3-mercaptopropionic acid (MPA), glutathione (GSH), and cysteine (CYS) [73,74]. Rogach *et al.* and Gao *et al.* later synthesized and optimized the formation of CdTe QDs in the presence of thiol capping agents (2-mercaptoethanol and 1-thioglycerol) with size ranging from 1.4 to 2.5 nm [75-77]. The pH of the medium has a great influence on the QY of QDs, in an acidic medium excess ligand, and Cd²⁺ in the reaction medium will deposit on the surface of QDs, leading to the formation of a shell-layer structure comprising of ligand-Cd complexes.

These ligand-Cd complexes effectively eliminate the nonradiative pathway for excitons and enhance the QY of QDs [78]. Here, in this thesis, we have investigated the photophysical properties of MSA-capped CdTe QDs using various spectroscopic techniques and utilized them as a luminescent maker to understand its self-assembly process in the presence of surfactant and polymer.

1.2. QD-Based Self-Assembled Nanostructure

Spontaneous assembly of molecular units into a well-organized ordered structure is known as self-assembly. Self-assembly occurs through the involvement of non-covalent interactions such as hydrophobic, hydrogen bonding, π - π stacking, electrostatic, and van der Waals forces between the molecular units [79]. Although noncovalent interactions are moderately weak but collective interactions between several units can lead to very stable structures. It is possible to generate a wide variety of self-assembled nanomaterials by simple optimization of various intermolecular forces between the molecular units (Scheme 1.5). Therefore, mechanistic investigation of self-assembly processes is highly desirable for the development of multifunctional nanomaterials



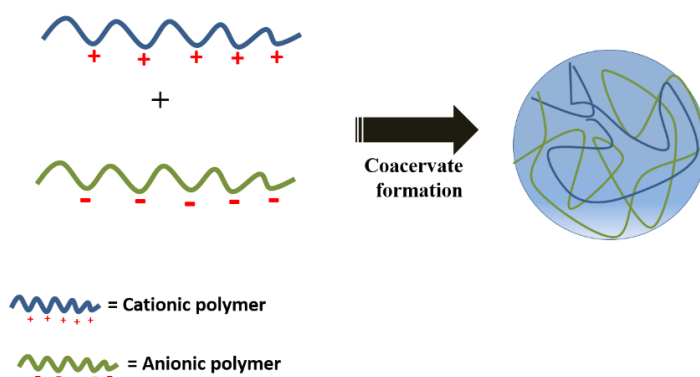
Scheme 1.5. Schematic representation of different types of self-assembled nanomaterials.

Recently, self-assembled three-dimensional networks, arrays, and composite like structures of NPs have been reported by several authors. For instance, self-assembly between plasmonic NPs and DNA/ proteins have been widely studied due to their significant application in material science, nanodevices, energy and environmental science, and biomedicine [80, 81]. Similarly, self-assembled nanocomposites such as

hydrogels, hybrid vesicles, nano-capsules have been fabricated for potential applications in drug delivery, enzymatic reaction, and antibacterial activity [82]. Here, in the present thesis, we have investigated the interaction of CdTe QDs with polymer and surfactant, which result in the formation of self-assembled multicolor luminescent hybrid coacervate droplets and vesicles, respectively.

1.2.1. QD-Polymer Self-Assembled Coacervates

In recent times, the design and synthesis of polymer-based colloidal nanocomposites with high stability in the aqueous medium have attracted substantial interest due to their potential applications in detergency, catalysis, and drug delivery [83-88]. In general, colloidal complexes are formed via self-assembly between oppositely charged molecules such as synthetic and natural polymers, fatty acids, biological macromolecules, poly or oligopeptides, and mononucleotides [89-91]. Importantly, the properties of such assemblies depend on various parameters, such as polymer chain length, grafting density, and rigidity of the polymer grafts [92]. Self-assembly of oppositely charged polymers leads to the formation of different types of assemblies such as worms, cylindrical, network, and spherical like structures [93-95]. Extensive studies have been performed on the self-assembly of oppositely charged polyelectrolytes that lead to the formation of spherical shaped structures called as coacervates. The term “coacervates” refers to organic/inorganic rich droplets formed via liquid-liquid phase separation in macromolecular systems (Scheme 1.6).



Scheme 1.6. Schematic representation of the coacervation process.

In general, coacervation is similar to the macromolecular phenomenon that results in a unique phase of soft, condensed liquid-like matter [96]. Coacervates find application in many fields such as micro-reactors, storage/release vectors, and serves as platforms for catalytic reactions [97, 98]. The interior of coacervates is structurally homogeneous with no surrounding membrane and has a lower dielectric constant compared to water. As a consequence, it can sequester external dye molecules, porphyrin macrocycles, and inorganic NPs [99,100].

Although previous studies provide great detail of the mechanisms, structures, stability, and sequestration properties of a wide range of coacervate droplets prepared mainly from organic molecules, there are no reports on the fabrication of organic–inorganic hybrid droplets. The self-assembled nanostructures of QD and polymer show enhanced thermal, mechanical, and optoelectronic properties because of their unique combination of both inorganic nanomaterial and polymer [101]. The inorganic components exhibit large surface area, excellent thermal stability, and size-dependent optoelectronic properties, on the other hand, organic polymer provides mechanical flexibility and good processability [102,103]. Therefore, self-assembled nanostructures with unique physical and biological properties have attracted significant attention for applications in drug delivery, catalysis, chemical storage, bioimaging, and biosensors [104-107].

One of the most common polyelectrolytes used for the formation of coacervates is poly(diallyldimethylammonium chloride) (PDADMAC). It is a water-soluble cationic polymer with quaternary ammonium groups on the rings of the polymer backbone. PDADMAC polymers were first prepared and studied in 1957 by Professor George Butler at the University of Florida [108]. The charge on the polymer is independent of solution pH. Complexation between PDADMAC and oppositely charged natural polymers such as fatty acid, and poly/oligopeptides has been previously explored [109, 110]. For example, Dirk *et al.* (1998) have investigated the formation of coacervate between PDADMAC and ATP/CM-dextran [111]. Tom *et*

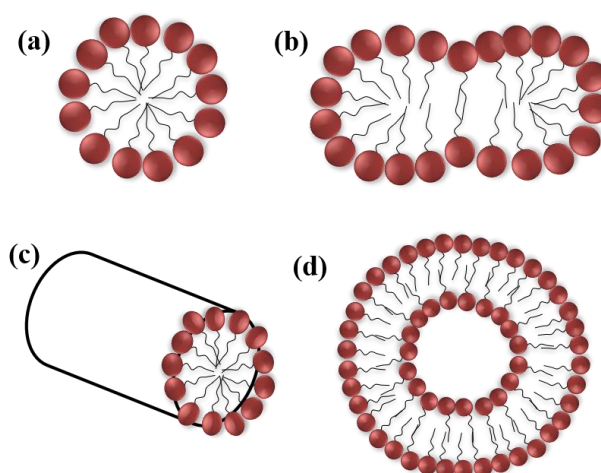
al. (2012) have studied the potential use of PDADMAC-ATP coacervate for stabilization of type II multi-enzyme complexes and their catalytic activity [99]. Here, in this thesis, we have explored the spontaneous formation of complex coacervate droplets in the binary mixture of MSA-capped CdTe QDs and PDADMAC in an aqueous medium over a broad range of composition, pH, and ionic strength.

1.2.2. QD-Surfactant Self-Assembled Hybrid Vesicles

Self-assembled hybrid vesicles have also been extensively investigated for their biological membrane-mimicking environments and applications in various fields such as protein carriers in immunology, diagnostic imaging of tumors, drug-delivery, and gene therapeutics [112-114]. Self-assembled vesicles are the nano-sized carrier and act as an ideal model system for unraveling and understanding the various activities of biological membranes such as fusion, adhesion, and fission [115-118].

Surfactants are amphiphilic molecules and contain both hydrophobic (tails) and hydrophilic groups (heads). The hydrophobic chain can interact with water-insoluble substances, and hydrophilic groups can interact with polar substances [119,120]. A unique property of surfactants is that they can form self-assembled structures such as micelles, lamellae, and vesicles [121]. These self-assembled structures can undergo transition from one phase to another, and their transitions depend upon the concentration of surfactants, electrostatic interaction, van der Waals forces, hydrophobic interaction, and composition of cationic/anionic surfactants [121].

In an aqueous medium, surfactant molecules self-assemble into different shapes of aggregates such as spherical, globular, rod, and spherical bilayers like structures upon increasing the concentration of surfactant molecules [122-124] (Scheme 1.7).



Scheme 1.7. Schematic representation of the different type of surfactant aggregates (a) spherical, (b) globular, (c) rod, and (d) spherical bilayers like structures.

Spherical assembly of surfactant molecules with the hydrophobic core is called micelles, whereas the spherical bilayer arrangement of surfactants containing hydrophilic core is known as vesicles. In surfactant systems, the spontaneous structural transformation from micellar aggregates to vesicles is unique and can be achieved via a variety of different routes [123]. Egelhaaf *et al.* demonstrated the transformation of micelles to vesicles in the mixture of lecithin/bile salt in an aqueous medium, and it has been concluded that transition takes place via an intermediate micellar arrangement having a disk-like structure. These intermediate structures appear very fast and are finally transformed into well-defined unilamellar vesicles [125]. Although phospholipid vesicles are more commonly explored, several authors have focused on the fabrication of vesicles from surfactants, block copolymers [126], dendrimers [127], polypeptides [128], and fatty acid [129] as they are more durable and sustain far greater areal strain before rupture compared to phospholipids vesicles. For example, Huang *et al.* presented a synthetic route to prepare self-assembled vesicles from polypeptide block copolymers with different block length ratios, which were obtained via polymerization of benzyl-L-glutamate and

propargylglycine (PG) N-carboxyanhydrides [128]. Very recently, Yadavalli *et al.* also demonstrated the self-assembly between 3,5-didodecyl benzoic ester mini-dendrons and 3,4,5-Tris-triethylele glycol benzoic ester to form stable giant dendrimersomes (DSs) in an aqueous medium. These DSs were delivered into the cytoplasm of HeLa cells after co-assembling with human membrane vesicles (HMs) to investigate their constituents in vitro and a more robust environment [127].

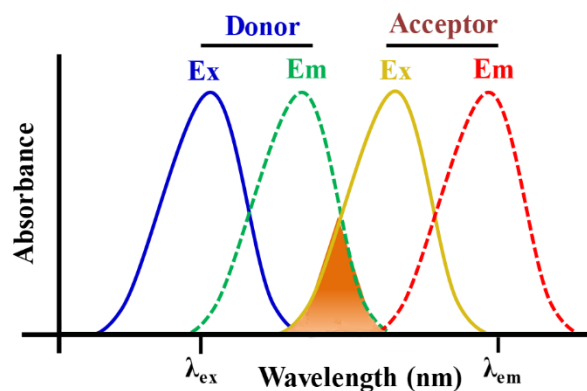
Although these recent studies highlight the multifunctional properties of self-assembled hybrid vesicles, there is a growing interest in the fabrication of stable, inherently luminescent hybrid vesicles. However, there are limited reports for the fabrication of inherently luminescent stable hybrid vesicles. Earlier, Sun *et al.* investigated the self-assembly mechanism of oppositely-charged carbon quantum dots (CQDs) and surfactants and shows the formation of supramolecular fluorescent vesicles [130,131]. Here, in this thesis, we have studied the interaction of negatively charged QDs with positively charged surfactant to explore the self-assembly mechanism that leads to the fabrication of luminescent vesicles.

In the later part of the thesis, we have investigated the tuning of excitation energy transfer (EET) processes in the presence of liposome. However, before discussing these studies, we would like to briefly introduce the mechanism of EET and the theories developed to explain this phenomenon.

1.3. Excitation Energy Transfer (EET)

Nonradiative transfer of excitation energy from a photoexcited fluorophore (donor) to another molecule or a metal NP (acceptor) is known as EET [132]. This technique has been widely exploited in various fields, including light-emitting diode, sensors, and photovoltaics, because of its sensitivity to the donor-acceptor distance and donor-acceptor spectral properties [47, 133]. The rate of energy transfer (k_{ET}) between a donor and acceptor depends on various factors

such as the orientation of the donor and acceptor transition dipole, the distance between the donor and acceptor, and spectral overlap between the emission spectrum of donor and absorption spectrum of acceptor [134] (Scheme 1.8).



Scheme 1.8. Spectral overlap between the emission spectrum of the donor and the excitation spectrum of the acceptor.

The rate of EET between a donor and acceptor can be expressed as follows,

$$k_{ET} = \frac{1}{\tau_D} \left(\frac{R_0}{R} \right)^n \quad (1)$$

where τ_D is the average lifetime of the donor in the excited state, R_0 is the distance at which the energy transfer efficiency is 50%, R is the estimated separation distance between the donor and acceptor, and n is the power dependence of the theory used to describe R_0 [132]. The parameters R_0 and n are highly dependent on the nature of the donor and acceptor. For a given donor-acceptor pair, i.e., a fixed value of R_0 and n , the rate of energy transfer is faster if the excited state lifetime of the donor and donor-acceptor separation distance is small. Various theories have been developed to understand the EET mechanism, such as Förster resonance energy transfer (FRET), Gersten-Nitzan (G-N), Chance-Prock-Silbey (CPS)-Kuhn, and size-dependent nanometal surface energy transfer (NSET) [135-141]. A brief description of these models is provided in the following sections.

1.3.1. Förster Resonance Energy Transfer (FRET)

According to this theory, the nonradiative energy transfer between a donor and an acceptor occurs via dipole-dipole interaction. This theory was first proposed by Theodor Förster in 1948 [132]. This distance-dependent interaction invokes the Fermi Golden rule approximation, which associates the k_{ET} to the product of interaction elements of the donor (F_D) and acceptor (F_A), i.e., $k_{ET} \approx F_D F_A$. For a single dipole, the interaction element F is related to donor-acceptor separation distance as $F \approx 1/R^3$, similarly, for a 2D dipole array $F \approx 1/R$ and for a 3D dipole array, $F = \text{constant}$, i.e., power of the distance (R) decreases as the dimension increases. Therefore, for two single dipoles, the rate constant of FRET is expressed as [132]:

$$k_{FRET} \approx \frac{1}{R^3 R^3} = \frac{1}{\tau_D} \left(\frac{R_0}{R} \right)^6 \quad (2)$$

It's evident that the rate of FRET varies inversely with the change in the 6th power of the distance between the donor and acceptor. The parameter R_0 is the distance at which the energy transfer efficiency reduces to 50% and is known as Förster distance. The parameter R_0 is estimated by using the following equation [132]:

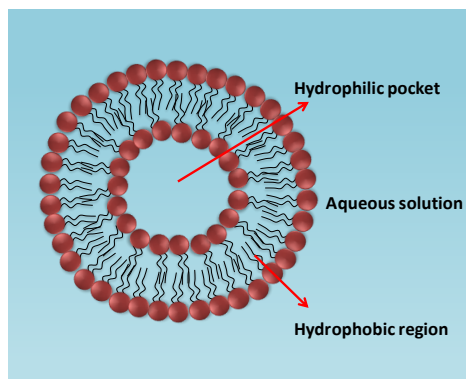
$$R_0 = [(8.8 \times 10^{-25})(\kappa^2 \eta^{-4} \phi_D J(\lambda))]^{1/6} \quad (3)$$

where κ^2 is the orientation factor of the transition dipoles of donor and the acceptor, η is the refractive index of the medium, ϕ_D is the quantum yield of the donor and $J(\lambda)$ is spectral overlap integral between the donor emission and the acceptor absorption spectrum. The value of κ^2 is governed by the relative orientation of the donor and acceptor transition dipoles. For randomly oriented dipoles, $\kappa^2 = 2/3$, and it varies between 0 and 4 in the case of orthogonal and parallel dipoles, respectively. Here, in this thesis, along with the demonstration of the mechanism of EET, the influence of liposome on the efficiency of EET has also been illustrated.

1.3.1.1. FRET in Liposome

The FRET between a donor and an acceptor plays an important role to investigate in many biological processes [142-145]. It enables us to find the distance between the donor and an acceptor with nanoscale accuracy in biological systems. Covalent attachment of the donor and an acceptor with a suitable spacer is the most conventional method for exploring intramolecular FRET [146-149]. On the other hand, tuning of intermolecular FRET has been demonstrated in various systems such as micelles, reverse micelles, liposomes, polymer matrices, and proteins [150-160].

Liposomes are composed of one or more phospholipid bilayers, which closely resembles the structure of cell membranes [161-162]. Liposome was first discovered in 1961 by a British haematologist Alec D Bangham at the Institute of Babraham, Cambridge [163]. The major components of liposomes are synthetic phosphatidylcholine (PC) natural (egg, or soy) phosphatidylcholine, and cholesterol [164-165]. These synthetic PC such as 2-distearoyl-sn-glycerophosphocholine (DSPC), 1,2-dimyristoyl-sn-glycero-3-phosphocholine (DMPC), dipalmitoylphosphatidylcholine (DPPC) are composed of a polar phosphate head group, and the hydrophobic portion composed of hydrocarbon chains [166]. The hydrocarbon chains from the interior and the polar head form the exterior of the liposomes bilayer (Scheme 1.9). Liposomes found enormous importance in the pharmaceutical field due to their biocompatibility and ability to entrap a variety of drugs [167]. The size of the liposomes varies in the range from 0.025 μm to 2.5 μm and they are classified as multilamellar vesicles (MLV), large unilamellar vesicles (LUV), and small unilamellar vesicles (SUV) [168].



Scheme 1.9. Schematic representation of different regions of the liposome.

FRET processes across lipid bilayer are of particular interest due to its potential in exploring various membrane related biophysical processes such as membrane fusion, trafficking, and receptor-ligand interactions. Very recently, Yoon *et al.* demonstrated real-time liposome fusion dynamics in a single fusion event and monitored the fusion of two proteoliposomes. [169]. Similarly, Madörin *et al.* studied the disintegration kinetics of liposomes in rat plasma using FRET techniques [170]. The FRET pair of rhodamine and N-(7-nitro-2,1,3-benzoxadiazol-4-yl) (NBD) allowed them to monitor the disintegration rate of liposomes upon increasing the monomer concentration. Yefimova *et al.* studied the change in the dynamics of living cells in the presence of liposomes [171]. FRET has also been used to monitor the interaction of plasmid DNA (labeled with cy3) with cationic liposome (labeled with NBD) during lipoplex formation [172]. In another study, You *et al.* studied the transmembrane helix dimerization in the native bilayer environment using FRET between fluorescein/rhodamine and cy3/cy5 labeled samples [173]. While these studies have illustrated the potential of FRET in elucidating various fundamental biophysical processes across the lipid bilayer, it is equally important to develop new donor-acceptor pairs that can probe the nanoscopic distance at the bilayer thickness. In this thesis, we have presented a liposome-based

FRET pair of DAPI (donor)-Ag NC (acceptor) and have shown that the FRET efficiency strongly depends on the location of donor DAPI within the DPPC liposome matrix.

FRET can be used to measure the donor-acceptor intermolecular distance only up to 8 nm [132]. However, FRET fails to explain the energy transfer process from photoexcited donors to metal NP (acceptor) that occurs at a distance greater than 8 nm [174].

1.4.2. Metal NP-Based Excitation Energy Transfer

The process of metal NP-based EET is very complex and depends on various factors such as size and shape of the NPs, separation distance, spectral overlap, and orientation of dipole with respect to the NP surface. Extensive experimental and theoretical studies have been performed to understand the fundamental mechanism behind this long-range electromagnetic coupling and subsequent fluorescence quenching at the metal NP surface [138,140,175-177]. A brief description of the initial models proposed to explain the mechanism of energy transfer between metal NP and fluorophore is provided in the next sections.

1.3.2.1. The Gersten-Nitzan (G-N) Model

One of the earliest models developed to explain the fluorescence quenching of fluorophores at the metal NP surface is Gersten-Nitzan (G-N) model [139]. In this model, the metal NP is assumed to be a spherical dipole of defined volume. The $1/R^6$ distance-dependent term is predicted, and since the volume of dipoles has all possible orientations, the orientation factor has not been considered. The G-N model is effective in estimating the quenching behaviour for metal NPs having a radius greater than 20 nm. However, it was unable to envisage the separation distance-dependent quenching process between metal NP and fluorophore [178-179]. The failure of the G-N model is due to its inability to correctly estimate the rates of energy transfer when metal NPs have insignificant scattering contributions.

1.3.2.2. CPS-Kuhn Model

In 1970, Kuhn proposed a model to explain the energy transfer from a dipole to a thin metal film [137]. It has been proposed that excited state emitter induces oscillations in the acceptor, which reflects back to the donor thereby, slowing down the donor oscillator. Thus, in Kuhn's theory, quenching is a retardation effect on the emitter due to the mirror-like behavior of the acceptor. However, it was observed that Kuhn's theory greatly overestimates the extent of energy transfer. Therefore, later it was modified by Chance, Prock, and Silbey, which is known as the CPS-Kuhn model [138]. In this model, the metal film is considered as an absorber of excited state oscillator energy in the near field through the formation of an image dipole. The CPS-Kuhn method predicts a R^{-4} distance dependency, and the distance (R_0) at which the energy transfer probability reduces to 50 % is given by the following equation [138]:

$$R_0^{cps-kuhn} = \frac{\alpha\lambda}{\eta} (A\phi)^{1/4} \left(\frac{\eta_r}{2\eta} \left(1 + \frac{\epsilon_1^2}{|\epsilon_2|^2} \right) \right)^{1/4} \quad (4)$$

Although the CPS-Kuhn model successfully explains the distance-dependent EET process between thin metal films and fluorophore, it fails to predict the size-dependent quenching behavior for NPs [175, 180]. This is because of the fact that with a change in the size of the NPs, the dipole properties (ϵ_2) and optical cross-section changes (A). Therefore, it was necessary to develop a model that can include size-dependent electronic properties of the metal NPs to account for the quenching of a fluorophore in the presence of metal NPs.

1.3.2.3. Size-Dependent NSET Theory

Very recently, Strouse *et al.* developed a size-dependent NSET theory by rewriting the CPS-Kuhn expression to account for the change in ϵ_2 (the dielectric function of metal NP) and A (absorptivity of metal NP) values with a decrease in size of the metal NPs [180-181].

According to this theory, the dielectric function (ϵ_2) can be expressed as a combination of bulk (ϵ_∞), drude (ϵ_{Drude}) and interband (ϵ_{IB}) contributions (equation 6).

$$\epsilon_2 = \epsilon_\infty + \epsilon_{Drude} + \epsilon_{IB} \quad (5)$$

Complex dielectric functions ϵ_{Drude} and ϵ_{IB} are given as:

$$\epsilon_{Drude} = 1 - \frac{\omega_p^2}{\omega^2 + \tau_r^2} + i \frac{\tau_r \omega_p^2}{\omega(\omega^2 + \tau_r^2)} \quad (5a)$$

$$\epsilon_{IB} = \sum_{i=1,2} \frac{A_i}{\omega_i} \left[\frac{e^{i\phi_i}}{\omega_i^{-1} - \omega^{-1} - \tau_i^{-1}} + i \frac{e^{i\phi_i}}{\omega_i^{-1} + \omega^{-1} + \tau_i^{-1}} \right] \quad (5b)$$

where ω is the dipole frequency, ω_P is the Drude plasmon frequency, and τ_r is the size-dependent damping constant which is expressed as:

$$\tau_r = \tau_\infty + (l_\infty)/r \quad (6)$$

wherein τ_∞ is the bulk damping constant, l_∞ is the mean free path of metal NPs, and r is the radius of NP. In equation (5b), A_i , ω_i , ϕ_i , and τ_i are fit parameters in frequency.

The absorptivity term (A) also need to be modified to incorporate the size dependence effect. The absorptivity of a bulk mirror (A_{mirror}) is expressed in terms of metal thickness (d) for a semi-infinite plane and extinction component of the complex refraction index (κ) for a given wavelength (λ).

$$A_{mirror} = \frac{4\pi\kappa_2 d}{\lambda} \quad (7)$$

Since small NPs are not a semi-infinite plane or a perfect mirror, therefore, absorptivity can be expressed as

$$A_{np} = 10^3 \ln(10) \left[\frac{\epsilon_\lambda \left(2r_{cm} \left(\frac{2r_{cm}}{\delta_{skin}} \right) \right)}{\lambda N_A V_{cm^3}} \right] \quad (8)$$

where ϵ_λ is the extinction coefficient of the metal NP at the emission wavelength maximum of the donor, r is the radius of the metal NP in cm, N_A is the Avogadro's number, and V is the volume of the particle in cm^3 . Inserting equations 5 and 8 into the equation of the CPS-Kuhn

model (eq. 5) size-dependent NSET expression to determine d_0 can be obtained. The $1/R^4$ distance-dependent term is utilized to finally calculate the efficiency of energy transfer.

$$E = \frac{1}{1 + \left(\frac{d}{d_0}\right)^4} \quad (9)$$

Using this theory, Strouse *et al.* predicted the size and distance-dependent interaction of AuNP (radius < 10 nm) with fluorophores such as FAM and Cy3B. The authors performed experiments to measure the PL quenching of FAM and Cy3B in the presence of Au NP of varying sizes (0.945 to 8.25 nm). The AuNP and the fluorophore were separated by a double-stranded DNA and the distance between them was tuned from 65 Å to 272 Å by changing the number of base pairs of DNA [177]. The theoretically predicted size and distance-dependent quenching behavior for Au NP were in excellent agreement with experimentally observed quenching phenomenon. Excellent agreement between experimental and theoretically predicted d_0 values further validates the model. Modification of the CPS-Khun expression by including the size-dependent electronic terms proved to be an efficient method to explain the size-dependent quenching behaviour for the Au NPs up to a distance of 50 nm.

Overall, the mechanism and dynamics of the EET from a photoexcited donor to a metal NP is best described by NSET theory that utilizes $1/d^4$ distance-dependent term. Several groups have observed similar $1/d^4$ distance-dependent fluorescence quenching in various nanocomposite systems [141, 182-184]. Among these nanocomposite systems, QD-metal NP hybrid nanostructures find particular attention due to their enormous potential in future technology related nanophotonic devices as a consequence of size-dependent facile tuning of optoelectronic properties.

Several studies have demonstrated that the intrinsic exciton dynamics of QDs can be efficiently tuned in the presence of plasmonic NP as a result of long-range electromagnetic coupling between exciton and LSPR of NPs [185-186]. This coherently coupled plasmon–exciton mode is known as plexciton. For example, Pons *et al.* have investigated

the process of EET from CdSe/ZnS QDs to ultrasmall (1.4 nm) Au NPs separated by a polypeptide chain of variable length, over a broad range of distance (5–20 nm) and correlated their experimental findings with various theoretical models [187].

Similarly, Li *et al.* have investigated the EET process between differently sized Au Nps and CdSe/ZnS QDs [188]. It has been reported that small-sized (3 nm) Au NPs having insignificant LSPR quench the PL of QDs via NSET mechanism, while larger sized (15 and 80 nm) Au NPs with well-defined LSPR band quench the PL via FRET mechanism. Recently, Zhang *et al.* have shown the effect of QDs size on the mechanism of EET between CdTe QDs and 5.5 nm-sized Au NPs in a bilayer structure and observed that their experimental parameters correlate well with both FRET and NSET theory [189]. Furthermore, enhancement of EET between donor and acceptor CdTe QDs in the presence of Au NPs has also been reported [34, 186, 188]. However, in the majority of previous studies involving hybrid QD-NP nanostructures, the size-dependent changes in the optoelectronic properties of the metal NP have not been appraised in the theoretical modeling. Instead, optical and physicochemical properties of the bulk metal have been considered to explain the observed quenching mechanism. Nevertheless, these earlier studies reveal the fact that the plasmonic-exciton coupling and subsequent nonradiative processes in hybrid QD-NP nanocomposites are very complex and depend on various factors such as spectral overlap, interparticle distance, surface charge, and orientation of the transition moment vector relative to the metal NP surface.

Although several studies have been performed to investigate the EET between molecular dyes and the NP surface, systematic and precise control of the nonradiative electromagnetic coupling in hybrid QD-metal NP nanocomposite as a function of QDs size, separation distance, and excitation wavelength between similarly charged colloidal QD and NP is rare. In this thesis, we have investigated the mechanism behind the size and wavelength-dependent PL quenching of three differently sized CdTe QDs in the presence of plasmonic NPs. In addition, the

interactions of citrate-capped Ag NPs whose LSPR is significantly off-resonance with respect to the excitonic emission of all the three QDs have also been explored to establish the mechanism behind PL the quenching of CdTe QDs.

1.3.2.4. NSET Processes in Liposome

Optical-based distance measurements are essential to detect molecular interactions in several systems and have applications in biology as well as in chemistry. There are only a few studies that demonstrate the distance-dependent NSET process in micelles, liposomes, and polymer matrices [185, 150, 190]. For instance, Maity *et al.* have monitored pH-induced reversible vesicle-to-micelle transition using Au NPs and Rhodamine-6G dye as NSET pair [185]. The Au NPs encapsulated within the hydrophobic region of the vesicles participate in the energy transfer process with fluorophores confined at the core of the vesicles. The transition from vesicles to micelle at pH<5.2 causes an increase in the distance between the Au NPs and dye molecules thereby, changing the NSET efficiency. In a similar study, Mandal *et al.* have investigated NSET process between Au NPs and dyes embedded inside the self-assembled micelles of P123 (an amphiphilic block copolymer) [191]. Authors have demonstrated tuning of NSET by encapsulating different dyes at different locations of P123 micelles [182]. Chen *et al.* have exploited NSET as an optical ruler to determine binding site distances in live-cell surfaces [192]. These studies reveal the significance of NSET as an optical ruler to measure nanoscopic distances in real biological systems.

EET between metal NPs and fluorophore has been elucidated in the micelle, reverse micelles, and liposomes. Among these, EET processes across the liposome bilayer are significantly important for exploring various membrane related biophysical processes. In this thesis, we have investigated the NSET process between Au NPs and CdTe QDs across the lipid bilayer and have shown that the efficiency of NSET strongly depends on the location of CdTe QD and Au NPs in the liposome matrix.

1.4. Overview of the Thesis

Chapter 1 discusses the unique optical properties of QDs and plasmonic NPs. Special attention was given to MSA-capped CdTe QDs because of its narrow bandgap and large exciton Bohr radius. We have also discussed the self-assembly processes of MSA-capped CdTe QDs with polymer and surfactant. Finally, the mechanism and dynamics of various EET theories have been discussed in detail and illustrate the effect of alternation in FRET and NSET in the presence of liposome.

Chapter 2 includes details of the chemicals as well as the methods employed to synthesize MSA-capped CdTe QDs, citrate/PEG-stabilized Au NP, citrate-stabilized Ag NP, DHLA-capped Ag NC, and SUV of DPPC. A brief description of the sample preparations and experimental techniques used to complete the entire work of this thesis has been provided here.

Chapter 3 demonstrates the formation of a new class of luminescent hybrid coacervate from MSA-capped CdTe QDs and PDADMAC. These hybrid coacervates are found to be stable over a broad range of composition, pH, and ionic strength of the medium.

Chapter 4 demonstrates the interaction of MSA-capped CdTe QDs with CTAB surfactant and subsequent formation of self-assemble multicolor luminescent vesicles in an aqueous medium.

Chapter 5 discusses the fabrication of a simple liposome-based donor-acceptor FRET system using DAPI as the donor and an ultrasmall Ag NCs as the acceptor.

Chapter 6 investigates the size and wavelength-dependent NSET between MSA-capped CdTe QDs and plasmonic NPs (Au and Ag NPs). Furthermore, it has been observed that the quenching efficiency of the green QDs and citrate stabilized Au NPs pair decreases due to ligand

exchange at the surface of Au NPs with PEG-SH. These results have been explained on the basis of a size-dependent NSET model.

Chapter 7 investigates the time-dependent selective uptake of MSA-capped CdTe QDs into liposome in its gel phase and subsequent alternation of NSET with Au NPs.

Chapter 8 concludes the work done in this thesis, along with the scope for future applications.

1.5. References

1. Rao C. N. R., Kulkarni G. U., Thomas P. J., Edwards P. P. (2002), Size-dependent chemistry: properties of nanocrystals, *Chem.: Eur. J.*, *8*, 28-35. (DOI: 10.1002/1521-3765)
2. Murphy C. J. (2002), Nanocubes and nanoboxes, *Science*, *298*, 2139-2141. (DOI: 10.1126/science.1080007)
3. Hunt L. B. (1976), The true story of purple of cassius, *Gold Bulletin*, *9*, 134-139. (DOI: 10.1007/bf03215423)
4. Wagner F. E., Haslbeck S., Stievano L., Calogero S., Pankhurst Q. A., Martinek K. P. (2000), Before striking gold in gold-ruby glass, *Nature*, *407*, 691-692. (DOI: 10.1038/35037661)
5. Brooke J. H. (1972), Chemistry studies in the history of chemistry. By Sir Harold Hartley. Oxford: Clarendon Press: Oxford University Press, *Br. J. Hist. Sci.*, *6*, 90-911971.
6. Jeevanandam J., Barhoum A., Chan Y. S., Dufresne A., Danquah M. K. (2018), Review on nanoparticles and nanostructured materials: history, sources, toxicity and regulations, *Beilstein J. Nanotechnol.*, *9*, 1050-1074. (DOI: 10.3762/bjnano.9.98)
7. Neupane G. P., Ma W., Yildirim T., Tang Y., Zhang L., Lu Y. (2019), 2D organic semiconductors, the future of green nanotechnology, *Nano Materials Science*, *1*, 246-259. (DOI: 10.1016/j.nanoms.2019.10.002)
8. Yamamoto H., Wilkinson J., Long J. P., Bussman K., Christodoulides J. A., Kafafi Z. H. (2005), Nanoscale organic light-emitting diodes, *Nano Lett.*, *5*, 2485-2488. (DOI: 10.1021/nl051811+)
9. Kim J.-J., Lee J., Yang S.-P., Kim H. G., Kweon H.-S., Yoo S., Jeong K.-H. (2016), Biologically inspired organic light-emitting diodes, *Nano Lett.*, *16*, 2994-3000. (DOI: 10.1021/acs.nanolett.5b05183)
10. Talapin D. V., Shevchenko E. V. (2016), Introduction: Nanoparticle chemistry, *Chem. Rev.*, *116*, 10343-10345. (DOI: 10.1021/acs.chemrev.6b00566)

11. Yang F., Cheng S., Zhang X., Ren X., Li R., Dong H., Hu W. (2018), 2D Organic materials for optoelectronic applications, *Adv. Mater.*, *30*, 1702415. (DOI: 10.1002/adma.201702415)
12. Tiwari J. N., Tiwari R. N., Kim K. S. (2012), Zero-dimensional, one-dimensional, two-dimensional and three-dimensional nanostructured materials for advanced electrochemical energy devices, *Prog. Mater. Sci.*, *57*, 724-803. (DOI: 10.1016/j.pmatsci.2011.08.003)
13. Khan I., Saeed K., Khan I. (2019), Nanoparticles: properties, applications and toxicities, *Arab. J. Chem.*, *12*, 908-931. (DOI: 10.1016/j.arabjc.2017.05.011)
14. Mody V. V., Siwale R., Singh A., Mody H. R. (2010), Introduction to metallic nanoparticles, *J. Pharm. Bioallied Sci.*, *2*, 282-289. (DOI: 10.4103/0975-7406.72127)
15. González A. L., Reyes-Esqueda J. A., Noguez C. (2008), Optical properties of elongated noble metal nanoparticles, *J. Phys. Chem. C*, *112*, 7356-7362. (DOI: 10.1021/jp800432q)
16. Fong K. E., Yung L.-Y. L. (2013), Localized surface plasmon resonance: A unique property of plasmonic nanoparticles for nucleic acid detection, *Nanoscale*, *5*, 12043-12071. (DOI: 10.1039/C3NR02257A)
17. Robenek H. (1990), Colloidal gold: principles, methods, and applications vols. I and II (vol. III in preparation) Edited by M. A. Hayat Academic Press, Inc., New York, 1989 ISBN 0-12-333927-8, Vol. I, 536 pages ISBN 0-12-333928-6, Vol. II, 484 pages, *Scanning*, *12*, 244-244. (DOI: 10.1002/sca.4950120410)
18. Jain P. K., Huang X., El-Sayed I. H., El-Sayed M. A. (2008), Noble Metals on the nanoscale: Optical and photothermal properties and some applications in imaging, sensing, biology, and medicine, *Acc. Chem. Res.*, *41*, 1578-1586. (DOI: 10.1021/ar7002804)
19. Yang L., Zhou Z., Song J., Chen X. (2019), Anisotropic nanomaterials for shape-dependent physicochemical and biomedical applications, *Chem. Soc. Rev.*, *48*, 5140-5176. (DOI: 10.1039/C9CS00011A)

20. Turkevich J., Stevenson P. C., Hillier J. (1951), A study of the nucleation and growth processes in the synthesis of colloidal gold, *Faraday Discuss.*, *11*, 55-75. (DOI: 10.1039/DF9511100055)
21. Uricanu V., Eastman J. R., Vincent B. (2001), Stability in colloidal mixtures containing particles with a large disparity in size, *J. Colloid Interface Sci.*, *233*, 1-11. (DOI: 10.1006/jcis.2000.7192)
22. Swierczewska M., Lee S., Chen X. (2011), The design and application of fluorophore-gold nanoparticle activatable probes, *Phys. Chem. Chem. Phys.*, *13*, 9929-9941. (DOI: 10.1039/c0cp02967j)
23. Jiang S., Win K. Y., Liu S., Teng C. P., Zheng Y., Han M.-Y. (2013), Surface-functionalized nanoparticles for biosensing and imaging-guided therapeutics, *Nanoscale*, *5*, 3127-3148. (DOI: 10.1039/C3NR34005H)
24. Samanta A., Medintz I. L. (2016), Nanoparticles and DNA – a powerful and growing functional combination in bionanotechnology, *Nanoscale*, *8*, 9037-9095. (DOI: 10.1039/C5NR08465B)
25. Kobayashi K., Wei J., Iida R., Ijiro K., Niikura K. (2014), Surface engineering of nanoparticles for therapeutic applications, *Polym.*, *46*, 460-468. (DOI: 10.1038/pj.2014.40)
26. Kong F.-Y., Zhang J.-W., Li R.-F., Wang Z.-X., Wang W.-J., Wang W. (2017), Unique roles of gold nanoparticles in drug delivery, targeting and imaging applications, *Molecules*, *22*, 1445. (DOI: 10.3390/molecules22091445)
27. Chen P. C., Mwakwari S. C., Oyelere A. K. (2008), Gold nanoparticles: From nanomedicine to nanosensing, *Nanotechnol Sci Appl*, *1*, 45-65. (DOI: 10.2147/nsa.s3707)
28. Alivisatos A., Waldeck D., Harris C. B., (1985), Nonclassical behavior of energy transfer from molecules to metal surfaces: Biacetyl ($3n\pi^*$)/Ag(111), *Chem. Phys.*, *82*, 541-547. (DOI: 10.1063/1.448778)
29. Gedi V., Kim Y.-P. (2014), Detection and characterization of cancer cells and pathogenic bacteria using aptamer-based nanoconjugates, *Sensors*, *14*, 18302-18327. (DOI: 10.3390/s141018302)
30. Chinen A. B., Guan C. M., Ferrer J. R., Barnaby S. N., Merkel T. J., Mirkin C. A. (2015), Nanoparticle probes for the detection of

cancer biomarkers, cells, and tissues by fluorescence, *Chem. Rev.*, *115*, 10530-10574. (DOI: 10.1021/acs.chemrev.5b00321)

31. Rosi N. L., Giljohann D. A., Thaxton C. S., Lytton-Jean A. K. R., Han M. S., Mirkin C. A. (2006), Oligonucleotide-modified gold nanoparticles for intracellular gene regulation, *Science*, *312*, 1027-1030. (DOI: 10.1126/science.1125559)

32. Ozel T., Hernandez-Martinez P. L., Mutlugun E., Akin O., Nizamoglu S., Ozel I. O., Zhang Q., Xiong Q., Demir H. V. (2013), Observation of selective plasmon-exciton coupling in nonradiative energy transfer: Donor-selective versus acceptor-selective plexcitons, *Nano Lett.*, *13*, 3065-3072. (DOI: 10.1021/nl4009106)

33. Acuna G. P., Bucher M., Stein I. H., Steinhauer C., Kuzyk A., Holzmeister P., Schreiber R., Moroz A., Stefani F. D., Liedl T., Simmel F. C., Tinnefeld P. (2012), Distance dependence of single-fluorophore quenching by gold nanoparticles studied on DNA origami, *ACS Nano*, *6*, 3189-3195. (DOI: 10.1021/nn2050483)

34. Li M., Cushing S. K., Wang Q., Shi X., Hornak L. A., Hong Z., Wu N. (2011), Size-dependent energy transfer between CdSe/ZnS quantum dots and gold nanoparticles, *J. Phys. Chem.*, *2*, 2125-2129. (DOI: 10.1021/jz201002g)

35. Farooq M. U., Novosad V., Rozhkova E. A., Wali H., Ali A., Fateh A. A., Neogi P. B., Neogi A., Wang Z. (2018), Gold nanoparticles-enabled efficient dual delivery of anticancer therapeutics to HeLa cells, *Sci. Rep.*, *8*, 2907. (DOI: 10.1038/s41598-018-21331-y)

36. Mieszawska A. J., Mulder W. J. M., Fayad Z. A., Cormode D. P. (2013), Multifunctional gold nanoparticles for diagnosis and therapy of disease, *Mol. Pharm.*, *10*, 831-847. (DOI: 10.1021/mp3005885)

37. Lee S. H., Jun B.-H. (2019), Silver nanoparticles: Synthesis and application for nanomedicine, *Int. J. Mol. Sci.*, *20*, 865. (DOI: 10.3390/ijms20040865.)

38. Zhang X.-F., Liu Z.-G., Shen W., Gurunathan S. (2016), Silver nanoparticles: Synthesis, characterization, properties, applications, and Therapeutic approaches, *Int J. Mol. Sci.*, *17*, 1534. (DOI: 10.3390/ijms17091534)

39. Hamouda R. A., Hussein M. H., Abo-elmagd R. A., Bawazir S. S. (2019), Synthesis and biological characterization of silver nanoparticles derived from the cyanobacterium *oscillatoria limnetica*, *Sci. Rep.*, *9*, 13071. (DOI: 10.1038/s41598-019-49444-y)
40. Filippo E., Serra A., Buccolieri A., Manno D. (2010), Green synthesis of silver nanoparticles with sucrose and maltose: Morphological and structural characterization, *J. Non-Cryst. Solids*, *356*, 344-350. (DOI: 10.1016/j.jnoncrysol.2009.11.021)
41. Agnihotri S., Mukherji S., Mukherji S. (2014), Size-controlled silver nanoparticles synthesized over the range 5–100 nm using the same protocol and their antibacterial efficacy, *RSC Adv.*, *4*, 3974-3983. (DOI: 10.1039/C3RA44507K)
42. Phan C. M., Nguyen H. M. (2017), Role of capping agent in wet synthesis of nanoparticles, *J. Phys. Chem. A* *121*, 3213-3219. (DOI: 10.1021/acs.jpca.7b02186)
43. Bastús N. G., Merkoçi F., Piella J., Puntès V. (2014), Synthesis of highly monodisperse citrate-stabilized silver nanoparticles of up to 200 nm: Kinetic control and catalytic properties, *Chem. Mater.*, *26*, 2836-2846. (DOI: 10.1021/cm500316k)
44. Hartmann G., Baumgartner T., Schuster M. (2014), Influence of particle coating and matrix constituents on the cloud point extraction efficiency of silver nanoparticles (Ag-NPs) and application for monitoring the formation of Ag-NPs from Ag⁺, *Anal. Chem.* *86*, 790-796. (DOI: 10.1021/ac403289d)
45. Virel A., Saa L., Pavlov V. (2009), Modulated growth of nanoparticles application for sensing nerve gases, *Anal. Chem.*, *81*, 268-272. (DOI: 10.1021/ac801949x)
46. Akter M., Sikder M. T., Rahman M. M., Ullah A. K. M. A., Hossain K. F. B., Banik S., Hosokawa T., Saito T., Kurasaki M. (2018), A systematic review on silver nanoparticles-induced cytotoxicity: Physicochemical properties and perspectives, *J. Adv. Res.*, *9*, 1-16. (DOI: 10.1016/j.jare.2017.10.008)
47. Nimmo M. T., Caillard L. M., De Benedetti W., Nguyen H. M., Seitz O., Gartstein Y. N., Chabal Y. J., Malko A. V. (2013), Visible to

near-infrared sensitization of silicon substrates via energy transfer from proximal nanocrystals: further insights for hybrid photovoltaics, *ACS Nano*, 7, 3236-3245. (DOI: 10.1021/nn400924y)

48. Fu G., Guan J., Li B., Liu L., Hui Y., Yu C., Zhang Z., Lv X. (2018), Efficient and weak efficiency-roll-off near-infrared (NIR) polymer light-emitting diode (PLED) based on PVK-supported Zn²⁺-Yb³⁺-containing metallopolymer, *J. Mater. Chem. C*, 6. (DOI: 10.1039/C7TC05400A)

49. Jia W., Chen Q., Chen L., Yuan D., Xiang J., Chen Y., Xiong Z. (2016), Molecular spacing modulated conversion of singlet fission to triplet fusion in rubrene-based organic light-emitting diodes at ambient temperature, *J. Phys. Chem. C*, 120, 8380-8386. (DOI: 10.1021/acs.jpcc.6b01889)

50. Song X.-R., Goswami N., Yang H.-H., Xie J. (2016), Functionalization of metal nanoclusters for biomedical applications, *Analyst*, 141, 3126-3140. (10.1039/C6AN00773B)

51. Jin R. (2015), Atomically precise metal nanoclusters: Stable sizes and optical properties, *Nanoscale*, 7, 1549-1565. (DOI: 10.1039/C4NR05794E)

52. Zheng J., Nicovich P. R., Dickson R. M. (2007), Highly fluorescent noble-metal quantum dots, *Annu. Rev. Phys.* 58, 409-431. (DOI: 10.1146/annurev.physchem.58.032806.104546)

53. Bao Y., Zhong C., Vu D. M., Temirov J. P., Dyer R. B., Martinez J. S. (2007), Nanoparticle-free synthesis of fluorescent gold nanoclusters at physiological temperature, *J. Phys. Chem. C*, 111, 12194-12198. (DOI: 10.1021/jp071727d)

54. Jiang Y., Huang Y., Cheng H., Liu Q., Xie Z., Yao T., Jiang Z., Huang Y., Bian Q., Pan G., Sun Z., Wei S. (2014), Solvent influence on the role of thiols in growth of thiols-capped Au nanocrystals, *J. Phys. Chem. C*, 118, 714-719. (DOI: 10.1021/jp408926n)

55. Collins G., Schmidt M., McGlacken G. P., O'Dwyer C., Holmes J. D. (2014), Stability, oxidation, and shape evolution of PVP-capped Pd nanocrystals, *J. Phys. Chem. C*, 118, 6522-6530. (DOI: 10.1021/jp500716z)

56. Zhang M., Dang Y.-Q., Liu T.-Y., Li H.-W., Wu Y., Li Q., Wang K., Zou B. (2013), Pressure-induced fluorescence enhancement of the BSA-protected gold nanoclusters and the corresponding conformational changes of protein, *J. Phys. Chem. C*, *117*, 639-647. (DOI: 10.1021/jp309175k)
57. Wang S., Wang Y., Peng Y., Yang X. (2019), Exploring the antibacteria performance of multicolor Ag, Au, and Cu nanoclusters, *ACS Appl. Mater. Interfaces*, *11*, 8461-8469. (DOI: 10.1021/acsami.8b22143)
58. Mishra D., Wang S., Jin Z., Xin Y., Lochner E., Mattoussi H. (2019), Highly fluorescent hybrid Au/Ag nanoclusters stabilized with poly(ethylene glycol)- and zwitterion-modified thiolate ligands, *Phys. Chem. Chem. Phys.*, *21*, 21317-21328. (DOI: 10.1039/C9CP03723C)
59. Zhang Q., Yang M., Zhu Y., Mao C. (2018), Metallic nanoclusters for cancer imaging and therapy, *Curr. Med. Chem.*, *25*, 1379-1396. (DOI: 10.2174/0929867324666170331122757)
60. Wang Q., Wang S., Hu X., Li F., Ling D. (2019), Controlled synthesis and assembly of ultra-small nanoclusters for biomedical applications, *Biomater. Sci.* *7*, 480-489. (10.1039/C8BM01200H)
61. Chang J., Waclawik E. R. (2014), Colloidal semiconductor nanocrystals: Controlled synthesis and surface chemistry in organic media, *RSC Adv.*, *4*, 23505-23527. (DOI: 10.1039/C4RA02684E)
62. Reed M. A., Randall J. N., Aggarwal R. J., Matyi R. J., Moore T. M., Wetsel A. E. (1988), Observation of discrete electronic states in a zero-dimensional semiconductor nanostructure, *Phys. Rev. Lett.*, *60*, 535-537. (DOI: 10.1103/PhysRevLett.60.535)
63. Alivisatos A. P. (1996), Semiconductor clusters, nanocrystals, and quantum dots, *Science*, *271*, 933-937. (DOI: 10.1126/science.271.5251.933)
64. Smith A. M., Nie S. (2010), Semiconductor nanocrystals: structure, properties, and band gap engineering, *Acc. Chem. Res.*, *43*, 190-200. (DOI: 10.1021/ar9001069)

65. Ng S. M., Koneswaran M., Narayanaswamy R. (2016), A review on fluorescent inorganic nanoparticles for optical sensing applications, *RSC Adv.*, *6*, 21624-21661. (DOI: 10.1039/C5RA24987B)
66. Riley E. A., Hess C. M., Reid P. J. (2012), Photoluminescence intermittency from single quantum dots to organic molecules: Emerging themes, *Int. J. Mol. Sci.*, *13*, 12487-12518. (DOI: 10.3390/ijms131012487)
67. Xu X. (2014), Surface recombination and charged exciton in nanocrystal quantum dots on photonic crystals under two-photon excitation, *Sci. Rep.*, *4*, 5039. (DOI: 10.1038/srep05039)
68. Zeng Z., Chen X., Wang H., Huang N., Shan C., Zhang H., Teng J., Xi P. (2015), Fast super-resolution imaging with ultra-high labeling density achieved by joint tagging super-resolution optical fluctuation imaging, *Sci. Rep.*, *5*, 8359-8359. (DOI: 10.1038/srep08359)
69. Bhandari S., Mondal D., Nataraj S. K., Balakrishna R. G. (2019), Biomolecule-derived quantum dots for sustainable optoelectronics, *Nanoscale Adv.*, *1*, 913-936. (DOI: 10.1039/C8NA00332G)
70. Yong K.-T., Law W.-C., Roy I., Jing Z., Huang H., Swihart M. T., Prasad P. N. (2011), Aqueous phase synthesis of CdTe quantum dots for biophotonics, *J. Biophotonics*, *4*, 9-20. (DOI: 10.1002/jbio.201000080)
71. Ma Y., Zhang Y., Yu W. W. (2019), Near infrared emitting quantum dots: Synthesis, luminescence properties and applications, *J. Mater. Chem. C*, *7*, 13662-13679. (DOI: 10.1039/C9TC04065J)
72. Resch U., Weller H., Henglein A. (1989), Photochemistry and radiation chemistry of colloidal semiconductors. 33. Chemical changes and fluorescence in CdTe and ZnTe, *Langmuir*, *5*, 1015-1020. (DOI: 10.1021/la00088a023)
73. Resch-Genger U., Grabolle M., Cavaliere-Jaricot S., Nitschke R., Nann T. (2008), Quantum dots versus organic dyes as fluorescent labels, *Nat. Methods*, *5*, 763-775. (DOI: 10.1038/nmeth.1248)
74. Rogach A. L., Franzl T., Klar T. A., Feldmann J., Gaponik N., Lesnyak V., Shavel A., Eychmüller A., Rakovich Y. P., Donegan J. F.

- (2007), Aqueous synthesis of thiol-capped CdTe nanocrystals: State-of-the-art, *J. Phys. Chem. C*, *111*, 14628-14637. (DOI: 10.1021/jp072463y)
75. Rogach A. L., Katsikas L., Kornowski A., Su D., Eychmüller A., Weller H. (1996), Synthesis and characterization of thiol-stabilized CdTe nanocrystals, *J. Phys. Chem.*, *100*, 1772-1778. (DOI: 10.1002/bbpc.19961001104)
76. Gao M., Kirstein S., Möhwald H., Rogach A. L., Kornowski A., Eychmüller A., Weller H. (1998), Strongly photoluminescent CdTe nanocrystals by proper surface modification, *J. Phys. Chem. B*, *102*, 8360-8363. (DOI: 10.1021/jp9823603)
77. Lesnyak V., Gaponik N., Eychmüller A. (2013), Colloidal semiconductor nanocrystals: The aqueous approach, *Chem. Soc. Rev.*, *42*, 2905-2929. (DOI: 10.1039/C2CS35285K)
78. Jing L., Kershaw S. V., Li Y., Huang X., Li Y., Rogach A. L., Gao M. (2016), Aqueous based semiconductor nanocrystals, *Chem. Rev.*, *116*, 10623-10730. (DOI: 10.1021/acs.chemrev.6b00041)
79. Dhotel A., Chen Z., Delbreilh L., Youssef B., Saiter J.-M., Tan L. (2013), Molecular motions in functional self-assembled nanostructures, *Int. J. Mol. Sci.*, *14*, 2303-2333. (DOI: 10.3390/ijms14022303)
80. Chen P. Z., Pollit L., Jones L., Gu F. X. (2018), Functional two- and three-dimensional architectures of immobilized metal nanoparticles, *Chem*, *4*, 2301-2328. (DOI: 10.1016/j.chempr.2018.07.009)
81. Zhang X., Gong C., Akakuru O. U., Su Z., Wu A., Wei G. (2019), The design and biomedical applications of self-assembled two-dimensional organic biomaterials, *Chem. Soc. Rev.*, *48*, 5564-5595. (DOI: 10.1039/C8CS01003J)
82. Li L.-L., An H.-W., Peng B., Zheng R., Wang H. (2019), Self-assembled nanomaterials: design principles, the nanostructural effect, and their functional mechanisms as antimicrobial or detection agents, *Mater. Horiz.*, *6*, 1794-1811. (DOI: 10.1039/C8MH01670D)
83. Kong I., Chapter 7 - Polymers with Nano-encapsulated functional polymers. In *design and applications of nanostructured polymer blends and nanocomposite systems*, Thomas, S.; Shanks, R.;

Chandrasekharakurup, S., Eds. William Andrew Publishing: Boston, 2016; pp 125-154.

84. Patra J. K., Das G., Fraceto L. F., Campos E. V. R., Rodriguez-Torres M. D. P., Acosta-Torres L. S., Diaz-Torres L. A., Grillo R., Swamy M. K., Sharma S., Habtemariam S., Shin H.-S. (2018), Nano based drug delivery systems: Recent developments and future prospects, *J. Nanobiotechnology*, *16*, 71-71. (DOI: 10.1186/s12951-018-0392-8)
85. Dzhardimalieva G. I., Rabinskiy L. N., Kydralieva K. A., Uflyand I. E. (2019), Recent advances in metallopolymer-based drug delivery systems, *RSC Adv.*, *9*, 37009-37051. (DOI: 10.1039/C9RA06678K)
86. Pyun J. (2007), Nanocomposite materials from functional polymers and magnetic colloids, *Polym. Rev.*, *47*, 231-263. (DOI: 10.1080/15583720701271294)
87. Poudyal R. R., Keating C. D., Bevilacqua P. C. (2019), Polyanion-assisted ribozyme catalysis inside complex coacervates, *ACS Chem. Biol.*, *14*, 1243-1248. (DOI: 10.1021/acscchembio.9b00205)
88. Poudyal R. R., Guth-Metzler R. M., Veenis A. J., Frankel E. A., Keating C. D., Bevilacqua P. C. (2019), Template-directed RNA polymerization and enhanced ribozyme catalysis inside membraneless compartments formed by coacervates, *Nat. Commun.*, *10*, 490. (DOI: 10.1038/s41467-019-08353-4)
89. Long M. S., Jones C. D., Helfrich M. R., Mangeney-Slavin L. K., Keating C. D. (2005), Dynamic microcompartmentation in synthetic cells, *Proc. Natl. Acad. Sci. U.S.A.*, *102*, 5920-5925. (DOI: 10.1073/pnas.0409333102)
90. Dora Tang T. Y., Rohaida Che Hak C., Thompson A. J., Kuimova M. K., Williams D. S., Perriman A. W., Mann S. (2014), Fatty acid membrane assembly on coacervate microdroplets as a step towards a hybrid protocell model, *Nat. Chem.*, *6*, 527-533. (DOI: 10.1038/nchem.1921)
91. Frankel E. A., Bevilacqua P. C., Keating C. D. (2016), Polyamine/nucleotide coacervates provide strong compartmentalization

- of Mg^{2+} , nucleotides, and RNA, *Langmuir*, 32, 2041-2049. (DOI: 10.1021/acs.langmuir.5b04462)
92. Singh M. K., Ilg P., Espinosa-Marzal R. M., Spencer N. D., Kröger M. (2016), Influence of chain stiffness, grafting density and normal load on the tribological and structural behavior of polymer brushes: A nonequilibrium-molecular-dynamics study, *Polymers*, 8, 254. (DOI: 10.3390/polym8070254)
93. Foster J. C., Varlas S., Couturaud B., Coe Z., O'Reilly R. K. (2019), Getting into shape: Reflections on a new generation of cylindrical nanostructures' self-assembly using polymer building blocks, *J. Am. Chem. Soc.*, 141, 2742-2753. (DOI: 10.1021/jacs.8b08648)
94. Li L., Raghupathi K., Song C., Prasad P., Thayumanavan S. (2014), Self-assembly of random copolymers, *Chem. Comm.*, 50, 13417-32. (DOI: 10.1039/c4cc03688c)
95. Zhang W., Yu X., Li Y., Su Z., Jandt K. D., Wei G. (2018), Protein-mimetic peptide nanofibers: Motif design, self-assembly synthesis, and sequence-specific biomedical applications, *Prog. Polym. Sci.*, 80, 94-124. (DOI: 10.1016/j.progpolymsci.2017.12.001)
96. Radhakrishna M., Basu K., Liu Y., Shamsi R., Perry S. L., Sing C. E. (2017), Molecular connectivity and correlation effects on polymer coacervation, *Macromolecules*, 50, 3030-3037. (DOI: 10.1021/acs.macromol.6b02582)
97. Zhang H., Liu Y., Yao D., Yang B. (2012), Hybridization of inorganic nanoparticles and polymers to create regular and reversible self-assembly architectures, *Chem. Soc. Rev.*, 41, 6066-6088. (DOI: 10.1039/C2CS35038F)
98. Li Y., Wang Y., Huang G., Gao J. (2018), Cooperativity principles in self-assembled nanomedicine, *Chem. Rev.*, 118, 5359-5391. (DOI: 10.1021/acs.chemrev.8b00195)
99. Williams D. S., Koga S., Hak C. R. C., Majrekar A., Patil A. J., Perriman A. W., Mann S. (2012), Polymer/nucleotide droplets as bio-inspired functional micro-compartments, *Soft Matter*, 8, 6004-6014. (DOI: 10.1039/C2SM25184A)

100. Crosby J., Treadwell T., Hammerton M., Vasilakis K., Crump M. P., Williams D. S., Mann S. (2012), Stabilization and enhanced reactivity of actinorhodin polyketide synthase minimal complex in polymer–nucleotide coacervate droplets, *Chem. Comm.*, *48*, 11832-11834. (DOI: 10.1039/C2CC36533B)
101. Wang M., Zhang M., Li J., Kumar S., Walker G. C., Scholes G. D., Winnik M. A. (2010), Self-assembly of colloidal quantum dots on the scaffold of triblock copolymer micelles, *ACS Appl. Mater. Interfaces*, *2*, 3160-3169. (DOI: 10.1021/am100645j)
102. Li J., Yu Y., Bi X. (2019), High-efficient NUV emission with excellent thermal stability in Cd/Pb-Free AS-ZnO QDs by ALD without surface passivation, *ACS Photonics*, *6*, 1715-1727. (DOI: 10.1021/acsp Photonics.9b00382)
103. Dong X., Xiong S., Luo B., Ge R., Li Z., Li J., Zhou Y. (2018), Flexible and transparent organic–inorganic hybrid thermoelectric modules, *ACS Appl. Mater. Interfaces*, *10*, 26687-26693. (DOI: 10.1021/acсами.8b08696)
104. Huang X., Jeong Y.-I., Moon B. K., Zhang L., Kang D. H., Kim I. (2013), Self-assembly of morphology-tunable architectures from tetraarylmethane derivatives for targeted drug delivery, *Langmuir*, *29*, 3223-3233. (DOI: 10.1021/la305069e)
105. Xu X., Megarajan S. K., Zhang Y., Jiang H. (2019), Ordered mesoporous alumina and their composites based on evaporation induced self-assembly for adsorption and catalysis, *Chem. Mater.* (DOI: 10.1021/acs.chemmater.9b03873)
106. Kimizuka N., Yanai N., Morikawa M. A. (2016), Photon upconversion and molecular solar energy storage by maximizing the potential of molecular self-assembly, *Langmuir*, *32*, 12304-12322. (DOI: 10.1021/acs.langmuir.6b03363)
107. Chen H., Zhang E., Yang G., Li L., Wu L., Zhang Y., Liu Y., Chen G., Jiang M. (2019), Aggregation-induced emission luminogen assisted self-assembly and morphology transition of amphiphilic glycopolyptide with bioimaging application, *ACS Macro Lett.*, *8*, 893-898. (DOI: 10.1021/acsmacrolett.9b00383)

108. Butler G. B., Angelo R. J. (1957), Preparation and polymerization of unsaturated quaternary ammonium compounds. VIII. A proposed alternating intramolecular-intermolecular chain propagation¹, *J. Am. Chem. Soc.*, *79*, 3128-3131. (DOI: 10.1021/ja01569a037)
109. Martin N., Li M., Mann S. (2016), Selective uptake and refolding of globular proteins in coacervate microdroplets, *Langmuir*, *32*, 5881-5889. (DOI: 10.1021/acs.langmuir.6b01271)
110. Priftis D., Xia X., Margossian K. O., Perry S. L., Leon L., Qin J., de Pablo J. J., Tirrell M. (2014), Ternary, tunable polyelectrolyte complex fluids driven by complex coacervation, *Macromolecules*, *47*, 3076-3085. (DOI: 10.1021/ma500245j)
111. van Swaay D., Tang T.-Y. D., Mann S., de Mello A. (2015), Microfluidic formation of membrane-free aqueous coacervate droplets in water, *Angew. Chem. Int. Ed.*, *54*, 8398-8401. (DOI: 10.1002/anie.201502886)
112. Krasia-Christoforou T., Georgiou T. K. (2013), Polymeric theranostics: Using polymer-based systems for simultaneous imaging and therapy, *J. Mater. Chem. B*, *1*, 3002-3025. (DOI: 10.1039/C3TB20191K)
113. Branco M. C., Schneider J. P. (2009), Self-assembling materials for therapeutic delivery, *Acta Biomater.*, *5*, 817-831. (DOI: 10.1016/j.actbio.2008.09.018)
114. Liu F., Kozlovskaya V., Medipelli S., Xue B., Ahmad F., Saeed M., Cropek D., Kharlampieva E. (2015), Temperature-sensitive polymersomes for controlled delivery of anticancer drugs, *Chem. Mater.*, *27*, 7945-7956. (DOI: 10.1021/acs.chemmater.5b03048)
115. Chan Y.-H. M., Boxer S. G. (2007), Model membrane systems and their applications, *Curr. Opin. Chem. Biol.*, *11*, 581-587. (DOI: 10.1016/j.cbpa.2007.09.020)
116. Lira R. B., Dimova R., Chapter Six - Fusion assays for model membranes: A critical review. In *Advances in Biomembranes and Lipid Self-Assembly*, Lipowsky, R., Ed. Academic Press: 2019; Vol. 30, pp 229-270.

117. Shnyrova A. V., Ayllon J., Mikhalyov I. I., Villar E., Zimmerberg J., Frolov V. A. (2007), Vesicle formation by self-assembly of membrane-bound matrix proteins into a fluidlike budding domain, *J. Cell. Biol.*, *179*, 627-633. (DOI: 10.1083/jcb.200705062)
118. Li X., Liu Y., Wang L., Deng M., Liang H. (2009), Fusion and fission pathways of vesicles from amphiphilic triblock copolymers: A dissipative particle dynamics simulation study, *Phys. Chem. Chem. Phys.*, *11*, 4051-9. (DOI: 10.1039/b817773b)
119. Laemmli U. K. (1970), Cleavage of structural proteins during the assembly of the head of bacteriophage T4, *Nature*, *227*, 680-685. (DOI: 10.1038/227680a0)
120. Ito E., Yip K. W., Katz D., Fonseca S. B., Hedley D. W., Chow S., Xu G. W., Wood T. E., Bastianutto C., Schimmer A. D., Kelley S. O., Liu F.-F. (2009), Potential use of cetrimonium bromide as an apoptosis-promoting anticancer agent for head and neck cancer, *Mol. Pharmacol.*, *76*, 969-983. (DOI: 10.1124/mol.109.055277)
121. Ghosh A., Seth S. K., Purkayastha P. (2018), Surfactant and cyclodextrin induced vesicle to micelle to vesicle transformation in aqueous medium, *Langmuir*, *34*, 11503-11509. (DOI: 10.1021/acs.langmuir.8b02233)
122. Nagarajan R., Ruckenstein E. (1991), Theory of surfactant self-assembly: A predictive molecular thermodynamic approach, *Langmuir*, *7*, 2934-2969. (DOI: 10.1021/la00060a012)
123. Nagarajan R. (2002), Molecular packing parameter and surfactant self-assembly: The neglected role of the surfactant tail, *Langmuir*, *18*, 31-38. (DOI: 10.1021/la010831y)
124. Marques E. F., Silva B. F. B. (2013), Surfactant self-assembly. *J. Colloid Interface Sci.*, Tadros, T., Ed. Springer Berlin Heidelberg: Berlin, Heidelberg, pp 1202-1241. (DOI: 10.1007/978-3-642-20665-8_169)
125. Egelhaaf S. U. (1998), Kinetics of structural transitions in surfactant solutions, *Curr. Opin. Colloid Interface Sci.*, *3*, 608-613. (DOI: 10.1016/S1359-0294(98)80087-3)

126. Discher D. E., Eisenberg A. (2002), Polymer vesicles, *Science*, 297, 967-973. (DOI: 10.1126/science.1074972)
127. Yadavalli S. S., Xiao Q., Sherman S. E., Hasley W. D., Klein M. L., Goulian M., Percec V. (2019), Bioactive cell-like hybrids from dendrimersomes with a human cell membrane and its components, *Proc. Natl. Acad. Sci.*, 116, 744-752. (DOI: 10.1073/pnas.1811307116)
128. Huang J., Bonduelle C., Thévenot J., Lecommandoux S., Heise A. (2012), Biologically active polymersomes from amphiphilic glycopeptides, *J. Am. Chem. Soc.*, 134, 119-122. (DOI: 10.1021/ja209676p)
129. Sakuma Y., Imai M. (2015), From vesicles to protocells: The roles of amphiphilic molecules, *Life*, 5, 651-675. (DOI: 10.3390/life5010651)
130. Sun X., Zhang Q., Yin K., Zhou S., Li H. (2016), Fluorescent vesicles formed by simple surfactants induced by oppositely-charged carbon quantum dots, *Chem. Comm.*, 52, 12024-12027. (DOI: 10.1039/C6CC05783G)
131. Sun X., Chen M., Zhang Y., Yin Y., Zhang L., Li H., Hao J. (2018), Photoluminescent and pH-responsive supramolecular structures from co-assembly of carbon quantum dots and zwitterionic surfactant micelles, *J. Mater. Chem. B*, 6, 7021-7032. (DOI: 10.1039/C8TB00630J)
132. Lakowicz J. R., (1999), *Principles of Fluorescence Spectroscopy*. 2nd ed.; Academic Press: New York. (ISBN: 0-306-46093-9)
133. Shan T., Liu Y., Tang X., Bai Q., Gao Y., Gao Z., Li J., Deng J., Yang B., Lu P., Ma Y. (2016), Highly efficient deep blue organic light-emitting diodes based on imidazole: Significantly enhanced performance by effective energy transfer with negligible efficiency roll-off, *ACS Appl. Mater. Interfaces*, 8, 28771-28779. (DOI: 10.1021/acsami.6b10004)
134. Wu X., Song Y., Yan X., Zhu C., Ma Y., Du D., Lin Y. (2017), Carbon quantum dots as fluorescence resonance energy transfer sensors

for organophosphate pesticides determination, *Biosens. Bioelectron.*, *94*, 292-297. (DOI: 10.1016/j.bios.2017.03.010)

135. Kulkarni B., Jayakannan M. (2017), Fluorescent-tagged biodegradable polycaprolactone block copolymer FRET probe for intracellular bioimaging in cancer cells, *ACS Biomater Sci Eng.*, *3*, 2185-2197. (DOI: 10.1021/acsbiomaterials.7b00426)

136. Förster T. (1948), Zwischenmolekulare Energiewanderung und Fluoreszenz, *Annalen der Physik*, *437*, 55-75. (DOI: 10.1002/andp.19484370105)

137. Kuhn H. (1970), Classical aspects of energy transfer in molecular systems, *Chem. Phys.*, *53*, 101-108. (DOI: 10.1063/1.1673749)

138. Molecular fluorescence and energy transfer near interfaces. *Adv. Chem. Phys.*, 1-65. (DOI: 10.1002/9780470142561.ch1)

139. Gersten J. I., Nitzan A. (1985), Photophysics and photochemistry near surfaces and small particles, *Surf. Sci.*, *158*, 165-189. (DOI: 10.1016/0039-6028(85)90293-6)

140. Persson B. N. J., Lang N. D. (1982), Electron-hole-pair quenching of excited states near a metal, *Phys. Rev. B*, *26*, 5409-5415. (DOI: 10.1103/PhysRevB.26.5409)

141. Breshike C. J., Riskowski R. A., Strouse G. F. (2013), Leaving Förster resonance energy transfer behind: Nanometal surface energy transfer predicts the size-enhanced energy coupling between a metal nanoparticle and an emitting dipole, *J. Phys. Chem. C*, *117*, 23942-23949. (DOI: 10.1021/jp407259r)

142. Murphy M. C., Rasnik I., Cheng W., Lohman T. M., Ha T. (2004), Probing single-stranded DNA conformational flexibility using fluorescence spectroscopy, *Biophys. J.*, *86*, 2530-2537. (DOI: 10.1016/S0006-3495(04)74308-8)

143. Ha T., Rasnik I., Cheng W., Babcock H. P., Gauss G. H., Lohman T. M., Chu S. (2002), Initiation and re-initiation of DNA unwinding by the Escherichia coli Rep helicase, *Nature*, *419*, 638-641. (DOI: 10.1038/nature01083)

144. Myong S., Bruno M. M., Pyle A. M., Ha T. (2007), Spring-loaded mechanism of DNA unwinding by hepatitis C virus NS3 helicase, *Science*, *317*, 513-516. (DOI: 10.1126/science.1144130)
145. Chen Y., Zhang L., Graf L., Yu B., Liu Y., Kochs G., Zhao Y., Gao S. (2017), Conformational dynamics of dynamin-like MxA revealed by single-molecule FRET, *Nat. Comm.*, *8*, 15744. (DOI: 10.1038/ncomms15744)
146. Hayashi G., Kamo N., Okamoto A. (2017), Chemical synthesis of dual labeled proteins via differently protected alkynes enables intramolecular FRET analysis, *Chem. Comm.*, *53*, 5918-5921. (DOI: 10.1039/C7CC02612A)
147. Huang C.-B., Xu L., Zhu J.-L., Wang Y.-X., Sun B., Li X., Yang H.-B. (2017), Real-time monitoring the dynamics of coordination-driven self-assembly by fluorescence-resonance energy transfer, *J. Am. Chem. Soc.*, *139*, 9459-9462. (DOI: 10.1021/jacs.7b04659)
148. Li N., Wang M., Gao X., Yu Z., Pan W., Wang H., Tang B. (2017), A DNA tetrahedron nanoprobe with controlled distance of dyes for multiple detection in living cells and in vivo, *Anal. Chem.*, *89*, 6670-6677. (DOI: 10.1021/acs.analchem.7b00889)
149. Bain D., Paramanik B., Patra A. (2017), Silver(I)-Induced Conformation Change of DNA: Gold nanocluster as a spectroscopic probe, *J. Phys. Chem. C*, *121*, 4608-4617. (DOI: 10.1021/acs.jpcc.6b10560)
150. Roy A., Kundu N., Banik D., Sarkar N. (2016), Comparative fluorescence resonance energy-transfer study in pluronic triblock copolymer micelle and niosome composed of biological component cholesterol: An investigation of effect of cholesterol and sucrose on the FRET parameters, *J. Phys. Chem. B*, *120*, 131-142. (DOI: 10.1021/acs.jpcc.5b09761)
151. Choudhury S., Mondal P. K., Sharma V. K., Mitra S., Sakai V. G., Mukhopadhyay R., Pal S. K. (2015), Direct observation of coupling between structural fluctuation and ultrafast hydration dynamics of fluorescent probes in anionic micelles, *J. Phys. Chem. B*, *119*, 10849-10857. (DOI: 10.1021/jp511899q)

152. Mandal R. P., De S. (2017), Organized assemblies of AOT determine nanoparticle characteristics and their performance as FRET donors, *Colloids Surf. A*, 528, 10-22. (DOI: 10.1016/j.colsurfa.2017.05.038)
153. Mondal S. K., Ghosh S., Sahu K., Mandal U., Bhattacharyya K. (2006), Ultrafast fluorescence resonance energy transfer in a reverse micelle: Excitation wavelength dependence, *J. Chem. Phys.*, 125, 224710. (DOI: 10.1063/1.2403131)
154. Rajdev P., Basak D., Ghosh S. (2015), Insights into noncovalently core cross-linked block copolymer micelles by fluorescence resonance energy transfer (FRET) studies, *Macromolecules*, 48, 3360-3367. (DOI: 10.1021/acs.macromol.5b00559)
155. Wu F., Minter S. D. (2013), Fluorescence characterization of co-immobilization-induced multi-enzyme aggregation in a polymer matrix using Förster resonance energy transfer (FRET): Toward the metabolon biomimic, *Biomacromolecules*, 14, 2739-2749. (DOI: 10.1021/bm400569k)
156. Trier S., Henriksen J. R., Andresen T. L. (2011), Membrane fusion of pH-sensitive liposomes – A quantitative study using giant unilamellar vesicles, *Soft Matter*, 7, 9027-9034. (DOI: 10.1039/C1SM05818E)
157. Ghatak C., Rao V. G., Pramanik R., Sarkar S., Sarkar N. (2011), The effect of membrane fluidity on FRET parameters: An energy transfer study inside small unilamellar vesicle, *Phys. Chem. Chem. Phys.*, 13, 3711-3720. (DOI: 10.1039/C0CP01925A)
158. Das N. K., Ghosh N., Kale A. P., Mondal R., Anand U., Ghosh S., Tiwari V. K., Kapur M., Mukherjee S. (2014), Temperature induced morphological transitions from native to unfolded aggregated states of human serum albumin, *J. Phys. Chem. B*, 118, 7267-7276. (DOI: 10.1021/jp5030944)
159. Das D. K., Mondal T., Mandal U., Bhattacharyya K. (2011), Probing deuterium isotope effect on structure and solvation dynamics of

- human serum albumin, *ChemPhysChem*, *12*, 814-822. (DOI: 10.1002/cphc.201000912)
160. Kim J., Pandya D. N., Lee W., Park J. W., Kim Y. J., Kwak W., Ha Y. S., Chang Y., An G. I., Yoo J. (2014), Vivid tumor imaging utilizing liposome-carried bimodal radiotracer, *ACS Med. Chem. Lett.*, *5*, 390-394. (DOI: 10.1021/ml400513g)
161. Nandi S., Mondal P., Chowdhury R., Saha A., Ghosh S., Bhattacharyya K. (2016), Amyloid beta peptides inside a reconstituted cell-like liposomal system: Aggregation, FRET, fluorescence oscillations and solvation dynamics, *Phys. Chem. Chem. Phys.*, *18*, 30444-30451. (DOI: 10.1039/C6CP06143E)
162. Thakur R., Das A., Chakraborty A. (2012), Photophysical and photodynamical study of ellipticine: An anticancer drug molecule in bile salt modulated in vitro created liposome, *Phys. Chem. Chem. Phys.*, *14*, 15369-15378. (DOI: 10.1039/C2CP41708A)
163. Bangham A. D., Horne R. W. (1964), Negative staining of phospholipids and their structural modification by surface-active agents as observed in the electron microscope, *J. Mol. Biol.*, *8*, 660-IN10. (DOI: 10.1016/S0022-2836(64)80115-7)
164. Van Hoogevest P., Wendel A. (2014), The use of natural and synthetic phospholipids as pharmaceutical excipients, *Eur. J. Lipid. Sci. Technol.*, *116*, 1088-1107. (DOI: 10.1002/ejlt.201400219)
165. Li J., Wang X., Zhang T., Wang C., Huang Z., Luo X., Deng Y. (2015), A review on phospholipids and their main applications in drug delivery systems, *Asian J. Pharm. Sci.*, *10*, 81-98. (DOI: 10.1016/j.ajps.2014.09.004)
166. Zhao L., Feng S.-S. (2005), Effects of lipid chain unsaturation and headgroup type on molecular interactions between paclitaxel and phospholipid within model biomembrane, *J. Colloid Interface Sci.*, *285*, 326-335. (DOI: 10.1016/j.jcis.2004.11.032)
167. Akbarzadeh A., Rezaei-Sadabady R., Davaran S., Joo S. W., Zarghami N., Hanifehpour Y., Samiei M., Kouhi M., Nejati-Koshki K. (2013), Liposome: Classification, preparation, and applications, *Nanoscale Res. Lett.*, *8*, 102-102. (DOI: 10.1186/1556-276X-8-102)

168. Bulbake U., Doppalapudi S., Kommineni N., Khan W. (2017), Liposomal formulations in clinical use: An updated review, *Pharmaceutics*, *9*, 12. (DOI: 10.3390/pharmaceutics9020012)
169. Yoon T.-Y., Okumus B., Zhang F., Shin Y.-K., Ha T. (2006), Multiple intermediates in SNARE-induced membrane fusion, *Proc. Natl. Acad. Sci.*, *103*, 19731-19736. (DOI: 10.1073/pnas.0606032103)
170. Madörin M., van Hoogevest P., Hilfiker R., Leuenberger H. (2000), The use of fluorescence resonance energy transfer to study the disintegration kinetics of liposomes containing lysolecithin and oleic acid in rat plasma, *Pharm. Res.*, *17*, 1118-1123. (DOI: 10.1023/A:1026413914687)
171. Yefimova S. L., Kurilchenko I. Y., Tkacheva T. N., Kavok N. S., Todor I. N., Lukianova N. Y., Chekhun V. F., Malyukin Y. V. (2014), Microspectroscopic study of liposome-to-cell interaction revealed by Förster resonance energy transfer, *J. Fluoresc.*, *24*, 403-409. (DOI: 10.1007/s10895-013-1305-8)
172. Zhang Y., Garzon-Rodriguez W., Manning M. C., Anchordoquy T. J. (2003), The use of fluorescence resonance energy transfer to monitor dynamic changes of lipid–DNA interactions during lipoplex formation, *Biochim. Biophys. Acta.*, *1614*, 182-192. (DOI: 10.1016/S0005-2736(03)00177-9)
173. You M., Li E., Wimley W. C., Hristova K. (2005), Förster resonance energy transfer in liposomes: Measurements of transmembrane helix dimerization in the native bilayer environment, *Anal. Biochem.*, *340*, 154-164. (DOI: 10.1016/j.ab.2005.01.035)
174. Clapp A., Medintz I., Mauro J., Fisher B., Bawendi M., Mattoussi H. (2004), Fluorescence resonance energy transfer between quantum dot donors and dye-labeled protein acceptors, *J. Am. Chem. Soc.*, *126*, 301-10. (DOI: 10.1021/ja037088b)
175. Dulkeith E., Ringler M., Klar T. A., Feldmann J., Muñoz Javier A., Parak W. J. (2005), Gold nanoparticles quench fluorescence by phase induced radiative rate suppression, *Nano Lett.*, *5*, 585-589. (DOI: 10.1021/nl0480969)

176. Yun C. S., Javier A., Jennings T., Fisher M., Hira S., Peterson S., Hopkins B., Reich N. O., Strouse G. F. (2005), Nanometal surface energy transfer in optical rulers, breaking the FRET barrier, *J. Am. Chem. Soc.*, *127*, 3115-3119. (DOI: 10.1021/ja043940i)
177. Jennings T. L., Singh M. P., Strouse G. F. (2006), Fluorescent lifetime quenching near $d = 1.5$ nm gold nanoparticles: Probing NSET validity, *J. Am. Chem. Soc.*, *128*, 5462-5467. (DOI: 10.1021/ja0583665)
178. Singh M. P., Strouse G. F. (2010), Involvement of the LSPR spectral overlap for energy transfer between a dye and Au nanoparticle, *J. Am. Chem. Soc.*, *132*, 9383-9391. (DOI: 10.1021/ja1022128)
179. Dulkeith E., Morteaux A. C., Niedereichholz T., Klar T. A., Feldmann J., Levi S. A., van Veggel F. C. J. M., Reinhoudt D. N., Möller M., Gittins D. I. (2002), Fluorescence quenching of dye molecules near gold nanoparticles: Radiative and nonradiative effects, *Phys. Rev. Lett.*, *89*, 203002. (DOI: 10.1103/PhysRevLett.89.203002)
180. Samanta A., Zhou Y., Zou S., Yan H., Liu Y. (2014), Fluorescence quenching of quantum dots by gold nanoparticles: A Potential long range spectroscopic ruler, *Nano Lett.*, *14*, 5052-5057. (DOI: 10.1021/nl501709s)
181. Rakshit S., Moulik S. P., Bhattacharya S. C. (2017), Understanding the effect of size and shape of gold nanomaterials on nanometal surface energy transfer, *J. Colloid Interface Sci.*, *491*, 349-357. (DOI: 10.1016/j.jcis.2016.12.052)
182. Mandal S., Ghatak C., Rao V. G., Ghosh S., Sarkar N. (2012), Pluronic micellar aggregates loaded with gold nanoparticles (Au NPs) and fluorescent dyes: A study of controlled nanometal surface energy transfer, *J. Phys. Chem. C*, *116*, 5585-5597. (DOI: 10.1021/jp2093127)
183. Chen C., Midelet C., Bhuckory S., Hildebrandt N., Werts M. H. V. (2018), Nanosurface energy transfer from long-lifetime terbium donors to gold nanoparticles, *J. Phys. Chem. C*, *122*, 17566-17574. (DOI: 10.1021/acs.jpcc.8b06539)
184. Yang T., Hou P., Zheng L. L., Zhan L., Gao P. F., Li Y. F., Huang C. Z. (2017), Surface-engineered quantum dots/electrospun

- nanofibers as a networked fluorescence aptasensing platform toward biomarkers, *Nanoscale*, *9*, 17020-17028. (DOI: 10.1039/C7NR04817C)
185. Maiti C., Banerjee R., Maiti S., Dhara D. (2015), pH-induced vesicle-to-micelle transition in amphiphilic diblock copolymer: investigation by energy transfer between in situ formed polymer embedded gold nanoparticles and fluorescent dye, *Langmuir*, *31*, 32-41. (DOI: 10.1021/la504165e)
186. Zhou N., Yuan M., Gao Y., Li D., Yang D. (2016), Silver nanoshell plasmonically controlled emission of semiconductor quantum dots in the strong coupling regime, *ACS Nano*, *10*, 4154-4163. (DOI: 10.1021/acsnano.5b07400)
187. Pons T., Medintz I. L., Sapsford K. E., Higashiya S., Grimes A. F., English D. S., Mattoussi H. (2007), On the quenching of semiconductor quantum dot photoluminescence by proximal gold nanoparticles, *Nano Lett.*, *7*, 3157-3164. (DOI: 10.1021/nl071729+)
188. Lunz M., Gerard V. A., Gun'ko Y. K., Lesnyak V., Gaponik N., Susha A. S., Rogach A. L., Bradley A. L. (2011), Surface plasmon enhanced energy transfer between donor and acceptor CdTe nanocrystal quantum dot monolayers, *Nano Lett.*, *11*, 3341-3345. (DOI: 10.1021/nl201714y)
189. Zhang X., Marocico C. A., Lunz M., Gerard V. A., Gun'ko Y. K., Lesnyak V., Gaponik N., Susha A. S., Rogach A. L., Bradley A. L. (2012), Wavelength, concentration, and distance dependence of nonradiative energy transfer to a plane of gold nanoparticles, *ACS Nano*, *6*, 9283-9290. (DOI: 10.1021/nn303756a)
190. Bene L., Szentesi G., Mátyus L., Gáspár R., Damjanovich S. (2005), Nanoparticle energy transfer on the cell surface, *J. Mol. Recognit.* *18*, 236-53. (DOI: 10.1002/jmr.730)
191. Rao V. G., Mandal S., Ghosh S., Banerjee C., Sarkar N. (2012), Study of fluorescence resonance energy transfer in zwitterionic micelle: Ionic-liquid-induced changes in FRET parameters, *J. Phys. Chem. B*, *116*, 12021-12029. (DOI: 10.1021/jp307883r)
192. Chen Y., O'Donoghue M. B., Huang Y.-F., Kang H., Phillips J. A., Chen X., Estevez M. C., Yang C. J., Tan W. (2010), A Surface

energy transfer nanoruler for measuring binding site distances on live cell surfaces, *J. Am. Chem. Soc.*, *132*, 16559-16570. (DOI: 10.1021/ja106360v)

Chapter 2

*Materials, Sample Preparation
and Experimental Techniques*

2.1. Introduction

This chapter mentions all the detail of synthesis and chemicals used for the synthesis of MSA-capped CdTe QDs, citrate-capped Au NPs, PEG-capped Au NP, citrate-capped Ag NP, dipalmitoylphosphatidylcholine (DPPC), and dihydrolipoic acid (DHLA)-capped Ag NC. All the sample preparation methods opted during the work of this thesis have been mentioned here. This chapter also covers the detailed experimental techniques used to complete the entire thesis work.

2.2. Chemicals

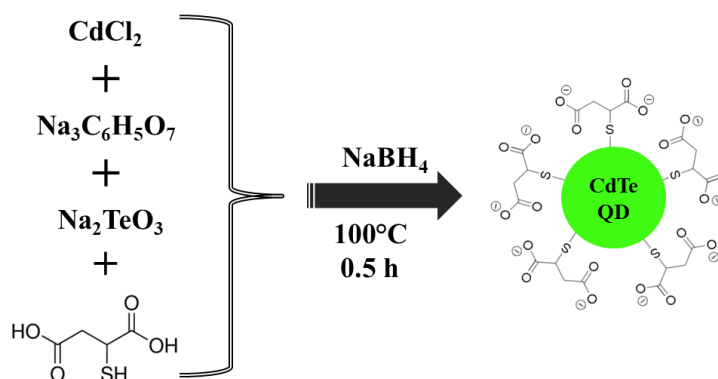
Cadmium chloride (CdCl_2), mercaptosuccinic acid (MSA), sodium tellurite (Na_2TeO_3), Tri-sodium citrate dihydrate (TSC), silver nitrate (Ag NO_3 , $\geq 99\%$), chloroauric acid hydrate ($\text{AuCl}_3 \cdot \text{HCl} \cdot 3\text{H}_2\text{O}$), poly (ethylene glycol) methyl ether thiol (PEG-SH), dipalmitoylphosphatidylcholine (DPPC), cetyltrimethylammonium bromide (CTAB, $\geq 98\%$), triton X-100 (TX-100, AR grade), sodium dodecyl sulfate (SDS, 98.5%), (\pm)- α -lipoic acid, 4',6-diamidino-2-phenylindole dihydrochloride (DAPI, $\geq 95\%$, HPLC), methanol, poly(diallyldimethylammoniumchloride) (PDADMAC, MW= 100000-200000), sodium hydroxide (NaOH), hydrochloric acid (HCl), methanol (HPLC), Rhodamine 6G dye, Nile blue, fluorescein isothiocyanate (FITC), human serum albumin (HSA), bovine serum albumin (BSA), hellmanex III and Pur-A-Lyzert Dialysis Kit (MWCO 3.5 kDa), were purchased from Sigma-Aldrich. Sodium borohydride (NaBH_4 , 96%) was purchased from SRL. Ethanol was purchased from Merck (Germany). Poly (vinylpyrrolidone) (PVP, MW=40,000) was purchased from TCI. Milli-Q water was obtained from a Millipore water purifier system (Milli-Q integral).

2.3. Synthesis

2.3.1. MSA-Capped CdTe QDs

CdTe QDs were prepared according to the reported method [1]. In a typical synthesis, cadmium chloride (CdCl_2 , 0.04 M, 4 mL) was diluted

to 50 mL in a one-necked flask, and trisodium citrate dihydrate (100 mg), Na_2TeO_3 (0.01 M, 1 mL), mercaptosuccinic acid (50 mg), and sodium borohydride (NaBH_4 , 100 mg) were added, with stirring at room temperature (Scheme 2.1).



Scheme 2.1. Synthesis of MSA-capped CdTe QDs.

When the color of the solution changes to green, the flask was attached to a condenser and refluxed under open-air conditions for 0.5, 3, and 5.0 h to obtain green, yellow, and red QDs, respectively. The resulting CdTe QDs were purified by dialysis for 24 h. The final product was kept at 4 °C in the dark for further use. The size and concentration of CdTe QDs were calculated by the equation proposed by Peng [2-3].

2.3.2. Citrate-Capped Au NPs

Au NPs were synthesized according to earlier literature with minor modifications [4-5]. First, 0.3 mM $\text{HAuCl}_4 \cdot 3\text{H}_2\text{O}$ was dissolved in 50 mL of ultrapure water. The solution was transferred into the flask and was heated for 0.5 h with stirring. Then, 0.9 mL of 38.80 mM citrate sodium solution was quickly added into the boiling solution and allowed to react for 1 h. The resulting wine red colloidal Au NPs were finally obtained. Then, the solution was removed from the heating element and stirred until cooled to room temperature. Next, unbound citrate was removed by repeated centrifugation (9000 rpm, 15 min), followed by redispersing the red precipitate in ultrapure water (40 mL) to get the pure Au NPs. The final concentration of Au NPs was estimated using the

reported molar extinction coefficient at the LSPR maximum ($\epsilon = 8.78 \times 10^8 \text{ M}^{-1}\text{cm}^{-1}$) [6].

2.3.3. Citrate-Capped Ag NP

Ag NPs were prepared according to the literature procedure [7-8]. Briefly, 25 mL of 1 mM AgNO_3 in water was taken into a round-bottom flask, and then 1 mL of 47 mM citrate solution and 1 mL of 52 mM citric acid were added with vigorous stirring. After 15 min of stirring, 200 μL of aqueous NaBH_4 was added dropwise to the solution with vigorous stirring to reduce all the Ag (I) to Ag (0). The final concentration of the as-synthesized Ag NPs was estimated using the molar extinction coefficient at the maximum LSPR wavelength ($\epsilon_{392} = 5.6 \times 10^8 \text{ M}^{-1} \text{ cm}^{-1}$) [9].

2.3.4. PEG-Capped Au NP

The preparation of PEG-capped Au NP was based on previous work with appropriate modifications [10-11]. The PEG-SH molecules with an average molecular weight of 6000 Da were employed to exchange citrate ions on the surface of Au NPs. The required amount of PEG-SH solution (2.0 mM, 4 mL) was added into 40 mL of synthesized citrate-capped Au NP solution and stirred overnight (12 h) with gentle mixing (100 rpm). After PEGylation, the solution was subjected to purification using centrifugation (6000 rpm, 10 min), followed by redispersing the red precipitate in ultrapure water (40 mL) to get the pure PEG-capped Au NPs.

2.3.5. DHLA-Capped Ag NCs

Ag NCs were synthesized according to the earlier literature with minor modifications [12-13]. 26.30 mg of lipoic acid and 10 mL of Milli-Q water were placed in a round bottom flask. To this insoluble mixture, ~1.5 mg of pure sodium borohydride was added and stirred well until a clear solution was obtained. In this step, the insoluble mixture of lipoic acid is reduced to water-soluble DHLA. Next, to prepare fluorescent Ag NCs, 500 μL of 25 mM aqueous AgNO_3 solution is added to the freshly

prepared above aqueous DHLA solution and this mixture was stirred well for 1 min. To this, a slight excess of dilute aqueous sodium borohydride solution was added slowly, and the stirring was continued for 3 h. The color of the solution changes from colorless to deep orange marking the completion of the reaction. The concentration of as-synthesized Ag NCs was estimated ~0.2 mM based on the assumption that all the silver in silver nitrate was reduced to form Ag NCs.

2.4. Sample Preparations

2.4.1. UV-vis and PL Experiment

The synthesized MSA-capped CdTe QDs, citrate-capped Au NPs, PEG-capped Au NP, citrate-capped Ag NP, and DHLA-capped Ag NC were further diluted as per the experimental requirements. The aqueous stock solution of DAPI, Nile blue, HSA, BSA, FITC, Rh6G, SDS, TX-100, PVP, PDADMAC, and CTAB were prepared by dissolving the desired amount in Milli-Q water.

2.4.2. Microscopy Experiment

For the microscopy experiment, the samples were spin-coated on a clean cover slide with a spin coater (Apex Instruments, Spin NXG-P1). Cleaning of the cover slides was done by using chromic acid, followed by 2% Hellmanex III (Sigma-Aldrich). Each of the cleaning steps was followed by repeated washing with Milli-Q water. Finally, the washed slides were rinsed with methanol and dried in a vacuum oven.

2.4.3. Fluorescence Quantum Yields (ϕ)

The fluorescence quantum yields (ϕ) of CdTe QDs, and DAPI were estimated by using the following equation:

$$\phi_{\text{QD}} = \phi_{\text{ST}} \left(\frac{I_{\text{QD}}}{I_{\text{ST}}} \right) \left(\frac{\eta_{\text{QD}}^2}{\eta_{\text{ST}}^2} \right) \left(\frac{A_{\text{ST}}}{A_{\text{QD}}} \right) \quad (1)$$

Here ϕ is the QY, I is the integrated fluorescence intensity, η is the refractive index of the solvent, and A is the optical density. The subscript “ST” stands for standard and “QD” stands for the CdTe QDs and DAPI sample. The estimated luminescence QY of DAPI, green, yellow and red QD is 0.021, 0.20, 0.59, and 0.65, respectively [14].

2.4.4. Preparation of Coacervate Droplets

Different binary mixtures of QDs and PDADMAC were prepared in Milli-Q water by keeping the concentration of QDs fixed at 0.33 μM , while the molar concentration of PDADMAC monomer was varied from 1.3-5000 μM . All the binary mixtures were equilibrated for 12 h before any measurements. Similarly, binary mixtures of QDs and PVP were prepared using different molar concentrations of PVP into 0.33 μM aqueous solutions of QDs. The pH of the binary aqueous mixtures was adjusted by adding an appropriate amount of diluted stock solution of HCl (1M) and NaOH (1M). The ionic strength was varied by adding an appropriate amount of diluted stock solution of NaCl (1M) into the binary mixture.

2.4.5. Preparation of Hybrid Vesicles

CTAB and SDS solutions were prepared by dissolving the required amount of surfactants in Milli-Q water. Triton X-100 solution was prepared by diluting the stock solution in Milli-Q water. The final concentration of CdTe QDs was kept fixed at 0.33 μM throughout the study. All QD-CTAB binary mixtures were kept undisturbed for 24 h to attain equilibrium before any measurements. The solution pH was adjusted by adding an appropriate amount of diluted stock solution of HCl and NaOH into the binary mixture. For PL and confocal imaging, samples were drop-casted on a clean coverslip.

2.4.6. Dye and Protein Encapsulation

The turbid binary mixture of 0.33 μM QDs and 130.0 μM PDADMAC was centrifuged at 10000 rpm for 30 min to collect the coacervate phase,

which was later redispersed in Milli-Q water. Separate stock solutions of dyes and proteins were also prepared in Milli-Q water. The required volume from these stock solutions was added to the coacervate solution to make the final working concentrations of 2.0 (FITC), 20.0 (Rh6G), 1.0 (Nile blue), 59.0 (HSA), and 47.0 μM (BSA). These mixtures were equilibrated for 12 h. Subsequently, these mixtures were centrifuged at 10000 rpm for 30 min to separate the supernatant from the coacervate phase. The concentrations of dyes and proteins in the supernatant were determined using UV-vis spectroscopy. The partition coefficient (K) was calculated by the ratio of the concentrations of dyes/proteins loaded in coacervates to the concentrations of dyes/proteins present in the supernatant.

To encapsulation Rh6G in hybrid vesicles, a required amount of Rh6G was dissolved in water to make a stock solution than a required amount of aliquot (working concentration ~ 0.11 nM) was added to the preformed self-assembled vesicles and incubated overnight. Subsequently, the mixture was dialyzed for 24 h against Milli-Q water to remove the excess free dye.

2.5. Instrumentation

2.5.1. UV-vis Spectroscopy

UV-vis absorption spectra were recorded in a quartz cuvette (1 cm \times 1 cm) using a Varian UV-vis spectrophotometer (Cary 100 Bio).

2.5.2. PL Spectroscopy

The PL spectra were recorded in a quartz cuvette (1 cm \times 1 cm) using Fluoromax-4 Spectrofluorometer (HORIBA Jobin Yvon, model FM-100) with excitation and emission slit widths at 5 nm.

2.5.3. Time-Correlated Single Photon Counting Technique (TCSPC)

To estimate the PL lifetime, TCSPC technique was used. Photoluminescence (PL) decays were recorded on a HORIBA Jobin Yvon picosecond time correlated single photon counting (TCSPC) spectrometer (model Fluorocube-01-NL). The PL decays were collected with the emission polarizer at a magic angle of 54.7° by a photomultiplier tube (TBX-07C). The instrument response function (IRF, fwhm ~ 140 ps) was recorded using a dilute scattering solution. The PL decays were analyzed using IBH DAS 6.0 software by the iterative reconvolution method, and the goodness of the fit was judged by reduced χ -square (χ^2) value [15-16]. All the decays were fitted as a sum of n-exponential function:

$$F(t) = \sum_{i=1}^n a_i \exp(-t/\tau_i) \quad (2)$$

Where $F(t)$ denotes normalized PL decay, τ_i and a_i are the i^{th} lifetime and the corresponding pre-exponential factor, respectively. The average lifetime was obtained from the equation

$$\tau_{avg} = \sum_{i=1}^n a_i \tau_i \quad (3)$$

2.5.4. Fourier Transform Infrared (FTIR) Spectroscopy

FTIR technique was used to confirm the formation of CdTe QDs, PEG-Au NPs, and Ag NCs. FTIR measurements were carried out in a Bruker spectrometer (Tensor-27) on a thin KBr pellet in the range of 800 to 4000 cm^{-1} wavenumber.

2.5.5. Transmission Electron Microscopy (TEM)

TEM measurement was performed using a 200 kV UHR FEG-TEM, JEOL JEM 2100F field emission transmission electron microscope. The sample was drop-casted on the carbon-coated copper grid for TEM measurement.

2.5.6. Field-Emission Scanning Electron Microscopy (FESEM)

The FESEM images were recorded using a field-emission scanning electron microscope (FESEM), Supra 55 Zeiss. For SEM measurements, samples were drop-casted on a cleaned glass slide and dried overnight in a desiccator. These dried samples were coated with gold.

2.5.7. DLS and Zeta Potential Measurements

DLS and zeta potential experiments were performed on a Particle analyzer (model-Litesizer and Anton Paar instrument) at 25 °C. All samples for DLS measurements were prepared in Milli-Q water, which was filtered through a 0.22 µm syringe filter (Whatman) before sample preparation.

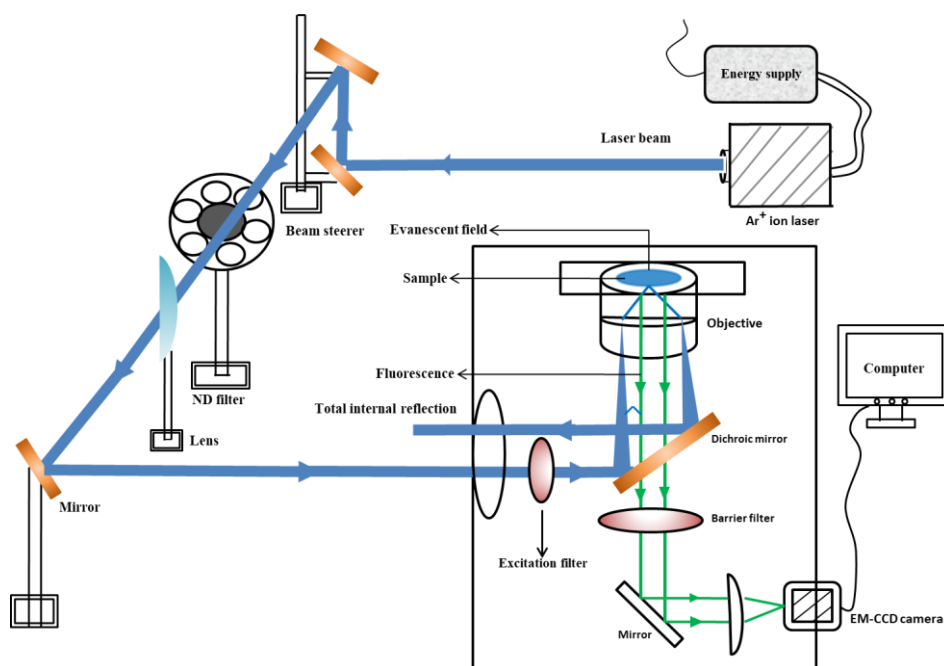
2.5.8. Confocal Laser Scanning Microscopy (CLSM)

The images were recorded with an inverted confocal microscope (Olympus, model no. FV1200MPE, IX-83) using an oil immersion objective (100×1.4 NA). Diode laser source at 488 and 559 nm was used to excite the samples using appropriate dichroic and emission filters (green channel: 490-550 nm; red channel: 570-670 nm) in the optical path. Two-photon imaging experiments were performed using confocal microscope attached to a Mai Tai eHP Spectra physics femtosecond laser as an excitation source (pulse width ≤ 70 fs, tuning range 790–1040 nm, average power >2.5 W, and repetition rate $80 \text{ MHz} \pm 1 \text{ MHz}$).

2.5.9. Epifluorescence Imaging

Epifluorescence imaging was performed on home-built microscopy setup (Scheme 2.2) [16]. Epifluorescence imaging of individual CdTe QD and droplets (T1 and T2) was carried out using a custom made microscopic setup based on an inverted fluorescence microscope (Nikon, Eclipse Ti-U), coupled with a back-illuminated electron-multiplying charge-coupled device (EM-CCD) camera (Andor, iXon X3 897). An air-cooled argon ion laser (Melles Griot, model 400-A03) with excitation wavelength at 488 nm was used as an excitation source. The

PL from the samples was collected through a B2A filter cube (Nikon) having a 505 nm dichroic mirror and a 520 nm long-pass filter. The images were captured with a frame rate of 200 ms and analyzed with ImageJ (Version 1.47v) NIH.



Scheme 2.2. Schematic representation of our home-built epifluorescence microscopy.

2.5.10. Atomic Force Microscopy (AFM)

The morphology of synthesized CdTe QDs as well as several nanostructures was determined by AFM technique. AFM images were recorded on a cleaned glass coverslip using a scanning probe microscope AIST-NT microscope (model SmartSPM-1000). The samples were deposited on the coverslip by spin-coating at 750 rpm for 3 minutes.

2.5.11. Liquid Chromatography-Mass Spectrometer (LC-MS)

In order to confirm the exact molecular mass and composition of the as-synthesized Ag NC core, mass spectrometric analysis was performed.

Mass spectrum was recorded using electrospray ionization (ESI) quadrupole time-of-flight liquid chromatography-mass spectrometer (Bruker Daltonik) in 1:1 water-methanol mixture as a solvent by positivemode.

2.5.12. Powder X-ray Diffractometer (PXRD)

The powder X-ray diffraction pattern of CdTe QDs was recorded on the dried sample using a Bruker D8 Advance X-ray diffractometer. The X-rays were produced using a sealed tube, and the wavelength of the X-ray was 0.154 nm (Cu K α , 60 kV and 50 mA).

2.5.13. X-ray Photoelectron Spectroscopy (XPS)

X-ray photoelectron spectroscopy (XPS) measurements of CdTe QDs were performed using an Al K α surface analysis AXIS Supra X-ray photoelectron spectrometer (Kratos Analytical, 189 U.K.). The chamber pressure during the XPS measurements was $<2 \times 10^{-7}$ Pa.

2.6. References

1. Zhang, L., Zou, X., Ying, E., Dong, S. (2008), Quantum dot electrochemiluminescence in aqueous solution at lower potential and its sensing application. *J. Phys. Chem. C*, *112*, 4451-4454. (DOI: 10.1021/jp7097944)
2. Yu, W. W., Qu, L., Guo, W., Peng, X. (2003), Experimental determination of the extinction coefficient of CdTe, CdSe, and CdS nanocrystals. *Chem. Mater.*, *15*, 2854-2860. (DOI: 10.1021/cm034081k)
3. Ali M., Zayed D., Ramadan W., Kamel O. A., Shehab M., Ebrahim S. (2019), Synthesis, characterization and cytotoxicity of polyethylene glycol-encapsulated CdTe quantum dots, *Int. Nano. Lett.*, *9*, 61-71. (DOI: 10.1007/s40089-018-0262-2)
4. Haiss, W., Thanh, N. T. K., Aveyard, J., Fernig, D. G. (2007), Determination of size and concentration of gold nanoparticles from UV-vis spectra. *Anal. Chem.*, *79*, 4215-4221. (DOI: 10.1021/ac0702084)
5. Bastús N. G., Comenge J., Puntes V. (2011), Kinetically controlled seeded growth synthesis of citrate-stabilized gold nanoparticles of up to 200 nm: Size focusing versus ostwald ripening, *Langmuir*, *27*, 11098-11105. (DOI: 10.1021/la201938u)
6. Liu, X., Atwater, M., Wang, J., Huo, Q. (2007), Extinction coefficient of gold nanoparticles with different sizes and different capping ligands. *Colloids Surf. B*, *58*, 3-7. (DOI: 10.1016/j.colsurfb.2006.08.005)
7. Lee, P. C., Meisel, D. (1982), Adsorption and surface-enhanced Raman of dyes on silver and gold sols. *J. Phys. Chem*, *86*, 3391-3395. (DOI: 10.1021/j100214a025)

8. Bastús N. G., Merkoçi F., Piella J., Puentes V. (2014), Synthesis of highly monodisperse citrate-stabilized silver nanoparticles of up to 200 nm: Kinetic control and catalytic properties, *Chem. Mater.*, *26*, 2836-2846. (DOI: 10.1021/cm500316k)

9. Paramelle, D., Sadovoy, A., Gorelik, S., Free, P., Hobbey, J., Fernig, D. G. (2014), A rapid method to estimate the concentration of citrate capped silver nanoparticles from UV-visible light spectra. *Analyst*, *139*, 4855-4861. (DOI: 10.1039/C4AN00978A)

10. Liu, J.-L., Yang, Y.-T., Lin, C.-T., Yu, Y.-J., Chen, J.-K., Chu, L.-K. (2017), Monitoring the transient thermal infrared emission of gold nanoparticles upon photoexcitation with a step-scan fourier-transform spectrometer. *J. Phys. Chem. C*, *121*, 878-885. (DOI: 10.1021/acs.jpcc.6b10044)

11. Manson J., Kumar D., Meenan B. J., Dixon D. (2011), Polyethylene glycol functionalized gold nanoparticles: the influence of capping density on stability in various media, *Gold Bull.*, *44*, 99-105. (DOI: 10.1007/s13404-011-0015-8)

12. Adhikari, B., Banerjee, A. (2010), Facile synthesis of water-soluble fluorescent silver nanoclusters and HgII sensing. *Chem. Mater.*, *22*, 4364-4371. (DOI: 10.1021/cm1001253)

13. Prajapati, R., Chatterjee, S., Kannaujiya, K. K., Mukherjee, T. K. (2016), Effect of compartmentalization of donor and acceptor on the ultrafast resonance energy transfer from DAPI to silver nanoclusters. *Nanoscale*, *8*, 13006-13016. (DOI: 10.1039/C6NR01792D)

14. Dong, B., Zheng, K., Tang, Y., Lin, W. (2016), Development of green to near-infrared turn-on fluorescent probes for the multicolour imaging of nitroxyl in living systems. *J. Mater. Chem. B*, *4*, 1263-1269. (DOI: 10.1039/C5TB02073E)

15. Vaishnav, J. K., Mukherjee, T. K. (2017), Tuning of resonance energy transfer from 4',6-diamidino-2-phenylindole to an ultrasmall silver nanocluster across the lipid bilayer. *Phys. Chem. Chem. Phys.*, *19*, 27305-27312. (DOI: 10.1039/C7CP05225A)

16. Chatterjee S., Mukherjee T. K. (2013), Size-dependent differential interaction of allylamine-capped silicon quantum dots with surfactant assemblies studied using photoluminescence spectroscopy and imaging technique, *J. Phys. Chem. C*, *117*, 10799-10808. (DOI: 10.1021/jp402408d)

Chapter 3

*Highly Photostable and Two-Photon Active
Quantum Dot-Polymer Multicolor Hybrid
Coacervate Droplets*

3.1. Introduction

In recent years, multifunctional self-assembled nanocomposites such as hybrid vesicles, polymersomes, hydrogels, nanocapsules, and colloidal coacervate droplets have gained vast attention due to their potential in basic research as well as in technology related fields [1-5]. Precise control of their self-assembly and physicochemical properties by varying various non-covalent interactions is critical in a wide range of research fields such as catalysis, sensing, drug-delivery, nano-reactor, biosensing, and biomedical research [6,7]. The design and fabrication of most of the nanocomposites are complex and time-consuming, spontaneous self-assembly of oppositely charged polyelectrolytes aqueous mixture into spherical coacervate droplets is relatively simple [5]. Coacervates find particular attention in artificial protocell research as a consequence of their inherent membrane-free structure and selective sequestration of a wide range of organic molecules as well as proteins and enzymes [8-11].

Till date, various groups have made significant contributions toward understanding the self-assembly between a diverse range of charged molecules such as synthetic and natural polymers, fatty acids, biological macromolecules, poly or oligopeptides as well as low molecular weight components such as surfactants and mononucleotides [12-16]. Although, these earlier studies provide great details about the mechanism, structure, stability, and sequestration properties of a wide range of coacervate droplets prepared mainly from organic molecules, there are no reports on the fabrication of organic-inorganic hybrid droplets. While these hybrid droplets are expected to retain the properties of both the organic and inorganic counterparts, at the same time the structural stability and applicability is expected to enhance significantly. With the aim towards fabricating new multifunctional organic-inorganic nanocomposites, we have undertaken the present study. To the best of our knowledge, this is the first report to demonstrate the fabrication of inherently luminescent hybrid coacervate droplets by simple mixing of inorganic quantum dots (QDs) with organic polymer.

The main objective of the present study is to understand the spontaneous self-assembly of mercaptosuccinic acid (MSA)-capped CdTe QDs and positively charged PDADMAC aqueous solution into well-defined multicolor luminescent droplets in a broad range of composition, pH, and ionic strength. It has been observed that the self-assembly of initial nanocomposites between negatively charged MSA-capped CdTe QDs and positively charged PDADMAC leads to the formation of stable supramolecular hybrid coacervate droplets. Their inherent photoluminescence (PL) properties have been explored by using epifluorescence and confocal laser scanning microscopy (CLSM). More importantly, these droplets are found to exhibit two-photon PL, which can be useful for in vivo cell and tissue imaging applications.

3.2. Results and Discussion

3.2.1. Characterization of CdTe QDs

The structure and morphology of synthesized CdTe QDs are characterized by UV-vis, PL, AFM, TEM, DLS, PXRD, XPS, and FTIR spectroscopy. The AFM images of green, yellow and red CdTe QDs shows well dispersed spherical dots with mean sizes of 2.1 ± 0.7 (Figure 3.1a), 3.1 ± 0.4 (Figure 3.1b), and 3.9 ± 0.3 , respectively (Figure 3.1c). Figure 3.1d shows the morphology and mean size of these green QDs is estimated from TEM measurements. The TEM image reveals well-dispersed spherical QDs with mean size of 2.3 ± 0.5 nm (Figure 3.1d inset). Notably, the calculated mean size from Peng equation using excitonic peak position is found to be 2.1 nm [21]. Figure 3.1e shows the normalized absorption and emission spectra of green, yellow and red CdTe QD in water. The emission peaks are observed at 522, 586, and 646 nm for green, yellow, and red CdTe QDs, respectively upon excitation at the absorption peak position [22]. The inset reveals the solution phase photographs of these QDs upon UV illumination ($\lambda_{ex} = 365$ nm).

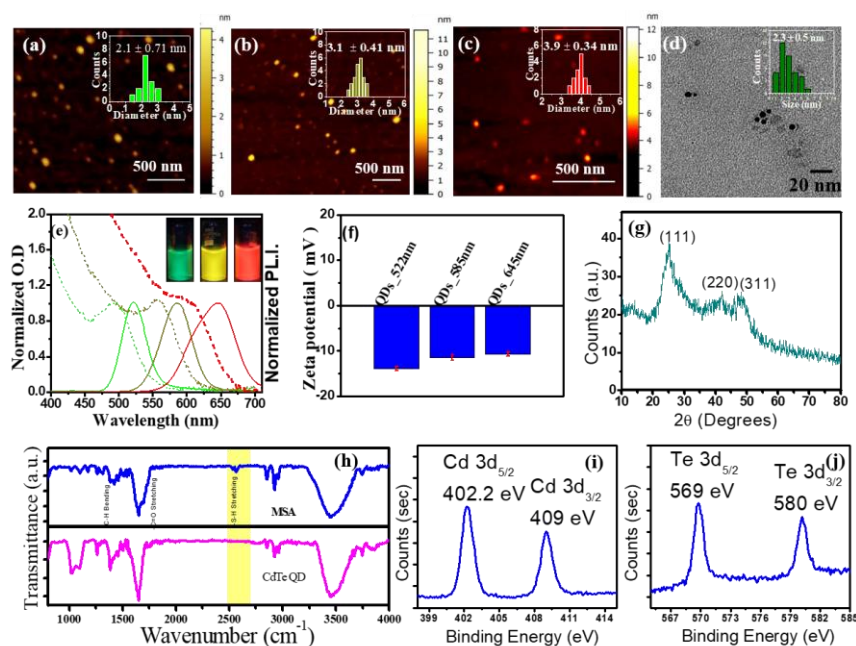


Figure 3.1. AFM images of (a) green, (b) yellow, and (c) red CdTe QDs. The insets show the height profile histograms with mean height. (d) TEM image of green CdTe QDs. The insets show the size distribution histograms with mean sizes. (e) Normalized absorption and PL spectra of green, yellow, and red QDs. (f) The estimated zeta potential of green, yellow, and red QDs. (g) XRD pattern of CdTe QDs. (g) X-ray diffraction (XRD) pattern of CdTe QDs. (h) FTIR spectra of MSA (upper panel) and synthesized MSA-capped CdTe QD (lower panel). XPS spectra of (i) Cd 3d and (j) Te 3d.

It is evident that the smallest (2.15 ± 0.71 nm), medium (3.13 ± 0.41 nm), and largest (3.92 ± 0.34 nm) sized QD shows PL in the green, yellow and red region of the electromagnetic spectrum, respectively. The estimated zeta potential is -13.9 ± 0.5 , -11.5 ± 0.6 , and -10.7 ± 0.5 mV for green, yellow, and red QDs, respectively (Figure 3.1f). The XRD pattern shows three peaks at 2θ values of 24.9 , 42.0 and 47.0° , corresponding to the (111), (220) and (311) crystalline planes, respectively. These data match the bulk cubic zinc blende CdTe structure (JCPDS no. 75-2086) (Figure 3.1g) [23]. The attachment of MSA ligand on the surface of CdTe QDs is confirmed from FTIR spectroscopy (Figure 3.1h). The stretching frequency of the S-H bond of free MSA at 2547 cm^{-1} disappears upon

attachment with QD surface, indicating the attachment of MSA to the QD surface through its free thiol end. Other peaks at 1638 and 1386 cm^{-1} can be assigned to the stretching of carboxylate groups and $-\text{C}-\text{H}$ bending, respectively (Figure. 3.1h). Figure 3.1i and j shows the XPS spectra of Cd 3d and Te 3d, respectively. The spectrum of Cd 3d reveals the presence of $3d_{5/2}$ and $3d_{3/2}$ peak at 402.2 and 409.1 eV, respectively. Similarly, the spectrum of Te 3d reveals the presence of $3d_{5/2}$ and $3d_{3/2}$ peak at 569.8 and 580.2 eV, respectively. These results indicate the successful synthesis of MSA-capped CdTe QDs.

3.2.2. Initial Nanocomposite Formation between QD and PDADMAC

Diluted aqueous solutions of QDs and PDADMAC were mixed in appropriate proportions to prepare different binary mixtures. The concentration of QD was kept fixed at 0.33 μM , while that of PDADMAC monomer was varied in the range of 1.3-5000 μM . All the

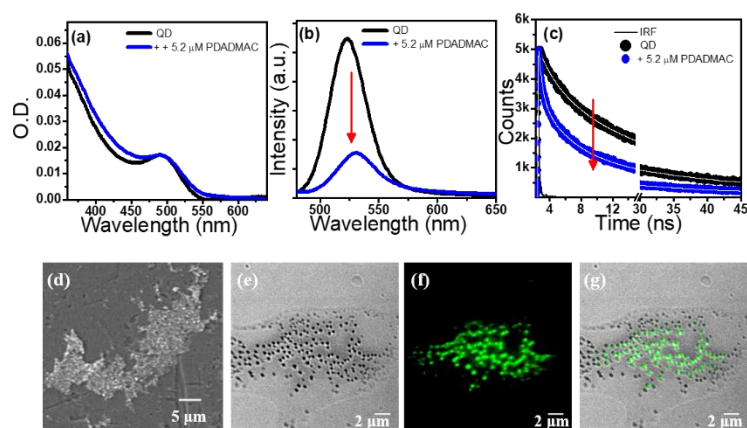


Figure 3.2. Changes in the (a) absorption spectra, (b) PL spectra ($\lambda_{\text{ex}} = 445 \text{ nm}$), and (c) PL decay traces ($\lambda_{\text{ex}} = 445 \text{ nm}$; $\lambda_{\text{em}} = 523 \text{ nm}$) of green QDs in the presence of 5.2 μM PDADMAC. (d) SEM image of QD-PDADMAC binary mixture in the C1 region. Confocal images (e) DIC, (f) fluorescence, and (g) merge of QD-PDADMAC binary mixture.

binary mixtures were equilibrated for 12 h before any measurements. The binary mixtures at very low concentrations of PDADMAC (1.3-19.2 μM) remain isotropic. While the absorption peak position of QD remains unaltered upon addition of initial concentrations of PDADMAC, the absorption band gets broaden (Figure 3.2a). In contrast, significant changes have been observed in the PL spectrum of QD in the presence of PDADMAC. The PL peak position of QD shifts from 523 to 531 nm upon addition of 5.2 μM of PDADMAC with 8 nm red shift (Figure 3.2b). Moreover, the PL intensity of QD quenches significantly in the presence of 5.2 μM of PDADMAC. Similar red-shift with decrease in PL intensity has been observed in the presence of different concentrations of PDADMAC in the range of 1.3-19.2 μM . In order to understand the mechanism behind this spectral change, we have measured the PL lifetimes of QDs in the presence of different concentrations of PDADMAC. Figure 3.2c displays the changes in the PL decay curves of QDs ($\lambda_{ex}=445$ nm; $\lambda_{em}=523$ nm) in the absence and presence of 5.2 μM of PDADMAC. In the absence of PDADMAC, the PL decay of QDs exhibits multiexponential decay kinetics and fit well with a three-exponential decay function (Table 3.1). QDs show three lifetime components of 0.57 (19%), 2.60 (27%), and 14.0 ns (54%) with an average lifetime of 8.40 ns, similar to those reported recently [22]. While the 2.60 ns component can be assigned due to the band edge exciton recombination, the 0.57 and 14.0 ns components arise due to the exciton recombination at the deep and shallow trap states, respectively. The PL decay of QDs in the presence of 5.2 μM of PDADMAC shows three lifetime components of 0.07 (82%), 1.17 (6%), and 13.3 ns (13%) with an average lifetime of 1.82 ns (Table 3.1).

Table 3.1. PL Decay parameters of green QD in the absence and presence of PDADMAC.

Samples	τ_1 (ns)	a_1	τ_2 (ns)	a_2	τ_3 (ns)	a_3	$\langle \tau \rangle$ (ns)	χ^2
Green QD	0.57	0.19	2.60	0.27	14.0	0.54	8.40	1.06
+ 5.2 μ M PDADMAC	0.07	0.82	1.17	0.06	13.3	0.13	1.82	1.12

Here it is important to note that the contribution of the shortest lifetime component due to deep trap states increases significantly from 19 to 82% in the presence of 5.2 μ M PDADMAC. In contrast, the contributions of the band edge and shallow trap states component decrease appreciably. These changes in relative contributions of lifetime components in the presence of PDADMAC clearly indicate alteration of surface trap states of QDs as a consequence of ligand reorganization [22]. This decrease in PL lifetime in the presence of PDADMAC is similar to that has been observed earlier in our steady-state PL measurements and originates mainly due to the exciton-exciton coupling between adjacent QDs in QD-PDADMAC nanocomposites. The FESEM image of the isotropic binary mixture at 5.2 μ M of PDADMAC (C1) confirms the formation of QD-PDADMAC nanocomposites (Figure 3.2d). CLSM has been performed to visualize the initial QD-PDADMAC nanocomposites (C1 region). Figure 3.2e shows the differential interference contrast (DIC) image of the QD-PDADMAC nanocomposites prepared in the presence of 5.2 μ M of PDADMAC. Distinct clusters of QDs in the PDADMAC matrix are clearly visible, which is consistent with our earlier SEM results. Confocal fluorescence image reveals green color luminescence from these polymer encapsulated clusters of QDs (Figure 3.2f). The merge image reveals that the luminescence appears exclusively from QD-PDADMAC nanocomposites (Figure 3.2g). Control experiment with neutral polyvinylpyrrolidone (PVP) reveals no such changes in the PL behavior

of QDs in the binary mixture, suggesting that the initial nanocomposite formation is mainly driven by long-range electrostatic attraction between oppositely charged QD-PDADMAC pair (Figure 3.3).

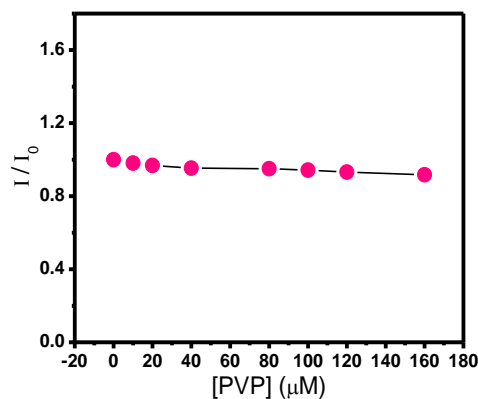


Figure 3.3. Change in the PL intensity ratio of green QD in the presence of different concentrations of PVP.

3.2.3. Coacervation and Hybrid Droplet Formation

Upon further increase in the concentrations of PDADMAC in the range of 22.4-160.0 μM, a continuous phase sequence from turbid (T1) to precipitate (P), and turbid (T2) has been observed in the binary mixture (Figure 3.4a). These observations clearly indicate the formation of supramolecular nanostructures and their continuous structural rearrangements in solution. The appearance of turbidity in the binary mixture indicates the formation of supramolecular self-assembled structures. The phase behavior of the binary mixtures was studied using turbidity profile. Turbidity of the binary mixtures was calculated using the following equation,

$$T = 100 - (100 \times 10^{-A}) \quad (1)$$

where T is the turbidity and A is the absorbance at 600 nm.

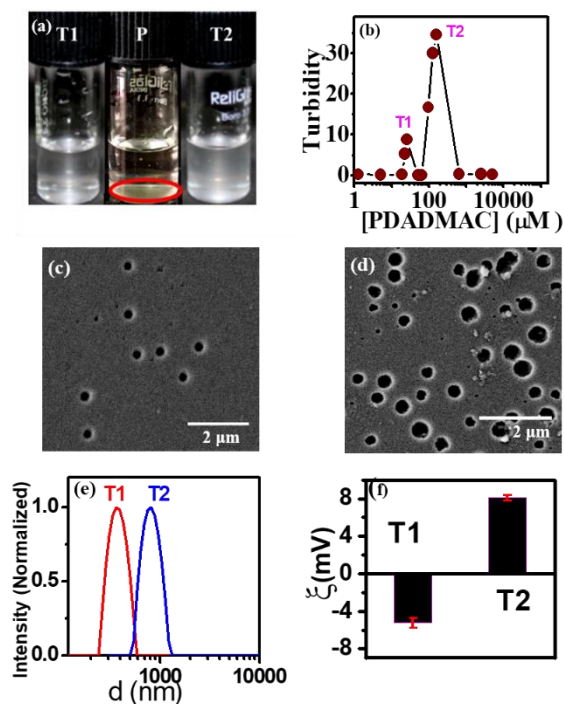


Figure 3.4. (a) Photographs of QD-PDADMAC binary solution in the presence of 25.5 (T1), 52.0 (P), and 130 μM (T2) of PDADMAC (Red circle indicates the precipitate phase of QD-PDADMAC binary mixture). (b) Plot of turbidity against PDADMAC monomer molar concentrations. FESEM images of the binary mixtures in the (c) T1, and (d) T2 regions of the phase profile. (e) Hydrodynamic size distribution of droplets in the T1 and T2 regions. (f) ξ potentials of droplets in the T1 and T2 regions.

Figure 3.4b shows the turbidity profile of binary mixtures in the concentration range of 5.0-5000.0 μM of PDADMAC. For the present study, we have mainly focused on the T1 and T2 regions of the binary mixture in the presence of 25.6 and 130.0 μM of PDADMAC, respectively. Notably, the binary mixtures in the T2 region are more turbid compared to those in T1 region (Figure 3.4b). FESEM image in the T1 region reveals distinct spherical self-assembled droplets with mean size of 383.9 ± 17.9 nm (Figure 3.4c and 3.5a). Relatively larger-sized droplets with mean size of 590.8 ± 23.8 nm is observed in the T2 region (Figure 3.4d and 3.5b), which account for its higher turbidity compared to T1 region.

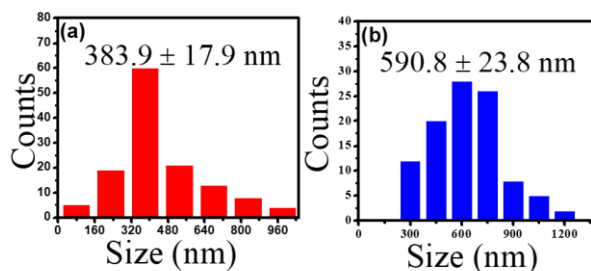


Figure 3.5. Size distribution histograms estimated from FESEM images of droplets in the (a) T1, and (b) T2 region.

The estimated mean hydrodynamic size of these droplets is 405 and 820 nm for T1 and T2 region, respectively (Figure 3.4e). In order to know the surface charge of these droplets in the T1 and T2 regions, we have measured their ζ potential. Our results reveal the presence of negatively and positively charged coacervate droplets in the T1 and T2 region, respectively. The estimated ζ potentials are -5.2 and +8.1 mV in the T1 and T2 regions, respectively (Figure 3.4f). Notably, droplets in both the regions (T1 and T2) show characteristic coalescence phenomenon (Figure 3.6a and 3.6b).

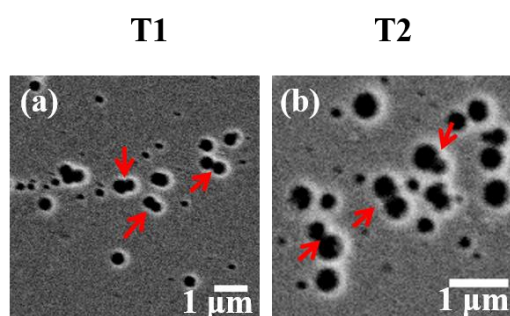
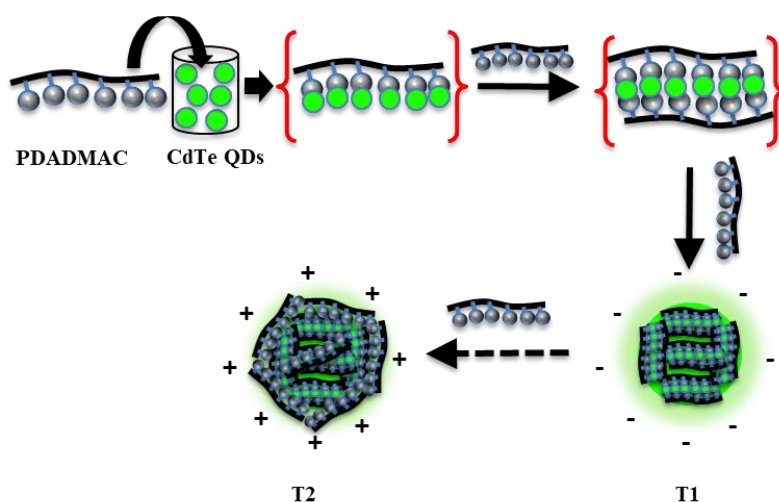


Figure 3.6. FESEM images of droplets in the (a) T1, and (b) T2 regions showing coalescence phenomenon. (Red arrows indicate representative coalescence intermediates).

Although droplet formation is a common phenomenon for oppositely charged aqueous polyelectrolytes [12-16], observation of this

phenomenon in QD-PDADMAC binary mixture is quite unique. This can be explained by considering electrostatic interactions between QD-PDADMAC nanocomposites and positively charged PDADMAC. Here negatively charged MSA-capped QDs are sandwiched between two positively charged PDADMAC chains (Scheme 3.1). The droplets in the T1 region show negative ζ -values due to the presence of uncomplexed free MSA ligands on QDs, whereas droplets in the T2 region contain excess of positively charged PDADMAC. Moreover, stoichiometric charge neutralization in the presence of 51.2-64.0 μM of PDADMAC accounts for the observed precipitation in the binary mixture [22].



Scheme 3.1. Schematic Representation of the Droplet Formation in the T1 and T2 Regions via QD-PDADMAC Nanocomposites.

In order to explore whether our organic-inorganic hybrid droplets can sequester foreign molecules as previously observed for organic coacervates [12-20], we investigated the sequestration of different solutes such as fluorescein isothiocyanate (2.0 μM), Rhodamine 6G (20 μM), Nile blue (1.0 μM), human serum albumin (59.0 μM), and bovine serum albumin (47.0 μM) by positively charged hybrid droplets (T2 region) using UV-vis spectroscopy. The partition coefficient (K) was calculated by the ratio of the concentrations of dyes/proteins loaded in coacervates to the concentrations of dyes/proteins present in the

supernatant. The partition coefficient (K) was calculated using following equation,

$$K = \frac{[\text{solute in coacervate}]}{[\text{solute in supernatant}]} \quad (2)$$

The estimated equilibrium partition coefficients (K) for different solutes are listed in Table 3.2.

Table 3.2. Estimated partition coefficients (K) of dyes and proteins inside coacervate droplets (T2 region).

Systems	Concentration used	K
FITC	2.0 μM	10.6 ± 2.5
Rh6G	20.0 μM	9.0 ± 1.6
Nile Blue	1.0 μM	136.0 ± 25.0
HSA	59.0 μM	34.1 ± 6.5
BSA	47.0 μM	35.0 ± 7.0

Significantly high value of K (137 ± 25) has been observed for Nile blue dye, possibly due to its low water solubility (0.16 mg/mL). Moreover, the estimated K value for human and bovine serum albumins is 34 ± 6 and 35 ± 7 , respectively. These high values of K clearly indicate preferential sequestration of different molecules irrespective of their charges, which is similar to those observed earlier for other organic coacervate droplets [12-16]. More importantly, our findings indicate that both hydrophobic and electrostatic interactions are responsible for the observed sequestrations.

3.2.4. Colloidal Stability as a Function of pH and Ionic Strength

The structural and colloidal stability of these droplets have been explored as a function of pH and ionic strength of the medium. While the binary mixtures in the T1 and T2 regions remain turbid in the pH range of 6.0-10.0, they become isotropic at lower acidic pH (3.0-5.5) (Figure 3.7a).

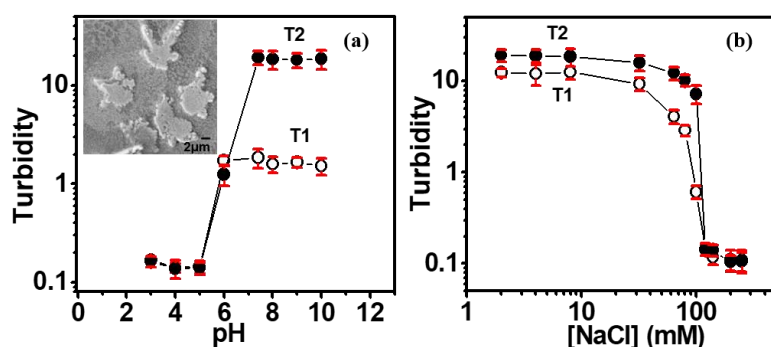


Figure 3.7. (a) Changes in the turbidity of the binary mixture as a function of solution pH in the T1 and T2 regions. The inset shows the FESEM image of the T1 region at pH 3. (b) Changes in the turbidity of the binary mixture as a function of NaCl concentrations in the T1 and T2 regions.

The plots of turbidity against pH of the medium for T1 and T2 regions are sigmoidal in nature and show a critical coacervation pH of 6.0. FESEM image of binary mixture in the T1 region clearly reveals the disassembled polymeric structures at pH 3 (Figure 3.7a, inset). Notably, these droplets are found to be stable even at pH 11.7. The observed disassembly at lower pH is due to the protonation of carboxylate groups of MSA ligands ($pK_a \sim 4.19$ and 5.64) at the surface of QD, which weakens the electrostatic interactions with positively charged PDADMAC [22]. This pH responsive assembly and disassembly makes them suitable candidates for *in vivo* sensing and drug delivery applications. Similarly, ionic strength of the medium has a profound effect on the present coacervation process. The turbidity of the binary

mixtures in the T1 and T2 region decreases slowly with increasing the ionic strength of the medium at lower concentrations of NaCl, followed by a steady decrease at higher NaCl concentrations indicating efficient screening of the electrostatic attraction between QD and PDADMAC (Figure 3.7b). The plot reveals a critical salt concentration of 120 mM for the present coacervation process.

3.2.5. PL Behavior of Hybrid Droplets

These hybrid droplets are expected to be inherently luminescent due to the presence of QDs. Next, we explored the luminescence properties of these hybrid droplets using confocal and epifluorescence microscopy. Figure 3.8 displays the CLSM images of hybrid coacervate droplets in the T1 and T2 regions of the binary mixture. As expected, distinct green color luminescent droplets have been observed in the T1 and T2 region of the binary mixture (Figure 3.8a, b).

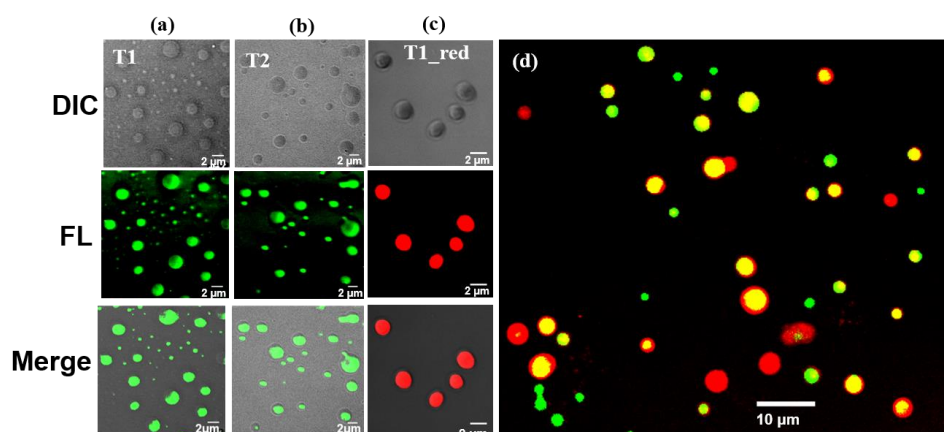


Figure 3.8. Confocal images (DIC, fluorescence, and merge) of coacervate droplets prepared with green QDs in the (a) T1, and (b) T2 region along with droplets prepared from red QDs in the (c) T1 region. (d) Confocal image showing coalescence of green and red color coacervate droplets prepared separately from green and red color QDs with PDADMAC aqueous solution. Yellow color appears due to the coalescence of green and red color droplets.

The merge images show that the green luminescence originates exclusively from the droplets. In order to illustrate that the present approach is suitable for fabrication of multicolor luminescent droplets, we synthesized a red-emitting MSA-capped CdTe QDs ($\lambda_{em} = 650$ nm) and mixed it with aqueous PDADMAC solution. The mean size of the red-emitting QDs is 3.9 ± 0.7 nm. The estimated ζ potential of red-emitting QDs is -10.9 ± 0.4 mV. The confocal images of the turbid binary mixture (T1 region) of red-emitting QD and PDADMAC reveal the formation of well-dispersed droplets with distinct red luminescence (Figure 3.8c). To visualize the coalescence behavior of these hybrid droplets, we performed mixing experiments with green and red color coacervate droplets prepared separately either from green or red QDs, respectively (Figure 3.8d). The mixture was equilibrated for 12 h before confocal imaging. It is evident that green and red color droplets undergo spontaneous coalescence to yield yellow color mixed droplets along with individual populations of green and red color droplets (Figure 3.8d). These observations clearly indicate that coalescence is a spontaneous and characteristic phenomenon for mixed populations of these hybrid droplets and may find tremendous importance in various enzymatic and catalytic reactions. More specifically, the characteristic coalescence phenomenon of these membrane-free luminescent droplets can be utilized in various chemical, enzymatic, and nanocatalysis reactions as well as for studying interactions between diverse encapsulated materials. Moreover, our findings reveal that the present approach can be easily extended for the fabrication of multicolor luminescent droplets for various bioimaging and sensing applications. Here it is important to mention that earlier reports on coacervate droplets have utilized external organic fluorophores such as fluorescein, cyanine [5], and green fluorescence protein for visualization under the fluorescence microscope, which is time consuming and inefficient [9,12,13]. In contrast, our hybrid droplets are unique in the sense that they are inherently luminescent and do not require external fluorophore labelling.

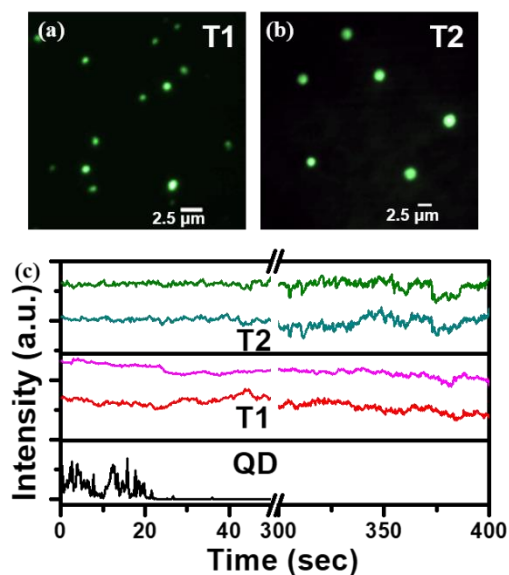


Figure 3.9. Epifluorescence images of droplets in the (a) T1, and (b) T2 regions. (c) Representative intensity trajectories of individual coacervate droplets in the T1 and T2 regions of the binary mixture along with green QD.

We analyzed the intensity trajectories of individual droplets and compared with those of bare QDs. Individual QD shows PL blinking or intermittence with single step photobleaching, which is a characteristic phenomenon of single emitters (Figure 3.9c) [22]. In contrast, intensity trajectories of luminescent droplets in both T1 and T2 region reveal absence of any PL blinking (Figure 3.9c). This is expected as these droplets are composed of several QDs which are electrostatically associated with the polymer networks. More importantly, these luminescent droplets are extremely photostable and don't show any photobleaching even after several minutes (observation time ~ 7 minutes) of laser exposure. This unusual photostability arises likely due to the efficient capping of QDs by the polymeric chains of PDADMAC inside these droplets. The slight fluctuations observed in the intensity profiles of droplets arise due to the PL blinking of QDs (individual/cluster) inside the coacervate droplets. The present finding of photobleaching resistant and nonblinking luminescence from coacervate droplets is unprecedented in the literature and may have significant impact on various bioimaging applications.

3.2.6. Fabrication of Mixed Two-Color and Two-Photon Active Hybrid Droplets

With the aim towards designing new multicolor and multifunctional hybrid materials, we fabricated mixed two-color luminescent droplets by simultaneously mixing (1:1) green and red emitting QDs with PDADMAC aqueous solution (Figure 3.10a). These droplets were characterized using confocal microscopy with appropriate green (490-550 nm) and red (570-670 nm) emission filter sets. Phase contrast image of this binary mixture (T1 region) confirms the formation

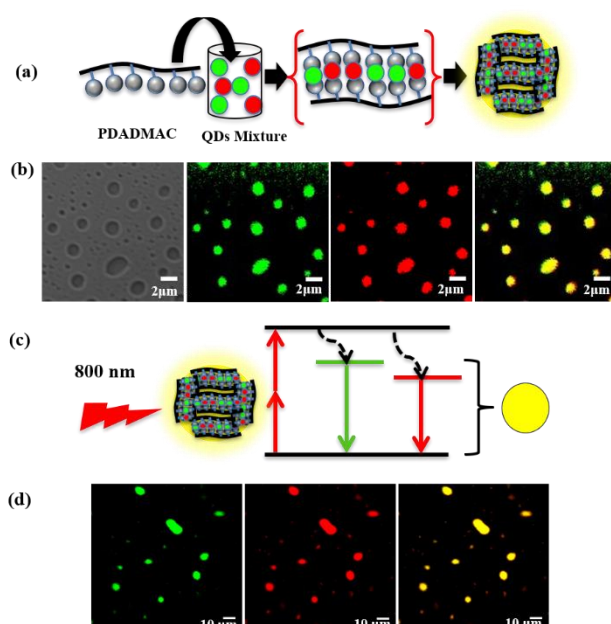


Figure 3.10. (a) Illustration of the mixed two-color droplet formation from green and red QDs mixture. (b) Confocal images in the green and red channels along with their DIC and merge images showing the formation of mixed two-color droplets from green and red QDs. (c) Schematic representation of the 2P excitation and emission of mixed two-color droplets upon 800 nm laser irradiation. (d) 2P confocal images of mixed two-color droplets in the green (490-550 nm) and red (570-670 nm) channels along with their merge image.

of coacervate droplets (Figure 3.10b), similar to those observed earlier. Confocal fluorescence images in the green and red channels clearly reveal the appearance of both green and red luminescence from these mixed droplets, respectively (Figure 3.10b). More importantly, the merged image of the green and red channels reveals distinct yellow color luminescent droplets, which unambiguously confirms the presence of both green and red QDs in each coacervate droplet (Figure 3.10b). Notably, absence of any individual population of green or red color luminescent droplets indicates that the initial QD-PDADMAC nanocomposite formation is purely electrostatic in nature and does not depend on the nature of QDs. The present strategy for the fabrication of mixed two-color hybrid droplets can be extended further with different combinations of inorganic nanoparticles (NPs) for a wide range of applications.

Finally, we explored the applicability of these hybrid droplets in two-photon (2P) PL imaging using 2P confocal microscopy. Importantly, 2P excitation provides high signal to noise ratio with enhanced penetration depth into biological specimens, which significantly reduces the phototoxicity [24]. These properties find particular importance in tissue engineering and in vivo bioimaging and sensing applications. Two-photon imaging experiments were performed using two-color hybrid droplets prepared using 1:1 mixture of green and red-emitting QDs with PDADMAC aqueous solution (Figure 3.10c). Samples were excited with a 800 nm pulsed laser and images were collected in the green and red channels separately. 2P confocal images reveal both green and red luminescence from mixed two-color droplets with intense two-photon yellow luminescence and very low background noise (Figure 3.10d). These findings clearly highlight the importance of these droplets as two-photon imaging probes for various bioimaging applications.

3.3. Conclusions

In this chapter, we have demonstrated the self-assembly process between CdTe QDs and PDADMAC polymer in aqueous medium. The self-assembly process is triggered by the formation of initial QD-PDADMAC nanocomposites, which subsequently associate with positively charged PDADMAC to form spherical coacervate droplets in aqueous medium. These hybrid droplets are found to be stable in a broad range of composition, pH, and ionic strength of the medium. This organic-inorganic hybrid coacervate droplets show 2P active properties as well as highly photostability. Hence have profound implications in various applications such as bioimaging, sensing, and light-emitting devices. The strategy for the fabrication of mixed two-color luminescent droplets presented here may open up a new avenue for the designing of other multifunctional hybrid materials for nanocatalysis and nanosensing applications.

Note: This is copyrighted material from permission of the American Chemistry Society.

3.4. References

1. Liu Y., He J., Yang K., Yi C., Liu Y., Nie L., Khashab N. M., Chen X., Nie Z. (2015), Folding up of gold nanoparticle strings into plasmonic vesicles for enhanced photoacoustic imaging. *Angew. Chem. Int. Ed.*, *54*, 15809-15812. (DOI:10.1002/anie.201508616)
2. Discher B. M., Won Y.-Y., Ege D. S., Lee J. C.-M., Bates F. S., Discher D. E., Hammer D. A. (1999), Polymersomes: Tough vesicles made from diblock copolymers. *Science*, *284*, 1143-1146. (DOI:10.1126/science.284.5417.1143)
3. Yuk H., Lu B., Zhao X. (2019), Hydrogel bioelectronics. *Chem. Soc. Rev.*, *48*, 1642-1667. (DOI: 10.1039/C8CS00595H)
4. Yan X., Delgado M., Fu A., Alcouffe P., Gouin S. G., Fleury E., Katz J. L., Ganachaud F., Bernard J. (2014), Simple but precise engineering of functional nanocapsules through nanoprecipitation. *Angew. Chem. Int. Ed.*, *53*, 6910-6913. (DOI:10.1002/anie.201402825)
5. Keating C. D. (2012), Aqueous phase separation as a possible route to compartmentalization of biological molecules. *Acc. Chem. Res.*, *45*, 2114-2124. (DOI:10.1021/ar200294y)
6. Zhang H., Liu Y., Yao D., Yang B. (2012), Hybridization of inorganic nanoparticles and polymers to create regular and reversible self-assembly architectures. *Chem. Soc. Rev.*, *41*, 6066-6088. (DOI: 10.1039/C2CS35038F)
7. Li, Y., Wang, Y., Huang, G., Gao, J. (2018), Cooperativity principles in self-assembled nanomedicine. *Chem. Rev.*, *118*, 5359-5391. (DOI: 10.1021/acs.chemrev.8b00195)
8. Crosby, J., Treadwell, T., Hammerton, M., Vasilakis, K., Crump, M. P., Williams, D. S., Mann, S. (2012), Stabilization and enhanced reactivity of actinorhodin polyketide synthase minimal complex in

polymer–nucleotide coacervate droplets. *Chem. Commun.*, 48, 11832–11834. (DOI: 10.1039/C2CC36533B)

9. Mason, A. F., Buddingh', B. C., Williams, D. S., van Hest, J. C. M. (2017), Hierarchical self-assembly of a copolymer-stabilized coacervate protocell. *J. Am. Chem. Soc.*, 139, 17309–17312. (DOI:10.1021/jacs.7b10846)

10. Drobot, B., Iglesias-Artola, J. M., Le Vay, K., Mayr, V., Kar, M., Kreysing, M., Mutschler, H., Tang, T. Y. D. (2018), Compartmentalised RNA catalysis in membrane-free coacervate protocells. *Nat. Commun.*, 9, 3643. (DOI: 10.1038/s41467-018-06072-w)

11. Strulson, C. A., Molden, R. C., Keating, C. D., Bevilacqua, P. C. (2012), RNA catalysis through compartmentalization. *Nat. Chem.*, 4, 941. (DOI:10.1038/nchem.1466)

12. Douliez, J.-P., Martin, N., Gaillard, C., Beneyton, T., Baret, J.-C., Mann, S., Beven, L. (2017), Catanionic coacervate droplets as a surfactant-based membrane-free protocell model. *Angew. Chem. Int. Ed.*, 56, 13689–13693. (DOI:10.1002/anie.201707139)

13. van Swaay, D., Tang, T.-Y. D., Mann, S., de Mello, A. (2015), Microfluidic formation of membrane-free aqueous coacervate droplets in water. *Angew. Chem. Int. Ed.*, 54, 8398–8401. (DOI:10.1002/anie.201502886)

14. Williams, D. S., Koga, S., Hak, C. R. C., Majrekar, A., Patil, A. J., Perriman, A. W., Mann, S. (2012), Polymer/nucleotide droplets as bio-inspired functional micro-compartments. *Soft Matter*, 8, 6004–6014. (DOI:10.1039/C2SM25184A)

15. Koga, S., Williams, D. S., Perriman, A. W., Mann, S. (2011), Peptide–nucleotide microdroplets as a step towards a membrane-free protocell model. *Nat. Chem.*, 3, 720–724. (DOI: 10.1038/nchem.1110)

-
16. Martin, N., Li, M., Mann, S. (2016), Selective uptake and refolding of globular proteins in coacervate microdroplets. *Langmuir*, *32*, 5881-5889. (DOI: 10.1021/acs.langmuir.6b01271)
17. Black, K. A., Priftis, D., Perry, S. L., Yip, J., Byun, W. Y., Tirrell, M. (2014), Protein encapsulation via polypeptide complex coacervation. *ACS Macro Lett.*, *3*, 1088-1091. (DOI: 10.1021/mz500529v)
18. Priftis, D., Leon, L., Song, Z., Perry, S. L., Margossian, K. O., Tropanikova, A., Cheng, J., Tirrell, M. (2015), Self-assembly of α -helical polypeptides driven by complex coacervation. *Angew. Chem. Int. Ed.*, *54*, 11128-11132. (DOI: 10.1002/anie.201504861)
19. Priftis, D., Xia, X., Margossian, K. O., Perry, S. L., Leon, L., Qin, J., de Pablo, J. J., Tirrell, M. (2014), Ternary, tunable polyelectrolyte complex fluids driven by complex coacervation. *Macromolecules*, *47*, 3076-3085. (DOI:10.1021/ma500245j)
20. Priftis, D., Tirrell, M. (2012), Phase behaviour and complex coacervation of aqueous polypeptide solutions. *Soft Matter*, *8*, 9396-9405. (DOI: 10.1039/C2SM25604E)
21. Yu, W. W., Qu, L., Guo, W., Peng, X. (2003), Experimental determination of the extinction coefficient of CdTe, CdSe, and CdS nanocrystals. *Chem. Mater.*, *15*, 2854-2860. (DOI:10.1021/cm034081k)
22. Vaishnav, J. K., Mukherjee, T. K. (2019), Surfactant-induced self-assembly of CdTe quantum dots into multicolor luminescent hybrid vesicles. *Langmuir*, *35*, 6409-6420. (DOI: 10.1021/acs.langmuir.9b00357)
23. Vaishnav, J. K., Mukherjee, T. K. (2018), Long-range resonance coupling-induced surface energy transfer from CdTe quantum dot to

plasmonic nanoparticle. *J. Phys. Chem. C*, 122, 28324-28336. (DOI: 10.1021/acs.jpcc.8b08757)

24. Tenório, D. P. L. A., Andrade, C. G., Cabral Filho, P. E., Sabino, C. P., Kato, I. T., Carvalho, L. B., Alves, S., Ribeiro, M. S., Fontes, A., Santos, B. S. (2015), CdTe quantum dots conjugated to concanavalin A as potential fluorescent molecular probes for saccharides detection in *Candida albicans*. *J. Photochem. Photobiol. B*, 142, 237-243. (DOI: 10.1016/j.jphotobiol.2014.11.010)

Chapter 4

*Surfactant-Induced Self-Assembly of CdTe
Quantum Dots into Multicolor Luminescent
Hybrid Vesicles*

4.1. Introduction

In the past few decades, extensive studies have been executed to understand the structure and dynamics of lipid bilayer in conventional phospholipid vesicles owing to their vast application in biology [1-5] and nanotechnology [6-12]. In recent times vesicles from other amphiphilic molecules such as block copolymers [13-14], dendrimers [15], polypeptides [16], surfactants [17], and fatty acid [18] have been fabricated successfully with enhanced colloidal and mechanical stability compared to conventional phospholipid vesicles. Among these, polymersomes from amphiphilic block copolymers have attracted significant research interest due to their robust structure and functionality. While the mechanical stability of polymersomes is an order of magnitude higher than conventional phospholipid vesicles, the membrane permeability is significantly less (<10 times) than phospholipid bilayers [13-14]. Moreover, the self-assembly and membrane properties of these polymersomes can be easily tuned by simply varying the chemical composition and molecular weight of polymers over a wide range.

However, there are limited reports for the fabrication of inherently luminescent stable hybrid vesicles. Earlier, Sun *et al.* have investigated the self-assembly mechanism of oppositely charged carbon quantum dots (CQDs)-surfactants mixture and shown the formation of supramolecular fluorescent vesicles [15-16]. In this chapter, we have investigated the interaction of MSA-capped CdTe QDs with surfactant assemblies and explored the self-assembly mechanism by using various spectroscopic and microscopic techniques and illustrate the role of electrostatic interactions between oppositely charged QDs and surfactants on the association and subsequent self-assembly process. It has been observed that the self-assembly of initial ion-pairs between negatively charged MSA-capped CdTe QDs and positively charged CTAB surfactants leads to the formation of stable supramolecular hybrid multicolor luminescent vesicles. Confocal microscopy shows that these hybrid vesicles can efficiently encapsulate a cationic water

soluble dye Rh6G into their hollow aqueous cavity. More importantly, these self-assembled vesicles exhibit pH-responsive reversible assembly and disassembly process in aqueous medium which may have potential application in sensing and drug delivery.

4.2. Results and Discussion

4.2.1. Phase Behavior of Binary Mixtures of QD and Different Surfactants

The phase behavior of binary mixture of negatively charged QDs with positively charged CTAB, negatively charged SDS, and neutral TX-100 surfactant has been studied using turbidity profile. Figure 4.1a shows the photographs of QD-CTAB binary mixture at selected concentrations of CTAB. It is evident that the binary mixture shows continuous phase transitions from clear to turbid, precipitate, turbid, and clear with increase in the concentrations of CTAB. Figure 4.1b displays the full phase profile of the binary mixture in the concentration range of 0.01-10 mM. Initially, at very low CTAB concentration range (0.01-0.08 mM), the binary mixture remains isotropic in nature.

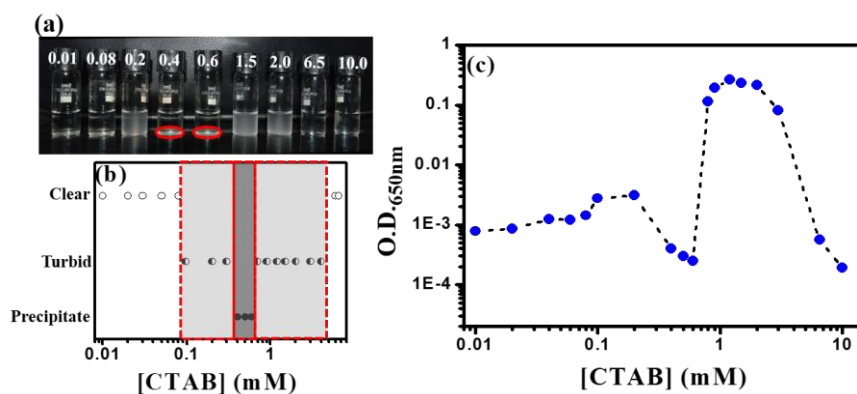


Figure 4.1. (a) Photographs of QD-CTAB binary mixtures at different concentrations of CTAB (Red circles indicate the precipitate phase of the QD-CTAB binary mixture). (b) Phase sequences of the binary mixture as a function of CTAB concentrations. (c) Plot of absorbance at 650 nm with molar concentrations of CTAB in the binary mixture. The concentration of QD is fixed at 0.33 μ M.

This clear isotropic solution gradually turns turbid upon increasing the CTAB concentration in the range of 0.09-0.3 mM. Further increase in the CTAB concentration (0.4-0.6 mM) results in precipitation (depicted via red circles in Figure 4.1a). These precipitates re-dispersed again upon increasing the CTAB concentration (0.7-4.0 mM) and results in the formation of turbid solution. The turbidity of the solution decreases gradually upon further increasing the CTAB concentration and a clear solution appears above 6 mM CTAB concentration. Figure 4.1c shows the changes in the absorbance of the binary mixture at 650 nm as a function of CTAB concentrations. Phase-dependent changes in the absorbance of the mixture are clearly evident. These findings clearly indicate the presence of five different phases in the QD-CTAB binary mixture and these phases can be classified as initial clear (C1), first turbid (T1), precipitate (P), second turbid (T2), and second clear (C2).

In contrary, no such changes in the absorbance or phase behavior have been observed in the presence of negatively charged SDS and neutral

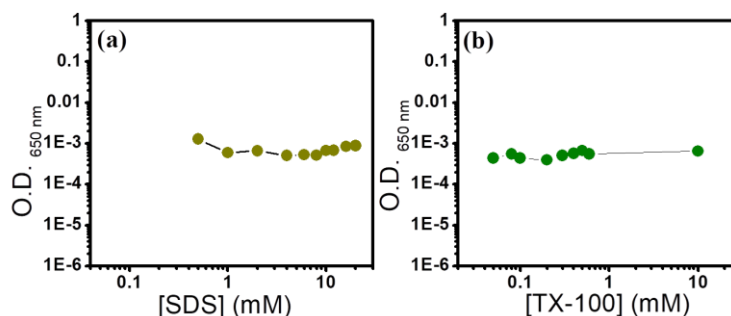


Figure 4.2. Changes in the absorbance ($\lambda=650$ nm) of QD in the presence of different concentrations of (a) SDS and (b) TX-100 surfactants.

TX-100 surfactants (Figure 4.2a and 4.2b), indicating the importance of electrostatic attraction between oppositely charged QD and CTAB pair behind the observed phase behavior in the QD-CTAB binary mixture. Notably, similar kind of phase behavior has been observed earlier in the binary mixture of oppositely charged CQDs and surfactants [15].

4.2.2. PL Behavior of QD-CTAB Binary Mixture in the C1 and C2 Region

Figure 4.3a displays the changes in the absorption spectra of green QDs in the C1 (0.01 mM) and C2 (10 mM) region of the phase profile. The absorbance of QD at 490 nm decreases with a noticeable redshift of 23 nm in the presence of 0.01 mM CTAB concentration (C1 region). Similar changes in the absorption spectra have been observed at other concentrations in the C1 region. However, the absorption peak position of QD in the C2 region (10 mM CTAB) of the binary mixture exhibits 6 nm blue shifts. These spectral shifts clearly indicate ground-state association between oppositely charged QD and CTAB in the binary mixture.

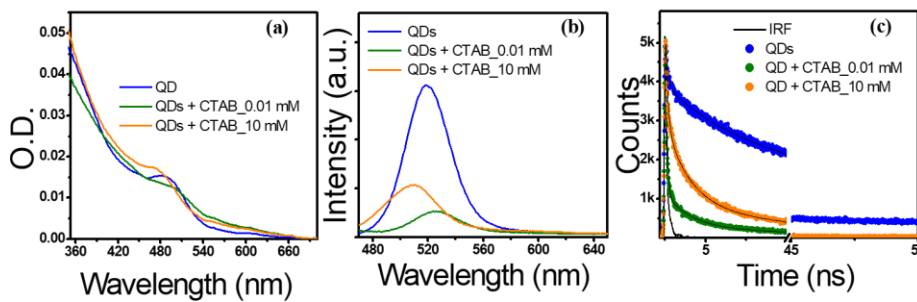


Figure 4.3. Changes in the (a) Absorption spectra, (b) PL spectra ($\lambda_{\text{ex}}=445$ nm), and (c) PL decay traces ($\lambda_{\text{ex}}=445$ nm; $\lambda_{\text{em}}=520$ nm) of green QDs in the presence of 0.01 and 10 mM CTAB.

Figure 4.3b shows the changes in the PL spectra of binary mixture in the C1 and C2 region at an excitation wavelength of 445 nm. A significant PL quenching has been observed in the steady-state PL intensity of QD in the presence of 0.01 mM CTAB (C1 region). Moreover, a red shift of 6 nm is clearly evident in the PL peak position relative to that of free QD in aqueous medium. In contrast, the binary mixture in the C2 region shows a 10 nm blue shift in the PL peak position. Notably, the PL intensity of the binary mixture in the C2 region increases slightly (~2%) relative to that in C1 region. To understand the nature of interaction

between QD and CTAB, we have studied the PL behavior of QD in the presence of anionic SDS and neutral TX-100 surfactants. The plot of PL ($\lambda_{em}=520$ nm) intensity ratio (I/I_0) against concentrations of SDS and TX-100 shows negligible variation (Figure 4.4a and 4.4b).

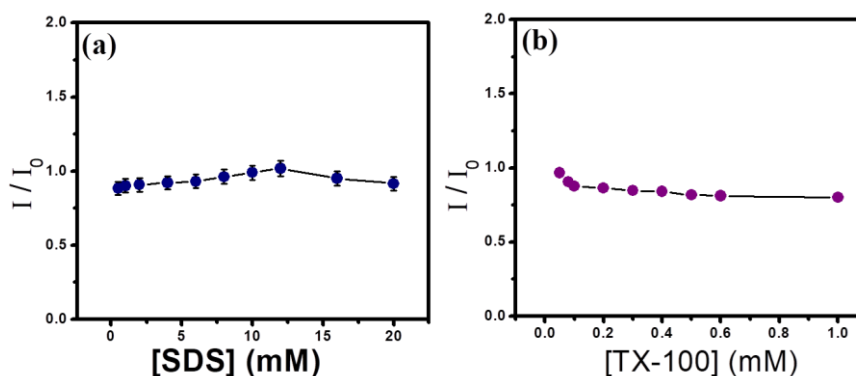


Figure 4.4. Changes in the PL intensity ratio of QD in the presence of (a) SDS, and (b) TX-100 surfactants.

Moreover, the PL peak position remains unaltered in the presence of both the surfactants. These results clearly establish the role of electrostatic interaction between oppositely charged QD-CTAB pair behind the observed spectral changes in the binary mixture. The binding constant between QD and CTAB in the C1 region is estimated by using Hill equation and shows a value of $6.6 \times 10^6 \text{ M}^{-1}$ (Figure 4.5) [17]. The binding constant between CTAB and QD in the C1 region of the binary mixture was estimated using Hill equation [44], which can be expressed as follows:

$$\frac{I_0 - I}{I_0 - I_{min}} = \frac{1}{1 + \left(\frac{K_D}{[CTAB]}\right)^n} \quad (1)$$

where I_0 and I are the luminescence intensities of QD in the absence and presence of CTAB, I_{min} is the minimum saturation intensity of QD in the presence of CTAB, K_D is the dissociation constant, and n is the Hill coefficient. The experimental data was fitted with Hill equation using

non-linear least square method and the goodness of fit was judged by correlation coefficient (R^2) value.

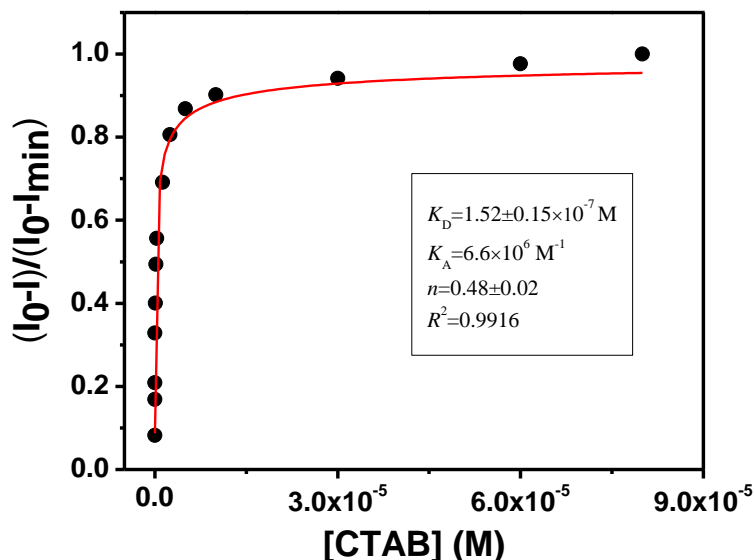


Figure 4.5. The Hill plot using fluorescence intensity of QD in the absence and presence of different concentrations of CTAB in the C1 region of the phase profile.

This high binding affinity further suggests electrostatic interactions and subsequent ion-pair formation between oppositely-charged QD and CTAB. Similar spectral changes have been observed earlier for oppositely charged fluorophore-surfactant pairs due to ion-pair complexation [18-19]. Therefore, the red shifts in the absorption and PL peak positions with concomitant PL quenching observed in the C1 region of the binary mixture arises mainly due to the formation of surfactant-induced aggregates of QDs via ion-pair complexation. In contrast, the opposite spectral shifts (blue shifts) observed in the C2 region of the binary mixture indicate much less polar local environment around QDs inside the surfactant-induced aggregates in C2 region compared to that in C1 region. Although, both the mixtures (C1 and C2) are isotropic in nature, the interaction and morphology of the self-assembled nanocomposites in the C2 region is expected to differ

significantly as a consequence of 1000 times higher concentrations of CTAB in the C2 region relative to that in C1 region. Moreover, the significant PL quenching observed in the C1 and C2 region of the phase profile may originate due to the exciton-exciton coupling between adjacent QDs in the self-assembled structures. To validate this statement, we have performed time-resolved PL measurements of QD-CTAB binary mixture in the C1 and C2 region. Figure 4.4c displays the changes in the PL decay curves of QDs ($\lambda_{\text{ex}}=445$ nm; $\lambda_{\text{em}}=520$ nm) in C1 and C2 region. All the decays show multiexponential decay kinetics and fit well with a three exponential decay function (Table 4.1).

Table 4.1. PL decay parameters of green QD in the absence and presence of 0.01 and 10 mM CTAB.

Samples	τ_1 (ns)	a_1	τ_2 (ns)	a_2	τ_3 (ns)	a_3	$\langle\tau\rangle$ (ns)	χ^2
Green QD	0.55	0.21	3.51	0.31	15.4	0.48	8.54	1.02
QD + 0.01 mM CTAB	0.10	0.85	1.07	0.12	4.60	0.02	0.31	1.19
QD + 10 mM CTAB	0.13	0.64	1.53	0.27	7.70	0.09	1.20	1.19

In absence of CTAB, QDs show three lifetime components of 0.55 (21%), 3.50 (31%), and 15.42 ns (48%) with an average lifetime of 8.54 ns. This triexponential decay kinetics is due to multiple recombination processes in MSA-capped CdTe QDs involving band edge as well as trap states (shallow and deep) exciton recombinations [20-21]. While the 3.50 ns component can be assigned due to the band edge exciton recombination, the shortest and longest lifetime component arises due to the presence of deep and shallow trap states, respectively. All the three lifetime components decrease upon addition of CTAB (Table 4.1). The PL decay of QD in the presence of 0.01 mM CTAB shows three lifetime components of 0.10 (85%), 1.07 (12%), and 4.60 ns (2%) with an average lifetime of 0.31 ns (Figure 4.3c, Table 4.1). This decrease in PL lifetime of QD in the C1 region is similar to that has been observed

earlier in our steady-state PL measurements and arises due to the exciton-exciton coupling between adjacent QDs in surfactant-induced aggregates. Notably, the contribution of the shortest lifetime component due to deep surface trap states increases significantly from 21 to 85% in the presence of 0.01 mM CTAB. In contrast, the contribution of the band edge and shallow trap component decreases from 31 to 12% and 48 to 2%, respectively. These changes in relative contributions of lifetime components upon ion-pair formation with CTAB clearly indicate alteration of surface trap states as a consequence of ligand reorganization at the surface of QDs. Here it is important to note that the initial ion-pairs between QDs and CTAB undergo aggregation through association of hydrophobic chains of CTAB which may result in uneven ligand distribution at the surface of QDs as a consequence of ligand reorganization. Similar phenomenon of ligand reorganization and subsequent self-assembly of various amphiphilic NPs has been reported earlier [15,22]. However, in the C2 region (10 mM CTAB), the average PL lifetime of QDs saturates to 1.20 ns with lifetime components of 0.13 (64%), 1.53 (27%), and 7.70 ns (9%) (Figure 4.3c, Table 4.1). Notably, the contribution of the shortest lifetime component due to deep trap states decreases from 85 to 64%, while that from core states increases from 12 to 27% upon increasing the CTAB concentrations from 0.01 to 10 mM, respectively. This observation indicates relatively more compact structural arrangement of QDs inside the self-assembled structures in C2 region compared to that in C1 region. This statement is quite reasonable as we earlier observed ~16 nm blue shifts in the PL maximum of QD in the C2 region relative to that in C1 region.

To better understand the PL behavior of individual particles in the C1 and C2 region, we have performed PL microscopy using epifluorescence set-up. Figure 4.6 shows the PL images of QDs in the absence and presence of 0.01 and 10 mM CTAB. Distinct diffraction limited PL spots have been observed for CdTe QDs in the absence of CTAB (Figure 4.6a).

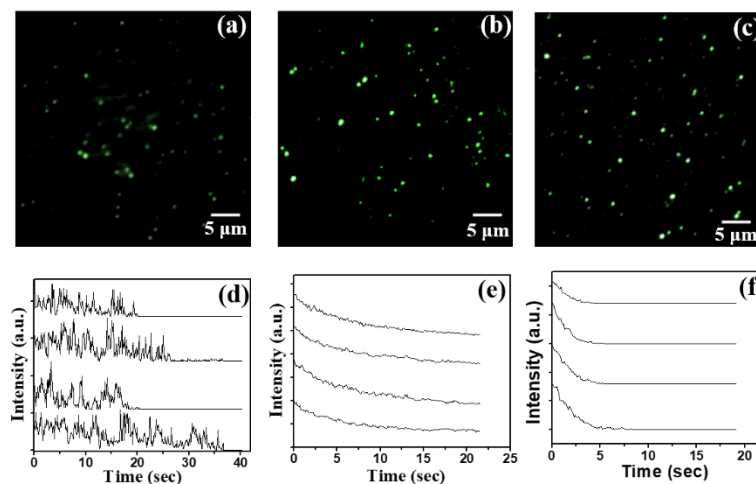


Figure 4.6. PL images of green QDs in the presence of (a) 0 mM, (b) 0.01 mM, and (c) 10 mM CTAB. Representative intensity profiles of luminescent spots in the presence of (d) 0 mM, (e) 0.01 mM, and (f) 10 mM CTAB.

Intensity profile of most of these spots (>95%) show characteristic PL blinking or on/off behavior (Figure 4.6d). The observation of two-state blinking phenomenon with a single step photobleaching clearly indicates the presence of well-dispersed single emitter in the QD sample [23]. However, the PL image of the binary mixture in the C1 region (0.01 mM CTAB) reveals the presence of much brighter PL spots compared to those observed in the absence of CTAB (Figure 4.6b). Intensity profiles of these brighter PL spots show gradual intensity decay with no clear photobleaching step suggesting the presence of surfactant-induced aggregates of QDs in the C1 region (Figure 4.6e). Earlier, similar kinds of results have been observed with Si-QDs in the presence of anionic SDS surfactant [23]. Therefore, the brighter PL spots in the C1 region appear due to the presence of multiple aggregated QDs in each pixel, which decay fast due to the exciton-exciton coupling between adjacent QDs. Similar bright PL spots have also been observed in the C2 region with no clear photobleaching steps (Figure 4.6c and 4.6f). Notably, PL spots in the C2 region show fast photobleaching (within 5 sec) relative to those observed in the C1 region

possibly due to the higher extent of exciton-exciton coupling between adjacent QDs in the C2 region of the self-assembled structures, as indicated earlier in PL measurements. Based on the above findings, we propose that the PL quenching observed in the C1 region of the binary mixture is mainly due to the formation of non-specific surfactant-induced aggregates/clusters as a consequence of ion-pair formation between oppositely charged QD and CTAB. In contrast, QDs in C2 region reside in more compact and hydrophobic microenvironment of complex self-assembled structures. In order to understand the structural and morphological transitions between different phases of the QD-CTAB binary mixture, we have performed SEM, AFM, and DLS measurements.

4.2.3. FESEM, AFM and DLS Measurements of Self-Assembled Structures in the T1 and T2 Region

The appearance of turbidity in the T1 and T2 region of the phase profile indicates the formation of supramolecular self-assembled nanostructures. FESEM, AFM, and DLS measurements have been performed to know the morphology, size and zeta potential of these self-assembled nanostructures. SEM measurements have been performed at three different CTAB concentrations namely, 0.08, 0.2, and 1.5 mM. While, the binary mixture at 0.08 mM CTAB remains isotropic in nature and represents borderline concentration between C1 and T1 region, clear turbidity appears at 0.2 and 1.5 mM CTAB concentrations in the T1 and T2 region of the phase profile, respectively. Distinct spherical-shaped self-assembled vesicle-like structures have been observed at 0.08 mM CTAB. The diameter of these self-assembled vesicles-like structures varies from 100-700 nm with mean size of 348.3 ± 16.5 nm (Figure 4.7a and 4.7g). Notably, clear fusion events with various fusion intermediates are also observed (Figure 4.7b). This characteristic fusion phenomenon clearly indicates that the observed self-assembled spherical nanocomposites are indeed hybrid vesicles [3]. Moreover, no such self-assembled vesicles have been observed with CTAB or QD solution alone indicating the presence of both QD and CTAB in these hybrid

vesicles. On the other hand, the vesicles observed in the T1 region are larger in size and the diameter varies in the range of 300-1000 nm with a mean diameter of 753.8 ± 20.5 nm (Figure 4.7c and 4.7h).

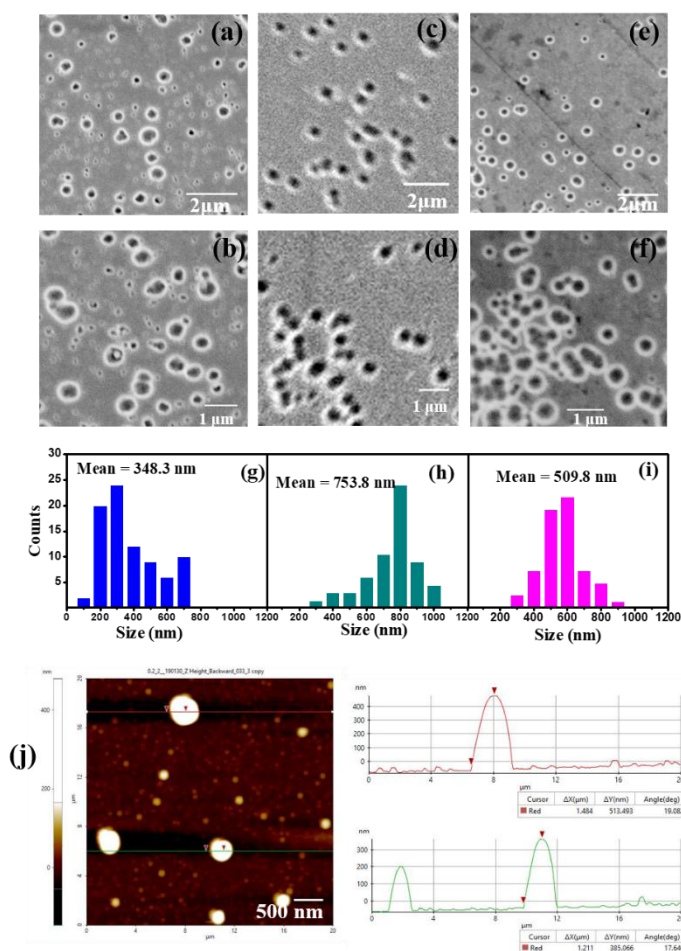


Figure 4.7. FESEM images of QD-CTAB binary mixture in the presence of (a),(b) 0.08 mM, (c),(d) 0.2 mM, and (e),(f) 1.5 mM CTAB. Size distribution histograms estimated from FSEM measurements for (g) 0.08 mM, (h) 0.2 mM, and (i) 1.5 Mm concentration of CTAB. (j) AFM Image of QD-CTAB binary mixture at 0.2 mM CTAB with cross section analysis.

Vesicles in the T1 region also exhibit characteristic fusion phenomenon (Figure 4.7d). AFM image in the T1 region further confirms the presence of spherical vesicles (Figure 4.7j). Height profile measurements of AFM image reveal vesicles with size in the range of

100-1200 nm (Figure 4.7j). Similar spherical vesicles have also been observed in the T2 region (1.5 mM CTAB) with diameters ranging from 300-900 nm (Figure 4.7e). Vesicles in T2 region shows mean diameter of 509.8 ± 15.2 nm (Figure 4.7e and 4.7i). Importantly, various non-spherical large fusion intermediates have also been observed in the T2 region (Figure 4.7f). The presence of these non-spherical fusion intermediates makes the T2 region more turbid than that of T1 region. Here it is important to note that the uniform vesicles observed in the T1 and T2 region of the binary mixture may differ in their inherent structure as these two phases are separated by a P phase and the effective concentration of CTAB in these two regions differs by a factor of 7.5. In order to gain further structural insights, we have performed DLS measurements.

Figure 4.8 displays the hydrodynamic sizes and ζ values of self-assembled vesicles. The estimated mean hydrodynamic diameters are 463.4 ± 18.5 , 856.1 ± 20.2 nm, and 553.6 ± 15.8 nm for vesicles observed in the presence of 0.08, 0.2 and 1.5 mM CTAB, respectively (Figure 4.8a, 4.8b, & 4.8c). These hydrodynamic diameters match well with those estimated from SEM measurements. Figure 4.8d shows the changes in the estimated ζ values as a function of CTAB concentrations. The aqueous dispersion of MSA-capped CdTe QDs shows ζ of -13.9 ± 0.5 mV (Figure 4.8d). However, this ζ value increases to -24.4 ± 2.8 mV for the vesicles observed in the presence of 0.08 mM CTAB (Figure 4.8d).

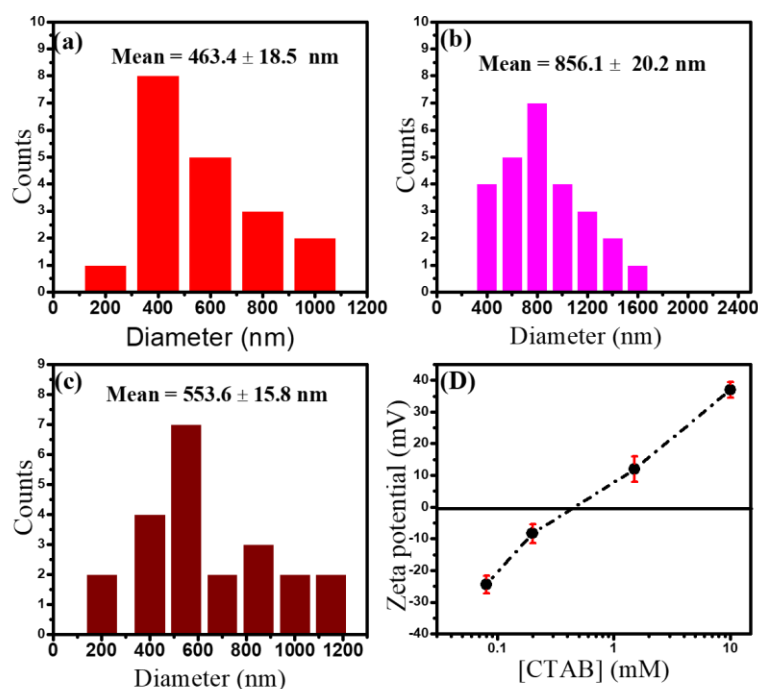
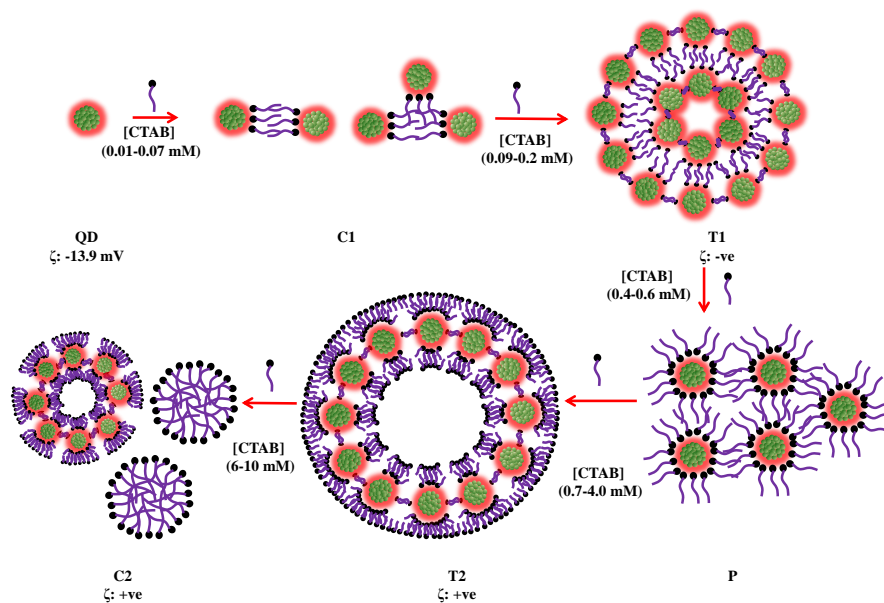


Figure 4.8. Size distribution histograms obtained from DLS measurements of QD-CTAB binary mixture in the presence of (a) 0.08 mM, (b) 0.2 mM, and (c) 1.5 mM CTAB. (d) Changes in the ζ values of self-assembled vesicles as a function of CTAB concentrations.

Notably, beyond this concentration of CTAB, the self-assembled vesicles show a continuous decrease in ζ value. The vesicles observed in the T1 region (0.2 mM) show a ζ value of -8.3 ± 1.6 mV (Figure 4.8d). In contrary, the vesicles in the T2 region exhibit a positive ζ value of $+12.0 \pm 1.5$ mV. Notably, the sign of the ζ changes from -ve to +ve in the concentration range of 0.4-0.6 mM CTAB (Figure 4.8d). Finally, the ζ at C2 region (10 mM) of the binary mixture shows a value of $+37.0 \pm 2.4$ mV (Figure 4.8d). The observed dynamic changes in the ζ values of the self-assembled vesicles as a function of CTAB concentrations clearly indicate sequential and continuous surface passivation of self-assembled vesicles by CTAB molecules. These ζ values not only reveal the effective surface potentials of self-assembled vesicles, but also provide insight into the structural arrangements of individual components. On the basis of our experimental findings we have proposed a schematic model for the observed self-assembly process and subsequent phase behavior of the QD-CTAB binary mixture (Scheme 4.1).



Scheme 4.1. Schematic representation of the self-assembly processes in the QD-CTAB binary mixture.

In the C1 region of the phase profile, individual negatively charged QD forms ion-pairs with positively charged CTAB. With increase in the CTAB concentrations in the C1 region more surfactants bind at each QD surface via electrostatic interactions. These initial QD-CTAB ion-pair complexes are unstable intermediates in aqueous medium due to their exposed hydrophobic surfactant chains (Scheme 4.1, C1). These partially charge-neutralized surfactant-stabilized QDs subsequently form non-specific aggregates via association of their hydrophobic surfactant chains (Scheme 4.1, C1). The significant PL quenching with red-shifted PL peak observed in the PL measurement is mainly due to the aggregation of these initial surfactant-stabilized QDs. Upon further increase in the CTAB concentration (~ 0.08 mM), the aggregated surfactant-stabilized QDs self-assemble into spherical vesicles with size in the range of 100-700 nm. Notably, these self-assembled vesicles are quite stable in aqueous medium and don't show turbidity even after 2-3 weeks. The outer and inner surface of these vesicles contains partially charge-neutralized self-assembled QDs. The increase in ζ from -13.9 ± 0.5 to -24.4 ± 2.8 mV in the presence of 0.08 mM CTAB with the

observation of uniform spherical vesicles in SEM measurements strongly validates this proposed structure. Beyond 0.08 mM CTAB, the binary mixture turns turbid indicating the formation of supramolecular self-assembled structure. At 0.2 mM CTAB, AFM measurements reveal the presence of larger-sized vesicles in the size range of 100-1200 nm. These larger-sized vesicles are formed via fusion of smaller size vesicles observed at 0.08 mM CTAB. Importantly, the ζ value of vesicles observed in the T1 region (0.2 mM) is lower than that observed at 0.08 mM CTAB concentration. This observation clearly indicates further surface passivation and subsequent charge neutralization of exposed negatively charged QD surface by excess CTAB in the self-assembled vesicles. As a consequence of this charge neutralization process with increasing concentration of CTAB, these vesicles become unstable in solution and undergo precipitation in the concentration range of 0.4-0.6 mM CTAB. Here it is important to mention that at this concentration range the negatively charged QD surface is fully passivated by positively charged CTAB molecules and as a result the ζ value approaches 0. With further increase in the CTAB concentration, these precipitates re-dispersed in solution and result in turbid solution. Observation of uniform vesicles with ζ of $+12 \pm 1.5$ mV suggests the formation of cationic vesicles where surfactant-passivated QDs self-assembled in such a way that both the outer and inner surfaces of self-assembled vesicles have positively charged CTAB molecules (Scheme 4.1, T2 region). Finally, at very high CTAB concentration (C2 region), these self-assembled cationic vesicles dissociate into smaller sized clusters as a consequence of significant electrostatic repulsion with the positively charged free micelles. Notably, the estimated ζ at C2 region is close to that reported for free CTAB micelle [24]. Here it would be interesting to compare our present findings with those obtained by Sun *et al.* in their recent report on fluorescence vesicle formation by negatively charged surfactants and positively charged CQDs.³⁹ Although, our proposed model matches closely with their results in the T1, P, and T2 region of the phase profile, differences have been observed in the C1 and C2 region. The reported ζ value of CQDs was $+19.28 \pm 1.68$

mV and upon addition of anionic surfactant they observed a continuous decrease of ζ which finally becomes negative in the T2 region [15]. These findings are uncorrelated with their proposed model of positively charged self-assembled vesicles at the initial concentrations of surfactants in the T1 region. In contrast, our findings reveal that the ζ of self-assembled vesicles formed at the initial phase in the T1 region is highly negative (-24.4 ± 2.8 mV) compared to that of bare QDs (-13.9 ± 0.5 mV). This finding is quite expected as partially charge-neutralized surfactant-stabilized QDs self-assembled to form supramolecular vesicles. Furthermore, at high surfactant concentrations, they proposed the formation of giant micelles where each surfactant-encapsulated CQD was covered by another surfactant layer [15]. In contrast, our PL spectroscopy and imaging results in combination with ζ measurements reveal the presence of small clusters of aggregated QDs along with free CTAB micelles. Nevertheless, the mechanism of self-assembly in the present QD-CTAB binary mixture matches closely with that reported earlier for oppositely-charged CQDs-surfactant mixture [15]. Next, we have performed confocal imaging to unambiguously establish the fact that these vesicles contain self-assembled QDs.

4.2.4. Confocal Imaging of the Luminescent Vesicles and Encapsulation of Rh6G

Laser scanning confocal microscopy has been performed to directly visualize the luminescence of QDs from the self-assembled vesicles (Figure 4.9).

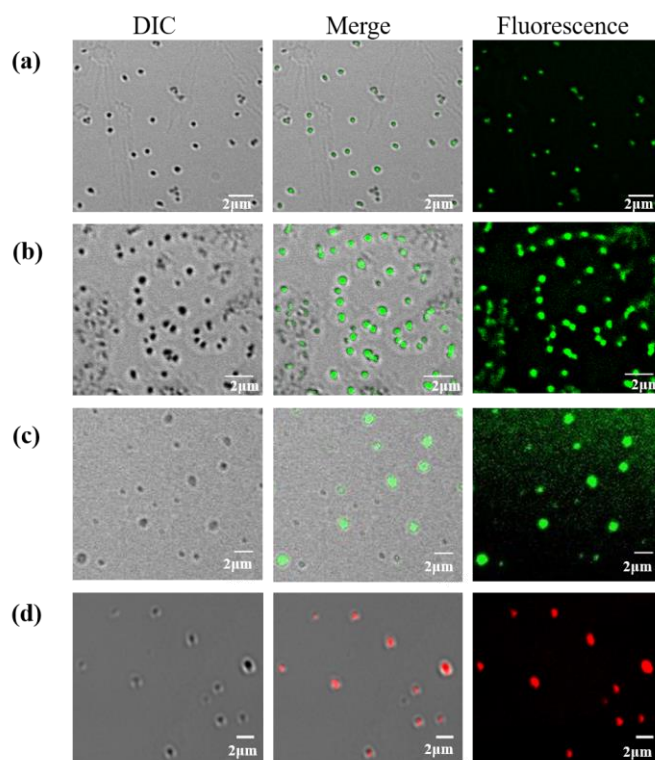


Figure 4.9. Confocal microscopy images of green QDs in the presence of (a) 0.08 mM, (b) 0.2 mM, and (c) 1.5 mM CTAB. Pink arrows indicate fusion of vesicles. (d) Confocal microscopy images of red QDs in the presence of 0.5 mM CTAB.

samples were drop-casted on cleaned glass slides and excited with a 488 nm diode laser. Confocal imaging has been performed at three different CTAB concentrations namely, 0.08, 0.2, and 1.5 mM. At 0.08 mM CTAB, the DIC image reveals the presence of distinct spherical vesicles similar to those observed earlier in SEM measurements (Figure 4.9a). Moreover, intense green luminescence has also been observed from the sample. The merge image reveals that the luminescence appears exclusively from the self-assembled vesicles. Similar green luminescence from self-assembled vesicles has also been observed in the presence of 0.2 and 1.5 mM CTAB (Figure 4.9 b&c). Characteristic fusion phenomena of these luminescent vesicles have been observed irrespective of the CTAB concentrations (Figure 4.10, red arrows).

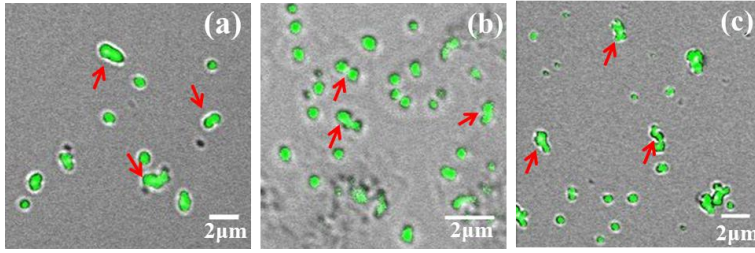


Figure 4.10. Confocal images of the binary mixture in the presence of (a) 0.08, (b) 0.2, and (c) 1.5 mM CTAB showing fusion events with various fusion intermediates (Red arrows showing few representative fusion events).

These observations unambiguously establish the presence of luminescent QDs inside these self-assembled vesicles. Moreover, our control experiment reveals that the presence of both QD and CTAB are essential for the fabrication of these luminescent vesicles.

In order to explore the possibility of fabricating multicolor luminescent vesicles with the present QD-CTAB binary mixture, we have synthesized a larger sized (~ 3.9 nm) MSA-capped CdTe QDs having emission at the red region (~ 650 nm, see Figure 3.1e in chapter 3) of the electromagnetic spectrum [20]. The observed phase profile of the red QD-CTAB binary mixture differs slightly from that of green QD-CTAB binary mixture, which is expected due to the differences in the size of QDs [25]. The red QD-CTAB binary mixture at 0.5 mM CTAB exhibits turbidity and falls in the T1 region of the phase profile. Figure 4.9d shows the confocal images of this binary mixture. Clear self-assembled vesicles have been observed in the DIC image. Moreover distinct red luminescence from these vesicles is clearly evident from the merge image. These results reveal that the fabrication of multicolor luminescent vesicles is indeed possible by simple tuning of the QD size in the QD-CTAB binary mixture.

Vesicles contain hollow aqueous cavity and act as nanocarriers [2-4]. In order to explore the hollow nature of the present hybrid vesicles, we have investigated the possibility of encapsulation of a

model cationic water soluble fluorescent dye, namely Rh6G inside these vesicles by using confocal imaging. The reason for using Rh6G as a model dye is due to its high water solubility and highly intense red emission which is well separated from the green PL of QDs. Vesicles formed in the T2 region (1.5 mM CTAB) were incubated with 0.11 nM Rh6G in aqueous medium for 24 h. After incubation, the mixture was dialyzed against Milli-Q water for overnight to remove excess free Rh6G. The dialyzed mixture was used for subsequent confocal imaging. Images were recorded upon excitation with a 488 nm diode laser and the luminescence was collected at green and red channel with appropriate emission filters. DIC image reveals the presence of spherical vesicles, which are similar to those observed earlier (Figure 4.11).

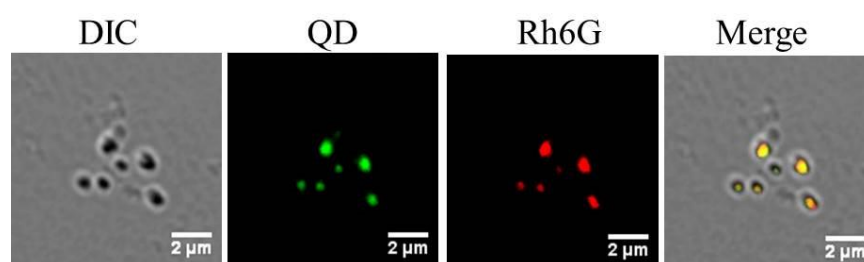


Figure 4.11. Confocal microscopy images showing encapsulation of Rh6G dye inside the self-assembled vesicles formed in the presence of 1.5 mM CTAB.

While the confocal image of the green channel shows distinct green luminescence from self-assembled QDs inside the vesicle, the red channel reveals localized bright red fluorescence signal from Rh6G. The merge image of the green and red channels with that of DIC image shows distinct yellow color luminescence spots from these self-assembled hybrid vesicles. The yellow signals clearly indicate the presence of Rh6G inside the aqueous cavity of these hybrid vesicles. The observed dye encapsulation occurs mainly via passive diffusion mechanism through the vesicle membrane [3]. Next, the pH-responsive behavior of these vesicles has been explored.

4.2.5. pH-Responsive Reversible Assembly and Disassembly of Luminescent Vesicles

The pH-triggered controlled release of vesicle-encapsulated drug is a promising strategy for the specific intracellular delivery of chemotherapeutic drugs. Therefore, the pH-responsive behavior of the present hybrid vesicles has been explored using SEM and confocal imaging. Figure 4.12a shows the daylight photographs of QD-CTAB binary mixture in the T2 region (1.5 mM CTAB) at pH 7.5 and 4.7.

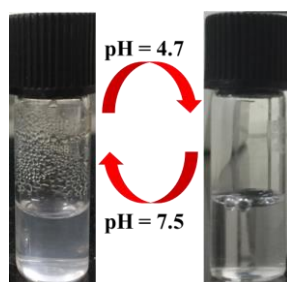


Figure 4.12. Photographs of QD-CTAB binary mixture in the presence of 0.2 mM CTAB (T1 region) at pH 4.7 and 7.5.

At physiological pH (~ 7.5), the binary mixture in the T2 region appears as turbid due to the presence of supramolecular self-assembled vesicles. However, the turbidity of the binary mixture disappears upon lowering the solution pH to 4.7. It is evident from Figure 4.12a that the binary mixture at pH 4.7 is isotropic in nature. PL measurements of this isotropic binary mixture at pH 4.7 reveal significant quenching in the PL intensity as well as lifetime relative to those of free QDs at pH 7.4, indicating aggregation of QDs at acidic pH (Figure 4.13).

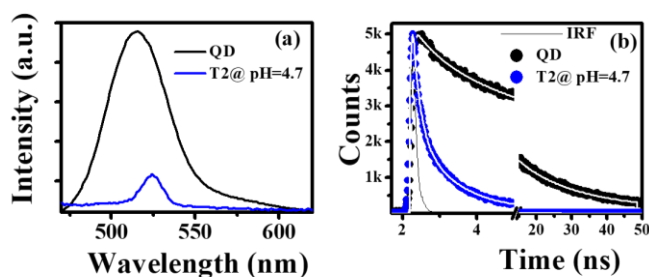


Figure 4.13. (a) PL spectra and (b) PL lifetime decay curves of QD and binary mixture in the T2 region at pH 4.7.

Interestingly, the turbidity reappears upon further increase in the pH from 4.7 to 7.5. While the turbidity of the binary mixture appears in the pH range of 6.5-11, the mixture turns isotropic in the pH range of 4-5.5. This pH-responsive reversible change in the phase behavior clearly indicates structural change of the self-assembled vesicles. Similar changes have been observed in the phase behavior of the binary mixture in the T1 region as a function of solution pH (Figure 4.14). In order to understand the underlying mechanism behind the observed pH-responsive reversible phase behavior, we have performed SEM and confocal imaging. The SEM image of the turbid binary mixture at pH 7.5 shows well-defined vesicles in the T2 region with size in the range of 200-900 nm (Figure 4.14b), which are similar to those observed earlier. However, SEM image of the same binary mixture at pH 4.7 reveals disassembled vesicle structures which arise mainly from the random QD-surfactant aggregates/clusters (Figure 4.14c). Importantly, further increase in pH from 4.7 to 7.5 results in the reappearance of turbidity. Figure 4.14d shows the SEM image of the turbid binary mixture at pH 7.5.

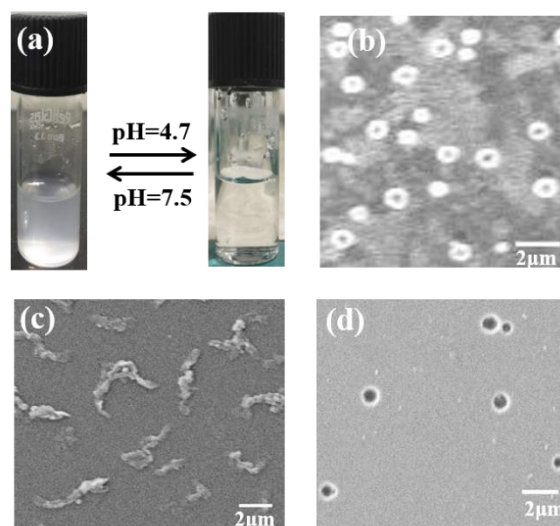


Figure 4.14. (a) Photographs of QD-CTAB binary mixture at pH 4.7 and 7.5 in the presence of 1.5 mM CTAB. FESEM images QD-CTAB binary mixture at pH (b) 7.5, (c) 4.7 and, (d) 7.5 in the presence of 1.5 mM CTAB.

The reappearance of uniform spherical vesicles in the size range between 400-1000 nm is clearly evident. These observations clearly indicate the pH-responsive reversible assembly-disassembly process of these vesicles. Similar reversible assembly-disassembly process of the vesicles in the T1 region has been observed in SEM measurements (Figure 4.15).

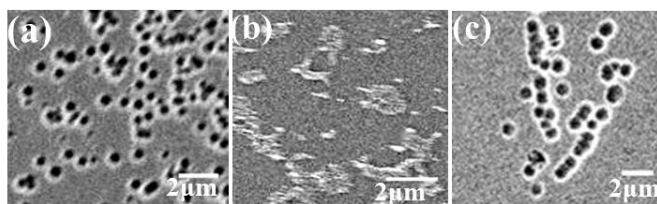


Figure 4.15. FESEM images of QD-CTAB binary mixture in the presence of 0.2 mM CTAB upon continuous change in pH from (a) 7.5, (b) 4.7, and (c) 7.5.

In order to explore the pH-responsive changes in the luminescence properties during this assembly-disassembly process, we have performed CLSM measurements. The confocal images of the binary mixture at pH 7.5 reveal the presence of uniform spherical vesicles with characteristic green luminescence (Figure 4.16a). In contrast, disassembled vesicles are clearly visible in the DIC image of the binary mixture at pH 4.7 (Figure 4.16b). In addition, the merge image shows that the green luminescence exclusively originates from these disassembled vesicle structures suggesting the presence of aggregated QDs in the cluster of surfactants (Figure 4.16b). Reappearance of uniform spherical vesicles with intrinsic green luminescence has been observed upon further increase in the solution pH from 4.7 to 7.5 (Figure 4.16c).

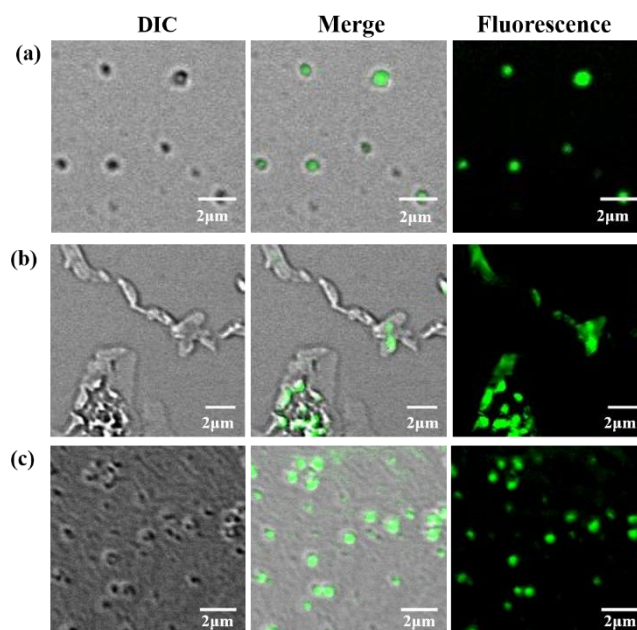


Figure 4.16. Confocal microscopy images of QD-CTAB binary mixture in the presence of 1.5 mM CTAB upon continuous change in pH from (a) 7.5, (b) 4.7, and (c) 7.5.

Similar results have been observed in the T1 region of the binary mixture (data not shown). These observations clearly indicate pH dependent dynamic changes in the structural arrangements of QDs and CTAB inside the self-assembled vesicles. Notably, these supramolecular spherical vesicles are formed due to the self-assembly of initial ion-pairs between oppositely charged QD and CTAB. While the surface of QDs contains negatively charged carboxylate ions, the positively charged CTAB contains quaternary ammonium ion. The reported pK_a values of the two carboxylic acid groups of succinic acid are 4.19 and 5.64 [26]. Therefore, at acidic pH (~ 4.0 - 5.5), the surface carboxylate groups of MSA get protonated and the ion-pair interactions with positively charged CTAB get weaker. Moreover, it is important to note that the stability of the self-assembled vesicles observed in the present study arises mainly due to the balance between hydrophobic and electrostatic interactions. At acidic pH (~ 4.0 - 5.5), this balance gets significantly

modulated due to the protonation of surface carboxylate groups of QDs and the vesicles become unstable. However, upon further increase in the pH (~6.5-11) results in deprotonation of surface carboxylic acid groups of QDs and restore the equilibrium between hydrophobic and electrostatic interactions in the self-assembled vesicles. The observed pH-responsive reversible change in the structure of these luminescent hybrid vesicles can have potential applications in sensing and bio-imaging. By considering the small size of these QDs along with very low effective concentrations of both the constituents, we believe that these hybrid vesicles will be biocompatible. However, their cytotoxicity effect needs to be investigated thoroughly before any in vivo applications. Our group is currently exploring the possibility of utilizing these hybrid vesicles for drug-delivery and bio-imaging applications.

4.3. Conclusions

In this chapter, we have systematically studied the interaction of negatively charged CdTe QDs with CTAB surfactants using various spectroscopic and microscopic techniques and demonstrated the fabrication of pH-responsive stable multicolor luminescent hybrid vesicles from QD-CTAB binary mixture. It has been observed that the self-assembly of initial ion-pairs between QDs and CTAB leads to the formation of supramolecular vesicles. As a consequence of gradual surface passivation of QDs by CTAB, the ζ -value of self-assembled vesicles changes continuously and five different phases have been observed in the concentration range of 0.01-10 mM CTAB. In addition, we have also shown fabrication of multicolor luminescent vesicles by simple tuning of QD size. The encapsulation property of these hybrid vesicles has been illustrated by loading Rh6G dye inside their hollow aqueous cavity. While, these hybrid vesicles are stable in neutral and basic pH (pH~ 6.5-11), they disassemble in acidic pH (pH~4.5-5.5). Furthermore, using SEM and confocal imaging we have shown that this pH-responsive assembly-disassembly process is reversible. The present findings clearly highlight the potential of these hybrid vesicles for various applications such as drug delivery and sensing.

Note: This is copyrighted material from permission of the American Chemistry Society.

4.5 References

1. Shum, H. C., Lee, D., Yoon, I., Kodger, T., Weitz, D. A. (2008), Double emulsion templated monodisperse phospholipid vesicles. *Langmuir*, *24*, 7651-7653. (DOI:10.1021/la801833a)
2. Barenholz, Y., Gibbes, D., Litman, B. J., Goll, J., Thompson, T. E., Carlson, F. D. (1977), A simple method for the preparation of homogeneous phospholipid vesicles. *Biochemistry*, *16*, 2806-2810. (DOI: 10.1021/bi00631a035)
3. Pattni, B. S., Chupin, V. V., Torchilin, V. P. (2015), New developments in liposomal drug delivery. *Chem. Rev.*, *115*, 10938-10966. (DOI: 10.1021/acs.chemrev.5b00046)
4. Soussan, E., Cassel, S., Blanzat, M., Rico-Lattes, I. (2009), Drug delivery by soft matter: Matrix and vesicular carriers. *Angew. Chem. Int. Ed.*, *48*, 274-288. (DOI: 10.1002/anie.200802453)
5. Lee, S.-M., Nguyen, S. T. (2013), Smart nanoscale drug delivery platforms from stimuli-responsive polymers and liposomes. *Macromolecules*, *46*, 9169-9180. (DOI: 10.1021/ma401529w)
6. Sweet, L. J., Wilden, P. A., Spector, A. A., Pessin, J. E. (1985), Incorporation of the purified human placental insulin receptor into phospholipid vesicles. *Biochemistry*, *24*, 6571-6580. (DOI: 10.1021/bi00344a040)
7. Kong, F., Zhang, X., Hai, M. (2014), Microfluidics fabrication of monodisperse biocompatible phospholipid vesicles for encapsulation

and delivery of hydrophilic drug or active compound. *Langmuir*, *30*, 3905-3912. (DOI: 10.1021/la404201m)

8. Backer, J. M., Dawidowicz, E. A. (1981), Mechanism of cholesterol exchange between phospholipid vesicles. *Biochemistry*, *20*, 3805-3810. (DOI: 10.1021/bi00516a021)

9. Vaishnav, J. K., Mukherjee, T. K. (2017), Tuning of resonance energy transfer from 4',6-diamidino-2-phenylindole to an ultrasmall silver nanocluster across the lipid bilayer. *Phys. Chem. Chem. Phys.*, *19*, 27305-27312. (DOI: 10.1039/C7CP05225A)

10. Tu, Y., Peng, F., Adawy, A., Men, Y., Abdelmohsen, L. K. E. A. Wilson, D. A. (2016), Mimicking the cell: Bio-inspired functions of supramolecular assemblies. *Chem. Rev.*, *116*, 2023-2078. (DOI: 10.1021/acs.chemrev.5b00344)

11. McNamara, K. P., Rosenzweig, Z. (1998), Dye-encapsulating liposomes as fluorescence-based oxygen nanosensors. *Anal. Chem.*, *70*, 4853-4859. (DOI: 10.1021/ac9803232)

12. Zhang, Y., Li, S., Zhao, Z. (2016), Using nanoliposomes to construct a FRET-based ratiometric fluorescent probe for sensing intracellular pH values. *Anal. Chem.*, *88*, 12380-12385. (DOI: 10.1021/acs.analchem.6b03632)

13. Discher, D. E., Eisenberg, A. (2002), Polymer vesicles. *Science*, *297*, 967-973. (DOI: 10.1126/science.1074972)

14. Discher, B. M., Won, Y.-Y., Ege, D. S., Lee, J. C.-M., Bates, F. S., Discher, D. E., Hammer, D. A. (1999), Polymersomes: Tough vesicles made from diblock copolymers. *Science*, *284*, 1143-1146. (DOI: 10.1126/science.284.5417.1143)

15. Sun, X., Zhang, Q., Yin, K., Zhou, S., Li, H. (2016), Fluorescent vesicles formed by simple surfactants induced by oppositely-charged carbon quantum dots. *Chem. Comm.*, 52, 12024-12027. (DOI: 10.1039/C6CC05783G)
16. Sun, X., Chen, M., Zhang, Y., Yin, Y., Zhang, L., Li, H., Hao, J. (2018), Photoluminescent and pH-responsive supramolecular structures from co-assembly of carbon quantum dots and zwitterionic surfactant micelles. *J. Mater. Chem. B*, 6, 7021-7032. (DOI: 10.1039/C8TB00630J)
17. Lacerda, S. H. D. P., Park, J. J., Meuse, C., Pristiniski, D., Becker, M. L., Karim, A., Douglas, J. F. (2010), Interaction of gold nanoparticles with common human blood proteins. *ACS Nano*, 4, 365-379. (DOI: 10.1021/nn9011187)
18. Mukherjee, T. K., Mishra, P. P., Datta, A. (2005), Photoinduced electron transfer from chlorin p6 to methyl viologen in aqueous micelles. *Chem. Phys. Lett.*, 407, 119-123. (DOI: 10.1016/j.cplett.2005.03.055)
19. Wang, Y.-Y., Xiang, X., Yan, R., Liu, Y., Jiang, F.-L. (2018), Förster resonance energy transfer from quantum dots to rhodamine B as mediated by a cationic surfactant: A thermodynamic perspective. *J. Phys. Chem. C*, 122, 1148-1157. (DOI: 10.1021/acs.jpcc.7b08236)
20. Vaishnav, J. K., Mukherjee, T. K. (2018), Long-range resonance coupling-induced surface energy transfer from CdTe quantum dot to plasmonic nanoparticle. *J. Phys. Chem. C*, 122, 28324-28336. (DOI: 10.1021/acs.jpcc.8b08757)
21. 49. Rogach, A. L., Franzl, T., Klar, T. A., Feldmann, J., Gaponik, N., Lesnyak, V., Shavel, A., Eychmüller, A., Rakovich, Y. P., Donegan, J. F. (2007), Aqueous synthesis of thiol-capped CdTe nanocrystals:

state-of-the-art. *J. Phys. Chem. C*, *111*, 14628-14637. (DOI: 10.1021/jp072463y)

22. Nikolic, M. S., Olsson, C., Salcher, A., Kornowski, A., Rank, A., Schubert, R., Frömsdorf, A., Weller, H., Förster, S. (2009), Micelle and vesicle formation of amphiphilic nanoparticles. *Angew. Chem. Int. Ed.*, *48*, 2752-2754. (DOI: 10.1002/anie.200805158)

23. Chatterjee, S., Mukherjee, T. K. (2013), Size-dependent differential interaction of allylamine-capped silicon quantum dots with surfactant assemblies studied using photoluminescence spectroscopy and imaging technique. *J. Phys. Chem. C*, *117*, 10799-10808. (DOI: 10.1021/jp402408d)

24. 51. Ghosh, S., Roy, A., Banik, D., Kundu, N., Kuchlyan, J., Dhir, A., Sarkar, N. (2015), How does the surface charge of ionic surfactant and cholesterol forming vesicles control rotational and translational motion of rhodamine 6G perchlorate (R6G ClO₄)? *Langmuir*, *31*, 2310-2320. (DOI: 10.1021/la504819v)

25. Liu, Y., Li, Y., He, J., Duelge, K. J., Lu, Z., Nie, Z. (2014), Entropy-driven pattern formation of hybrid vesicular assemblies made from molecular and nanoparticle amphiphiles. *J. Am. Chem. Soc.*, *136*, 2602-2610. (DOI: 10.1021/ja412172f)

26. Chirea, M., García-Morales, V., Manzanares, J. A., Pereira, C., Gulaboski, R., Silva, F. (2005), Electrochemical characterization of polyelectrolyte/gold nanoparticle multilayers self-assembled on gold electrodes. *J. Phys. Chem. B*, *109*, 21808-21817. (DOI: 10.1021/jp0537815)

Chapter 5

*Tuning of Resonance Energy Transfer from
4',6-Diamidino-2-Phenylindole to an
Ultrasmall Silver Nanocluster Across the
Lipid Bilayer*

5.1. Introduction

Efficient tuning of FRET efficiency as a function of separation distance is of fundamental importance. Covalent attachment of a donor and an acceptor with suitable spacers is the most conventional method for exploring intramolecular FRET [1-4]. On the other hand, tuning of intermolecular FRET has been demonstrated in various systems such as micelles [5,6], reverse micelles [7,8], polymer matrices [9,10], spherical vesicles [11,12], and proteins [13,14]. Among these, FRET processes across the liposome bilayer are of particular interest due to its potential in exploring various membrane related biophysical processes such as membrane fusion, trafficking, and receptor–ligand interactions.

The lipid bilayer of liposomes is one of the simplest model systems to understand various fundamental processes at the cell membrane by using FRET. For example, Yoon *et al.* have demonstrated real-time liposome fusion dynamics in a single fusion event using a single molecule FRET technique [18]. Yefimova *et al.* have studied the dynamics of interaction between liposomes and living cells using FRET [19]. FRET has also been used to study the interaction of DNA with liposome during lipoplex formation [20]. While these studies have illustrated the potential of FRET in elucidating various fundamental biophysical processes across the lipid bilayer, it is equally important to develop a new donor–acceptor pair that can probe the nanoscopic distance at the bilayer thickness. Herein, we have developed a liposome-based FRET pair between DAPI and an ultrasmall ligand-capped Ag NC and have shown that the FRET efficiency is strongly dependent on the location of donor DAPI within the dipalmitoylphosphatidylcholine (DPPC) liposome matrix. DAPI is soluble in aqueous buffer and undergoes rapid excited-state intramolecular proton transfer and shows strong binding affinity towards a variety of hydrophobic environments [21]. In the present study, a DAPI–liposome complex has been prepared using two distinct procedures. In the first method, DAPI is mixed with preformed liposomes in aqueous buffer (method I), while in the second method liposomes are prepared by adding ethanolic stock solution of

lipid into the aqueous solution of DAPI (method II). The aim of the present study is to explore this nonradiative FRET process between DAPI and the Ag NC across the lipid bilayer of small unilamellar vesicles (SUV) of DPPC.

5.2. Results and Discussion

5.2.1. Characterization of Liposomes and Ag NC

The morphology and mean size of synthesized liposome have been estimated from scanning electron microscopy (SEM) and dynamic light scattering (DLS) measurements. The SEM image shows that the vesicles are spherical in shape with an average diameter of 75.77 ± 24.46 nm (Figure 5.1a and b). The DLS measurement reveals that the vesicles have a mean hydrodynamic diameter of 86.91 ± 6.41 nm (Figure 5.1c). These results indicate that the synthesized liposomes are small unilamellar vesicles (SUV).

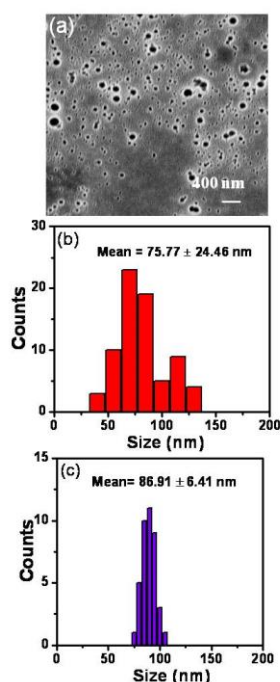


Figure 5.1. (a) SEM image of liposome. Size distribution histogram of liposomes estimated from (b) SEM and (c) DLS measurements.

The capping of the DHLA ligand on the surface of the Ag NC has been established by using FTIR spectroscopy (Figure 5.2). The S–H stretching frequency of free DHLA at 2574 cm^{-1} disappears upon binding with the Ag NC surface.

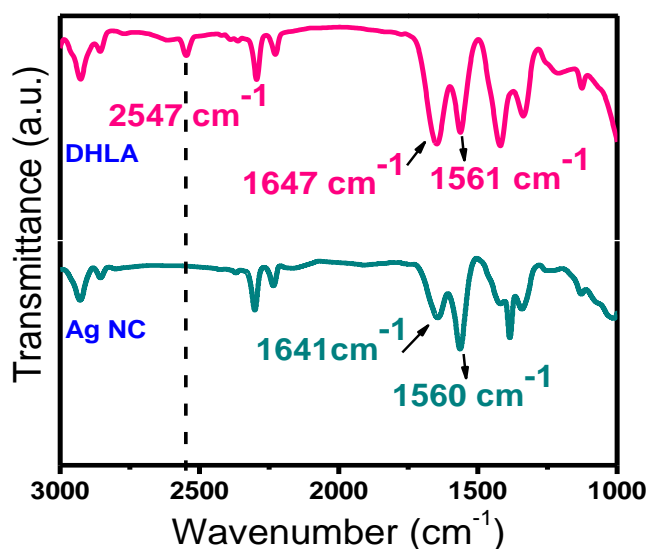


Figure 5.2. FTIR spectra of dihydrolipoic acid (DHLA) and synthesized DHLA-capped Ag NC.

The synthesized Ag NCs are spherical in shape with an average diameter of $1.5 \pm 0.22\text{ nm}$ (Figure 5.3a). The ESI-mass spectrum of the DHLA capped Ag NC is recorded in a 1:1 water–methanol mixture (Figure 5.3b). The major peak at m/z 477.80 corresponds to the $[\text{Ag}_4 + 2\text{Na}]^+$ cluster and the peak at m/z 578.03 corresponds to the $[\text{Ag}_5 + \text{K}]^+$ cluster. The mass spectrum of these Ag NCs correlates well with the earlier reports [21, 22]. The absorption spectrum of the DHLA-capped Ag NC reveals two intense peaks at 329 and 426 nm and a shoulder at 497 nm, and characteristics of molecular-like electronic transitions (Figure 5.3c). These bands originate due to various intra and inter band electronic transitions [23, 24]. These Ag NCs show an emission maximum at 675 nm upon excitation at 375 nm (Figure 5.3c). The excitation spectrum of

the Ag NC at 675 nm emission wavelength reveals multiple peaks centered at 331, 425, and 497 nm similar to its absorption spectrum.

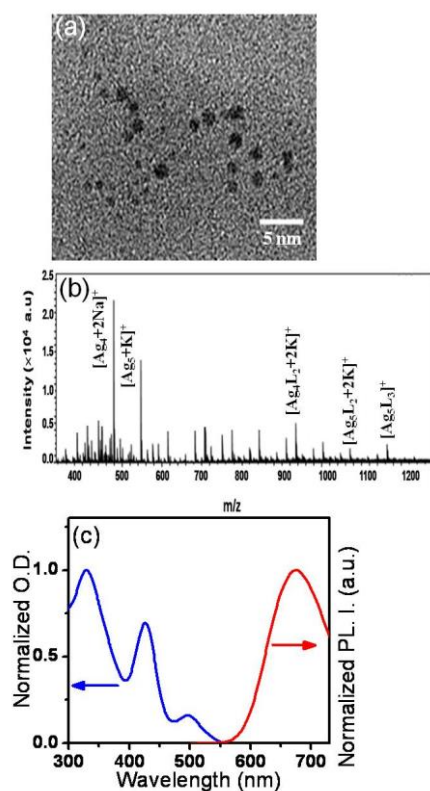


Figure 5.3. (a) HRTEM image of Ag NC. (b) Electrospray ionization (ESI) mass spectrum of DHLA-capped Ag NC in 1:1 water-methanol mixture (L represents DHLA ligand). (c) The normalized absorption (blue line) and PL (red line) spectra of Ag NC.

5.2.2. Interaction of DAPI with Ag NC and Liposomes

As a consequence of significant spectral overlap (Figure 5.4a) between the emission and absorption spectrum of DAPI and the Ag NC, respectively, they form an excellent FRET pair in aqueous solution as demonstrated in our earlier report [21].

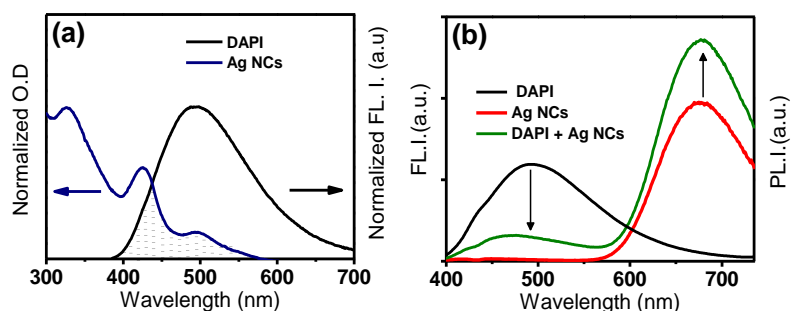


Figure 5.4. (a) Normalized absorption spectrum of Ag NC (blue line) and fluorescence spectrum (black line) of 2.5 μM DAPI ($\lambda_{\text{ex}} = 375 \text{ nm}$). The black dotted region shows the spectral overlap between the absorption spectrum of Ag NC and fluorescence of DAPI. (b) Changes in the emission spectra of DAPI (black line) and Ag NC (red line) upon mixing (green line). The excitation wavelength is 375 nm.

In aqueous buffer, the fluorescence intensity of DAPI at 492 nm quenches significantly in the presence of the Ag NC with a concomitant PL enhancement of the Ag NC at 675 nm (Figure 5.4 b). Previously, we have shown that the excited-state fluorescence lifetime of DAPI decreases from 81.50 ps to 3.71 ps in the presence of the Ag NC due to nonradiative FRET [21]. The efficiency (ϕ_{eff}) of this nonradiative FRET process is calculated to be 76%, which matches well with our earlier report [21]. The aim of the present study is to explore the influence of zwitterionic DPPC liposome on this nonradiative FRET process between DAPI and the Ag NC.

Confocal laser scanning microscopy (CLSM) has been performed to directly visualize the location of DAPI inside the liposome matrix. Images were recorded upon excitation with a 405 nm diode laser. Distinct blue fluorescence has been observed from the DAPI–liposome complex (Figure 5.5, right panel).

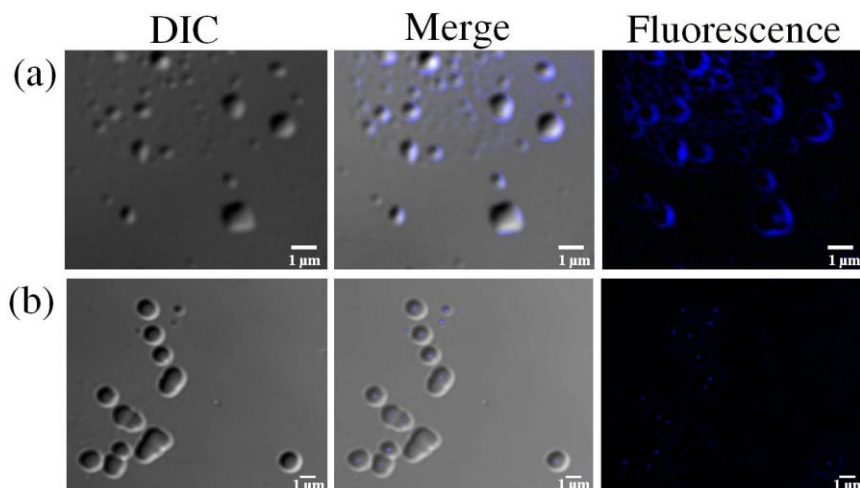


Figure 5.5. Confocal microscopy images of (a) complex I (surface) and (b) complex II (core).

The merged image shows that the blue fluorescence of the DAPI–liposome complex prepared by method I localizes mainly at the liposome surface (Fig. 5.5a). In contrast, the blue fluorescence of the DAPI–liposome complex prepared by method II localizes mainly at the centre of the liposomes (Fig. 5.5 b). The image of the DAPI–liposome complex prepared by method I indicates that DAPI specifically interacts with the liposome surface *via* favourable electrostatic interaction between positively charged DAPI and zwitterionic lipid head groups. A similar kind of association of DAPI with the negatively charged micellar surface has been reported earlier [25]. However, the image of the DAPI–liposome complex prepared by method II reveals that DAPI molecules are entrapped inside the confined water pool of liposomes and may interact electrostatically with the inner head groups of lipids. These observations clearly indicate that the DAPI–liposome complexes prepared by both the methods attain equilibrium with our present experimental conditions. In our subsequent discussion, the DAPI–liposome complex prepared by method I will be referred as complex I (surface) and the same prepared by method II will be referred as complex II (core).

5.2.3. Interaction of Complex I (Surface) with Ag NC

Figure 5.6a displays the changes in the fluorescence spectra of DAPI in complex I (surface) upon addition of the Ag NC. DAPI shows fluorescence maximum at 492 nm ($\lambda_{ex} = 375$ nm) in phosphate buffer of pH 7.4, with a quantum yield of 0.021. The emission maximum of DAPI shifts to 465 nm with a 3-fold enhancement of its quantum yield upon formation of complex I (surface) (Figure 5.6a). The observed fluorescence enhancement with a 27 nm blue-shift of the emission maximum clearly indicates that the dye is associated with the liposome matrix.

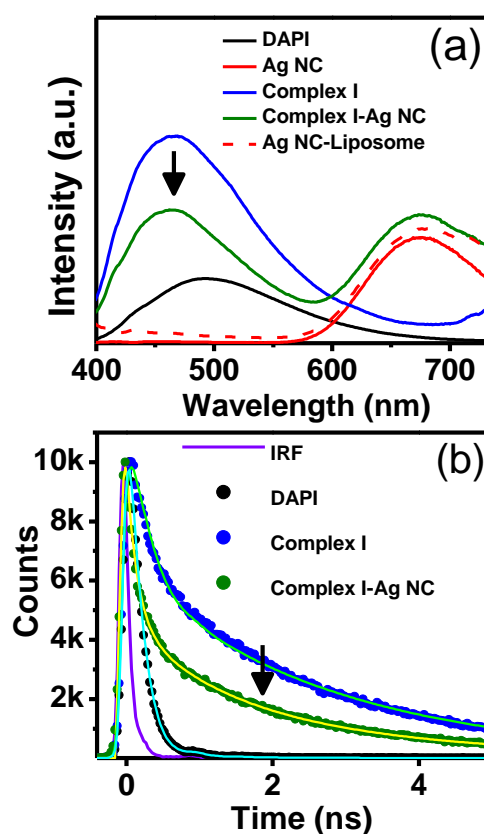


Figure 5.6. (a) Changes in the fluorescence spectra ($\lambda_{ex} = 375$ nm) of DAPI in complex I (surface) upon addition of Ag NC. (b) Fluorescence decay traces of complex I (surface) in the absence and presence of Ag NC.

A similar blue shift in the emission spectrum of DAPI has been observed in the presence of various nonpolar systems such as micelles, reverse

micelles, DNA, and cyclodextrins due to its association with relatively less polar microenvironments than the bulk aqueous medium [25,26]. On the other hand, the enhancement observed in the fluorescence quantum yield of DAPI is due to the retarding effect of the less polar microenvironment on the nonradiative water-mediated excited state proton transfer process.

These spectral changes further confirm that the positively charged DAPI is associated with the zwitterionic liposome surface possibly *via* favorable electrostatic interactions. This argument further gains support from our confocal imaging experiment. Subsequent addition of the Ag NC into the DAPI–liposome complex I (surface) results in fluorescence quenching of DAPI with a concomitant increase in the PL intensity of the Ag NC. Notably, the extent of fluorescence quenching is significantly less in the presence of liposome compared to that in its absence, indicating less efficient energy transfer from liposome associated DAPI to aqueous Ag NCs. In order to explore the dynamics of this quenching process, we have performed time-resolved fluorescence measurements. DAPI in aqueous buffer exhibits ultrafast decay kinetics (Figure 5.6b), which is well below our current instrument response function (IRF \sim 140 ps) [21]. However, upon association with the liposome surface the average lifetime increases to 1.23 ns with lifetime components of 0.24 ns (61%) and 2.76 ns (39%) (Figure 5.6b and Table 5.2). This increase in the fluorescence lifetime of DAPI in complex I (surface) further substantiate the fact that DAPI is associated with the less polar liposome surface and as a consequence the nonradiative ESPT process gets retarded. The average fluorescence lifetime of DAPI in complex I (surface) is shortened to 0.77 ns in the presence of the Ag NC (Figure 5.6b and Table 5.2). This shortening of the fluorescence lifetime in the presence of the Ag NC clearly indicates nonradiative resonance excitation energy transfer from liposome-associated DAPI to the Ag NC. However, we could not detect the characteristic rise in time associated with the PL decay of Ag NCs due to limited time resolution (IRF \sim 140 ps) of our current TCSPC

instrument. The Förster distance R_0 for complex I (surface) and Ag NCs has been estimated by using the following equation,

$$R_0 = \left[(8.8 \times 10^{-25}) \left(\kappa^2 n^{-4} \phi_D J(\lambda) \right) \right]^{\frac{1}{6}} \quad (1)$$

where κ^2 is the orientation factor of the transition dipoles of the liposome-associated DAPI and the Ag NC, ϕ_D is the fluorescence quantum yield of DAPI in complex I (surface), n is the refractive index of the medium, and $J(\lambda)$ is the spectral overlap integral between the emission spectrum of complex I (surface) and the absorption spectrum of the Ag NC. Complex I (surface) shows a significant spectral overlap with the absorption spectrum of the Ag NC (Figure 5.7a).

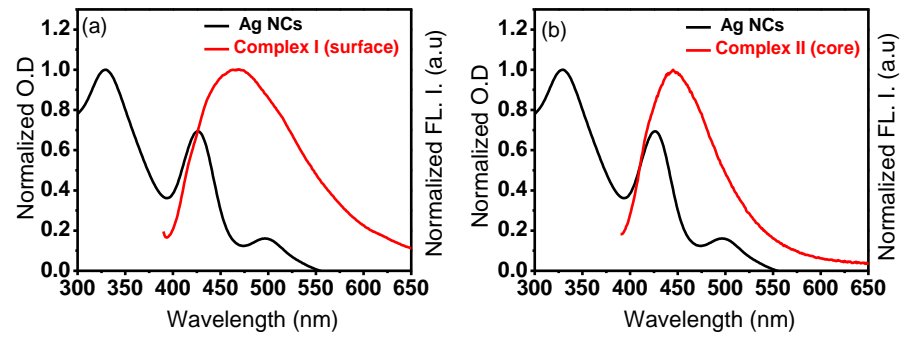


Figure 5.7. Spectral overlap of (a) Complex I (surface)-Ag NC and (b) complex II (core)-Ag NC.

For complex I (surface) and Ag NC pair, the calculated overlap integral is $7.24 \times 10^{-14} \text{ M}^{-1} \text{ cm}^3$ and the estimated R_0 is 2.97 nm (Table 5.1). The efficiency (ϕ_{eff}) of this nonradiative EET process is estimated using the following equation,

$$\phi_{\text{eff}} = 1 - \frac{\phi_{\text{DA}}}{\phi_{\text{D}}} = 1 - \frac{\tau_{\text{DA}}}{\tau_{\text{D}}} \quad (2)$$

where ϕ_{DA} and ϕ_{D} are the quantum yields of donors in the presence and absence of Ag NC, respectively. The parameters τ_{DA} and τ_{D} represent the fluorescence lifetimes of DAPI in the presence and absence of Ag NC, respectively. The estimated energy transfer efficiency (ϕ_{eff}) from steady-state and time-resolved measurements is 0.39 and 0.37, respectively.

Since, these estimated FRET parameters we have calculated the average separation distance between the liposome associated DAPI and the Ag NC by using the following equation,

$$\phi_{\text{eff}} = \frac{1}{1 + \left(\frac{r}{R_0}\right)^6} \quad (3)$$

where ϕ_{eff} is the energy transfer efficiency, R_0 is the Förster distance, and r is the separation distance. The estimated average separation distance between the liposome-associated DAPI and the Ag NC is 3.20 nm (Table 5.1).

Table 5.1. Estimated quantum yields (ϕ_D), spectral overlap integral ($J(\lambda)$), energy transfer efficiency (ϕ_{eff}), Förster distance (R_0) and calculated distance (r) between DAPI and the Ag NC.

System	ϕ_D	$J(\lambda)$ ($\text{M}^{-1} \text{cm}^3$)	ϕ_{eff}	R_0 (nm)	r (nm)
DAPI	0.0210	—	—	—	—
DAPI–Ag NC	0.0050	5.92×10^{-14}	0.76	2.48	2.06
Complex I (surface)	0.0612	—	—	—	—
Complex I (surface)–Ag NC	0.0374	7.24×10^{-14}	0.39	2.97	3.20
Complex II (core)	0.0045	—	—	—	—
Complex II (core)– Ag NC	0.0044	7.87×10^{-14}	0	—	—

On the other hand, the separation distance between DAPI and the Ag NC in bulk aqueous medium is calculated to be 2.06 nm, which matches well with our previous report [44]. Notably, this increase in separation distance (~ 1.14 nm) in the presence of liposome (complex I) is due to the selective association of DAPI with the liposome surface.

Table 5.2. Fluorescence decay parameters of complex I (surface) in the absence and presence of Ag NCs.

System	τ_1 (ns)	a_1	τ_2 (ns)	a_2	$\langle \tau \rangle$ (ns)	χ^2
Complex I (surface)	0.24	0.61	2.76	0.39	1.23	1.19
Complex I (surface)– Ag NC	0.18	0.74	2.45	0.26	0.77	1.20

5.2.4. Interaction of Complex II (Core) and Ag NC

Figure 5.8a shows the changes in the fluorescence spectra of DAPI in complex II (core) upon addition of the Ag NC. The fluorescence maximum of DAPI shifts to 445 nm with significant quenching ($\sim 62\%$) in its fluorescence intensity upon the formation of complex II (core) with DPPC vesicles. In general, DAPI shows blue shift with a concomitant increase in its fluorescence quantum yield upon association with less polar hydrophobic environments [25,26]. However, the present spectral changes reveal significant quenching with 47 nm blue shifts upon the formation of complex II (core). DAPI in complex II (core) mainly remains at the aqueous core of the liposome as revealed earlier in confocal microscopy.

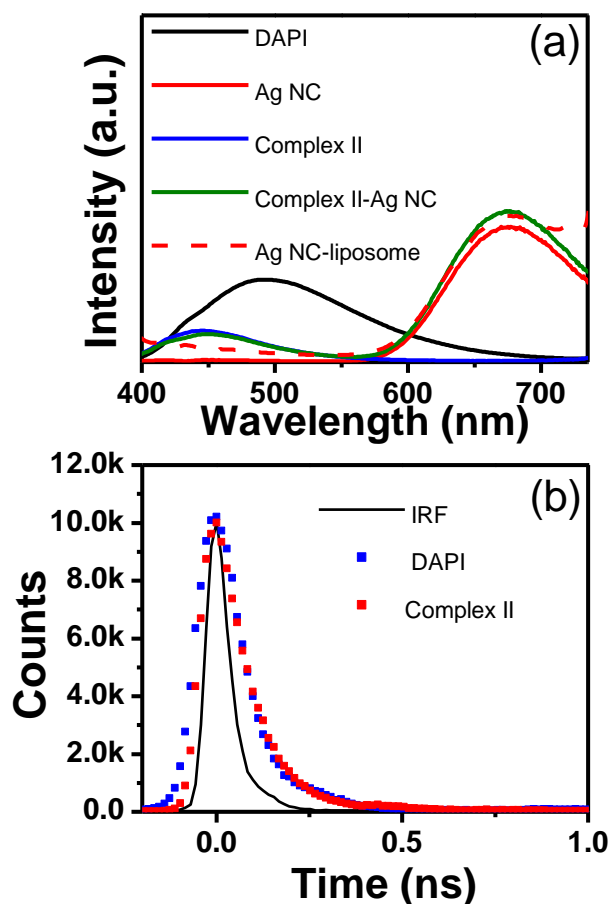
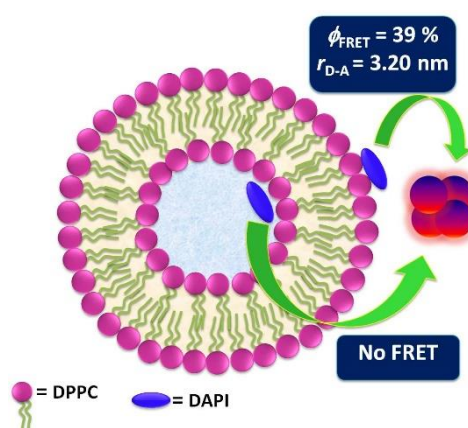


Figure 5.8. (a) Changes in the fluorescence spectra ($\lambda_{\text{ex}} = 375 \text{ nm}$) of DAPI in complex II (core) upon addition of Ag NC. (b) Fluorescence decay traces of DAPI and complex II (core).

Hence, the blue shift of the emission maximum of DAPI in complex II (core) is due to the less polar aqueous core of the DPPC liposome compared to bulk and surface environments. Earlier, Bhattacharyya and co-workers have demonstrated ultraslow solvation dynamics of various dyes inside the liposome matrix using fluorescence spectroscopy [27-29]. It has been shown that the polarity and viscosity of water molecules inside the core of vesicles significantly differ from that of bulk water molecules. On the other hand, the quenching of DAPI fluorescence in complex II (core) can be explained by considering the favorable

nonradiative ESPT process involving confined hydrogen-bonded water molecules at the liposome core. This has further gained support from fluorescence lifetime measurements of DAPI in complex II (core). DAPI in aqueous buffer shows ultrafast fluorescence decay kinetics which is well beyond the time resolution of our current instrument (Figure 5.8b). Notably, the decay curve gets steeper upon the formation of complex II (core) indicating the presence of a nonradiative decay channel due to the ESPT process (Figure 5.7b). Interestingly, no noticeable change in the fluorescence intensity of DAPI in complex II (core) has been observed in the presence of the Ag NC, indicating the lack of nonradiative energy transfer from liposome-encapsulated DAPI to the Ag NC (Figure 5.8a). Similarly, a negligible enhancement in the PL intensity of the Ag NC has been observed. A control experiment shows that this negligible enhancement is not due to FRET from the liposome-encapsulated DAPI to the Ag NC, rather it is due to the weak interaction of the Ag NC with the liposome (Figure 5.7a, dashed line). These results show that the nonradiative FRET from DAPI to the Ag NC completely hinders in complex II (core) due to complete encapsulation of DAPI inside the liposome matrix (Scheme 5.1).



Scheme 5.1. Schematic representation of liposome mediated tuning of FRET between DAPI and Ag NC.

Although the emission spectrum of complex II (core) shows a significant overlap with the absorption spectrum of the Ag NC (Figure 5.8b and Table 5.1), the increase in the separation distance beyond the FRET range (~ 10 nm) results in complete suppression of this EET. Hence, our study highlights that the present donor–acceptor pair (DAPI–Ag NC) has the potential to be used as a FRET marker for understanding various lipid bilayer-associated biophysical processes.

5.3. Conclusions

The present study demonstrates a simple liposome-based tuning of FRET between DAPI and an ultrasmall ligand-capped Ag NC. In aqueous buffer, the Ag NC efficiently quenches the fluorescence of nearby DAPI by a nonradiative FRET process. It has been observed that the efficiency of EET from the liposome bound DAPI to the Ag NC is strongly dependent on the location of the donor DAPI within the liposome matrix. In aqueous buffer, DAPI transfers its excitation energy to the nearby Ag NC with an efficiency of 76%. However, the association of DAPI with the outer surface of the liposome results in lowering of the energy transfer efficiency from a bulk value of 76% to 39%. In contrast, complete encapsulation of DAPI into the hydrophilic aqueous core of the liposome results in complete inhibition of this FRET process. This location specific interaction between DAPI and the Ag NC inside the liposome matrix is important to understand various fundamental biophysical processes across the cell membrane.

Note: This is copyrighted material from permission of the Royal Society of Chemistry.

5.4. References

1. Hayashi, G., Kamo, N., Okamoto, A. (2017), Chemical synthesis of dual labeled proteins via differently protected alkynes enables intramolecular FRET analysis. *Chem. Comm.*, 53, 5918-5921. (DOI: 10.1039/C7CC02612A)
2. Huang, C.-B., Xu, L., Zhu, J.-L., Wang, Y.-X., Sun, B., Li, X., Yang, H.-B. (2017), Real-time monitoring the dynamics of coordination-driven self-assembly by fluorescence-resonance energy transfer. *J. Am. Chem. Soc.*, 139, 9459-9462. (DOI: 10.1021/jacs.7b04659)
3. Li, N., Wang, M., Gao, X., Yu, Z., Pan, W., Wang, H., Tang, B. (2017), A DNA tetrahedron nanoprobe with controlled distance of dyes for multiple detection in living cells and in vivo. *Anal. Chem.*, 89, 6670-6677. (DOI: 10.1021/acs.analchem.7b00889)
4. Bain, D., Paramanik, B., Patra, A. (2017), Silver(I)-induced conformation change of DNA: Gold nanocluster as a spectroscopic probe. *J. Phys. Chem. C*, 121, 4608-4617. (10.1021/acs.jpcc.6b10560)
5. Roy, A., Kundu, N., Banik, D., Sarkar, N. (2016), Comparative fluorescence resonance energy-transfer study in pluronic triblock copolymer micelle and niosome composed of biological component cholesterol: An investigation of effect of cholesterol and sucrose on the FRET parameters. *J. Phys. Chem. B*, 120, 131-142. (DOI: 10.1021/acs.jpcc.5b09761)
6. Choudhury, S., Mondal, P. K., Sharma, V. K., Mitra, S., Sakai, V. G., Mukhopadhyay, R., Pal, S. K. (2015), Direct observation of coupling between structural fluctuation and ultrafast hydration dynamics of fluorescent probes in anionic micelles. *J. Phys. Chem. B*, 119, 10849-10857. (DOI: 10.1021/jp511899q)

7. Mandal, R. P., De, S. (2017), Organized assemblies of AOT determine nanoparticle characteristics and their performance as FRET donors. *Colloids Surf. A*, 528, 10-22. (DOI: 10.1016/j.colsurfa.2017.05.038)
8. Mondal, S. K., Ghosh, S., Sahu, K., Mandal, U., Bhattacharyya, K. (2006), Ultrafast fluorescence resonance energy transfer in a reverse micelle: Excitation wavelength dependence. *J. Chem. Phys*, 125, 224710. (DOI: 10.1063/1.2403131)
9. Rajdev, P., Basak, D., Ghosh, S. (2015), Insights into noncovalently core cross-linked block copolymer micelles by fluorescence resonance energy transfer (FRET) studies. *Macromolecules*, 48, 3360-3367. (DOI: 10.1021/acs.macromol.5b00559)
10. Wu, F., Minter, S. D. (2013), Fluorescence characterization of co-immobilization-induced multi-enzyme aggregation in a polymer matrix using Förster resonance energy transfer (FRET): Toward the metabolon biomimic. *Biomacromolecules*, 14, 2739-2749. (DOI: 10.1021/bm400569k)
11. Trier, S., Henriksen, J. R., Andresen, T. L. (2011), Membrane fusion of pH-sensitive liposomes – A quantitative study using giant unilamellar vesicles. *Soft Matter*, 7, 9027-9034. (DOI: 10.1039/C1SM05818E)
12. Ghatak, C., Rao, V. G., Pramanik, R., Sarkar, S., Sarkar, N. (2011), The effect of membrane fluidity on FRET parameters: an energy transfer study inside small unilamellar vesicle. *Phys. Chem. Chem. Phys.*, 13, 3711-3720. (DOI: 10.1039/C0CP01925A)
13. Das, N. K., Ghosh, N., Kale, A. P., Mondal, R., Anand, U., Ghosh, S., Tiwari, V. K., Kapur, M., Mukherjee, S. (2014), Temperature induced morphological transitions from native to unfolded aggregated

states of human serum albumin. *J. Phys. Chem. B*, *118*, 7267-7276. (DOI: 10.1021/jp5030944)

14. Das, D. K., Mondal, T., Mandal, U., Bhattacharyya, K. (2011), Probing deuterium isotope effect on structure and solvation dynamics of human serum albumin. *ChemPhysChem*, *12*, 814-822. (DOI: 10.1002/cphc.201000912)

18. Yoon, T.-Y., Okumus, B., Zhang, F., Shin, Y.-K., Ha, T. (2006), Multiple intermediates in SNARE-induced membrane fusion. *Proc. Natl. Acad. Sci. U.S.A.*, *103*, 19731-19736. (DOI: 10.1073/pnas.0606032103)

19. Yefimova, S. L., Kurilchenko, I. Y., Tkacheva, T. N., Kavok, N. S., Todor, I. N., Lukianova, N. Y., Chekhun, V. F., Malyukin, Y. V. (2014), Microspectroscopic Study of liposome-to-cell interaction revealed by Förster resonance energy transfer. *J. Fluoresc.*, *24*, 403-409. (DOI: 10.1007/s10895-013-1305-8)

20. Zhang, Y., Garzon-Rodriguez, W., Manning, M. C., Anchordoquy, T. J. (2003), The use of fluorescence resonance energy transfer to monitor dynamic changes of lipid-DNA interactions during lipoplex formation. *Biochim. Biophys. Acta*, *1614*, 182-192. (DOI: 10.1016/s0005-2736(03)00177-9)

21. Prajapati, R., Chatterjee, S., Kannaujiya, K. K., Mukherjee, T. K. (2016), Effect of compartmentalization of donor and acceptor on the ultrafast resonance energy transfer from DAPI to silver nanoclusters. *Nanoscale*, *8*, 13006-13016. (DOI: 10.1039/C6NR01792D)

22. Adhikari, B., Banerjee, A. (2010), Facile synthesis of water-soluble fluorescent silver nanoclusters and HgII sensing. *Chem. Mater.*, *22*, 4364-4371. (DOI: 10.1021/cm1001253)

23. Bakr, O. M., Amendola, V., Aikens, C. M., Wenseleers, W., Li, R., Dal Negro, L., Schatz, G. C., Stellacci, F. (2009), Silver nanoparticles with broad multiband linear optical absorption. *Angew. Chem. Int. Ed.*, *48*, 5921-5926. (DOI: 10.1002/anie.200900298)
24. Bousquet, B., Cherif, M., Huang, K., Rabilloud, F. (2015), Absorption spectra of aryl thiol-coated silver nanoclusters: A time-dependent density-functional study. *J. Phys. Chem. C*, *119*, 4268-4277. (DOI: 10.1021/jp512209p)
25. Banerjee, D., Pal, S. K. (2008), Excited-state solvation and proton transfer dynamics of DAPI in biomimetics and genomic DNA. *J. Phys. Chem. A*, *112*, 7314-7320. (DOI: 10.1021/jp801778e)
26. Sayed, M., Mohanty, J., Bhasikuttan, A. C., Pal, H. (2012), Host-guest interaction of 4',6-diamidino-2-phenylindole (DAPI) with β - and γ -cyclodextrins: Modulation in the photophysical properties. *J. Spectrosc. Dyn.*, *21*, 1-14.
27. Pal, S. K., Sukul, D., Mandal, D., Sen, S., Bhattacharyya, K. (2000), Solvation dynamics of DCM in dipalmitoyl phosphatidylcholine lipid. *Tetrahedron*, *56*, 6999-7002. (DOI: 10.1016/S0040-4020(00)00522-6)
28. Halder, A., Sen, S., Burman, A. D., Patra, A., Bhattacharyya, K. (2004), Solvation dynamics in dimyristoyl-phosphatidylcholine entrapped inside a sol-gel matrix. *J. Phys. Chem. B*, *108*, 2309-2312. (DOI: 10.1021/jp035685e)
29. Dutta, P., Sen, P., Mukherjee, S., Bhattacharyya, K. (2003), Solvation dynamics in DMPC vesicle in the presence of a protein. *Chem. Phys. Lett.*, *382*, 426-433. (DOI: 10.1016/j.cplett.2003.10.091)

Chapter 6

*Long-Range Resonance Coupling-Induced
Surface Energy Transfer from CdTe
Quantum Dot to Plasmonic Nanoparticle*

6.1. Introduction

Understanding and precise control over EET in nanoscale material is utmost important due to enormous importance in fundamental research as well as in various technology-related fields such as photovoltaics [1,2], light-emitting diodes (LEDs) [3,4], sensors [5,6], and bioimaging [7,8]. It has been extensively study the donor-acceptor nanocomposite systems which made of metal and semiconductor NPs due to their size-dependent optoelectronic properties and also allow easy tuning of various energy transfer related parameters [9-22]. Moreover, these nanocomposite systems offer great advantage over conventional dipole-dipole systems by surpassing the limited FRET distance due to the strong near field effect of metal NPs [16-22]. It has often been observed that noble metal NPs with distinct LSPR significantly alter the emission properties of nearby fluorophores via electromagnetic coupling [16-22]. The interaction of metal NP and a nearby dipole is very complex and depends on various factors such as size and shape of the NPs, separation distance, spectral overlap, and orientation of dipole with respect to the NP surface. The electromagnetic field of metal NPs can either enhances or quenches the fluorescence of nearby fluorophores. The LSPR-induced enhancement occurs either due to an increase in the radiative decay rate of fluorophores or the enhanced electromagnetic field at the NP surface and fluorescence quenching occurs due to modulation of either a radiative or a nonradiative decay or both in the presence of metal NPs. To understand the fundamental mechanism behind this long range electromagnetic coupling many experimental and theoretical studies have been conducted. The quenching of excited donor in the presence of metal surface is demonstrated earlier by Chance *et al* [23] and later extended by Persson and Lang by using a Fermi Golden Rule [24]. This dipole-to-metal surface energy transfer is known as surface energy transfer (SET). Although, this SET theory originally developed to explain the interaction of excited dipole near a thin metal surface, it successfully accounts the experimentally observed EET in the presence of small (<2 nm) Au NPs [16-18]. This dipole-to-NP surface EET is known as nonmetal surface energy transfer (NSET). Earlier, Strouse

and coworkers have demonstrated the distance-dependent fluorescence quenching of different dyes attached to 1.5 nm Au NPs and observed a $1/d^4$ distance-dependent quenching behaviour which correlates well with the NSET theory [16-18]. However, the theory failed to predict the experimentally observed radiative and nonradiative rates for oscillating dipole near larger sized NPs [19, 25]. Recently, Breshike *et al.* have demonstrated the validity of original SET theory for Au NPs with diameter in the range of 2-16.5 nm by incorporating the size-dependent absorption and dielectric terms for the Au NPs [26]. Several studies have shown that the intrinsic exciton recombination of quantum dots (QDs) can be efficiently tuned near a plasmonic NP as a consequence of long range electromagnetic coupling between exciton and LSPR of NPs [12,22,27,28] substantial amount of work have been executed to understand the interaction of oscillating dipole of molecular dyes at the NP surface, systematic and precise control of the nonradiative electromagnetic coupling in QD-metal NP hybrid nanostructure as a function of QDs size, distance and excitation wavelength between similarly charged colloidal QD-NP pair is rare.

In this chapter, we have demonstrated the mechanism behind size and wavelength-dependent PL quenching of three differently sized CdTe QDs (green, yellow and red) in the presence of plasmonic NPs. The main objective behind the present work is to illustrate the role of resonance coupling and distance on the extent of interaction between similarly charged colloidal QD and plasmonic NP pair.

6.2. Results and Discussion

6.2.1. Characterization of Au NPs

The AFM image of citrate-capped Au NPs reveals well dispersed spots with mean size of 20.4 ± 3.15 nm (Figure 6.1a). The mean hydrodynamic diameter of these Au NPs is 25.3 ± 3.45 nm with a zeta potential of -30.3 ± 0.6 mV (Figure 6.1b). The LSPR peak appears at 522 nm, which correlate well with the estimated size from AFM measurement. Here, it

is important to note that the LSPR band of Au NPs overlaps with the excitonic emission of green, yellow, and red QDs to different extent (Figure 6.1c).

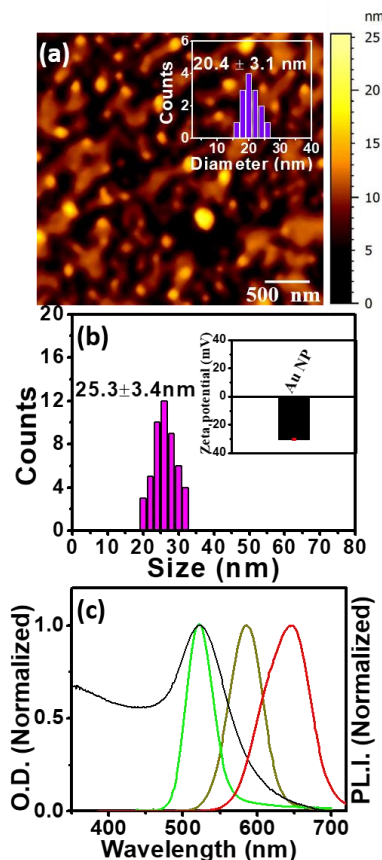


Figure 6.1. (a) AFM image of citrate-capped Au NPs. The inset shows the height profile histogram with mean size. (b) Histogram of hydrodynamic diameter of Au NPs with mean hydrodynamic diameter estimated from DLS measurement. The inset shows the zeta potential of citrate-capped Au NPs. (c) Spectral overlap between absorption spectrum of Au NPs (black line) with emission spectra ($\lambda_{\text{ex}} = 376$ nm) of green, yellow and red QDs.

While the PL peak of green QDs coincides with the LSPR peak of Au NPs, the PL peak of yellow and red QDs is red-shifted by 64 and 124 nm, respectively from the LSPR band of Au NPs.

6.2.2. PL Measurements of CdTe QDs in the Presence of Au NPs

The interaction of negatively-charged MSA-capped CdTe QDs with similarly charged Au NPs have been probed by steady-state and time-resolved PL measurements. Figure 6.2a shows the changes in the absorption spectra of green QDs upon gradual addition of Au NPs. The absorption peak of green QDs is centred at 496 nm. The characteristic LSPR peak of Au NPs appears at 522 nm upon addition of Au NPs. The absorbance at 496 nm increases gradually with increase in the concentrations of Au NPs (Figure 6.2a).

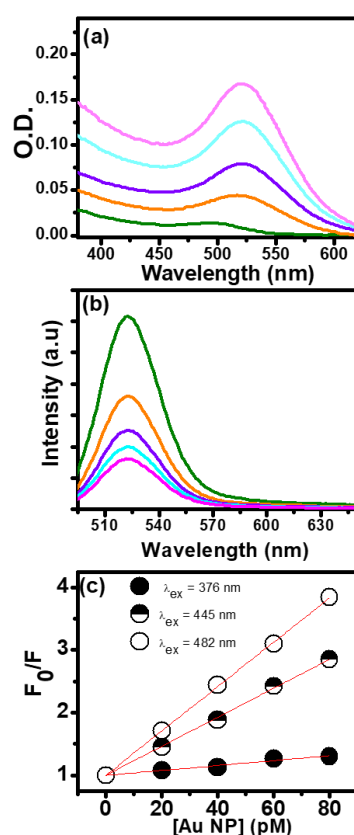


Figure 6.2. Changes in the (a) absorption and (b) PL spectra ($\lambda_{\text{ex}}=482$ nm) of green QDs upon gradual addition of Au NPs (0, 20, 40, 60 and 80 pM). (c) Stern-Volmer plots for the PL quenching of green QDs in the presence of Au NPs at three different excitation wavelengths.

To explore the effect of excitation wavelength on the extent of interaction between QD-NP pair, we have chosen three excitation wavelengths namely, 376, 445, and 482 nm for further PL measurements. While the longest excitation wavelength (482 nm) is

close to the LSPR of Au NPs (522 nm), the shortest wavelength (376 nm) is far away from the same. These wavelengths are chosen on the basis of our convenience for subsequent time-resolved measurements. The PL peak of green QDs appears at 522 nm upon excitation at 482 nm (Figure 6.2b). Significant quenching in the PL of green QDs has been observed in the presence of Au NPs. However, a substantial amount of overlaps in the extinction spectrum of QDs and Au NPs possess a major challenge for the determination of actual steady-state luminescence intensity of QDs in the presence of Au NPs. To circumvent this problem, we have corrected the recorded PL spectra of QDs in the presence of Au NPs [29]. The corrected PL spectra of QDs in the presence of Au NPs by considering the changes in the absorbance at the excitation wavelength is corrected using the following equation:

$$C = \frac{1-10^{-A}}{2.303A} \quad (1)$$

where C is the correction factor and A is the change in the absorbance of the sample at the excitation wavelength in presence and absence of the fluorophore.

Notably, the relative changes in the corrected steady-state PL intensities correlate well with the time-resolved results which are not affected by the Au NP extinction. This correction has been performed for all the three excitation wavelengths and the corrected PL spectra for green QDs in the presence of Au NPs are shown in Figure 6.2b. The PL intensity at 522 nm decreases gradually with increasing the concentrations of Au NPs in the range of 0-80 pM (Figure 6.2b). Similar PL quenching of green QDs has also been observed at 376 and 445 nm excitation wavelengths (Figure 6.3).

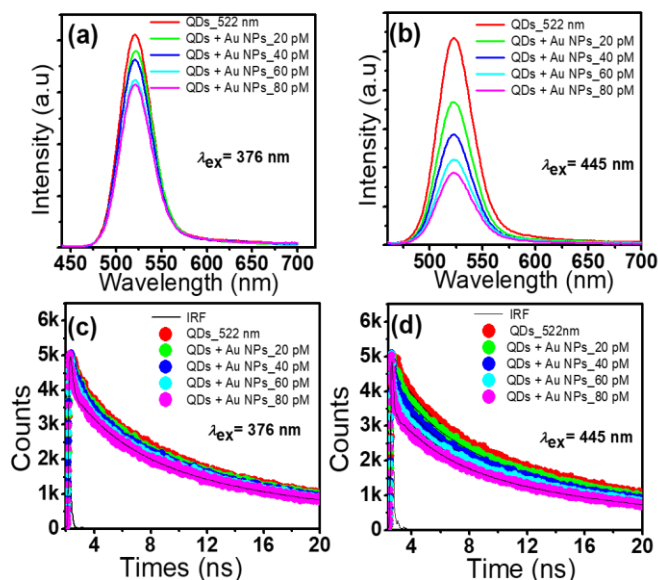


Figure 6.3. Changes in the PL spectra (a and b) and PL decay traces (c and d) of green QDs upon addition of citrate-capped Au NPs at 376 and 445 nm excitation wavelength.

To compare the quenching efficiencies at different excitation wavelengths, we have constructed Stern-Volmer (SV) plots with steady-state PL intensities, which can be expressed as equation (2) as follow:

$$\frac{F_0}{F} = 1 + K_{SV} [Q] \quad (2)$$

where F_0 and F are the PL intensities in the absence and presence of a quencher, respectively. K_{SV} is the SV constant and $[Q]$ is the molar concentration of a quencher, here CdTe QDs. It is evident from figure 3c that the SV plots are linear, and the slope increases with increase in the excitation wavelength. The estimated SV constants are 3.9×10^9 , 2.3×10^{10} , and $3.5 \times 10^{10} \text{ M}^{-1}$ at an excitation wavelength of 376, 445, and 482 nm, respectively (Table 6.1).

Table 6.1. Steady-state and time-resolved SV constants (K_{sv}) for green QDs in the presence of citrate-capped Au NPs.

Green QD-Au NP	PL	TCSPC
$\lambda_{ex} = 376$ nm	3.9×10^9	3.9×10^9
$\lambda_{ex} = 445$ nm	2.3×10^{10}	2.0×10^{10}
$\lambda_{ex} = 482$ nm	3.5×10^{10}	3.0×10^{10}

The quenching constant increases almost an order of magnitude upon shifting the excitation wavelength from 376 to 482 nm which is close to the LSPR of Au NPs. These results indicate the possible role of LSPR of Au NPs in the observed PL quenching of CdTe QDs. Next, we have performed time-resolved PL measurements to explore the mechanism further. Figure 6.4a shows the lifetime decay curves ($\lambda_{ex}=482$ nm; $\lambda_{em}=522$ nm) of green QDs in the absence and presence of different concentrations of Au NPs. All the decays show multiexponential decay kinetics and fit well with a three exponential decay function.

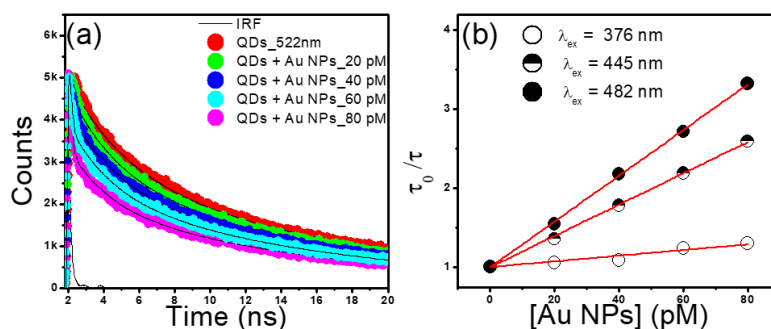


Figure 6.4. (a) Changes in the PL decay traces ($\lambda_{ex}= 482$ nm) of green QDs upon addition of citrate –capped Au NPs. Black solid lines represent fitted decay functions. (b) Stern–Volmer plots for the PL

quenching of green QDs at three different excitation wavelengths (375, 445 and 482 nm) as a function of Au NP concentrations.

In the absence of Au NPs, the green QDs show three lifetime components of 0.67 (21%), 3.54 (35%), and 15.77 ns (44%) with an average lifetime of 8.56 ns. This multiexponential decay kinetics is due to complex recombination processes in thiol-capped CdTe QDs involving band edge and trap states (shallow and deep) exciton recombinations [30]. The PL lifetime decreases gradually with increase in the concentrations of Au NPs (Figure 6.4a, Table 6.2).

Table 6.2. PL decay parameters ($\lambda_{em}= 522$ nm) of green QDs in the absence and presence of citrate and PEG-capped Au NPs at λ_{ex} of 482.nm.

Samples	τ_1 (ns)	a_1	τ_2 (ns)	a_2	τ_3 (ns)	a_3	$\langle\tau\rangle$ (ns)	χ^2
Green QDs	3.54	0.35	15.77	0.44	0.67	0.21	8.56	1.03
+ AuNPs_20pM	2.85	0.24	14.23	0.43	0.22	0.33	5.59	1.30
+ AuNPs_40pM	2.07	0.18	11.90	0.30	0.14	0.52	3.98	1.15
+ AuNPs_60pM	1.45	0.16	10.27	0.28	0.09	0.56	3.19	1.15
+ AuNPs_80pM	1.10	0.14	9.26	0.27	0.01	0.59	2.62	1.19
+PEG-Au NP_80pM	2.16	0.18	9.77	0.51	0.30	0.31	5.41	1.09

The average PL lifetime decreases to 2.62 ns in the presence of 80 pM Au NPs (Table 6.2). Similar decrease in the PL lifetime has been observed at 376 and 445 nm excitation wavelengths (Table 6.3).

Table 6.3. PL decay parameters of green QD in the absence and presence of citrate-capped Au NPs at 376 nm and 445 nm.

$\lambda_{\text{ex}} = 376 \text{ nm}$	τ_1 (ns)	a_1	τ_2 (ns)	a_2	τ_3 (ns)	a_3	$\langle \tau \rangle$ (ns)	χ^2
Green QD	3.55	0.29	14.93	0.50	0.41	0.21	8.61	1.02
+AuNPs_20pM	3.09	0.28	14.27	0.50	0.29	0.22	8.12	1.04
+AuNPs_40pM	2.77	0.26	13.60	0.52	0.29	0.22	7.86	1.02
+AuNPs_60pM	2.64	0.25	13.52	0.47	0.18	0.28	7.00	1.05
+AuNPs_80pM	2.39	0.23	12.99	0.46	0.15	0.31	6.61	1.04
$\lambda_{\text{ex}} = 445 \text{ nm}$								
Green QD	3.68	0.29	14.61	0.51	0.36	0.20	8.54	1.08
+AuNPs_20pM	3.07	0.23	14.84	0.37	0.11	0.40	6.32	1.12
+AuNPs_40pM	2.79	0.18	14.54	0.29	0.05	0.53	4.77	1.07
+AuNPs_60pM	2.56	0.14	13.88	0.26	0.04	0.60	3.93	1.04
+AuNPs_80pM	2.10	0.11	12.40	0.24	0.04	0.65	3.30	1.00

To estimate the relative quenching efficiencies at different excitation wavelengths, we have constructed SV plots at different excitation wavelengths. Figure 6.4b shows the SV plots for three different excitation wavelengths. All the plots are linear, and the slope (SV constant) increases with increase in excitation wavelength from 376 to 482 nm similar to that has been observed in our earlier steady-state PL measurements. The estimated SV constants for the green QD-Au NP

pair are 3.9×10^9 , 2.0×10^{10} , and $3.0 \times 10^{10} \text{ M}^{-1}$ at the excitation wavelengths of 376, 445, and 482 nm, respectively (Table 6.1). Notably, these SV constants are very close to those estimated from steady-state PL measurements. These findings clearly indicate the involvement of excitation wavelength-dependent nonradiative process behind the observed PL quenching of green QDs in the presence of Au NPs. To explore the mechanism further, we have studied the interactions of these Au NPs with yellow and red QDs with their PL peaks red-shifted appreciably from the LSPR peak of Au NPs. Notably, the PL spectra of yellow and red QDs show noticeable spectral overlap with the LSPR band of Au NPs.

Figure 6.5 shows the PL behaviours of yellow and red QDs in the absence and presence of different concentrations of Au NPs. It is evident that the steady-state PL ($\lambda_{ex}=482 \text{ nm}$) of yellow and red QDs is unaltered in the presence of Au NPs (Figure 6.5a and b).

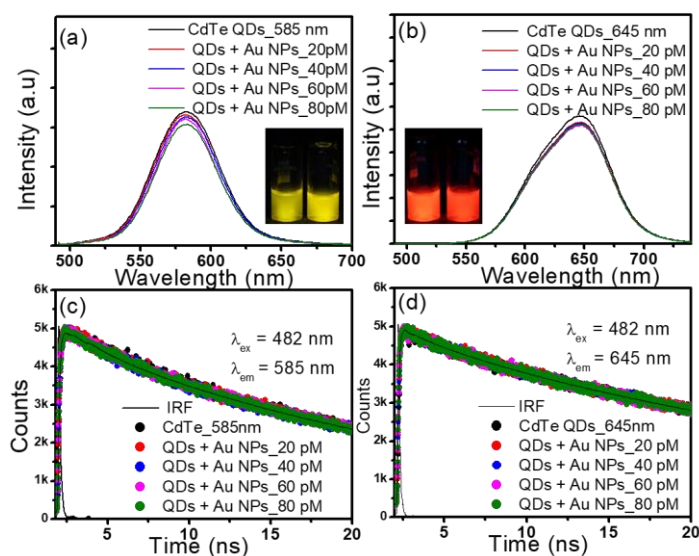


Figure 6.5. Changes in the PL spectra ($\lambda_{ex} = 482 \text{ nm}$) of (a) yellow and (b) red QDs upon gradual addition of Au NPs. PL decay traces ($\lambda_{ex} = 482 \text{ nm}$) of (c) yellow and (d) red QDs upon gradual addition of Au NPs.

The insets show the unchanged solution phase photographs of yellow and red QDs in the absence and presence of 80 pM Au NPs upon UV illumination, further supporting the fact that the steady-state luminescence intensity of the yellow and red QDs remains unchanged

in the presence of highest concentration of Au NPs. To substantiate these observations, we have performed PL lifetime measurements in the absence and presence of Au NPs. Both the QDs show multiexponential decay kinetics in the absence of Au NPs and the decays fit well with a biexponential decay function (Figure 6.5c and d, Table 6.4).

Table 6.4. PL decay parameters of yellow and red QDs in the absence and presence of citrate-capped Au NPs at λ_{ex} of 482 nm.

Samples	τ_1 (ns)	a_1	τ_2 (ns)	a_2	$\langle\tau\rangle$ (ns)	χ^2
Yellow QD	1.94	0.07	25.33	0.93	23.72	1.02
+ Citrate _AuNPs_80pM	1.92	0.07	25.25	0.93	23.65	1.05
Red QD	0.64	0.16	32.35	0.84	27.25	1.04
+ Citrate – AuNPs_80pM	0.65	0.16	32.42	0.84	27.33	1.03

Notably, the triexponential decay behaviour of green QDs changes to biexponential for yellow and red QDs. This size-dependent PL decay behaviour of CdTe QDs is a common phenomenon and arises due to the changes in the density and population of various surface trap states [30]. The estimated average lifetime of yellow QDs is 20.92 ns with lifetime components of 1.34 (10%) and 23.02 ns (90%) and remains almost unchanged in the presence of 80 pM Au NPs (Table 6.4). Similarly, the decay profile and average PL lifetime of red QDs remains unaltered in the presence of 80 pM Au NPs. (Figure 6.5d and Table 6.4). These results are in sharp contrast to our earlier observation of significant PL quenching of the green QDs in the presence of similar concentrations of Au NPs.

Next, we have calculated the radiative and nonradiative decay rates of QDs in the absence and presence of Au NPs according to the following equations:

$$k_r = \frac{\phi_D}{\tau} \quad (3a)$$

$$k_{nr} = \frac{(1-\phi_D)}{\tau} \quad (3b)$$

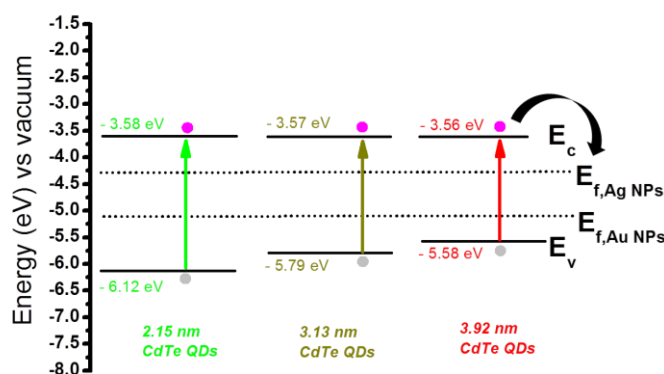
where k_r and k_{nr} are the radiative and nonradiative decay rates, respectively. ϕ_D is the PL quantum yield and τ is the average PL lifetime of QDs. All the estimated parameters are listed in Table 6.5.

Table 6.5. Estimated quantum yields, average PL lifetimes, radiative rates, nonradiative rates, energy transfer rates and efficiencies of energy transfer for green CdTe QDs ($\lambda_{ex} = 482$ nm) in the absence and presence of 80 pm citrate and PEG-capped Au NPs.

Systems	ϕ_D	$\langle\tau\rangle$ (nm)	k_r ($\times 10^9$ s^{-1})	k_{nr} ($\times 10^9$ s^{-1})	k_{ET} ($\times 10^9$ s^{-1})	ϕ_{ET} (τ)	ϕ_{ET} (ϕ_D)
Green QD	0.2	8.56	0.02	0.09	-	-	-
+ citrate-Au NPs	0.05	2.62	0.02	0.36	0.26	0.69	0.74
+PEG-Au NPs	0.12	5.41	0.02	0.16	0.07	0.37	0.37

While the nonradiative decay rate of green QDs increases by a factor of 3.9, the radiative decay rate remains unaltered in the presence of 80 pM Au NPs. This increase in the nonradiative decay rate of green QDs in the presence of Au NPs could be due to either aggregation of QDs on the surface of NPs, photoinduced charge transfer, and/or excitation energy transfer. Among these possibilities, aggregation of QDs on the surface of NP can be ruled out by considering similar negative surface charge on both the particles and absence of any PL quenching in the

yellow and red QDs. Observation of neither peak shifts nor any new peaks in absorption and emission spectra of green QDs in the presence of Au NPs further support this argument. It is known that metal NPs often quench the emission yield of nearby fluorophores either by electron transfer or energy transfer. In practice, it is challenging to distinguish between charge and energy transfer process involving metal NPs as dark acceptor. Efficient ultrafast charge transfer from photoexcited QD to various NP is well explored in the literature [31-36]. Earlier, Mondal and Samanta have demonstrated ultrafast charge transfer dynamics in a colloidal mixture of similarly charged MPA-capped CdTe QDs and citrate-capped Ag NPs using transient absorption measurements [31]. Similarly, Jana *et al.* have demonstrated size-dependent hole transfer dynamics in CdTe QD-polymer NP hybrid nanocomposite system [32]. In another study, Chauhan *et al.* have studied the ultrafast photoinduced charge separation in colloidal 2-dimensional CdSe/CdS-Au hybrid nanoplatelets and demonstrated efficient photocatalytic reactions under direct sun light [34]. These earlier reports suggest that charge (electron/hole) transfer from photoexcited CdTe QDs to Au NPs could be a reason for the observed PL quenching of the green QDs. However, the observed PL quenching in the present system is size dependent. While significant quenching has been observed for the green QDs, no appreciable change in the PL properties has been observed for the yellow and red QDs. This observation is quite unexpected in the charge transfer context as the fermi level of Au NPs remains in the band gap region of all the three differently sized QDs (Scheme 6.1) [37, 38].



Scheme 6.1. Schematic Representation of Valence Band (VB) and Conduction Band (CB) Position of Green, Yellow and Red QDs with Respect to Fermi Level of Au and Ag NPs.

To establish whether or not charge transfer is responsible behind the observed PL quenching of green QDs by Au NPs, we have synthesized citrate capped Ag NPs having LSPR far away from the excitonic emission of all the three differently-sized QDs. Earlier, it has been established that MPA-capped CdTe QDs undergo charge transfer dynamics in the presence of citrate-capped Ag NPs [31]. Here our aim is to explore the feasibility of nonradiative PL quenching of three differently sized QDs by Ag NPs. The synthesized citrate-capped Ag NPs show a characteristic LSPR at 394 nm (Figure 6.6), which corresponds to a mean size of 10 nm [39].

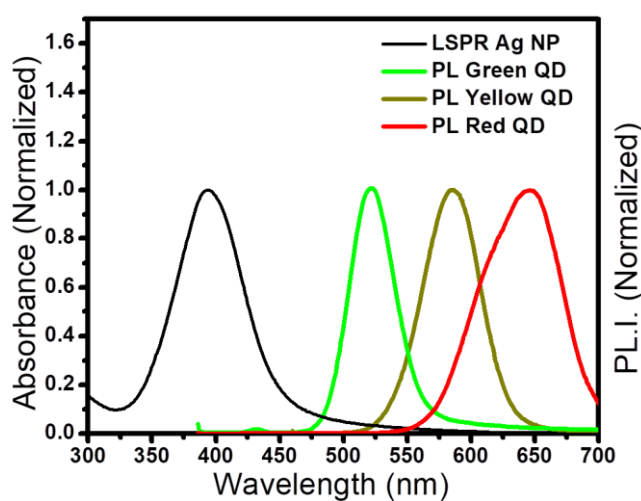


Figure 6.6. Normalized absorption (black) and PL spectra (green, yellow, and red) of Ag NPs and three differently sized QDs, respectively.

As discussed above, the LSPR of Ag NPs is significantly off resonance with the excitonic emission of all the three QDs. The LSPR band appears at 394 nm upon gradual addition of Ag NPs in the QDs solution (Figure 6.7). Interestingly, irrespective of the size of QDs the PL intensity ($\lambda_{ex} =$

376 nm) quenches in the presence of Ag NPs (Figure 6.7). This observation is in sharp contrast to the results obtained in the presence of Au NPs. The PL lifetime measurements ($\lambda_{\text{ex}} = 376$ nm) reveal shortening of the lifetime decay curves in the presence of Ag NPs irrespective of the sizes of QDs (Figure 6.7).

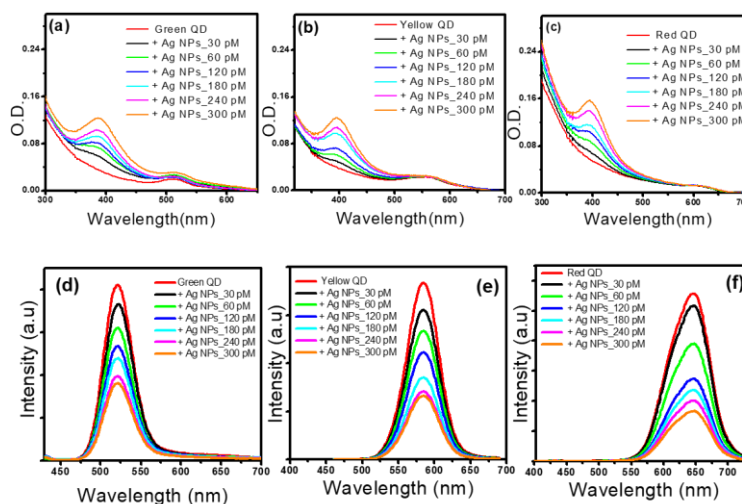


Figure 6.7. Changes in the absorption spectra of (a) green, (b) yellow and (c) red QDs upon addition of citrate-capped Ag NPs. Changes in the PL spectra of (d) green, (e) yellow and (f) red QDs upon addition of citrate-capped Ag NPs at λ_{ex} of 376 nm.

The average PL lifetime of green QDs decreases from 8.76 ns to 3.85 ns in the presence of 300 pM Ag NPs. Similarly, the average lifetime of yellow and red QDs decreases from 23.72 and 27.49 ns to 8.75 and 9.27 ns in the presence of 300 pM Ag NPs, respectively (Figure 6.8, Table 6.6).

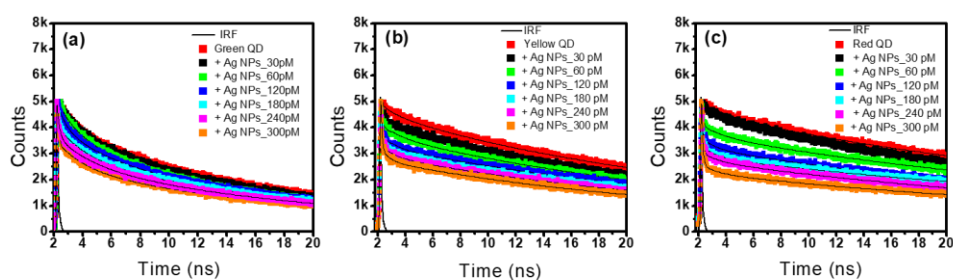


Figure 6.8. Changes in the PL decay traces of (a) green, (b) yellow and (c) red QDs upon addition of citrate capped Ag NPs $\lambda_{\text{ex}} = 376$ nm.

Table 6.6. PL decay parameters of green, yellow and red QD in the absence and presence of citrate-capped Ag NPs at $\lambda_{\text{ex}} = 376$ nm.

Samples	τ_1 (ns)	a_1	τ_2 (ns)	a_2	τ_3 (ns)	a_3	$\langle\tau\rangle$ (ns)	χ^2
Green QD	3.51	0.29	19.53	0.49	0.35	0.22	8.67	1.05
+ Ag NPs_30pM	3.00	0.29	19.40	0.35	0.15	0.36	7.69	1.05
+ Ag NPs_60pM	2.57	0.18	19.30	0.32	0.10	0.50	6.68	1.03
+AgNPs_120pM	2.56	0.18	19.26	0.27	0.10	0.55	5.71	1.03
+AgNPs_180pM	2.20	0.12	17.55	0.26	0.08	0.62	4.97	1.07
+AgNPs_240pM	1.87	0.11	16.00	0.25	0.07	0.64	4.30	1.07
+AgNPs_300pM	1.67	0.11	15.01	0.24	0.066	0.65	3.85	1.07
Yellow QD	1.94	0.07	25.33	0.93	-	-	23.72	1.02
+Ag NPs_30pM	0.57	0.15	23.06	0.85	-	-	19.66	1.05
+Ag NPs_60pM	0.33	0.25	22.65	0.75	-	-	16.98	1.08
+AgNPs_120pM	0.21	0.39	22.27	0.61	-	-	13.95	1.11
+AgNPs_180pM	0.17	0.48	21.67	0.52	-	-	11.37	1.19
+AgNPs_240pM	0.15	0.56	22.06	0.44	-	-	9.82	1.20
+AgNPs_300pM	0.15	0.59	21.00	0.41	-	-	8.75	1.20
Red QD	0.68	0.16	32.55	0.84	-	-	27.49	1.03
+AgNPs_30pM	0.62	0.12	29.83	0.88	-	-	26.36	1.03
+AgNPs_60pM	0.28	0.31	28.92	0.69	-	-	19.95	1.12
+AgNPs_120pM	0.17	0.48	28.73	0.52	-	-	15.0	1.17
+AgNPs_180pM	0.16	0.59	27.65	0.41	-	-	11.49	1.12
+AgNPs_240pM	0.13	0.63	27.79	0.37	-	-	10.53	1.13
+AgNPs_300pM	0.13	0.68	27.00	0.32	-	-	9.27	1.24

Figure 6.9 shows the SV plots of green, yellow and red QDs generated from steady-state and time-resolved PL measurements.

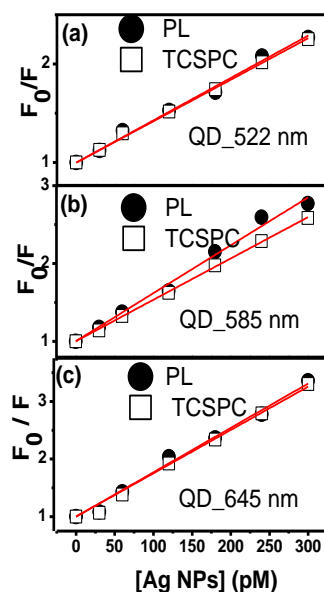


Figure 6.9. Steady-state and time-resolved Stern-Volmer plots for (a) green, (b) yellow and (c) red QDs in the presence of Ag NPs at an excitation wavelength of 376 nm.

All the plots are linear and the estimated SV constants and quenching rate constants are listed in table 6.7. This nonradiative decrease in the PL intensity as well as the lifetime of all the three QDs in the presence of Ag NPs indicates that the mechanism of PL quenching by Ag NP is quite different from that of Au NPs. The possibility of aggregation of QDs on the surface of Ag NPs can be ruled out by considering similar negative surface charge on both the particles.

Table 6.7. Steady-state and time-resolved SV constants (K_{sv}) for green, yellow, and red QD in presence of citrate-capped Ag NPs.

QD-Ag NP	PL	TCSPC
Green	4.3×10^9	4.2×10^9
Yellow	6.2×10^9	5.8×10^9
Red	7.7×10^9	6.7×10^9

Moreover, absence of any spectral overlap between LSPR of Ag NPs and excitonic emission of QDs ruled out the possibility of excitation energy transfer from QDs to Ag NPs. The most probable process that might contribute to the observed nonradiative PL quenching of all the three QDs by Ag NPs is photoinduced charge transfer from QDs to Ag NPs (Scheme 6.1) [37,40]. This argument gain support from a recent observation of ultrafast charge transfer dynamics in a colloidal mixture of MPA-capped CdTe QDs and citrate-capped Ag NPs. Direct evidence of electron transfer from the photoexcited CdTe QDs to Ag NPs has been demonstrated via accelerated bleach recovery of the exciton band of the QDs and a faster carrier cooling in the presence of Ag NPs using transient absorption measurements [31]. Importantly, our present study reveals that this nonradiative electron transfer from CdTe QDs to Ag NPs is feasible for all the three differently sized QDs. Therefore, the mechanism behind size and wavelength dependent PL quenching observed for green QDs in the presence of Au NPs is unlikely due to electron transfer mechanism.

The presence of significant spectral overlap between LSPR of Au NPs and excitonic emission of green QDs indicates the possible involvement of EET from photoexcited QDs to Au NPs. The estimated spectral overlap integrals are 5.90×10^{-9} , 1.60×10^{-9} , and $1.10 \times 10^{-9} \text{ M}^{-1} \text{ cm}^3$ for green, yellow, and red QDs, respectively. The higher value of spectral overlap integral for green QD-Au NP pair along with coincidence of their peak positions account for the significant PL quenching observed due to EET. Moreover, the observation of efficient quenching near the LSPR of Au NPs suggests efficient electromagnetic coupling of excitonic emission of green QDs with the LSPR of Au NPs, which facilitate the EET. Similar EET via wavelength-dependent electromagnetic coupling has been observed earlier [19,22]. Hence, our present results clearly indicate the involvement of EET from photoexcited CdTe QDs to the Au NPs in the observed PL quenching. The rate of this nonradiative EET is estimated by using the following equation:

$$k_{\text{ET}} = \frac{1}{\tau_{\text{DA}}} - \frac{1}{\tau_{\text{D}}} \quad (4)$$

where τ_{DA} and τ_{D} are the average PL lifetimes of green QDs in the presence and absence of Au NPs, respectively. The estimated k_{ET} is $0.27 \times 10^9 \text{ s}^{-1}$. The efficiency of the EET process is estimated using the following equations:

$$\phi_{\text{Eff}} = 1 - \frac{\phi_{\text{D-A}}}{\phi_{\text{D}}} = 1 - \frac{\tau_{\text{D-A}}}{\tau_{\text{D}}} \quad (5)$$

where ϕ_{D} and $\phi_{\text{D-A}}$ are the steady-state PL quantum yields of green QDs in the absence and presence of Au NPs, respectively. τ_{D} and $\tau_{\text{D-A}}$ are the average PL lifetimes of QDs in the absence and presence of Au NPs, respectively. The estimated EET efficiency from the lifetime measurements in the presence of 80 pM Au NPs is 0.69, which matches closely with that estimated from steady-state PL measurements (Table 6.2). Next, we have investigated the effect of ligand exchange at the surface of Au NPs with PEG-SH on the extent of EET from photoexcited green QDs.

6.2.3. Effect of Ligand Exchange on the EET

The effect of ligand exchange with PEG-SH on the extent of EET between green QDs and PEG-capped Au NPs has been explored. For the present study we have used PEG-SH (MW 6000 Da) to replace the citrate molecules on the surface of Au NPs. The PEG-capped Au NPs have been characterised by UV-vis, FTIR, DLS, and zeta potential measurements. A noticeable change in the LSPR band of Au NPs has been observed upon ligand exchange with PEG-SH (Figure 6.10a).

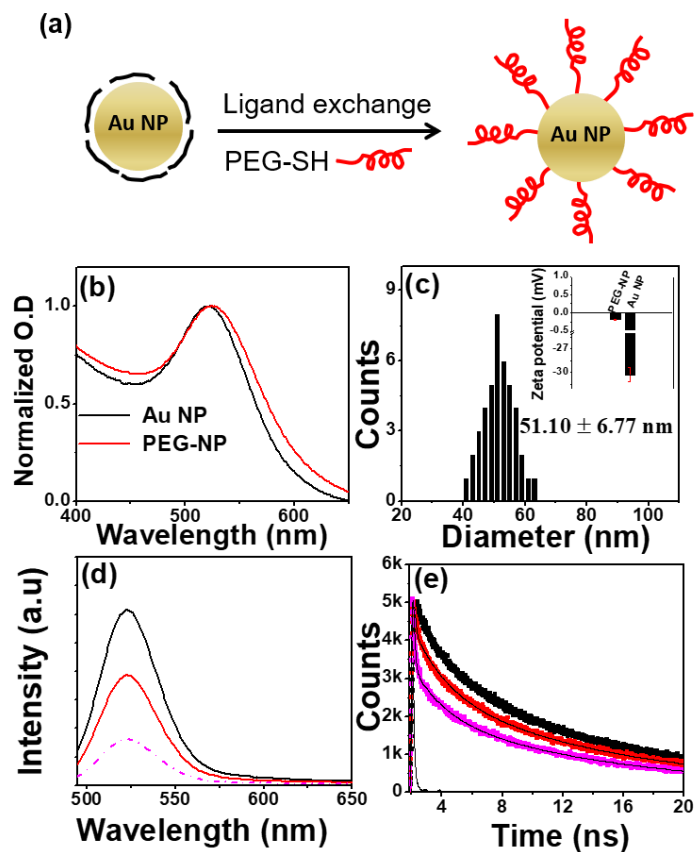


Figure 6.10. (a) Schematic representation of ligand exchange reaction of citrate-capped Au NPs with PEG-SH ligand. (b) Normalized absorption spectrum of citrate and PEG-capped Au NPs. (c) Size distribution histogram of PEG-capped Au NPs from DLS measurement. The mean hydrodynamic diameter is mentioned with the standard deviation. The Inset compares the estimated zeta potentials of citrate and PEG-capped Au NPs. (d) Changes in the PL spectra ($\lambda_{\text{ex}} = 482$ nm) of green QDs in the absence (black line) and presence of 80 pM PEG (solid red line) and citrate (dash dot magenta line)-capped Au NPs. (e) Changes in the PL decay traces ($\lambda_{\text{ex}} = 482$ nm) of green QDs in the absence (black) and presence of 80 pM PEG (red) and citrate (magenta)-capped Au NPs. The black solid lines are the fitted curves.

The LSPR peak of PEG-capped Au NPs is observed at 525 nm with a 3 nm red shift compared to that of citrate-capped Au NPs. Similar spectral change has been observed earlier upon ligand exchange due to the

change in dielectric constant at the NP surface [41]. The covalent attachment of PEG-SH molecules on the surface of Au NPs has been confirmed from FTIR measurements where the stretching frequency of free –S-H groups disappears in the presence of Au NPs (Figure 6.11).

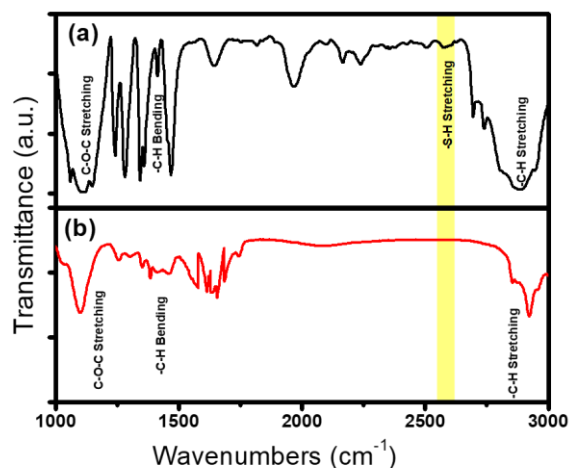


Figure 6.11. FTIR spectra of (a) Poly (ethylene glycol) methyl ether thiol (PEG-SH) and (b) synthesized PEG-capped Au NPs.

Significant change in the hydrodynamic diameter and zeta potential has been observed in the DLS measurements (Figure 6.10b). The mean hydrodynamic diameter of PEG-capped Au NPs is estimated to be 51.10 ± 6.77 nm, which is significantly higher than that of citrate-capped Au NPs. Moreover, the estimated zeta potential is found to be -0.180 ± 0.005 mV, indicating the presence of neutral PEG molecules at the surface of Au NPs. The characteristic LSPR of Au NPs appears in the absorption spectra of green QDs upon gradual addition of PEG-capped Au NPs (Figure 6.12), similar to that has been observed for citrate-capped Au NPs. Figure 6.10d shows the changes in the PL spectra ($\lambda_{\text{ex}} = 482$ nm) of green QDs in the absence and presence of 80 pM PEG-capped Au NPs along with the PL spectrum in the presence of 80 pM citrate-capped Au NPs (Dash dotted line).

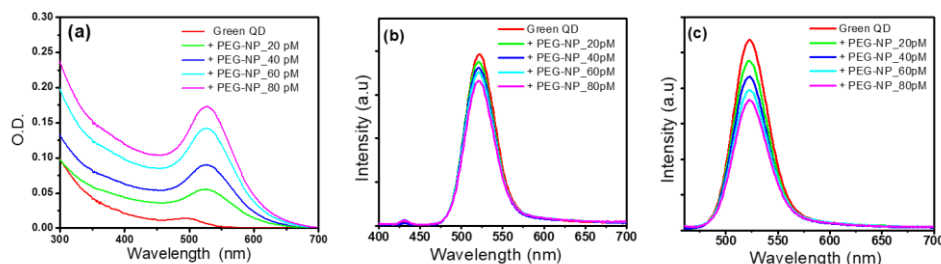


Figure 6.12. (a) Changes in the absorption spectra and PL spectra of green QD upon addition of PEG-capped Au NPs at λ_{ex} of (b) 376 nm and (c) 445 nm.

It is evident that the PL of green QDs quenches in the presence of PEG-capped Au NPs without any noticeable peak shift (Figure 6.10d). Notably, the extent of PL quenching is significantly lower compared to that in the presence of citrate-capped Au NPs. While the PL intensity of green QDs decreases by 3.8 times in the presence of citrate-capped Au NPs, the same decreases by only 1.6 times in the presence of PEG-capped Au NPs. Control experiment with only PEG-SH ligand reveals no appreciable quenching in the PL intensity of green QDs, indicating that the observed quenching is solely due to the Au NPs. Similar excitation wavelength dependent PL quenching has also been observed at 376 and 445 nm excitation wavelengths in the presence of PEG-capped Au NPs (Figure 6.13).

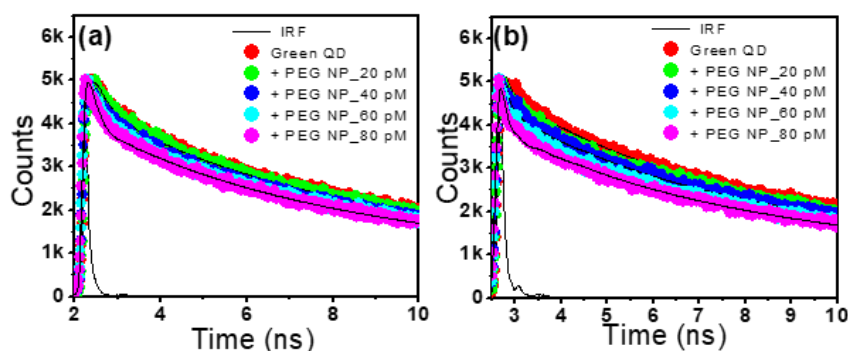


Figure 6.13. Changes in the PL decay traces of green QD upon addition of PEG-capped Au NPs at λ_{ex} of (a) 376 nm and (b) 445 nm.

Lifetime decay measurements have been performed to gain further knowledge on the dynamics and extent of EET in the presence of PEG-

capped Au NPs. The PL decay trace ($\lambda_{\text{ex}} = 482 \text{ nm}$) of green QDs shortens in the presence of PEG-capped Au NPs, indicating nonradiative EET from QDs to PEG-capped Au NPs (Figure 6.10e). The average PL lifetime of green QDs decreases from 8.56 ns to 5.41 ns in the presence of 80 pM PEG-capped Au NPs (Table 6.1). This 1.6-fold decrease in the average lifetime of green QDs in the presence of PEG-capped Au NPs is significantly lower than that observed (3.3 fold) in the presence of citrate-capped Au NPs. These observations clearly reveal that the nonradiative EET from the photoexcited QDs to Au NPs hinders due to the presence of bulky PEG ligands at the surface. The calculated radiative and nonradiative rates for the green QDs in the presence of PEG-capped Au NPs are listed in Table 6.5. While the nonradiative rate of QDs increases by a factor of 1.74, the radiative rate remains unchanged in the presence of 80 pM PEG-capped Au NPs. The estimated rate and efficiency of this nonradiative EET process in the presence of 80 pM PEG-capped Au NP is $0.07 \times 10^9 \text{ s}^{-1}$ and 0.37, respectively (Table 6.5). These values are lower than those estimated for citrate-capped Au NPs, suggesting less efficient EET due to the presence of PEG molecules. Here it is important to note that the size of Au NPs and the extent of spectral overlap remain almost unchanged upon ligand exchange with PEG molecules. Therefore, the observed less efficient EET in the presence of PEG-capped Au NPs can be explained by considering increase in the separation distance between CdTe QDs and the surface of Au NPs due to the presence of PEG molecules. Similar distance-dependent EET has been demonstrated earlier by using various organic and inorganic spacers between donor-acceptor pair [14,16-22]. In the next section we have discussed different models of excitation energy transfer in the context of our experimental findings.

6.2.4. Mechanism of EET from QDs to Au NPs

The classical FRET model of EET is based on the nonradiative dipole-dipole interaction between two molecular dyes (donor and acceptor) and is limited for short range distances of up to 10 nm. The most characteristic parameter related to FRET model is the Förster distance

R_0 and can be defined as the distance at which the EET efficiency is 50%. For a typical donor-acceptor pair, it varies in the range of 2-8 nm and for a given donor and acceptor the value of R_0 can be estimated by using the following equation,

$$R_0 = [(8.8 \times 10^{-25})(\kappa^2 \eta^{-4} \phi_D J(\lambda))]^{1/6} \quad (6)$$

where κ^2 is the orientation factor of the transition dipoles of the donor and the acceptor, η is the refractive index of the medium, ϕ_D is the quantum yield of the donor, and $J(\lambda)$ is the spectral overlap integral between the donor emission and the acceptor absorption spectrum. The estimated R_0 value for the green QDs-Au NPs pair is 24.60 nm, which is well beyond the range of conventional FRET theory.

The electromagnetic coupling of an excited state oscillating dipole with the near field of a metallic surface was described earlier by Chance *et al.* [23] and extended further by Persson and Lang to the metal's conduction electrons and known as surface energy transfer (SET) [24]. According to this model, the LSPR modes represent the collective oscillation of many strongly coupled electrons and hence the electromagnetic coupling of the oscillator can be described as an interaction with the array of coupled dipoles. Although this SET model is appropriate for a thin metal film with mirror-like behaviour, it successfully accounts the experimentally observed nonradiative EET from various molecular dyes to small (<2 nm) Au NPs [16-22] This correlation has been explained on the basis of formation of an image dipole at the NP surface. While this model is quite successfully predicts the experimentally observed trends for thin metal surfaces and small Au NPs, it has failed to accurately predict the observed changes in the radiative and nonradiative rate constants of dyes in the near field of larger sized metal NPs [19,25] This discrepancy is possibly due to the inability of the NSET model to account the size of the metal NP and the spectral overlap of the donor-acceptor pair. For the present system, we have incorporated the size-dependent dielectric and optical properties of the Au NPs in the original SET theory, similar to that has been

demonstrated recently [26]. The distance d_0 at which the nonradiative EET is 50% efficient can be express as follows:

$$d_0 = \frac{\alpha\lambda}{n_m} (A\phi)^{1/4} \left\{ \frac{n_r}{2n_m} \left(1 + \frac{\varepsilon_1^2}{|\varepsilon_2|^2} \right) \right\}^{1/4} \quad (7)$$

where α is the orientation of the donor transition dipole to the metal plasmon vector [26], λ is the emission wavelength maximum of the donor, n_m is the refractive index of the medium, A is the absorptivity of the metal NP, ϕ is the quantum yield of the donor, n_r is the refractive index of the metal, ε_1 is the solvent dielectric constant, and ε_2 is the complex dielectric function of the metal. The size-dependent complex dielectric function of metal can be express as follows:

$$\varepsilon_2 = \varepsilon_\infty + \varepsilon_{\text{Drude}} + \varepsilon_{\text{IB}} \quad (8a)$$

$$\varepsilon_{\text{Drude}} = 1 - \frac{\omega_p^2}{\omega^2 + \Gamma_r^2} + i \frac{\Gamma_r \omega_p^2}{\omega(\omega^2 + \Gamma_r^2)} \quad (8b)$$

$$\varepsilon_{\text{IB}} = \sum_{i=1,2} \frac{A_i}{\omega_i} \left[\frac{e^{i\phi_i}}{\omega_i^{-1} - \omega^{-1} - \Gamma_i^{-1}} + \frac{e^{-i\phi_i}}{\omega_i^{-1} + \omega^{-1} + \Gamma_i^{-1}} \right] \quad (8c)$$

where ε_∞ is the bulk dielectric constant of Au, ω is the dipole frequency, ω_p is the Drude plasmon frequency, and Γ_r is the size-dependent damping constant. Γ_r can be express as follows:

$$\Gamma_r = \Gamma_\infty + \frac{(l_\infty)}{r} \quad (9)$$

where Γ_∞ is the bulk damping constant, l_∞ is the mean free path in Au ($l_\infty = 420 \text{ \AA}$), and r is the Au NP radius. The absorptivity term for metal NP has also been corrected according to the literature [26] and can be express as follows:

$$A_{\text{NP}} = 10^3 \ln(10) \left[\frac{\varepsilon_\lambda \left(2r_{\text{cm}} \left(\frac{2r_{\text{cm}}}{\delta_{\text{skin}}} \right) \right)}{N_A V_{\text{cm}^3}} \right] \quad (10)$$

where ε_λ is the extinction coefficient of the NP at the maximum emission wavelength of the donor [42,43], r_{cm} is the radius of the NP in cm, N_A is

the Avogadro's number, and V_{cm}^3 is the volume of the NP in cm^3 . δ_{skin} is the skin depth of the Au NP and can be express as follows:

$$\delta_{skin} = \frac{\lambda}{2\pi k} \quad (11)$$

where λ the emission wavelength maximum of the donor and k is the refractive index.

The calculated dielectric function and absorptivity values for the present system are listed in table 6.8.

Table 6.8. Experimental and theoretical SET parameters for green, yellow and red QDs in the presence of citrate-capped Au NPs.

Donor	λ_{max} (nm)	n_r	NP radius (10^{-7} cm)	NP extinction ($M.cm$) ⁻¹ $\times 10^8$	d_0 (nm)	ϵ_2'	ϵ_2''	$ \epsilon_2 ^2$	δ_{skin} (10^{-7} cm)
Green QD	522	0.6	10	8.78	22.5	-5.30	3.4	39.4	34.49
Yellow QD	585	0.3	10	1.85	19.0	-9.65	1.7	95.9	29.87
Red QD	645	0.3	10	0.55	13.5	-14.3	1.1	204.6	27.22

The estimated d_0 value for the green QD-Au NP pair is 22.48 nm. The average separation distance between the green QDs and the surface of Au NPs is estimated from experimentally obtained efficiency (ϕ_{Eff}) and calculated d_0 values using the following equation:

$$\phi_{Eff} = \frac{1}{1 + \left(\frac{d}{d_0}\right)^4} \quad (12)$$

We have estimated the average separation distance between green QDs and the surface of Au NPs by using the experimental values of ϕ_{Eff} and calculated d_0 values at 80 pM citrate and PEG-capped Au NPs. The estimated average distance is 18.3 and 25.4 nm for citrate and PEG-

capped Au NPs, respectively. Here, it is important to comment on the large separation distances estimated for citrate and PEG-capped Au NPs. The large separation distance between QD and the surface of citrate-capped Au NPs in colloidal mixture is expected due to their similar negative surface charges. As the surface of both the particles is negatively charged, they will repel each other and leads to a large effective separation distance. Interestingly, our present findings reveal that the nonradiative through space EET is quite possible at large separation distance due to the strong electromagnetic coupling of the excitonic emission of green QD and the LSPR of Au NP. Absence of any EET in yellow and red QDs indicates insufficient electromagnetic coupling due to the red-shifted excitonic peaks relative to the LSPR peak of Au NPs. Notably, the observed 7 nm increase in the separation distance due to PEGylation of the Au NPs observed in our present study is very close to the estimated Flory radius of PEG 6000 which is 6.7 nm [44,45]. This correlation strongly justifies the validity of the theoretical SET model used in the present study to account the observed EET from QD to Au NP surface. The observed enhancement in the separation distance due to PEGylation of the NP surface can be explained by considering steric effect of bulky PEG molecules which limit the access of QDs to the NP surface.

6.3. Conclusions

The present study demonstrates the size and wavelength-dependent electromagnetic coupling and subsequent long range EET from negatively charged MSA-capped CdTe QDs to negatively charged citrate-capped Au NPs. While Au NPs significantly quench the PL intensity and lifetime of green QDs, no such quenching phenomenon has been observed for yellow and red QDs even with noticeable spectral overlap. These results clearly indicate that mere spectral overlap between emission spectrum of donor and LSPR of metal NP in hybrid colloidal mixture is not sufficient for resonant EET. Moreover, the estimated quenching efficiency shows a maximum value close to the LSPR of Au NPs, indicating the involvement of LSPR in the quenching

process. Our findings reveal strong electromagnetic coupling of LSPR of Au NPs and excitonic emission of green QDs, which leads to significant PL quenching due to nonradiative EET from photoexcited QDs to the surface of Au NPs. In contrast, size-independent PL quenching in the presence of 10 nm sized citrate-capped Ag NPs having LSPR significantly off resonance with the excitonic emission of all the three differently sized QDs arises as a consequence of nonradiative PET process. Furthermore, it has been observed that ligand exchange with bulky PEG 6000 molecules at the surface of Au NPs results in significant lowering of the efficiency of this EET process due to the increase in the effective separation distance between QD and the surface of Au NPs. The effective separation distance between QD and the surface of citrate and PEG-capped Au NP has been estimated using a modified SET model and the obtained distances correlate well with our present system. Our study reveals that it is possible to tune the optoelectronic properties of hybrid plexcitonic system by modulating inherent complex nonradiative processes which in turn depend on various factors such as size and nature of metal NPs, spectral overlap, separation distance and surface charge on particles. The present findings may be useful to understand the fundamental nonradiative processes in various hybrid plexcitonic systems.

Note: This is copyrighted material from permission of the American Chemistry Society.

6.4. References

1. Nimmo, M. T., Caillard, L. M., De Benedetti, W., Nguyen, H. M., Seitz, O., Gartstein, Y. N., Chabal, Y. J., Malko, A. V. (2013), Visible to near-infrared sensitization of silicon substrates via energy transfer from proximal nanocrystals: Further insights for hybrid photovoltaics. *ACS Nano*, 7, 3236-3245. (DOI: 10.1021/nn400924y)
2. Trinh, C., Kirlikovali, K. O., Bartynski, A. N., Tassone, C. J., Toney, M. F., Burkhard, G. F., McGehee, M. D., Djurovich, P. I., Thompson, M. E. (2013), Efficient energy sensitization of C60 and application to organic photovoltaics. *J. Am. Chem. Soc.*, 135, 11920-11928. (DOI: 10.1021/ja4043356)
3. Fu, G., Guan, J., Li, B., Liu, L., He, Y., Yu, C., Zhang, Z., Lü, X. (2018), An efficient and weak efficiency-roll-off near-infrared (NIR) polymer light-emitting diode (PLED) based on a PVK-supported Zn²⁺-Yb³⁺-containing metallopolymer. *J. Mater. Chem. C*, 6, 4114-4121. (10.1039/C7TC05400A)
4. Jia, W., Chen, Q., Chen, L., Yuan, D., Xiang, J., Chen, Y., Xiong, Z. (2016), Molecular spacing modulated conversion of singlet fission to triplet fusion in rubrene-based organic light-emitting diodes at ambient temperature. *J. Phys. Chem. C*, 120, 8380-8386. (DOI: 10.1021/acs.jpcc.6b01889)
5. Ueno, Y., Furukawa, K., Matsuo, K., Inoue, S., Hayashi, K., Hibino, H. (2013), Molecular design for enhanced sensitivity of a FRET aptasensor built on the graphene oxide surface. *Chem. Commun.*, 49, 10346-10348. (DOI: 10.1039/C3CC45615C)
6. Ma, H., Gibson, E. A., Dittmer, P. J., Jimenez, R., Palmer, A. E. (2012), High-throughput examination of fluorescence resonance energy

transfer-detected metal-ion response in mammalian cells. *J. Am. Chem. Soc.*, *134*, 2488-2491. (DOI: 10.1021/ja2101592)

7. Zhao, Q., Huo, F., Kang, J., Zhang, Y., Yin, C. (2018), A novel FRET-based fluorescent probe for the selective detection of hydrogen sulfide (H₂S) and its application for bioimaging. *J. Mater. Chem. B*, *6*, 4903-4908. (DOI: 10.1039/C8TB01070F)

8. Yuan, L., Lin, W., Zheng, K., Zhu, S. (2013), FRET-based small-molecule fluorescent probes: Rational design and bioimaging applications. *Acc. Chem. Res.*, *46*, 1462-1473. (DOI: 10.1021/ar300273v)

9. Sönnichsen, C., Reinhard, B. M., Liphardt, J., Alivisatos, A. P. (2005), A molecular ruler based on plasmon coupling of single gold and silver nanoparticles. *Nat. Biotechnol.*, *23*, 741-745. (DOI: 10.1038/nbt1100)

10. Liu, X., Yue, Q., Yan, T., Li, J., Yan, W., Ma, J., Zhao, C., Zhang, X. (2016), Competition between local field enhancement and nonradiative resonant energy transfer in the linear absorption of a semiconductor quantum dot coupled to a metal nanoparticle. *J. Phys. Chem. C*, *120*, 18220-18227. (DOI: 10.1021/acs.jpcc.6b03637)

11. Lei, K. W., Zhu, X. Y., Fan, D. L. (2015), Rational fabrication of arrays of plasmonic metal-quantum dot sandwiched nanodisks with enhanced Förster resonance energy transfer. *J. Phys. Chem. C*, *119*, 16230-16238. (DOI: 10.1021/acs.jpcc.5b03904)

12. Ozel, T., Hernandez-Martinez, P. L., Mutlugun, E., Akin, O., Nizamoglu, S., Ozel, I. O., Zhang, Q., Xiong, Q., Demir, H. V. (2013), Observation of selective plasmon-exciton coupling in nonradiative energy transfer: Donor-selective versus acceptor-selective plexcitons. *Nano Lett.*, *13*, 3065-3072. (DOI: 10.1021/nl4009106)

13. Ray, M., Basu, T. S., Bandyopadhyay, N. R., Klie, R. F., Ghosh, S., Raja, S. O., Dasgupta, A. K. (2014), Highly lattice-mismatched semiconductor–metal hybrid nanostructures: gold nanoparticle encapsulated luminescent silicon quantum dots. *Nanoscale*, *6*, 2201-2210. (DOI: 10.1039/C3NR05960J)
14. Prajapati, R., Chatterjee, S., Bhattacharya, A., Mukherjee, T. K. (2015), Surfactant-induced modulation of nanometal surface energy transfer from silicon quantum dots to silver nanoparticles. *J. Phys. Chem. C*, *119*, 13325-13334. (DOI: 10.1021/acs.jpcc.5b02903)
15. Prajapati, R., Bhattacharya, A., Mukherjee, T. K. (2016), Resonant excitation energy transfer from carbon dots to different sized silver nanoparticles. *Phys. Chem. Chem. Phys.*, *18*, 28911-28918. (DOI: 10.1039/C6CP05451J)
16. Yun, C. S., Javier, A., Jennings, T., Fisher, M., Hira, S., Peterson, S., Hopkins, B., Reich, N. O., Strouse, G. F. (2005), Nanometal surface energy transfer in optical rulers, breaking the FRET barrier. *J. Am. Chem. Soc.*, *127*, 3115-3119. (DOI: 10.1021/ja043940i)
17. Jennings, T. L., Singh, M. P., Strouse, G. F. (2006), Fluorescent lifetime quenching near $d = 1.5$ nm gold nanoparticles: Probing NSET validity. *J. Am. Chem. Soc.*, *128*, 5462-5467. (DOI: 10.1021/ja0583665)
18. Singh, M. P., Strouse, G. F. (2010), Involvement of the LSPR spectral overlap for energy transfer between a dye and Au nanoparticle. *J. Am. Chem. Soc.*, *132*, 9383-9391. (DOI: 10.1021/ja1022128)
19. Reineck, P., Gómez, D., Ng, S. H., Karg, M., Bell, T., Mulvaney, P., Bach, U. (2013), Distance and wavelength dependent quenching of molecular fluorescence by Au@SiO₂ core–shell nanoparticles. *ACS Nano*, *7*, 6636-6648. (DOI: 10.1021/nm401775e)

20. Acuna, G. P., Bucher, M., Stein, I. H., Steinhauer, C., Kuzyk, A., Holzmeister, P., Schreiber, R., Moroz, A., Stefani, F. D., Liedl, T., Simmel, F. C., Tinnefeld, P. (2012), Distance dependence of single-fluorophore quenching by gold nanoparticles studied on DNA origami. *ACS Nano*, *6*, 3189-3195. (DOI: 10.1021/nn2050483)
21. Pons, T., Medintz, I. L., Sapsford, K. E., Higashiya, S., Grimes, A. F., English, D. S., Mattoussi, H. (2007) On the quenching of semiconductor quantum dot photoluminescence by proximal gold nanoparticles. *Nano Lett.*, *7*, 3157–3164.
22. Zhang X., Marocico C. A., Lunz M., Gerard V. A., Gun'ko Y. K., Lesnyak V., Gaponik N., Susa A. S., Rogach A. L., Bradley A. L. (2012), Wavelength, concentration, and distance dependence of nonradiative energy transfer to a plane of gold nanoparticles, *ACS Nano*, *6*, 9283-9290. (DOI: 10.1021/nn303756a)
23. Chance R. R., Prock A., Silbey R. (1975), Comments on the classical theory of energy transfer, *J. Chem. Phys.*, *62*, 2245-2253. (DOI: 10.1063/1.430748)
24. Persson B. N. J., Lang N. D. (1982), Electron-hole-pair quenching of excited states near a metal, *Phys. Rev. B*, *26*, 5409-5415. (DOI: 10.1103/PhysRevB.26.5409)
25. Chhabra R., Sharma J., Wang H., Zou S., Lin S., Yan H., Lindsay S., Liu Y. (2009), Distance-dependent interactions between gold nanoparticles and fluorescent molecules with DNA as tunable spacers, *Nanotechnology*, *20*, 485201. (DOI: 10.1088/0957-4484/20/48/485201)
26. Breshike C. J., Riskowski R. A., Strouse G. F. (2013), Leaving Förster resonance energy transfer behind: Nanometal surface energy

transfer predicts the size-enhanced energy coupling between a metal nanoparticle and an emitting dipole, *J. Phys. Chem. C*, *117*, 23942-23949. (DOI: 10.1021/jp407259r)

27. Zhou N., Yuan M., Gao Y., Li D., Yang D. (2016), Silver nanoshell plasmonically controlled emission of semiconductor quantum dots in the strong coupling regime, *ACS Nano*, *10*, 4154-4163. (DOI: 10.1021/acsnano.5b07400)

28. Lunz M., Gerard V. A., Gun'ko Y. K., Lesnyak V., Gaponik N., Susa A. S., Rogach A. L., Bradley A. L. (2011), Surface plasmon enhanced energy transfer between donor and acceptor CdTe nanocrystal quantum dot monolayers, *Nano Lett.*, *11*, 3341-3345. (DOI: 10.1021/nl201714y)

29. Birdsall B., King R. W., Wheeler M. R., Lewis C. A., Goode S. R., Dunlap R. B., Roberts G. C. K. (1983), Correction for light absorption in fluorescence studies of protein-ligand interactions, *Anal. Biochem.*, *132*, 353-361. (DOI: 10.1016/0003-2697(83)90020-9)

30. Rogach A. L., Franzl T., Klar T. A., Feldmann J., Gaponik N., Lesnyak V., Shavel A., Eychmüller A., Rakovich Y. P., Donegan J. F. (2007), Aqueous synthesis of thiol-capped CdTe nanocrystals: State-of-the-art, *J. Phys. Chem. C*, *111*, 14628-14637. (DOI: 10.1021/jp072463y)

31. Mondal N., Samanta A. (2016), Ultrafast charge transfer and trapping dynamics in a colloidal mixture of similarly charged CdTe quantum dots and silver nanoparticles, *J. Phys. Chem. C*, *120*, 650-658. (DOI: 10.1021/acs.jpcc.5b08630)

32. Jana B., Ghosh A., Maiti S., Bain D., Banerjee S., Ghosh H. N., Patra A. (2016), Size of CdTe quantum dots controls the hole transfer rate in CdTe quantum dots–MEHPPV polymer nanoparticle hybrid, *J. Phys. Chem. C*, *120*, 25142-25150. (DOI: 10.1021/acs.jpcc.6b09986)

33. Kissling G. P., Miles D. O., Fermín D. J. (2011), Electrochemical charge transfer mediated by metal nanoparticles and quantum dots, *Phys. Chem. Chem. Phys.*, *13*, 21175-21185. (DOI: 10.1039/C1CP21996K)
34. Chauhan H., Kumar Y., Dana J., Satpati B., Ghosh H. N., Deka S. (2016), Photoinduced ultrafast charge separation in colloidal 2-dimensional CdSe/CdS-Au hybrid nanoplatelets and corresponding application in photocatalysis, *Nanoscale*, *8*, 15802-15812. (DOI: 10.1039/C6NR03610D)
35. Kaniyankandy S., Rawalekar S., Ghosh H. N. (2012), Ultrafast charge transfer dynamics in photoexcited CdTe quantum dot decorated on graphene, *J. Phys. Chem. C*, *116*, 16271-16275. (DOI: 10.1021/jp303712y)
36. Dana J., Anand P., Maiti S., Azlan F., Jadhav Y., Haram S. K., Ghosh H. N. (2018), Inhibiting interfacial charge recombination for boosting power conversion efficiency in CdSe{Au} nanohybrid sensitized solar cell, *J. Phys. Chem. C*, *122*, 13277-13284. (DOI: 10.1021/acs.jpcc.7b08448)
37. Haram S. K., Kshirsagar A., Gujarathi Y. D., Ingole P. P., Nene O. A., Markad G. B., Nanavati S. P. (2011), Quantum confinement in CdTe quantum dots: Investigation through cyclic voltammetry supported by density functional theory (DFT), *J. Phys. Chem. C*, *115*, 6243-6249. (DOI: 10.1021/jp111463f)
38. Qin F., Chang N., Xu C., Zhu Q., Wei M., Zhu Z., Chen F., Lu J. (2017), Underlying mechanism of blue emission enhancement in Au decorated p-GaN film, *RSC Adv.*, *7*, 15071-15076. (DOI: 10.1039/C7RA01193H)

39. Paramelle D., Sadovoy A., Gorelik S., Free P., Hobley J., Fernig D. G. (2014), A rapid method to estimate the concentration of citrate capped silver nanoparticles from UV-visible light spectra, *Analyst*, *139*, 4855-4861. (DOI: 10.1039/C4AN00978A)
40. Scanlon M. D., Peljo P., Méndez M. A., Smirnov E., Girault H. H. (2015), Charging and discharging at the nanoscale: Fermi level equilibration of metallic nanoparticles, *Chem. Sci.*, *6*, 2705-2720. (DOI: 10.1039/C5SC00461F)
41. Liu J.-L., Yang Y.-T., Lin C.-T., Yu Y.-J., Chen J.-K., Chu L.-K. (2017), Monitoring the transient thermal infrared emission of gold nanoparticles upon photoexcitation with a step-scan fourier-transform spectrometer, *J. Phys. Chem. C*, *121*, 878-885. (DOI: 10.1021/acs.jpcc.6b10044)
42. Liu X., Atwater M., Wang J., Huo Q. (2007), Extinction coefficient of gold nanoparticles with different sizes and different capping ligands, *Colloids surf.*, *58*, 3-7. (DOI: 10.1016/j.colsurfb.2006.08.005)
43. Jain P. K., Lee K. S., El-Sayed I. H., El-Sayed M. A. (2006), Calculated absorption and scattering properties of gold nanoparticles of different size, shape, and composition: Applications in biological imaging and biomedicine, *J. Phys. Chem. B*, *110*, 7238-7248. (DOI: 10.1021/jp057170o)
44. de Gennes P. G. (1980), Conformations of polymers attached to an interface, *Macromolecules*, *13*, 1069-1075. (DOI: 10.1021/ma60077a009)
45. Cruje, C., Chithrani, D. B., Cruje, C., Chithrani, D. B. (2014), Polyethylene glycol density and length affects nanoparticle uptake by

cancer cells. *J. Nanomed. Res.*, 1, 00006.
(DOI: 10.15406/jnmr.2014.01.00006)

Chapter 7

*Selective Uptake and Modulation of
Nanometal Surface Energy Transfer from
Quantum Dot to Au Nanoparticle Across
Lipid Bilayer of Liposomes*

7.1. Introduction

Functional nanoparticles (NPs) find tremendous importance in nanomedicine as diagnostic and therapeutic agents due to their inherent optical, electrical, and magnetic properties along with their unique physicochemical properties. Various hybrid NPs have been fabricated in recent times for a wide range of diagnostic and therapeutic applications [1-5]. Designing of functional NPs for nanomedicine applications require fundamental understanding of the interaction of these NPs with the cell membrane to minimize nanotoxicity [6]. Therefore, in-depth understanding of the interaction mechanism between functionalized NPs and cell membrane is essential to avoid nanotoxicity inside the cellular compartment. Various cell membrane mimicking systems such as micelles, liposomes, and polymersomes with biocompatible interfaces have been utilized to understand the fundamental interactions with various NPs [7-9]. Among these, the lipid bilayers of liposomes have been the subject of extensive studies due to their structural resemble with the cell membrane [10]. The NP-liposome hybrid nanocomposites are promising candidates for drug delivery, bio-imaging, and biosensors [11-18]. For example, Lira *et al.* demonstrated intracellular delivery of liposome-encapsulated hydrophilic CdTe QDs into live human stem cells and red blood cells [11]. Aizik *et al.* developed a liposome-based delivery system containing CdSe/CdZnS QDs and shown high accumulation and retention of these hybrid nanocomposites following intravenous administration in carotid-injured rats [14]. Till date, various mechanisms have been proposed for the spontaneous formation of NP-liposome nanocomposites depending on the size, shape, composition, and surface charge of both liposomes and NPs [19]. Moreover, a wide range of spectroscopic and microscopic techniques such as UV-vis, fluorescence, differential scanning calorimetry (DSC), small angle X-ray scattering (SAXS), transmission electron microscopy (TEM), atomic force microscopy (AFM), and dynamic light scattering (DLS) have been used to characterized NP-liposome hybrid nanocomposites [14,18-22]. Among these, fluorescence-based excitation energy transfer (EET) is a very sensitive and highly selective technique towards real

time monitoring of the location and the dynamic changes in the distance between donor and acceptor.

Nonradiative EET from a photoexcited donor to an acceptor via dipole-dipole interactions is well known as Förster resonance energy transfer (FRET) [23]. However, the classical FRET theory has serious limitation at large donor-acceptor separation distance (>10 nm) [24-28]. Moreover, the dipole-dipole FRET theory failed to account the distance dependency of the rate of EET for metal NP-based donor-acceptor systems [24-28]. Extensive studies have been performed to understand the highly efficient NP-based EET processes in various systems. EET from photoexcited donors to metal NPs is known as nanometal surface energy transfer (NSET) [24-28]. Both these EET theories have been extensively utilized to understand various complex chemical and biological processes across lipid bilayers of liposomes and cell membrane [29-36]. Here in this thesis, we have studied the selective uptake and partitioning of donor and acceptor across the lipid bilayer of liposome by monitoring the changes in the NSET efficiency. In the present study, we have used mercaptosuccinic acid-capped CdTe QD as donor and citrate-capped Au NP as acceptor. The partitioning of these donor and acceptor across the lipid bilayer of dipalmitoylphosphatidylcholine (DPPC) liposome has been explored as a function of time. Recently, we have demonstrated that similarly-charged CdTe QDs and Au NPs undergo long-range resonance coupling-induced NSET in bulk aqueous medium and explored the fundamental mechanism in great details [25]. The aim of the present study is to explore this long-range NSET process between MSA-capped CdTe QDs and citrate-capped Au NPs across the lipid bilayer of small unilamellar vesicles (SUV) of DPPC.

7.2. Results and Discussion

7.2.1. Interactions of QDs and Au NPs with Liposome

The interactions of QDs and Au NPs with the gel-phase of DPPC liposomes were monitored using UV-vis, PL spectroscopy, CLSM, and AFM. The absorption spectrum of QDs shows no appreciable change upon instant mixing (time= 0 h) with liposome (Figure 7.1a). The excitonic peak position of QDs remains unaltered at 492 nm in the presence of liposomes upon instant mixing. In contrast, significant changes in the excitonic absorption spectrum of QDs have been observed upon equilibrating the binary mixture of QDs and liposomes for 24 h.

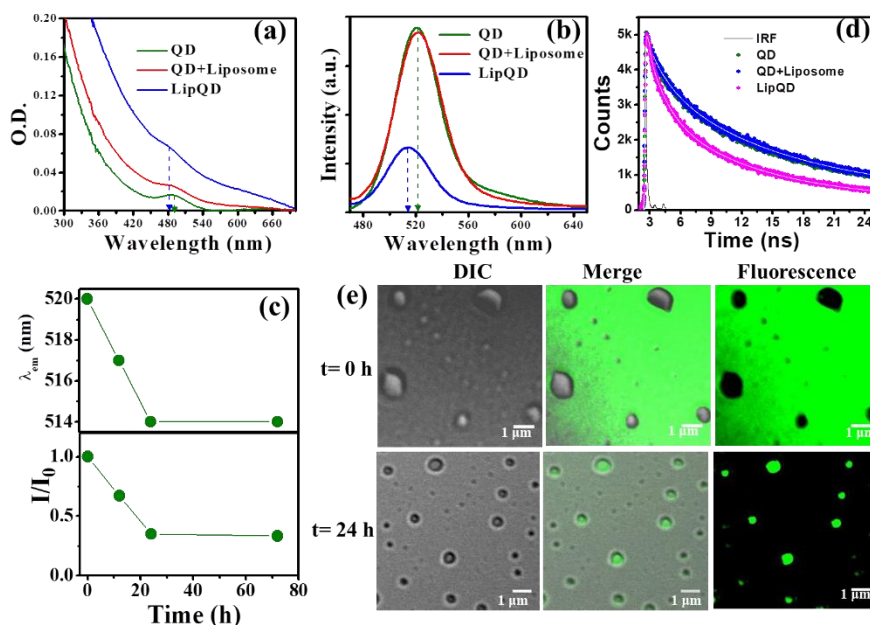


Figure 7.1. Change in the (a) absorption and (b) PL ($\lambda_{ex} = 450$ nm) spectra of CdTe QDs in the presence of liposome at 0 and 24 h of equilibration. (c) Change in the peak position and PL intensity ratio of CdTe QDs in the presence of liposome as a function of equilibration time. (d) PL lifetime decay traces ($\lambda_{ex} = 445$ nm; $\lambda_{em} = 520$ nm) of QDs in the absence and presence of liposomes at 0 and 24 h of equilibration. (e) Confocal images of QD-liposome binary mixtures at 0 and 24 h of equilibration.

The excitonic peak position of QDs shifts to 483 nm with a blue shift of 7 nm (Figure 7.1a). Moreover, the absorption spectrum gets broaden in the wavelength region between 600-700 nm (Figure 7.1a). The observed blue shift in the excitonic peak position of QDs in the binary mixture upon 24 h of equilibration indicates less polar microenvironment around QDs in the binary mixture and may arise due to the association of QDs with liposomes [37]. On the other hand, the broadening of the spectrum in the long wavelength region (600-700 nm) suggests some kind of exciton-exciton coupling between closely associated QDs inside the liposomes.

To gain further knowledge, we have recorded the PL spectrum of QDs in the presence of liposomes. Figure 7.1b displays the changes in PL spectrum of QDs in the absence and presence of liposomes. It is evident that the PL spectrum of QDs remains unaltered in the presence of liposomes upon instant mixing (0 h). However, significant changes in the PL spectrum of QDs have been observed upon equilibrating the mixture for 24 h. The PL intensity decreases appreciably (2.8 times) along with 6 nm blue shift in its PL peak position (Figure 7.1b). The kinetic aspect of their interaction has been explored by monitoring the PL properties of QDs as a function of equilibration time in the presence of the liposome. A continuous decrease in the PL peak position as well as in PL intensity has been observed as a function of equilibration time (Figure 7.1c). Notably, both these parameters saturate beyond 24 h of equilibration (Figure 7.1c). These findings clearly indicate that the interaction of QDs with the gel-phase of DPPC liposome depends on the equilibration time.

To further substantiate our claim from steady-state PL measurements, we have performed PL lifetime measurements of QDs in the absence and presence of liposomes as a function of equilibration time. Figure 7.1d displays the PL lifetime decay curves ($\lambda_{ex} = 445$ nm; $\lambda_{em} = 520$ nm) of QDs in the absence and presence of liposomes as a function of equilibration time. The PL decay curve of CdTe QD fits satisfactorily with a three exponential decay function (Figure 7.1d and

Table 7.1). The fitted decay parameters reveal three-lifetime components of 13.75 (54%), 2.68 (30%), and 0.34 ns (16%) and the average lifetime is determined to be 8.27 ns. The observed multiexponential decay profile of CdTe QDs is due to various radiative decay channels involving band edge and different trap states.²⁵ The 2.68 ns component can be assigned due to the band edge exciton recombination, the shortest (0.34 ns) and longest lifetime (13.75 ns) component arise due to the presence of deep and shallow trap states, respectively. The decay trace and the average PL lifetime of QDs remain unchanged upon instant mixing with liposomes, indicating absence of any interaction (Figure 7.1d and Table 7.1).

Table 7.1. PL lifetime decay parameters of CdTe QD in the absence and presence of Au NPs and liposome at different incubation times.

Samples	τ_1 (ns)	a_1	τ_2 (ns)	a_2	τ_3 (ns)	a_3	$\langle\tau\rangle$ (ns)	χ^2
Incubation time = 0 h								
CdTe QD	0.34	0.16	2.68	0.30	13.75	0.54	8.27	1.00
QD + 80pM Au NP	0.09	0.40	1.57	0.28	8.84	0.32	3.31	1.00
Liposome + QD	0.30	0.17	2.79	0.32	14.19	0.51	8.20	1.00
Liposome+QD+Au NP	0.11	0.40	1.60	0.28	9.09	0.32	3.30	1.03
Incubation time = 24 h								
LipQD	0.14	0.40	1.61	0.29	8.74	0.32	3.28	1.10
LipQD + Au NP	0.14	0.40	1.61	0.29	8.73	0.32	3.27	1.09
AuLipQD	0.09	0.46	1.34	0.26	7.33	0.28	2.50	1.05

This observation is similar to that has been observed earlier in steady-state measurements. However, the PL lifetime decreases from 8.27 to 3.28 ns upon equilibrating the binary mixture for 24 h (Figure 7.1d, Table 7.1). These findings clearly indicate that the interaction of QDs with the gel phase of DPPC liposome is time-dependent. Moreover, our steady-state and time-resolved data indicate the formation of QD-liposome hybrid nanocomposite upon 24 h of equilibration.

Next, we have performed CLSM to further explore the nature of these hybrid nanocomposites and the location of QDs inside the liposomal matrix. CLSM measurements have been performed at two different equilibration time, namely 0 and 24 h to substantiate the time-dependent association between QDs and liposomes. The differential interference contrast (DIC) image at 0 h reveals the presence of spherical liposomes (Figure 7.1e). However, the fluorescence and merged images of the QD-liposome binary mixture upon instant mixing reveal lack of any green luminescence from liposomes, instead liposomes appear as dark in the background of intense green luminescence from free QDs. This observation clearly suggests lack of any specific association between QDs and DPPC liposomes upon instant mixing. On the other hand, totally contrasting behavior has been observed upon equilibrating the mixture for 24 h. It is evident from the DIC image that the shape of the liposomes does not change upon equilibrating the mixture for 24 h (Figure 7.1e). More importantly, the fluorescence image reveals distinct green luminescent spherical spots. The merged image unambiguously shows that the green luminescence appears exclusively from the core of liposomes (Figure 7.1e). Here, it would be interesting to correlate our findings from UV-vis and PL measurements with those obtained from CLSM. The absence of any spectral changes upon instant mixing (0 h) of QDs and liposomes indicates lack of any specific association. CLSM reveals that upon instant mixing, QDs mainly remain in the bulk aqueous phase and do not interact with liposomes. In contrast, significant PL quenching of QDs along with 6 nm blue shift in its PL peak position upon equilibrating the mixture for 24 h suggest strong exciton-exciton

coupling between adjacent QDs and less polar microenvironment surrounding QDs. CLSM measurement reveals that these spectral changes arise due to the encapsulation of QDs into the less polar aqueous core of liposomes. Therefore, our findings reveal that equilibrating the QD-liposome binary mixture for 24 h results in the formation of liposome encapsulated QDs (LipQD). The formation of these LipQD nanocomposites can be rationalized by considering diffusion of QDs from bulk aqueous medium to liposome core through the lipid bilayer. Notably, this diffusion of QDs through the lipid bilayer of zwitterionic DPPC liposomes may be facilitated by favorable electrostatic as well as van der Waals interactions. Similar uptake of small-sized QDs into the liposomal matrix has been demonstrated earlier [16,38-40] For example, Zhou *et al.* fabricated liposome-QD hybrid nanocomposites by incorporating 2.80 ± 0.25 and 4.60 ± 0.34 nm-sized QDs into the hydrophobic lipid bilayer without perturbing the liposome integrity [16]. Zheng *et al.* demonstrated the phase-dependent structure, photostability, and site-selective functionalization of 3.0 nm-sized CdSe QDs encapsulated within phospholipid membranes [38]. Recently, Wlodek *et al.* shown that hydrophobic CdS QDs with diameter of 2.7-5.4 nm can be successfully incorporated into the hydrophobic lipid bilayer [39]. Similarly, Lehn *et al.* studied the size-dependent spontaneous penetration of monolayer protected gold (Au) NPs with lipid bilayers of liposomes and shown that the critical first step in the penetration process was the fusion of Au NPs with lipid bilayers [40]. Moreover, using free energy calculations it has been shown that the fusion of Au NPs with lipid bilayers was favorable below a critical Au NP size of 3.5 nm. Furthermore, our findings clearly indicate that penetration of 2.3 ± 0.5 nm sized CdTe QDs into the liposome core via lipid bilayer of DPPC liposomes is quite feasible without perturbing the integrity of the lipid bilayer and the morphology of the liposomes.

The interaction of Au NPs with DPPC liposomes has been monitored using UV-vis and AFM measurements. Figure 7.2a displays the changes in the absorption spectrum of Au NPs in the absence and presence of

liposomes. The LSPR peak of Au NPs appears at 520 nm in aqueous phosphate buffer. The shape and peak position of the LSPR band of Au NPs remain unchanged upon instant mixing with liposome ($t=0$ h). However, the LSPR band of Au NPs displays a red shift of 7 nm upon equilibration with liposomes for 24 h (Figure 7.2a).

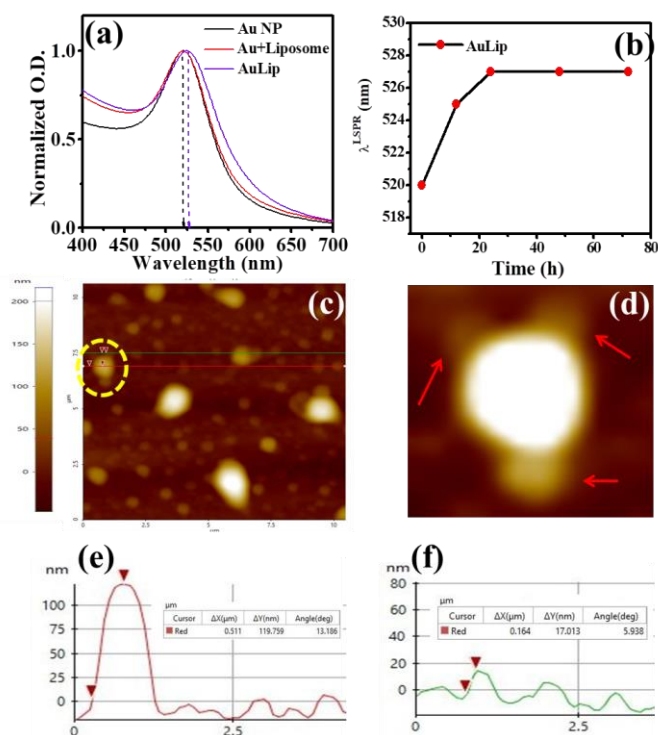


Figure 7.2. (a) Changes in the absorption spectra of Au NPs in the presence of liposome at 0 and 24 h of equilibration. (b) Plot of LSPR peak positions of Au NPs in the presence of liposome against equilibration time. (c) AFM image of liposome-Au NP system after 24 h of equilibration. (d) Magnified AFM image showing the adsorption of Au NPs on the surface of liposome (red arrows indicate adsorbed Au NPs). Cross-section analysis of liposome-Au NPs system for (e) liposome, and (f) adsorbed Au NP.

Notably, no new peak or shoulder appears in the long wavelength region, indicating absence of any aggregation of Au NPs [24]. The observed red shift indicates changes in the dielectric constant of the surrounding environment of Au NPs upon equilibration with liposomes. Moreover, it has been observed that spectral shift of the LSPR band

saturates beyond 24 h of equilibration (Figure 7.2b). Previously, numerous studies have been undertaken to understand the adsorption, stability, and membrane integrity of liposomes in the presence of various NPs [21, 22, 41-42]. The observed changes in the LSPR band of Au NPs in the presence of liposomes upon 24 h of equilibration indicate association between Au NPs and liposomes. To know the nature of these nanocomposites and the bilayer integrity of liposomes, we have performed AFM measurements. AFM image of the Au NP-liposome binary mixture upon 24 h of equilibration reveals well dispersed spherical liposomes. Careful examination of the surface of these spherical liposomes reveals the presence of surface adsorbed Au NPs (Figure 7.2c and d). The enlarged image clearly indicates the presence of Au NPs on the surface of spherical liposome (Figure 7.2d red arrows). More importantly, it is evident that the adsorption of Au NPs does not disrupt the shape and integrity of liposomes.

The cross-section analysis of AFM image further confirms the presence of Au NP at the surface of the liposome (Figure 7.2e and f). The cross-section analysis reveals the expected diameter of 119.8 and 17 nm for liposome and adsorbed Au NP, respectively. These findings clearly indicate the formation of Au NP-liposome nanocomposites (AuLip) upon equilibrating the mixture for 24 h. Here it is important to mention that favourable electrostatic interactions between negatively-charged Au NPs and zwitterionic DPPC liposomes may initiate the adsorption process. However, unlike QDs, these relatively larger-sized Au NPs cannot internalize inside the liposomal matrix which is reasonable as the lipid bilayer is quite compact in its gel phase. Earlier, Liu *et al.* shown that the integrity and morphology of DPPC liposomes in the gel phase do not perturbed in the presence of 13 nm-sized citrate-capped Au NPs [43]. Moreover, It has been shown that DOPC liposome with transition temperature (T_c) of $-17\text{ }^{\circ}\text{C}$ exhibits leakage in the presence of Au NPs.

Taken together, our findings reveal the formation of LipQD and AuLip hybrid nanocomposites upon equilibrating the respective binary

mixtures for 24 h. Next, we have explored the possibility of the fabrication of multi-component hybrid ternary complex between QDs, Au NPs, and liposomes upon simple equilibration. The ternary mixture was equilibrated for 24 h and characterized using CLSM measurements. Figure 7.3 shows the CLSM images of the ternary mixture. The DIC image reveals the presence of well-dispersed spherical liposomes. The enlarged DIC image clearly shows the adsorbed Au NPs on the surface of spherical liposomes (Figure 7.3 inset). The fluorescence and merged images reveal distinct green luminescence from these spherical liposomes indicating the presence of encapsulated QDs. These observations clearly reveal the formation of multi-component hybrid nanocomposites between QDs, Au NPs, and liposomes (AuLipQD) upon equilibration for 24 h. Here it is important to note that the relative intensity of the green luminescence from the liposome encapsulated QDs in AuLipQD nanocomposite is quenched noticeably relative to that in the absence of Au NPs (LipQD). The mechanism behind this PL quenching of encapsulated QDs in AuLipQD nanocomposites has been explored in details using steady-state and time-resolved PL measurements in the next section.

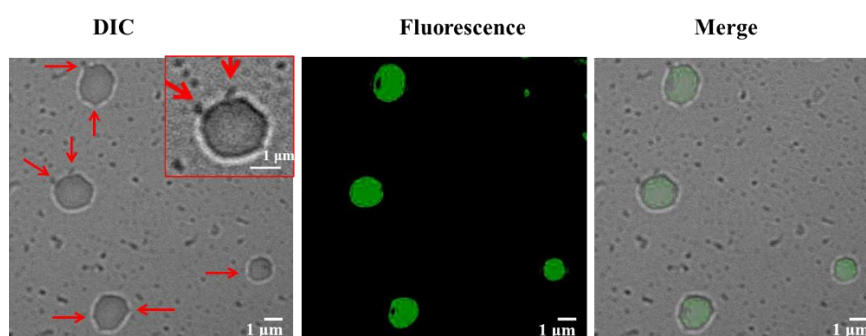


Figure 7.3. Confocal microscopy images of AuLipQD complex upon 24 h of equilibration. The inset shows the enlarged DIC image of surface adsorbed Au NPs on a liposome. The red arrows in the DIC image indicate surface adsorbed Au NPs.

7.2.2. Influence of Au NPs on the PL Properties of LipQD and AuLipQD Nanocomposites

Figure 7.4 shows the spectral overlap between the PL spectrum of QDs and LSPR of Au NPs in the absence and presence of liposome.

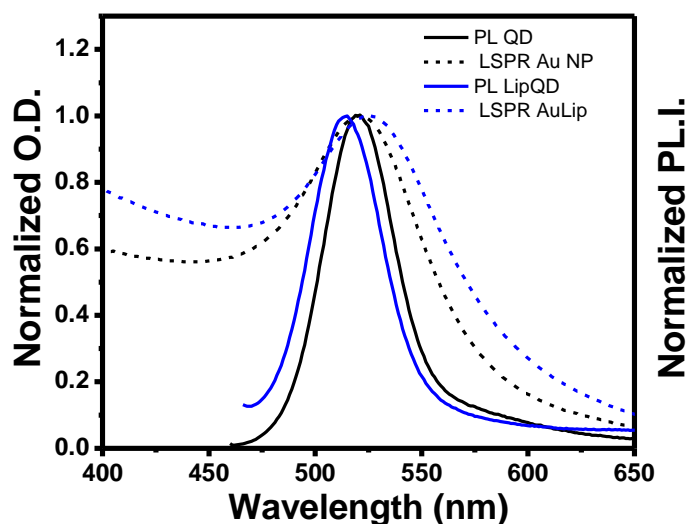


Figure 7.4. Spectral Overlap between PL spectra of QDs and LSPR band of Au NPs in the absence and presence of liposomes for the present system.

It is evident that the PL spectrum of QDs completely overlaps with the LSPR of Au NPs in the absence of liposome. However, the spectral overlap decreases in the presence of liposomes. The estimated spectral overlap integral for the QD-Au NP pair in bulk and AuLipQD system is 5.5×10^{-9} and $5.2 \times 10^{-9} \text{ M}^{-1} \text{ cm}^3$, respectively (Figure 7.4). Notably, the PL intensity of QDs alone gets quenched in the presence of 80 pM Au NPs (Figure 7.5a).

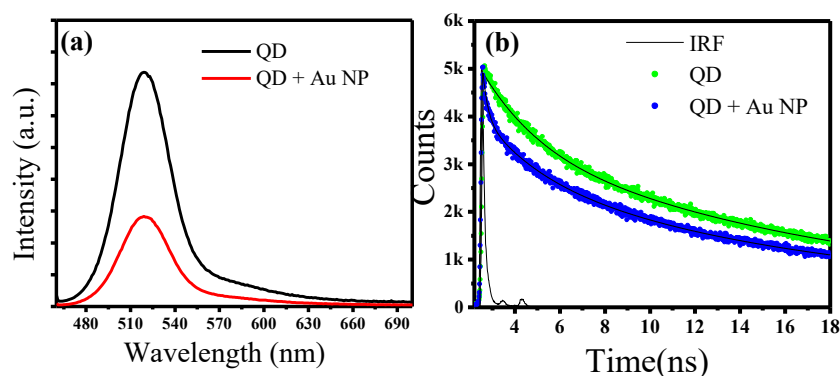


Figure 7.5. Changes in the (a) PL spectra and (b) PL decay traces of QDs in the presence of 80 pM Au NPs.

Here it is important to mention that the PL intensity of QDs was corrected for the contribution of the extinction spectrum of Au NPs at the excitation wavelength [25]. Similar extent of quenching in the PL lifetime of QDs has been observed in the presence of 80 pM Au NPs (Figure 7.5b). The average PL lifetime decreases from 8.27 ns to 3.31 ns in the presence of 80 pM Au NPs (Table 7.1). These findings indicate the role of nonradiative processes in the PL quenching process. The fundamental mechanism behind this nonradiative PL quenching in bulk aqueous medium has been demonstrated recently by our group [25]. It has been shown that the nonradiative PL quenching of 2.1 ± 0.7 nm-sized MSA-capped CdTe QD by 20.4 ± 3.1 nm-sized citrate-capped Au NP in bulk aqueous medium does not follow classical FRET process, instead it follows the NSET model. By considering the complex dielectric function and the size-dependent absorptivity of the Au NP we have successfully account the observed nonradiative NSET process. The aim of the present study is to illustrate the effect of partitioning of donor and acceptor inside the gel-phase of DPPC liposome on the long-range NSET process between 2.3 ± 0.5 nm-sized MSA-capped CdTe QDs and 18.0 ± 0.2 nm-sized citrate-capped Au NPs.

In the present study, we have prepared two-nanocomposites namely, LipQD and AuLipQD by equilibrating the respective mixtures

for 24 h. For control experiments, we have also prepared simple ternary mixture with QDs, liposomes, and Au NPs without equilibration (0 h).

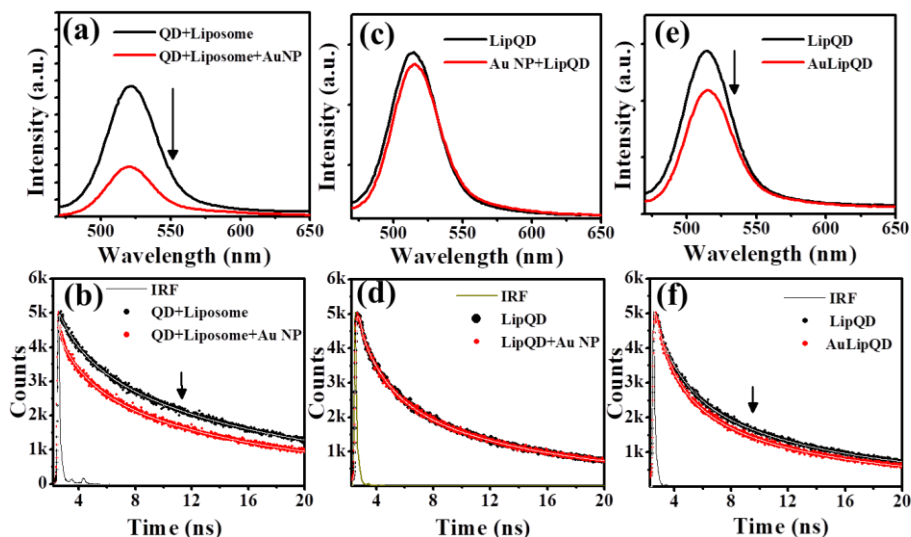


Figure 7.6. Changes in the PL spectra ($\lambda_{\text{ex}} = 450 \text{ nm}$) of QDs in the presence of Au NPs for (a) QD-Liposome, (c) LipQD, and (e) AuLipQD systems. Changes in the PL lifetime decay traces ($\lambda_{\text{ex}} = 445 \text{ nm}$; $\lambda_{\text{em}} = 520 \text{ nm}$) of QDs in the presence of Au NPs for (b) QD-liposome, (d) LipQD, and (f) AuLipQD systems.

Figure 7.6a shows the changes in the PL spectrum of QDs upon instant mixing with liposomes in the presence of 80 pM Au NPs. It is evident that the PL intensity of QDs in the ternary mixture gets quenched (2.6 times) upon addition of 80 pM Au NPs. Similar extent of quenching has been observed in bulk aqueous medium without liposomes (Figure 7.5).

PL lifetime measurements of the ternary mixture at 0 h reveal shortening of PL lifetime (2.5 times) of QDs in the presence of Au NPs (Figure 7.6b). The PL lifetime of QDs in the simple ternary mixture decreases to 3.30 ns in the presence of 80 pM Au NPs (Table 7.1). These findings clearly indicate that the donor (QD) and acceptor (Au NP) remain in bulk aqueous phase and do not interact with liposomes upon instant mixing. In contrast, no appreciable change in the PL spectrum of LipQD nanocomposites has been observed upon addition of Au NP

(Figure 7.6 c). Moreover, the PL lifetime of QDs in LipQD nanocomposites remains unchanged upon instant addition of Au NPs (Figure 7.6 d). The estimated average lifetime of QDs in LipQD nanocomposites is 3.27 ns in the presence of 80 pM Au NPs (Table 7.1), which is close to that of LipQD nanocomposite alone. These findings indicate the absence of any interaction between Au NPs and liposome encapsulated QDs in LipQD nanocomposites.

However, notable changes in the PL intensity as well as in PL lifetime of QDs in AuLipQD nanocomposites have been observed compared to that of LipQD nanocomposites. The PL intensity of QDs decreases appreciably (1.3 times) upon formation of AuLipQD nanocomposite relative to that of LipQD nanocomposites (Figure 7.6e). This decrease in the PL intensity is relatively less than that observed earlier in the absence of liposomes indicating lower extent of EET between encapsulated QD and surface-adsorbed Au NP. To validate this point, we have recorded the changes in the PL lifetime of QDs in the AuLipQD nanocomposites. The average PL lifetime of QDs decreases from 3.28 to 2.50 ns upon formation of AuLipQD nanocomposite (Figure 7.6 f, Table 7.1).

The origin behind the observed PL quenching in the AuLipQD nanocomposite can be rationalized by considering EET as a consequence of significant spectral overlap between LSPR of surface adsorbed Au NPs (AuLip) and excitonic emission of liposome-encapsulated QDs (LipQD) (Figure 7.4) [25]. The decrease in the PL lifetime of QD in the presence of Au NPs suggests changes either in the radiative or nonradiative decay rate. The radiative and nonradiative decay rates of QDs in the nanocomposites were estimated according to the literature report (Table 7.2) [25]. It is evident that the radiative decay rate of QD in LipQD and AuLipQD nanocomposites remains unaltered in the presence of Au NPs. In contrast, the nonradiative decay rate of QD in AuLipQD nanocomposite increases appreciably compared to bare QDs and LipQD system. This increase in the nonradiative decay rate of

QDs inside AuLipQD nanocomposite can be explained by considering nonradiative EET from liposome encapsulated QD to surface adsorbed Au NP across the lipid bilayer. Here it is important to note that the significant increase (0.09×10^9 to 0.28×10^9 s⁻¹) in the nonradiative decay rate of QDs in LipQD nanocomposite compared to bare QDs strongly substantiates our earlier claim of nonradiative exciton-exciton coupling between adjacent QDs inside liposome core. The efficiency (ϕ_{Eff}) of this nonradiative EET process is estimated using the following equations:

$$\phi_{\text{Eff}} = 1 - \frac{\phi_{D-A}}{\phi_D} = 1 - \frac{\tau_{D-A}}{\tau_D} \quad (1)$$

where ϕ_{D-A} and ϕ_D are the steady-state quantum yields of QDs in the presence and absence of Au NPs, respectively. τ_{D-A} and τ_D are the excited-state lifetimes of QDs in the presence and absence of Au NPs, respectively. The estimated EET efficiencies from the lifetime values are 62 and 24% for QD-AuNP pair in bulk aqueous medium and AuLipQD nanocomposites, respectively. These values match well with those estimated from steady-state PL QY values (Table 7.2). The observed decrease in the ϕ_{Eff} value clearly indicates lower extent of EET from liposome-encapsulated QD to surface adsorbed Au NP in AuLipQD nanocomposite compared to that in bulk aqueous medium. The observed EET could be account either by considering classical FRET model or NSET model. The estimated R_0 values for QD-Au NP in bulk aqueous medium and AuLipQD nanocomposite are 22.3 and 19.3 nm, which are well beyond the expected range of conventional FRET theory [23-25].

Table 7.2. Estimated EET parameters of QD and Au NPs pair in the absence and presence of liposomes.

Systems	ϕ_D	$\langle\tau\rangle$ (ns)	k_r ($\times 10^9 \text{ s}^{-1}$)	k_{nr} ($\times 10^9 \text{ s}^{-1}$)	k_{ET} ($\times 10^9 \text{ s}^{-1}$)	ϕ_{ET} (τ)
QD	0.20	8.30	0.02	0.09	-	-
QD + Au NP	0.08	3.31	0.02	0.27	0.18	0.62
LipQD	0.08	3.28	0.02	0.28	-	-
AuLipQD	0.05	2.50	0.02	0.38	0.10	0.24
LipQD+ Au NP	0.08	3.27	0.02	0.28	-	-

In the past few decades, various theoretical models have been developed to account the PL quenching of photoexcited donors by metal NPs. Fluorescence quenching of an oscillating dipole on a thin metal surface was described earlier by Chance *et al.* [44] and extended further by Persson and Lang to the metal's conduction electrons and known as surface energy transfer (SET) [45]. Although the original SET model is applicable for a thin metal film, it successfully accounts the experimentally observed nonradiative EET from various molecular dyes to small Au NPs (<2 nm) [27-28]. However, it fails to accurately envisage the observed changes in the radiative and nonradiative rate constants of donors in the presence of larger-sized metal NPs [46, 47]. This is due to the inability of the model to account the size-dependent dielectric and optical properties of the metal NPs [48]. Recently, we have demonstrated NSET between differently-sized CdTe QDs and Au NPs by incorporating the complex dielectric function and the absorptivity of the Au NP [25]. According to this modified NSET model, the distance d_0 at which the nonradiative EET is 50% efficient can be estimated from the following expression:

$$d_0 = \frac{\alpha\lambda}{n_m} (A\phi)^{1/4} \left\{ \frac{n_r}{2n_m} \left(1 + \frac{\varepsilon_1^2}{|\varepsilon_2|^2} \right) \right\}^{1/4} \quad (2)$$

Here α is an orientation factor [48], λ is the emission wavelength of donor, n_m is the refractive index of water, n_r is the refractive index of gold, Φ is the quantum yield of donor, ϵ_1 is the dielectric constant of water, and ϵ_2 is the dielectric constant of gold and A is the absorptivity of the Au NP. The absorptivity of Au NPs can be expressed as follows:

$$A_{\text{NP}} = 10^3 \ln(10) \left[\frac{\epsilon_\lambda \left(2r_{\text{cm}} \left(\frac{2r_{\text{cm}}}{\delta_{\text{skin}}} \right) \right)}{N_A V_{\text{cm}^3}} \right] \quad (3)$$

Here ϵ_λ is the extinction coefficient of the Au NPs at the maximum emission wavelength of QDs, r_{cm} is the radius of the Au NP in cm, δ_{skin} is the skin depth of the Au NP, N_A is the Avogadro's number, and V_{cm} is the volume of the Au NP in cm^3 . The calculated dielectric function and absorptivity values for the present system are tabulated in Table 7.3.

Table 7.3 Experimental and theoretical size-dependent NSET parameters for QD and LipQD complex in the presence of 80 pM Au NP.

Donor	λ_{max} (nm)	n_r	r_{NP} (10^{-7} cm)	ϵ_{NP} (M.cm) ⁻¹	d_0 (nm)	ϵ_2'	ϵ_2''	$ \epsilon_2 ^2$	δ_{skin} (10^{-7} cm)
QD	520	0.62	9.0	6.51×10^8	21.2	-5.2	3.0	36.0	34.6
LipQD	514	0.62	9.0	6.68×10^8	15.7	-4.9	3.2	34.3	35.0

The estimated d_0 value for the LipQD-AuLip pair in AuLipQD nanocomposite is 15.7 nm (Table 7.3). Notably, the d_0 value of QD-Au NP pair in absence of liposome shows a value of 21.2 nm, which is close to the earlier reported value [25]. The average separation distance between liposome-encapsulated QDs and the surface adsorbed Au NPs is estimated from experimentally obtained efficiency (ϕ_{Eff}) and calculated d_0 values according to the following equation:

$$\phi_{\text{Eff}} = \frac{1}{1 + \left(\frac{d}{d_0}\right)^4} \quad (4)$$

The estimated average separation distance between encapsulated QDs and the surface of adsorbed Au NPs is 21.0 nm for AuLipQD nanocomposites, which is comparatively higher than that in the absence of liposome. Notably, the average separation distance increases from a value of 18.7 to 21.0 nm upon formation of AuLipQD nanocomposite. This increase in the separation distance of QD-Au NP pair is due to complete encapsulation of CdTe QDs inside the liposome core and absorption of Au NPs on the surface of the liposome. Therefore, our present findings reveal that NSET can be a useful technique for monitoring real-time partition of donor and acceptor across the lipid bilayer of liposomes. Moreover, the present study also shines light on the fundamental interaction of negatively-charged CdTe QD and Au NPs with the gel phase of DPPC liposome. These findings may be useful to understand the interactions of various functional NPs with cell membrane for bio-imaging and sensing applications.

7.3. Conclusion

The effect of partitioning of donor and acceptor inside DPPC liposome on the extent of EET has been demonstrated using PL spectroscopy and CLSM. Au NPs efficiently quench the PL of CdTe QDs by nonradiative NSET process in bulk aqueous medium. Modulation of this NSET process across the lipid bilayer of DPPC liposome has been demonstrated in the present study. It has been observed that the extent of NSET between QDs and Au NPs does not alter in the presence of DPPC liposome upon instant mixing. However, the NSET process completely disappears upon formation of LipQD nanocomposite, where QDs are selectively encapsulated into the aqueous core of liposomes. This has been explained by considering increased separation distance between donor (LipQD) and acceptor (Au NPs). Interestingly, the formation of AuLipQD nanocomposites results in the reappearance of NSET between encapsulated QDs and adsorbed Au NPs at the surface of liposomes. It has been observed that the efficiency of NSET decreases

from 62% in bulk aqueous medium to 24% in AuLipQD nanocomposites due to the increase in the effective mean separation distance from 18.7 to 21.0 nm. Our present findings of selective uptake and modulation of NSET between QDs and Au NPs across the lipid bilayer of DPPC liposomes may find importance in understanding various fundamental biophysical processes across the lipid bilayer and biological cell membrane.

7.4. References

1. Nguyen K. T., Zhao Y. (2015), Engineered hybrid nanoparticles for on-demand diagnostics and therapeutics, *Acc. Chem. Res.*, *48*, 3016-3025. (DOI: 10.1021/acs.accounts.5b00316)
2. Kostevšek N., Žužek Rožman K., Arshad M. S., Spreitzer M., Kobe S., Šturm S. (2015), Multimodal hybrid FePt/SiO₂/Au nanoparticles for nanomedical applications: Combining photothermal stimulation and manipulation with an external magnetic field, *J. Phys. Chem. C*, *119*, 16374-16382. (DOI: 10.1021/acs.jpcc.5b03725)
3. Katagiri K., Ohta K., Sako K., Inumaru K., Hayashi K., Sasaki Y., Akiyoshi K. (2014), Development and potential theranostic applications of a self-assembled hybrid of magnetic nanoparticle clusters with polysaccharide nanogels, *ChemPlusChem*, *79*, 1631-1637. (DOI: 10.1002/cplu.201402159)
4. Hadipour Moghaddam S. P., Saikia J., Yazdimamaghani M., Ghandehari H. (2017), Redox-responsive polysulfide-based biodegradable organosilica nanoparticles for delivery of bioactive agents, *ACS Appl. Mater. Interfaces*, *9*, 21133-21146. (DOI: 10.1021/acsami.7b04351)
5. Simon-Yarza T., Giménez-Marqués M., Mrimi R., Mielcarek A., Gref R., Horcajada P., Serre C., Couvreur P. (2017), A smart metal-organic framework nanomaterial for lung targeting, *Angew. Chem., Int. Ed.*, *56*, 15565-15569. (DOI: 10.1002/anie.201707346)
6. Nagy A., Robbins N. L. (2019), The hurdles of nanotoxicity in transplant nanomedicine, *Nanomedicine*, *14*, 2749-2762. (DOI: 10.2217/nnm-2019-0192)
7. Chatterjee S., Mukherjee T. K. (2013), Size-dependent differential interaction of allylamine-capped silicon quantum dots with surfactant assemblies studied using photoluminescence spectroscopy

and imaging technique, *J. Phys. Chem. C*, *117*, 10799-10808. (DOI: 10.1021/jp402408d)

8. Živanović V., Kochovski Z., Arenz C., Lu Y., Kneipp J. (2018), SERS and cryo-EM directly reveal different liposome structures during interaction with gold nanoparticles, *J. Phys. Chem. Lett.*, *9*, 6767-6772. (DOI: 10.1021/acs.jpcllett.8b03191)

9. Hickey R. J., Haynes A. S., Kikkawa J. M., Park S.-J. (2011), Controlling the self-assembly structure of magnetic nanoparticles and amphiphilic block-copolymers: From micelles to vesicles, *J. Am. Chem. Soc.*, *133*, 1517-1525. (DOI: 10.1021/ja1090113)

10. Rideau E., Dimova R., Schwille P., Wurm F. R., Landfester K. (2018), Liposomes and polymersomes: a comparative review towards cell mimicking, *Chem. Soc. Rev.*, *47*, 8572-8610. (DOI: 10.1039/C8CS00162F)

11. Lira R. B., Seabra M. A. B. L., Matos A. L. L., Vasconcelos J. V., Bezerra D. P., de Paula E., Santos B. S., Fontes A. (2013), Studies on intracellular delivery of carboxyl-coated CdTe quantum dots mediated by fusogenic liposomes, *J. Mater. Chem. B*, *1*, 4297-4305. (DOI: 10.1039/C3TB20245C)

12. Mukthavaram R., Wrasidlo W., Hall D., Kesari S., Makale M. (2011), Assembly and targeting of liposomal nanoparticles encapsulating quantum dots, *Bioconjugate Chem.*, *22*, 1638-1644. (DOI: 10.1021/bc200201e)

13. Bothun G. D., Rabideau A. E., Stoner M. A. (2009), Hepatoma cell uptake of cationic multifluorescent quantum dot liposomes, *J. Phys. Chem. B*, *113*, 7725-7728. (DOI: 10.1021/jp9017458)

14. Aizik G., Waiskopf N., Agbaria M., Levi-Kalisman Y., Banin U., Golomb G. (2017), Delivery of liposomal quantum dots via

monocytes for imaging of inflamed tissue, *ACS Nano*, *11*, 3038-3051. (DOI: 10.1021/acsnano.7b00016)

15. Hao N., Zhang Y., Zhong H., Zhou Z., Hua R., Qian J., Liu Q., Li H., Wang K. (2017), Design of a dual channel self-reference photoelectrochemical biosensor, *Anal. Chem.*, *89*, 10133-10136. (DOI: 10.1021/acs.analchem.7b03132)

16. Zhou J., Wang Q.-x., Zhang C.-y. (2013), Liposome–quantum dot complexes enable multiplexed detection of attomolar DNAs without target amplification, *J. Am. Chem. Soc.*, *135*, 2056-2059. (DOI: 10.1021/ja3110329)

17. Beloglazova N. V., Shmelin P. S., Speranskaya E. S., Lucas B., Helmbrecht C., Knopp D., Niessner R., De Saeger S., Goryacheva I. Y. (2013), Quantum dot loaded liposomes as fluorescent labels for immunoassay, *Anal. Chem.*, *85*, 7197-7204. (DOI: 10.1021/ac401729y)

18. De Leo V., Milano F., Paiano A., Bramato R., Giotta L., Comparelli R., Ruscigno S., Agostiano A., Bucci C., Catucci L. (2017), Luminescent CdSe@ZnS nanocrystals embedded in liposomes: A cytotoxicity study in HeLa cells, *Toxicol. Res.*, *6*, 947-957. (DOI: 10.1039/c7tx00172j)

19. Liu J. (2016), Interfacing zwitterionic liposomes with inorganic nanomaterials: Surface forces, membrane integrity, and applications, *Langmuir*, *32*, 4393-4404. (DOI: 10.1021/acs.langmuir.6b00493)

20. Kojima C., Hirano Y., Yuba E., Harada A., Kono K. (2008), Preparation and characterization of complexes of liposomes with gold nanoparticles, *Colloids Surf. B*, *66*, 246-252. (DOI: <https://doi.org/10.1016/j.colsurfb.2008.06.022>)

21. Xing X., Ma W., Zhao X., Wang J., Yao L., Jiang X., Wu Z. (2018), Interaction between surface charge-modified gold nanoparticles

- and phospholipid membranes, *Langmuir*, *34*, 12583-12589. (DOI: 10.1021/acs.langmuir.8b01700)
22. Liu Y., Liu J. (2016), Adsorption of nanoceria by phosphocholine liposomes, *Langmuir*, *32*, 13276-13283. (DOI: 10.1021/acs.langmuir.6b03342)
23. Scholes G. D. (2003), Long-range resonance energy transfer in molecular systems, *Annu. Rev. Phys. Chem.*, *54*, 57-87. (DOI: 10.1146/annurev.physchem.54.011002.103746)
24. Prajapati R., Chatterjee S., Bhattacharya A., Mukherjee T. K. (2015), Surfactant-induced modulation of nanometal surface energy transfer from silicon quantum dots to silver nanoparticles, *J. Phys. Chem. C*, *119*, 13325-13334. (DOI: 10.1021/acs.jpcc.5b02903)
25. Mondal N., Samanta A. (2016), Ultrafast charge transfer and trapping dynamics in a colloidal mixture of similarly charged CdTe quantum dots and silver nanoparticles, *J. Phys. Chem. C*, *120*, 650-658. (DOI: 10.1021/acs.jpcc.5b08630)
26. Prajapati R., Bhattacharya A., Mukherjee T. K. (2016), Resonant excitation energy transfer from carbon dots to different sized silver nanoparticles, *Phys. Chem. Chem. Phys.*, *18*, 28911-28918. (DOI: 10.1039/C6CP05451J)
27. Yun C. S., Javier A., Jennings T., Fisher M., Hira S., Peterson S., Hopkins B., Reich N. O., Strouse G. F. (2005), Nanometal surface energy transfer in optical rulers, breaking the FRET barrier, *J. Am. Chem. Soc.*, *127*, 3115-3119. (DOI: 10.1021/ja043940i)
28. Jennings T. L., Singh M. P., Strouse G. F. (2006), Fluorescent lifetime quenching near $d = 1.5$ nm gold nanoparticles: Probing NSET validity, *J. Am. Chem. Soc.*, *128*, 5462-5467. (DOI: 10.1021/ja0583665)
29. Vaishnav J. K., Mukherjee T. K. (2017), Tuning of resonance energy transfer from 4',6-diamidino-2-phenylindole to an ultrasmall

silver nanocluster across the lipid bilayer, *Phys. Chem. Chem. Phys.*, *19*, 27305-27312. (DOI: 10.1039/C7CP05225A)

30. Hamilton D. J., Coffman M. D., Knight J. D., Reed S. M. (2017), lipid-coated gold nanoparticles and FRET allow sensitive monitoring of liposome clustering mediated by the synaptotagmin-7 C2A domain, *Langmuir*, *33*, 9222-9230. (DOI: 10.1021/acs.langmuir.7b01397)

31. Lee E. C., Valencia T., Allerson C., Schairer A., Flaten A., Yheskel M., Kersjes K., Li J., Gatto S., Takhar M., Lockton S., Pavlicek A., Kim M., Chu T., Soriano R., Davis S., Androsavich J. R., Sarwary S., Owen T., Kaplan J., Liu K., Jang G., Neben S., Bentley P., Wright T., Patel V. (2019), Discovery and preclinical evaluation of anti-miR-17 oligonucleotide RGLS4326 for the treatment of polycystic kidney disease, *Nat. Commun.*, *10*, 4148. (DOI: 10.1038/s41467-019-11918-y)

32. Bian X., Zhang Z., Xiong Q., De Camilli P., Lin C. (2019), A programmable DNA-origami platform for studying lipid transfer between bilayers, *Nat. Chem. Biol.*, *15*, 830-837. (DOI: 10.1038/s41589-019-0325-3)

33. Sun S., Liu Y., Xia J., Wang M., Tang R., Lei C., Huang Y., Nie Z., Yao S. (2019), A semisynthetic fluorescent protein assembly-based FRET probe for real-time profiling of cell membrane protease functions in situ, *Chem. Comm.*, *55*, 2218-2221. (DOI: 10.1039/C8CC09634A)

34. Chen Y., O'Donoghue M. B., Huang Y.-F., Kang H., Phillips J. A., Chen X., Estevez M. C., Yang C. J., Tan W. (2010), A surface energy transfer nanoruler for measuring binding site distances on live cell surfaces, *J. Am. Chem. Soc.*, *132*, 16559-16570. (DOI: 10.1021/ja106360v)

35. Carnevale K. J. F., Riskowski R. A., Strouse G. F. (2018), A gold nanoparticle bio-optical transponder to dynamically monitor intracellular pH, *ACS Nano*, *12*, 5956-5968. (DOI: 10.1021/acsnano.8b02200)

36. Waduge P., Bilgin I., Larkin J., Henley R. Y., Goodfellow K., Graham A. C., Bell D. C., Vamivakas N., Kar S., Wanunu M. (2015), Direct and scalable deposition of atomically thin low-noise MoS₂ membranes on apertures, *ACS Nano*, *9*, 7352-7359. (DOI: 10.1021/acsnano.5b02369)
37. Vaishnav J. K., Mukherjee T. K. (2019), Surfactant-induced self-assembly of CdTe quantum dots into multicolor luminescent hybrid vesicles, *Langmuir*, *35*, 6409-6420. (DOI: 10.1021/acs.langmuir.9b00357)
38. Zheng W., Liu Y., West A., Schuler E. E., Yehl K., Dyer R. B., Kindt J. T., Salaita K. (2014), Quantum dots encapsulated within phospholipid membranes: phase-dependent structure, photostability, and site-selective functionalization, *J. Am. Chem. Soc.*, *136*, 1992-1999. (DOI: 10.1021/ja411339f)
39. Wlodek M., Kolasinska-Sojka M., Szuwarzynski M., Kereiche S., Kovacik L., Zhou L., Islas L., Warszynski P., Briscoe W. H. (2018), Supported lipid bilayers with encapsulated quantum dots (QDs) via liposome fusion: Effect of QD size on bilayer formation and structure, *Nanoscale*, *10*, 17965-17974. (DOI: 10.1039/C8NR05877F)
40. Van Lehn R. C., Atukorale P. U., Carney R. P., Yang Y.-S., Stellacci F., Irvine D. J., Alexander-Katz A. (2013), Effect of particle diameter and surface composition on the spontaneous fusion of monolayer-protected gold nanoparticles with lipid bilayers, *Nano Lett.*, *13*, 4060-4067. (DOI: 10.1021/nl401365n)
41. Wang F., Liu J. (2015), A stable lipid/TiO₂ interface with headgroup-inversed phosphocholine and a comparison with SiO₂, *J. Am. Chem. Soc.*, *137*, 11736-11742. (DOI: 10.1021/jacs.5b06642)
42. Liu X., Li X., Xu W., Zhang X., Huang Z., Wang F., Liu J. (2018), Sub-angstrom gold nanoparticle/liposome interfaces controlled

by halides, *Langmuir*, 34, 6628-6635. (DOI: 10.1021/acs.langmuir.8b01138)

43. Wang F., Liu J. (2015), Self-healable and reversible liposome leakage by citrate-capped gold nanoparticles: probing the initial adsorption/desorption induced lipid phase transition, *Nanoscale*, 7, 15599-15604. (DOI: 10.1039/C5NR04805B)

44. Chance R. R., Prock A., Silbey R. (1975), Comments on the classical theory of energy transfer, *J. Chem. Phys.*, 62, 2245-2253. (DOI: 10.1063/1.430748)

45. Persson B. N. J., Lang N. D. (1982), Electron-hole-pair quenching of excited states near a metal, *Phys. Rev. B*, 26, 5409-5415. (DOI: 10.1103/PhysRevB.26.5409)

46. Reineck P., Gómez D., Ng S. H., Karg M., Bell T., Mulvaney P., Bach U. (2013), Distance and wavelength dependent quenching of molecular fluorescence by Au@SiO₂ core-shell nanoparticles, *ACS Nano*, 7, 6636-6648. (DOI: 10.1021/nm401775e)

47. Chhabra R., Sharma J., Wang H., Zou S., Lin S., Yan H., Lindsay S., Liu Y. (2009), Distance-dependent interactions between gold nanoparticles and fluorescent molecules with DNA as tunable spacers, *Nanotechnology*, 20, 485201. (DOI: 10.1088/0957-4484/20/48/485201)

48. Breshike C. J., Riskowski R. A., Strouse G. F. (2013), Leaving Förster resonance energy transfer behind: Nanometal surface energy transfer predicts the size-enhanced energy coupling between a metal nanoparticle and an emitting dipole, *J. Phys. Chem. C*, 117, 23942-23949. (DOI: 10.1021/jp407259r)

Chapter 8

Conclusions and Future Scopes

8.1. Conclusions

In recent years, multifunctional self-assembled nanocomposites such as hybrid vesicles, polymersomes, hydrogels, nanocapsules, and colloidal coacervate droplets have gained vast attention due to their potential in basic research as well as in technology related fields. The design and fabrication of most of the nanocomposites are complex and time-consuming, spontaneous self-assembly of oppositely charged polymer and the surfactant is relatively simple. Such QDs and polymer and surfactant-based nanostructures will certainly pave the way for exploring new smart nanomaterials with tunable properties and good stability. Therefore, it's important to understand the mechanism of the formation and broad range of stability of these nanostructures. Here in this thesis, the detailed investigation of self-assembled nanostructures between CdTe QDs and PDADMAC as well as with CTAB has been illustrated.

Next, understanding, and precise control over EET in nanoscale materials are of utmost importance due to enormous importance in fundamental research and various technology-related fields such as photovoltaics, light-emitting diodes (LEDs), sensors, and bioimaging. Efficient tuning of EET efficiency as a function of separation distance is of fundamental importance. Despite numerous reports, it's important to develop a new donor-acceptor pair to probe the nanoscopic distance at the bilayer thickness. Here in this thesis, EET's detailed mechanism from CdTe QDs as a donor to plasmonic NPs (Au and Ag NPs) as acceptors has been demonstrated. Furthermore, the effect of the modulation of the separation distance between donor-acceptor pair such as CdTe QDs-AuNPs and DAPI-Ag NCs in the presence of liposome on the efficiency of energy transfer has also been demonstrated in detail. The next section discusses the chapter-wise conclusion of the entire work of this thesis.

In chapter three, the fabrication of inherent luminescent organic-inorganic hybrid coacervate of CdTe QDs and PDADMAC is demonstrated in an aqueous medium. This coacervates are highly

photostable as well as 2P active. Initially, at a very low concentration of polymer, formation of nanocomposite of QD-PDADMAC is take place which subsequently forms spherical droplets upon increasing the concentration of polymer. These hybrids droplets show stability over the broad range of composition, pH and ionic strength of the medium. Moreover, the fabrication of mixed two-color luminescent droplets also shown here which may open up a new avenue for the design of multifunctional hybrid materials for nanocatalysis and nanosensing application.

In chapter four, the fabrication of multicolor luminescent hybrid vesicles are shown upon the interaction of CdTe QDs and CTAB surfactant. Initially, CdTe QDs and CTAB surfactant form small aggregate through ion-pairs formation which finally leads to the formation of vesicles. In addition, we have also shown the formation of multicolor luminescent vesicles by simple tuning of QD size. The encapsulation property of these hybrid vesicles has been illustrated by loading Rh6G dye inside their hollow aqueous cavity. While these hybrid vesicles are highly pH sensitive at acidic pH (pH~4.5-5.5) shows diassebility whereas stable in basic pH (pH~ 6.5-11). Furthermore, using SEM and confocal imaging we have shown that this pH-responsive assembly-disassembly process is reversible. The present findings clearly highlight the potential of these hybrid vesicles for various applications such as drug delivery and sensing.

In chapter five, simple liposome-based tuning of FRET are shown for DAPI and Ag NCs system. In aqueous buffer, the Ag NC efficiently quenches the fluorescence of nearby DAPI by a nonradiative FRET process. It has been observed that the efficiency of EET from the liposome bound DAPI to the Ag NC is strongly dependent on the location of the donor DAPI within the liposome matrix. In aqueous buffer, DAPI transfers its excitation energy to the nearby Ag NC with an efficiency of 76%. However, the association of DAPI with the outer surface of the liposome results in lowering of the energy transfer efficiency from a bulk value of 76% to 39%. In contrast, complete

encapsulation of DAPI into the hydrophilic aqueous core of the liposome results in complete inhibition of this FRET process. This location specific interaction between DAPI and the Ag NC inside the liposome matrix is important to understand various fundamental biophysical processes across the cell membrane.

In chapter six, the fundamental mechanism behind the size and wavelength-dependent electromagnetic coupling and subsequent long range EET between three different size CdTe QDs and plasmonic NPs (Au and Ag NPs) have been explored. While Au NPs significantly quench the PL intensity and lifetime of green QDs and shows maximum quenching close to the LSPR of Au NPs. However, there is no such quenching phenomenon has been observed for yellow and red QDs even with noticeable spectral overlap. These results clearly indicate that mere spectral overlap between the emission spectrum of donor and LSPR of metal NP in a hybrid colloidal mixture is not sufficient for resonant EET. Our findings reveal strong electromagnetic coupling of LSPR of Au NPs and excitonic emission of green QDs, which leads to significant PL quenching due to nonradiative EET from photoexcited QDs to the surface of Au NPs. In contrast, size-independent PL quenching in the presence of Ag NPs having LSPR significantly off resonance with the excitonic emission of all the three differently sized QDs arises as a consequence of nonradiative PET process. Furthermore, it has been observed that surface passivation with the help of bulky PEG 6000 molecules at the surface of Au NPs results in a significant lowering of the efficiency of this EET process due to the increase in the effective separation distance between QD and the surface of Au NPs. The effective separation distance between QD and the surface of citrate and PEG-capped Au NP has been estimated using a modified SET model and the obtained distances correlate well with our present system. Our study reveals that it is possible to tune the optoelectronic properties of a hybrid plexcitonic system by modulating inherent complex nonradiative processes which in turn depend on various factors such as size and nature of metal NPs, spectral overlap, separation distance and surface

charge on particles. The present findings may be useful to understand the fundamental nonradiative processes in various hybrid plexcitonic systems.

In chapter seven, the effect of the partitioning of donor and acceptor inside DPPC liposome on the extent of EET has been demonstrated using PL spectroscopy and CLSM. Au NPs efficiently quench the PL of CdTe QDs by nonradiative NSET process in bulk aqueous medium. Modulation of this NSET process across the lipid bilayer of DPPC liposome has been demonstrated in the present study. It has been observed that the extent of NSET between QDs and Au NPs does not alter in the presence of DPPC liposome upon instant mixing. However, the NSET process completely disappears upon the formation of LipQD nanocomposite, where QDs are selectively encapsulated into the aqueous core of liposomes. This has been explained by considering increased separation distance between the donor (LipQD) and acceptor (Au NPs). Interestingly, the formation of AuLipQD nanocomposites results in the reappearance of NSET between encapsulated QDs and adsorbed Au NPs at the surface of liposomes. Our present findings of selective uptake and modulation of NSET between QDs and Au NPs across the lipid bilayer of DPPC liposomes may find importance in understanding various fundamental biophysical processes across the lipid bilayer and biological cell membrane.

8.2. Scope for Future Works

Self-assembly is one of the most important areas of chemistry, materials science, and biology. The present thesis shows the fabrication of a new class of luminescent hybrid self-assembled nanostructures. The systematic fabrication of luminescent organic-inorganic hybrid biomimetic nanostructures such as coacervate and vesicle have been demonstrated in chapter 3 and 4. The present study can be easily extended to fabricate a wide range of hybrid self-assembled nanostructures with various inorganic counterparts such as CdSe QDs, CdS QDs, CDs, Cu NCs, Ag NCs, and Au NCs having unique

optoelectronic properties, which will further expand their applicability in nanocatalysis, bioimaging, and biosensing. There has been significant interest in self-assembled coacervate droplets due to the membraneless organelles. These properties make coacervate droplets ideal as promising bioreactors. Therefore, complex enzymatic reactions can be studied effectively inside the highly charged and crowded interior of coacervate droplets.

Further, in chapters 5,6 and 7, the fundamental mechanism of the EET and tuning of the EET in the presence of liposome from various photoexcited donors such as MSA-capped CdTe QDs and DAPI to Au NPs and Ag NCs as acceptors has been illustrated. The influence of metal nanostructures on the fluorescence yield of the nearby fluorophore is very complex and depends on various parameters such as the size and shape of the metal nanostructures, the distance between the fluorophore and metal nanostructure, and spectral overlap. It has often been observed that noble metal NPs with distinct LSPR significantly alter nearby fluorophores' emission properties. This phenomenon is either observed as enhancement or quenching of the fluorescence quantum yield of nearby fluorophores. It is important to understand the mechanism and dynamics of PL quenching of photoexcited donor in the presence of metal NPs. Therefore, the effect of PL quenching of different types of QDs and core-shell QDs such as CdSe, CdS and CdSe/ZnS QDs in the presence of metal NPs such as Au NPs, Ag NPs, and Cu NPs can be studied systematically to gain a better understanding about the mechanism behind the EET processes.